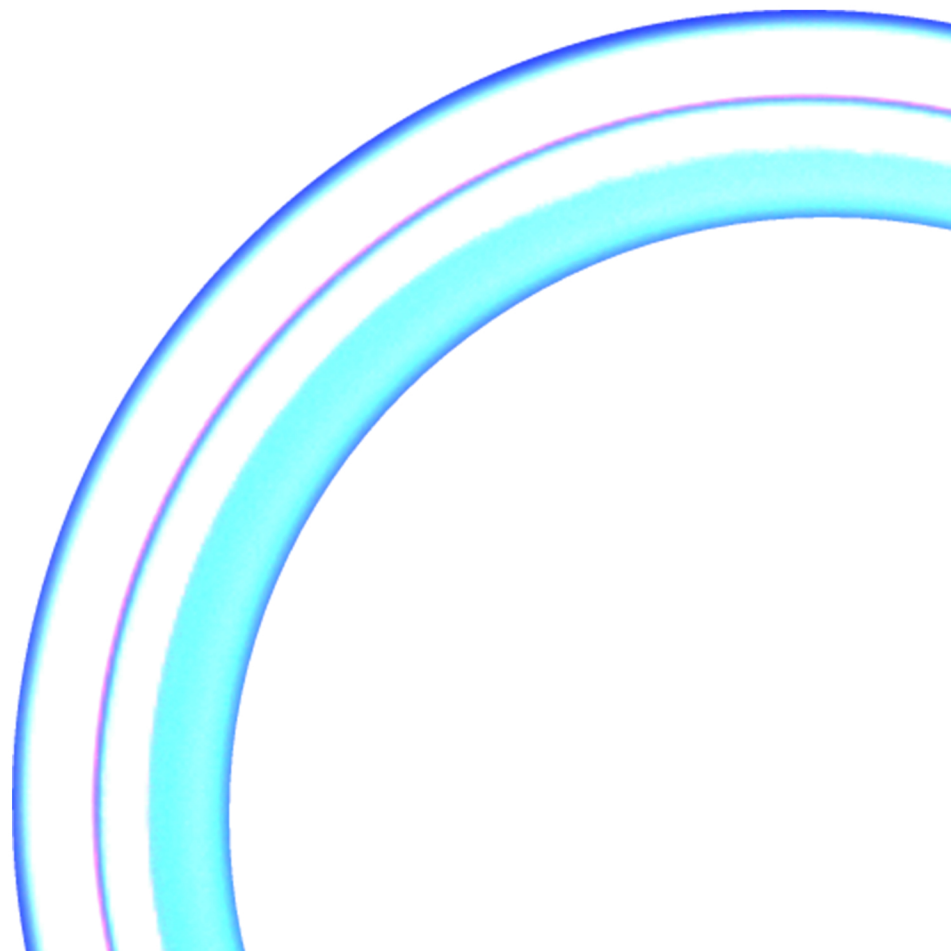
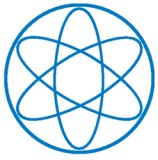


Fakultät für Physik der Technischen Universität München  
Forschungs-Neutronenquelle Heinz Maier-Leibnitz (FRM II)  
Physik-Department E13

Tobias Hollmer

# Development of a PVD-based manufacturing process of monolithic LEU irradiation targets for $^{99}\text{Mo}$ production





Fakultät für Physik der Technischen Universität München  
Forschungs-Neutronenquelle Heinz Maier-Leibnitz (FRM II)  
Physik-Department E13

Tobias Hollmer

# Development of a PVD-based manufacturing process of monolithic LEU irradiation targets for $^{99}\text{Mo}$ production

Vollständiger Abdruck der von der Fakultät für Physik der Technischen Universität München zur Erlangung des akademischen Grades eines

Doktors der Naturwissenschaften (Dr. rer. nat.)

genehmigten Dissertation.

Vorsitzender: Univ.-Prof. Dr. Martin Zacharias

Prüfer der Dissertation:

1. Univ.-Prof. Dr. Winfried Petry

2. Univ.-Prof. Dr. Peter Böni

Die Dissertation wurde am 13. Juli 2015 bei der Technischen Universität München eingereicht und durch die Fakultät für Physik am 3. August 2015 angenommen.

## ABSTRACT

$^{99}\text{Mo}$  is the most widely used radioactive isotope in nuclear medicine worldwide. Its main production route is the fission of uranium. A major challenge for a reliable supply of  $^{99}\text{Mo}$ , is the conversion from high enriched uranium (HEU) to low enriched uranium (LEU). A promising candidate to realize this conversion is the cylindrical LEU irradiation target. The target consists of a uranium foil, which is encapsulated between two coaxial aluminum cladding cylinders. The main advantage of this target is a high mechanical stability against potential critical swelling and the possibility to separate the uranium from the aluminum. The separation is made possible by an interlayer material between the uranium and the aluminum cladding. This allows a separate processing of the irradiated uranium foil and the cladding when recovering the  $^{99}\text{Mo}$ . In current processing schemes the target is dissolved in alkaline or acidic solution. Due to the removal of the aluminum cladding, the necessary volume of the dissolver liquid and the processing time is reduced. Thereby, both the costs and the amount of highly radioactive liquid waste are significantly reduced.

Within this work, the complete fabrication of a cylindrical LEU target was demonstrated using a newly developed manufacturing method. Hereby, the uranium as well as the interlayer material is coated directly on the inside of the outer cladding cylinder. This process was realized by a cylindrical magnetron enhanced PVD technique (sputtering). Main design goal was the production of a self-supporting uranium foil with a homogenous thickness and a controllable adhesion to the aluminum cladding. At the same time a high material utilization should be assured. The design of the apparatus allowed the adjustment of following process parameters: magnetic field, gas pressure, sputter power, substrate temperature and movement of the sputter source. Using copper as a surrogate material for uranium, the coating device was extensively parametrized. Magnetic field and gas pressure were optimized to guarantee both a stable process and a high deposition rate. To control the layer thickness, an algorithm was developed, which allows to describe the layer growth in real time and to simulate different coating procedures. This algorithm was used to optimize the movement of the sputter source in order to achieve a homogenous thickness profile and maximize the material utilization of the process.

The mechanical properties of the produced layers were adjusted by the deposition temperature, which is a result of the externally applied substrate temperature and the sputter power. Using a high deposition temperature, layers with a good mechanical strength were produced. Their adhesion to the cladding could successfully be controlled by the application of aluminum or graphite interlayers. In this way, self-supporting foils were produced, which were easily separable from the cladding. The material utilization of the uranium sputter process was approximately 92%. Together with the efficiency obtained at the production of sputter targets by casting, the overall material utilization was approximately 87%.

Next to the coating process, the assembly of the irradiation target was investigated. To assemble the target, the inner cladding cylinder is inserted after the coating process and then widened to guarantee a good thermal contact to the uranium foil. Within this work, the feasibility of two forming processes was tested: conventional forming using a hydraulic actuated plug and electromagnetic forming. It showed that both processes are capable to perform a suitable deformation of the target cylinders. However, for the electromagnetic forming a high forming energy was necessary, which made the process hard to control. In contrast, the conventional hydraulic forming proved to be highly practical and well-defined.



# Table of contents

---

<b>1</b>	<b>Motivation</b> .....	<b>1</b>
1.1	Properties of technetium-99m .....	1
1.2	Technetium-99m supply chain .....	3
1.3	Challenges to the reliability of the <sup>99</sup> Mo supply .....	9
1.4	Next level irradiation targets and the cylindrical foil target .....	10
1.5	Target manufacturing by sputtering and aim of this thesis .....	12
<b>2</b>	<b>Theoretical background</b> .....	<b>15</b>
2.1	Low pressure plasma .....	16
2.2	Particle ejection .....	18
2.3	Sputter target.....	24
2.4	Layer growth.....	25
2.5	Technical realization .....	27
<b>3</b>	<b>Instrumentation</b> .....	<b>33</b>
3.1	Predevelopment: fixed target set-up .....	33
3.2	Concept of the moving target set-up .....	36
3.3	Substrate .....	38
3.4	Sputter source .....	39
3.5	Vacuum and gas supply system .....	42
3.6	Magnetic coil.....	44
3.7	Cooling und temperature control .....	46
3.8	PLC control .....	48
3.9	Glove box integration .....	50
3.10	Coating procedure .....	52
<b>4</b>	<b>Deposition results</b> .....	<b>55</b>
4.1	Materials .....	55
4.2	Sputter parameters.....	60
4.3	Thickness profile.....	69
4.4	Sputter behavior .....	76
4.5	Adhesion.....	88
<b>5</b>	<b>Irradiation target assembly</b> .....	<b>97</b>
5.1	Background .....	97
5.2	Axial hydraulic forming .....	100
5.3	Magnetic forming.....	107
<b>6</b>	<b>Conclusion and outlook</b> .....	<b>115</b>
<b>7</b>	<b>Appendix</b> .....	<b>i</b>
A	List of figures .....	i
B	List of tables .....	xi
C	Bibliography.....	xiii



# 1 MOTIVATION

The introduction of technetium-99m ( $^{99m}\text{Tc}$ ) for thyroid imaging in 1964 marks the beginning of diagnostic nuclear medicine. Since then  $^{99m}\text{Tc}$  is the most widely used radioisotope in nuclear medicine for diagnostic imaging worldwide. To guarantee a reliable and sufficient supply of  $^{99m}\text{Tc}$ , its production methods are still a research topic of great interest. In this thesis, a novel manufacturing method for irradiation targets, which are used to produce molybdenum-99 ( $^{99}\text{Mo}$ ), the mother nuclide of  $^{99m}\text{Tc}$ , is investigated.

## 1.1 PROPERTIES OF TECHNETIUM-99M

$^{99m}\text{Tc}$  is a metastable nuclear isomer of  $^{99}\text{Tc}$ . It is obtained by the  $\beta^-$ -decay of molybdenum-99 ( $^{99}\text{Mo}$ ). A detailed decay scheme of  $^{99}\text{Mo}$  is shown in [Figure 1](#). Approximately 86.5% of the  $^{99}\text{Mo}$  nuclei decay to the metastable isotope  $^{99m}\text{Tc}$ , whereas the rest relaxes to its ground state  $^{99}\text{Tc}$ . The ground state decays further with a  $\beta^-$ -decay to the stable ruthenium-99 ( $^{99}\text{Ru}$ ). This decay features a physical half-life of  $2 \cdot 10^6$  a and a beta energy of 200 keV.

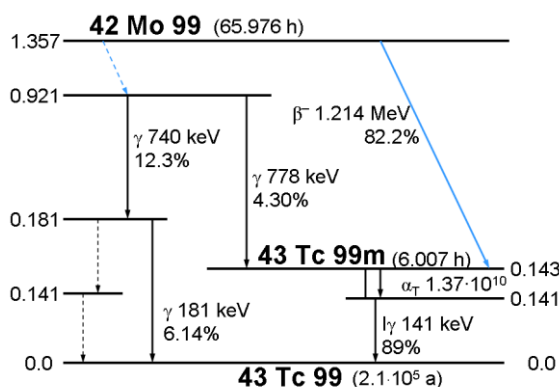


*Figure 1: Detailed decay scheme of  $^{99}\text{Mo}$ . [1]*

With a half-life of approximately 6 hours, the metastable  $^{99m}\text{Tc}$  undergoes an isomeric transition to  $^{99}\text{Tc}$ . Thereby, it emits a 141 keV photon. Due to the short half-life, the decay process of  $^{99m}\text{Tc}$  features a high gamma activity. This activity together with the low energy of the photon allow for an easy detection with scintillation instruments, such as gamma cameras.

Next to these suitable physical properties,  $^{99m}\text{Tc}$  also features a very versatile chemistry. This means that technetium can be combined with a large variety of organic and biological active substances. Therefore, a wide variety of radio pharmaceuticals can be fabricated. To produce such a radio pharmaceutical, in most cases a chelating group is attached to the bioactive molecule of interest. The resulting combined ligand forms a complex with  $^{99m}\text{Tc}$  [2]. Injected in the human blood circulation these labeled molecules accumulate in the region of interest. This accumulation can then be localized by the detection of the emitted radiation with medical imaging equipment. Due to the short biological half-life<sup>1</sup> of 1d, the absorbed dose is relatively

<sup>1</sup> The biological half-life is the time until the radioactivity of the radio pharmaceutical is reduced to a half inside the human body. It is defined by the body's cleansing process.

low, when introduced into a human body. The variety of bioactive molecules that can be labeled with  $^{99m}\text{Tc}$  is large. This allows for a multitude of medical applications e.g. imaging and functional studies of the brain, myocardium, thyroid, lungs, liver, gallbladder, kidneys, skeleton, blood and tumors.

To give an example, a SPECT/CT scintigraphy of a human ankle is shown in **Figure 2**. A SPECT/CT is a single-photon emission computed tomography, which is overlapped with a conventional X-ray computed tomography. A SPECT uses a gamma camera to determine the three dimensional distribution of photon emitting radionuclides in the human body. The radionuclide is injected into the patient's blood circulation, from where it is distributed to the different organs and tissues. By studying the transport and accumulation of the radionuclide, conclusions about the metabolism processes can be drawn. A CT uses X-rays to produce a three dimensional model of the patient's bone structure and organs. By combining these two methods, the metabolism activity can be mapped to the bone structure or organs [3].

In case of **Figure 2**, a bone scintigraphy of the upper ankle joint was performed. For the examination, 457 MBq of  $^{99m}\text{Tc}$ -hydroxydiphosphonate ( $^{99m}\text{Tc}$ -HDP) was used as radio pharmaceutical.  $^{99m}\text{Tc}$ -HDP accumulates in bones with high osteogenic activity and skeletal blood flow. The bone scintigraphy was done in three phases. One series of records was taken directly after the injection of the pharmaceutical. Another set was made several minutes afterwards. And a last one was taken approximately 2h later. Depending on the pathology, the  $^{99m}\text{Tc}$ -HDP concentration peaks in one or several of these phases. In the current case, a concentration in phase one and two indicates an inflammatory process in the ankle joint. A remaining concentration in phase 3 is caused by an increased bone turnover indicating an osteochondral lesion [4, 5].

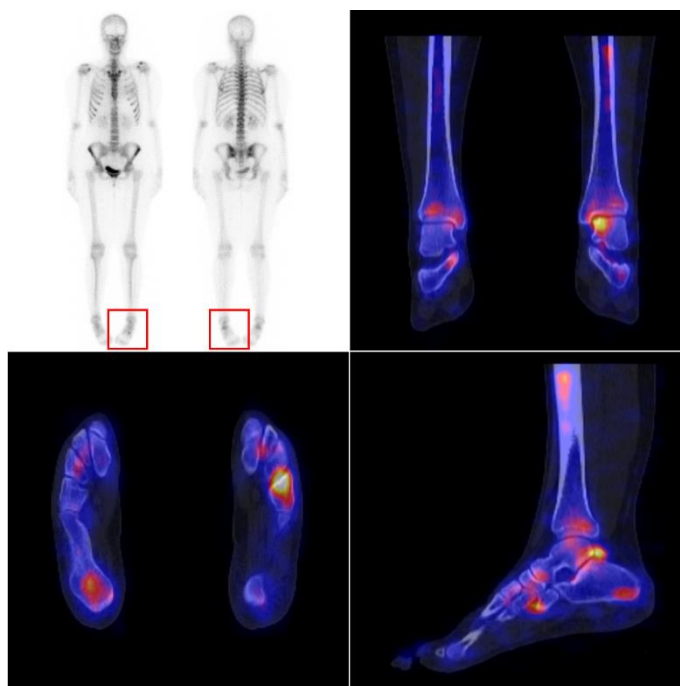


**Figure 2: Bone scintigraphy of the Articulatio talocruralis.** The images show a SPECT-CT recording of a left ankle. Hereby a conventional X-ray CT is superposed by a scintigraphy using  $^{99m}\text{Tc}$  as a  $\gamma$ -emitting radioisotope. The bright/red areas show an increased bone metabolism due to inflammation. [6]

The described advantageous physical and chemical properties make  $^{99m}\text{Tc}$  the work-horse of nuclear medicine. In 2012 approximately 85% of the diagnostic nuclear medicine procedures



were performed with  $^{99m}\text{Tc}$ , accumulating to approximately 30 million procedures per year [7]. This high demand and its importance in medical imaging require a sufficient and reliable supply of  $^{99m}\text{Tc}$  and consequently  $^{99}\text{Mo}$ .

## 1.2 TECHNETIUM-99M SUPPLY CHAIN

### 1.2.1 PRODUCTION OF $^{99}\text{Mo}$

$^{99}\text{Mo}$  and  $^{99m}\text{Tc}$  can theoretically be produced in variety of different ways. An overview is given in **Figure 3**. A feasibility study and the technology readiness of each process is given in [8].

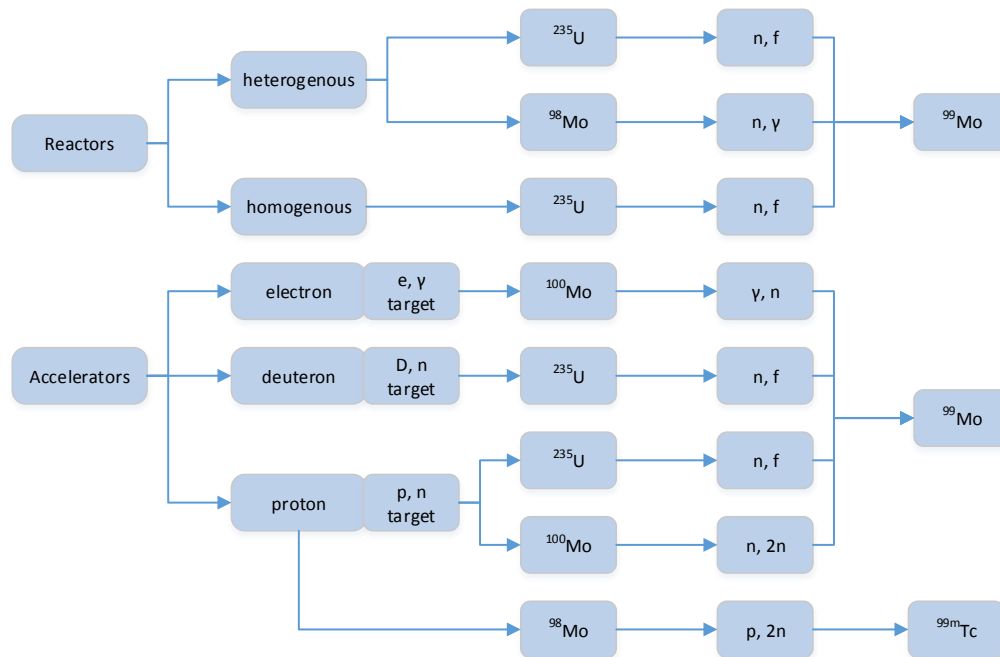


**Figure 3: Overview of  $^{99}\text{Mo}$  and  $^{99m}\text{Tc}$  production schemes. [9]**

The two main ways to produce  $^{99}\text{Mo}$  are the fission of  $^{235}\text{U}$  with neutrons or, in a minor extent, the direct neutron capture of  $^{98}\text{Mo}$ . The production rate  $R$  of both processes is expressed by

$$R \sim N\sigma\Phi \quad (1)$$

where  $N$  is the target number density ( $^{235}\text{U}$  or  $^{98}\text{Mo}$ ),  $\Phi$  the neutron flux and  $\sigma$  the reaction cross-section in barn ( $=10^{-24} \text{ cm}^2$ ). The cross-section is a measure for the probability of the reaction of interest.

The production of  $^{99}\text{Mo}$  is counteracted by its decay. Therefore, a saturation value is reached, which directly depends on the production rate. The build-up of  $^{99}\text{Mo}$  can be approximated by following formula:

$$A(t) \sim N\sigma\Phi(1 - e^{-\lambda t}) \quad (2)$$

where  $A(t)$  is the activity of the produced  $^{99}\text{Mo}$  and  $\lambda$  the decay constant of  $^{99}\text{Mo}$ .

In case of the fission process, the effective cross-section results from the fission cross-section of  $^{235}\text{U}$  and the resulting yield of  $^{99}\text{Mo}$ . The thermal-neutron fission cross-section of  $^{235}\text{U}$  is 582.6 barn at a neutron energy of 25 meV [10]. **Figure 4** shows the mass spectrum of the resulting fission products for thermal fission of  $^{235}\text{U}$ . The spectrum features two peaks approximately positioned at mass numbers 95 and 140.

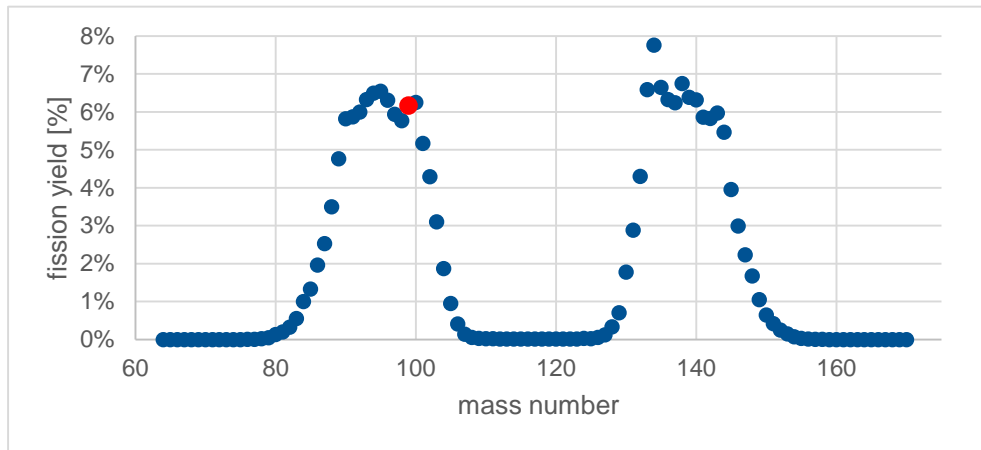


**Figure 4: Chain yield for the thermal neutron fission of  $^{235}\text{U}$ .** The red marking shows mass number 99 with a fission yield of 6.132%. [1]

Mass number 99 is located near the center of the left peak and has a high yield rate of 6.132% of all fission elements [1]. Stable heavy nuclei (like  $^{235}\text{U}$ ) have a certain neutron excess in order to compensate the increasing repulsion of the protons. At the fission process, this neutron excess is passed on to the direct fission products. In these fission products, however, lower energy states can be realized by the transition of these excess neutrons to protons. Therefore, most of the direct fission products are unstable and relax by a  $\beta^-$ -decay. In case of mass number 99, all elements with a proton number higher than 42 ( $^{99}\text{Mo}$ ) have a half-life less than 3 minutes (see **Figure 5**).

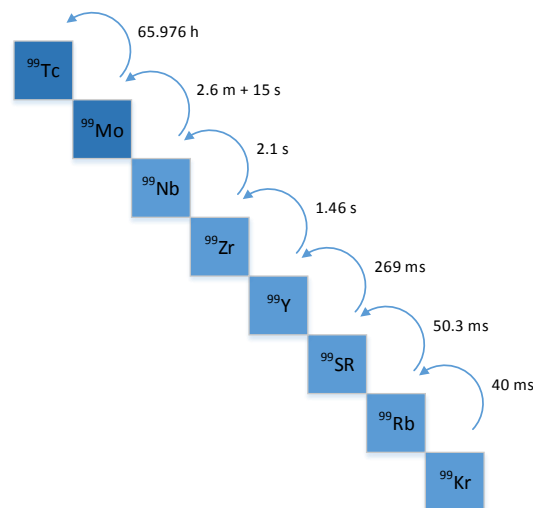


**Figure 5:  $\beta^-$  decays of mass number 99.** Due to their neutron excess the isotopes with a mass number of 99 and a proton number below 44 undergo a  $\beta^-$ -decay with the indicated half-life times. [11]

These low half-life times, when compared to 65.976h of  $^{99}\text{Mo}$ , result in an accumulation of the fission products at neutron number 42. Therefore, the fission of uranium yields approximately 6%  $^{99}\text{Mo}$ , almost identical to the whole fission yield of mass number 99. Taking this yield into consideration, the effective cross-section for the production of  $^{99}\text{Mo}$  results in approximately 35 barn.

In comparison, the direct neutron capture process of  $^{98}\text{Mo}$  has a cross-section of 0.13 barn for thermal neutrons [12]. The resulting lower production rate and, therefore, total yield is to a certain extent compensated by the much easier and faster processing of irradiated  $^{98}\text{Mo}$  due to its significantly lower radioactivity compared to irradiated  $^{235}\text{U}$ . However, the direct neutron capture process also suffers from a low specific activity since the product is contaminated with a high amount of  $^{98}\text{Mo}$ . Since a later isotope separation is not feasible, this would result in significantly larger  $^{99\text{m}}\text{Tc}$ -generators (see chapter 1.2.4).

Because of these reasons, the main production method of  $^{99}\text{Mo}$  is the fission of uranium in nuclear reactors. Since the saturation value directly depends on the available thermal neutron flux, preferably high-flux nuclear reactors (e.g. research reactors) are used. An overview over the reactor-based  $^{99\text{m}}\text{Tc}$  supply chain is shown in Figure 6.

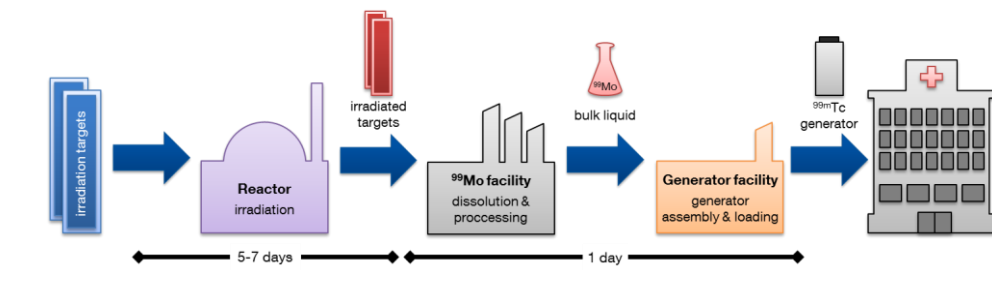


Figure 6:  $^{99\text{m}}\text{Tc}$  supply chain. [13]

For  $^{99}\text{Mo}$  production, the uranium is irradiated in dedicated so-called *irradiation targets*. One target is typically irradiated for 6 days. By then approximately 78% of the saturation value is reached. After a cooling period of typically 12 h, the irradiation target is packed into a heavy container and shipped to a processing facility. There it is chemically dissolved in a hot cell and the  $^{99}\text{Mo}$  is extracted by subsequent chemical isolation. In a further step, the  $^{99}\text{Mo}$  is loaded into  $^{99\text{m}}\text{Tc}$ -generators, which are then shipped to the hospitals. A typical build-up of  $^{99}\text{Mo}$  during irradiation of a target and its activity during subsequent processing and use is shown in Figure 7.

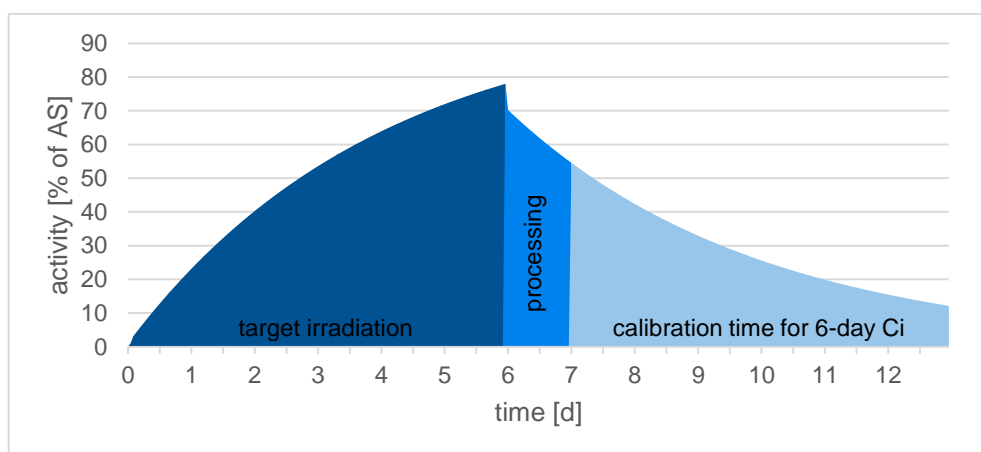


Figure 7: Build-up of  $^{99}\text{Mo}$ . During an irradiation time from 5 to 7 days  $^{99}\text{Mo}$  is built-up to approximately 78% of the saturation value. Afterwards the target is mechanically and chemically processed to extract the  $^{99}\text{Mo}$  from the irradiation targets. In this process around 10% of activity is lost. After a processing time of 24h, the  $^{99}\text{Mo}$  is ready for shipping. The  $^{99}\text{Mo}$  is sold on units of activity, usually calibrated to the activity 6 days after processing. This quantity is called 6-day curies. [12]

### 1.2.2 THE IRRADIATION TARGET

Usually, irradiation targets consist of a uranium compound or alloy in a matrix material, the so-called *meat*, and an outer surface, the so-called *cladding*. These irradiation targets have to fulfil certain safety requirements:

- The targets have to contain the radioactive fission products to guarantee a safe operation and prevent any release of radioactive contamination.
- While the targets have to contain a sufficient amount of fissile  $^{235}\text{U}$  (typically 4 g), they also have to provide an effectual heat dissipation to remove the generated fission heat. For example at an average thermal neutron flux of  $2 \cdot 10^{14} \frac{\text{n}}{\text{cm}^2 \text{s}}$ , a fission heat of approximately 30 kW is produced in 4 g of  $^{235}\text{U}$ . These values are calculated for a planned irradiation site at the FRM II reactor (D) [14].
- The targets have to be compatible with the mechanical and chemical process used to recover the produced  $^{99}\text{Mo}$ .

Irradiation targets exist in a variety of different shapes and material compositions. The targets differ in geometry (e.g. plate-type targets, pin-type targets), meat material (e.g.  $\text{UO}_2$ , metallic U, U alloy) or the cladding material (e.g. Al, Zr). Irradiation targets can be categorized into two main categories, LEU-targets using low enriched uranium and HEU-targets using high enriched uranium. The enrichment refers to the percentage of fissile  $^{235}\text{U}$  isotopes in the uranium. Natural uranium consists of 0.72%  $^{235}\text{U}$ , 99.2%  $^{238}\text{U}$  and a minor amount of other isotopes. In enriched uranium the share of  $^{235}\text{U}$  is increased by isotope separation to make the uranium usable in nuclear reactors. The term high-enriched uranium is usually used for an enrichment above 20% [15]. Hence, the term low-enriched uranium is used for an enrichment below 20%.

For the last decades the work-horse for  $^{99}\text{Mo}$  production is the HEU target used in two geometries: pin-type and plate-type. The plate-type target consists of a uranium aluminide/aluminum-alloy dispersion meat with an aluminum cladding. The pin-type target uses a uranium aluminum alloy in an aluminum cladding. **Table 1** shows the four main producers of  $^{99}\text{Mo}$  and their target geometries. In 2009 these four companies produced approximately 99% of the  $^{99}\text{Mo}$  world supply.

**Table 1: Major  $^{99}\text{Mo}$  producers.** [13, 16]

$^{99}\text{Mo}$ producers	Reactors	Target type	Target enrichment	Share of world supply in 2009
<b>MDS-Nordion (CA)</b>	NRU (CA)	Pin-type	HEU	40
<b>Malinckrodt (USA, NL)</b>	HFR (NL), BR2 (BE), Osiris (F)	Plate-type	HEU	29
<b>IRE (BE)</b>	HFR (NL), BR2 (BE), Osiris (F)	Plate-type <sup>2</sup>	HEU	12
<b>NTP (ZA)</b>	Safari (ZA)	Plate-type	HEU	18

<sup>2</sup> The IRE target is a HEU-aluminide dispersion plate target, which is curved and welded to a cylindrical target. [17]

### 1.2.3 CHEMICAL PROCESSING OF THE IRRADIATION TARGET

After irradiation, the targets are chemically dissolved in order to recover the produced  $^{99}\text{Mo}$ . Depending on the type of target this dissolution can be done by an alkaline or acidic process.

Usually targets containing aluminum are dissolved in an alkaline process. One user of this process is the Institute National des Radioelements (IRE), a major producer of  $^{99}\text{Mo}$ . Their process is described in [18]. First, the target including its cladding is dissolved in sodium hydroxide ( $\text{NaOH}$ ) and sodium nitrate ( $\text{NaNO}_3$ ). This leads to a release of the fission gas xenon-133 ( $^{133}\text{Xe}$ ), which is trapped and shipped to a purification plant. The remaining uranium and a large part of the fission products precipitate and can be filtered from the liquid. This liquid contains the molybdenum in form of molybdate  $\text{MoO}_4^{2-}$ . In a next step, the liquid is acidified by the addition of nitric acid ( $\text{HNO}_3$ ). This process releases gaseous iodine-131 ( $^{131}\text{I}$ ), which is also trapped and purified. The remaining liquid is then passed through an alumina column, where the  $^{99}\text{Mo}$  is adsorbed. 90% of the other fission products are eliminated in this step. Afterwards the  $^{99}\text{Mo}$  is again washed out of the column by ammonium hydroxide ( $\text{NH}_4\text{OH}$ ) and adsorbed to a resin. This resin is then washed with water and again eluted with carbon trioxide ( $\text{CO}_3$ ). The resulting liquid is once again acidified and then adsorbed to activated carbon. In a last step, the  $^{99}\text{Mo}$  is eluted from the carbon with sodium hydroxide. The resulting liquid is then qualified by measuring the total activity and the radionuclide purity.

As an alternative there is the acidic process. This process is usually used for uranium oxide and uranium metal. One version is the Cintichem production process, which was used during the 1980s by the Cintichem reactor (USA) to process uranium dioxide targets. This process is described in [19]. First, the target meat is dissolved by a mixture of sulfuric acid ( $\text{H}_2\text{SO}_4$ ) and nitric acid. In this step, the gaseous fission products and nitrous oxides are released and trapped. The  $\text{UO}_2$  is oxidized by the nitric acid to  $\text{UO}_2^{2+}$  and the sulfuric acid builds uranyl sulfate complexes. The resulting acidic fission product solution is then filtered and a low amount of a non-radioactive molybdenum carrier is added. This carrier guarantees a full isolation of the  $^{99}\text{Mo}$ . By adding potassium permanganate ( $\text{KMnO}_4$ ) to the solution, the molybdenum is oxidized to  $\text{Mo}^{6+}$  and subsequently precipitated by  $\alpha$ -benzoin oxime. The precipitate is then filtered and washed with sulfuric acid. In the next step, the precipitate is dissolved by sodium hydroxide and then purified by chromatography columns to remove organic residues from the  $\alpha$ -benzoin oxime. After filtering the resulting liquid, the final solution is obtained. This liquid is a solution of  $\text{Na}_2\text{MoO}_4$  in  $\text{NaOH}$ .

Each of the two dissolution processes has its own assets and drawbacks, however both processes can deliver a highly pure product with a  $^{99}\text{Mo}$  recovery yield of 85 to 90% and both processes can be used for low-enriched uranium (LEU) and high-enriched uranium (HEU) targets [12]. At present day, the only major producer of  $^{99}\text{Mo}$ , which uses an acidic process, is MDS-Nordion.

### 1.2.4 THE $^{99\text{m}}\text{Tc}$ -GENERATOR

After chemical isolation, the  $^{99}\text{Mo}$  is adsorbed onto alumina columns, which are then built into radiation-shielded vessels, so-called  $^{99\text{m}}\text{Tc}$ -generators (Figure 8). These generators are shipped to the hospitals, where the generated  $^{99\text{m}}\text{Tc}$  can be used for medical applications. Inside the generator the  $^{99}\text{Mo}$  continuously decays to  $^{99\text{m}}\text{Tc}$ . Unlike the adsorbed  $^{99}\text{Mo}$ , the  $^{99\text{m}}\text{Tc}$  can be washed out from the generator with a saline solution. This process is called elution. Hereby, the  $^{99\text{m}}\text{Tc}$  is dissolved in the liquid whereas the  $^{99}\text{Mo}$  stays on the alumina column. For this reason, a  $^{99\text{m}}\text{Tc}$ -generator can be eluted several times a day for approximately one week. An exemplary elution of a  $^{99\text{m}}\text{Tc}$ -generator is shown in Figure 9.

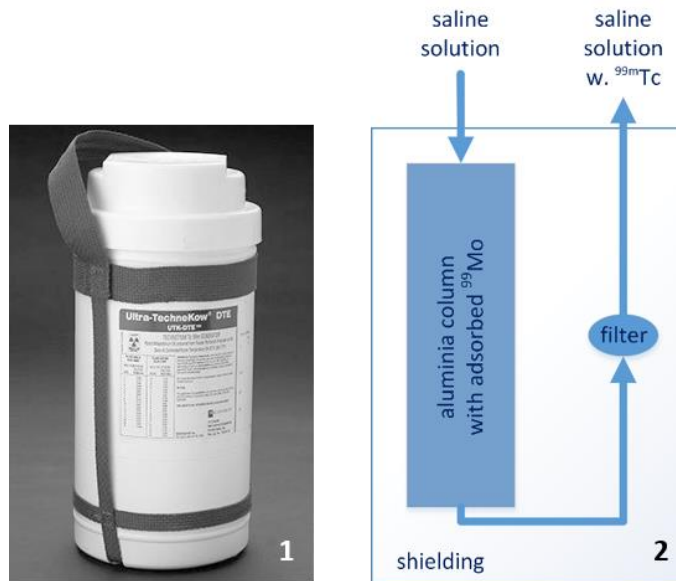


**Figure 8:  $^{99\text{m}}\text{Tc}$  generator.** 1) Photo of a Ultra-TechneKow DTE generator from Mallinckrodt Pharmaceuticals [20]. 2) Working principle of a  $^{99\text{m}}\text{Tc}$  generator: A saline solution is passed through an alumina column with adsorbed molybdenum. In this process the liquid gets enriched with pertechnetate. The enriched solution is then filtered to remove any particles from the liquid and guarantee a sterile product. [21]

The eluted  $^{99\text{m}}\text{Tc}$  is in form of a pertechnetate ( $\text{TcO}_4^-$ ) anion, which is then inserted in a so-called *cold kit*. These cold kits are commercially available for a variety of different applications. They contain the necessary chemicals to form the desired  $^{99\text{m}}\text{Tc}$  pharmaceutical. This pharmaceutical can then be injected in the patient's blood circulation. Due to the short half-life of  $^{99\text{m}}\text{Tc}$ , the kit is used right after preparation.

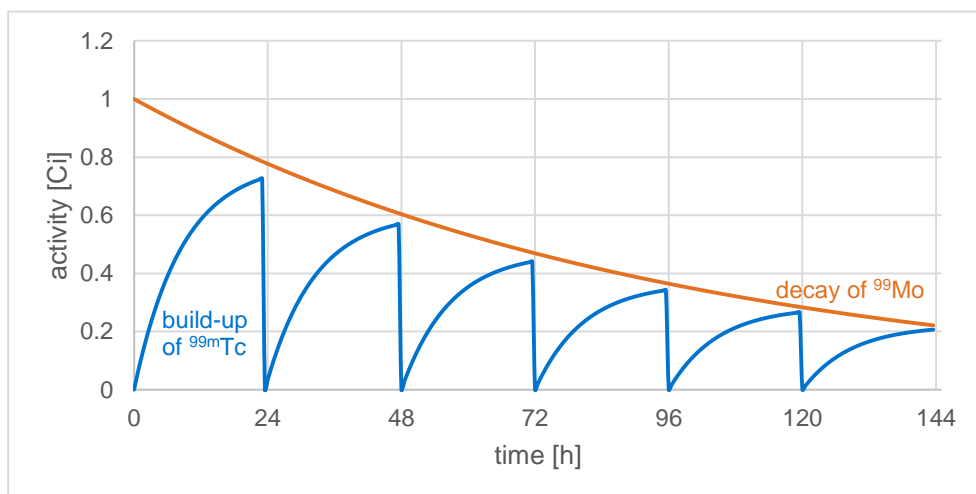


**Figure 9: Elution of a  $^{99\text{m}}\text{Tc}$ -generator.** The upper line shows the activity of  $^{99}\text{Mo}$ , which is defined by its radioactive decay. The lower line represents the  $^{99\text{m}}\text{Tc}$  activity in the generator. In this example the  $^{99\text{m}}\text{Tc}$ -generator is eluted once every 24h. As one can see, the  $^{99\text{m}}\text{Tc}$  activity restores after each elution until it reaches the activity of its mother isotope  $^{99}\text{Mo}$ .

### 1.3 CHALLENGES TO THE RELIABILITY OF THE <sup>99</sup>Mo SUPPLY

In the following years, the conventional supply chain, as described so far, will have to face two major challenges: the drop out of aged supply reactors and the conversion from high-enriched to low-enriched uranium targets. Both present a challenge to guarantee a sufficient and reliable supply of <sup>99</sup>Mo.

**Table 2** gives an overview of the currently available reactors producing <sup>99</sup>Mo. Except for the LVR-15 and the OPAL reactor, all current reactors are more than 40 years of age. Their planned shutdown within the next few decades will have a major impact on the future supply of <sup>99</sup>Mo. According to a study performed by the Organization for Economic Co-operation and Development (OECD) in 2014 [22], the predicted irradiation capacity of the current reactor fleet will be sufficient to avoid supply shortages until 2016. From then on, the fleet is able to provide enough irradiation capacity to cover the minimum demand but without the necessary outage reserve capacity. This increases the risk of supply interruptions caused by unplanned reactor shut-downs. The situation is worse, when considering the processing capacity. The processing capacity takes also into consideration the geographical proximity of the reactor sites and the processor sites. According to the study, the currently available processing capacity is insufficient to secure a safe supply of <sup>99</sup>Mo from 2016. Taking into consideration new reactor- and non-reactor based production routes, this lack of capacity can be compensated but the processing capacity will still be below the necessary demand (including outage reserve capacity) from 2016 until end of 2017. This situation worsens when project delays appear. Assuming a delay of 2 years in all new projects, a sufficient supply can again be established by the end of 2019. The study used a yearly demand of 270000 6-day Ci in 2014 and an annual increase of 0.5% per year as basis for its forecast.

**Table 2: Current suppliers of <sup>99</sup>Mo.** The potential annual production is the maximum weekly production times the operation weeks. This value does not represent the actual production of the reactor. [23, 24]

Reactor	Commissioning	Target enrichment	Potential annual production [6-day Ci]	Estimated stop of production
BR-2	1961	HEU	156 000	2026
HFR	1961	HEU	187 200	2022
LVR-15	1995	HEU	80 000	2028
MARIA	1974	HEU	42 500	2030
NRU	1957	HEU	200 600	2016
OPAL	2006	LEU	41 450	>2030
OSIRIS	1966	HEU	34 300	2015
RA-3	1967	LEU	19 200	2027
SAFARI-1	1965	HEU	130 700	2025

Another challenge for the <sup>99</sup>Mo production will be the conversion from high-enriched to low-enriched uranium targets. In the mid-1970s concerns arose about the use of HEU in research reactors as a potential source of material usable for nuclear weapons. Therefore, in 1976 the Reduced Enrichment for Research and Test Reactors program (RERTR) was founded by the Department of Energy (DOE, USA). Purpose of the RERTR program is to minimize the use of

HEU in research reactors, both for the reactor fuel and for irradiation targets used to produce medical isotopes. With the American Medical Isotope Production Act in 2012, United States will restrict export of HEU for the purpose of  $^{99}\text{Mo}$  production 7 years after its enactment [25]. Since the current  $^{99}\text{Mo}$  production is almost completely based on high-enriched uranium targets,  $^{99}\text{Mo}$  producers are forced to convert their irradiation targets from HEU to LEU.

In the first stage of the conversion, commercial-ready target designs are used. These so-called *phase I targets* are currently available targets, which are modified to increase their uranium density from approximately  $1 \text{ g/cm}^3$  to  $2.6 \text{ g/cm}^3$ . Decreasing the enrichment of uranium, not only decreases the amount of fissile  $^{235}\text{U}$  but also increases the neutron absorbance due to a higher  $^{238}\text{U}$  amount. These two effects cannot fully be compensated by phase I targets. Therefore, the resulting yield will be decreased by at least a factor of 2. This loss adds up to the difficulties caused by the aging reactor fleet.

Current targets mainly use uranium compounds in an aluminum matrix or aluminum alloy covered by an aluminum cladding. With increasing target volume, the volume of the aluminum is raised. Since the aluminum is also dissolved in the processing of the target, the amount of highly radioactive waste increases significantly. Therefore, the reprocessing costs are higher compared to the conventional HEU process. An OECD study from 2012 [23] numbers a price increase of 8% from the radiopharmacy.

To compensate these effects, work is underway to develop new high-density irradiation targets, the so-called *phase II targets*. One promising approach is the cylindrical LEU foil target, which accommodates 4 g of  $^{235}\text{U}$  using LEU, which is equal to the amount in current HEU targets. A higher increase of the  $^{235}\text{U}$  content is limited by the resulting higher activity and heat production.

#### 1.4 NEXT LEVEL IRRADIATION TARGETS AND THE CYLINDRICAL FOIL TARGET

The cylindrical LEU foil target was originally developed by the Y-12 National Security Complex, in collaboration with Argonne National Laboratory (ANL), University of Missouri and its MURR research reactor, Oak Ridge National Laboratory (ORNL) and Korea Atomic Energy Research Institute (KAERI) [26]. The target consists of a metal uranium foil (125-150  $\mu\text{m}$  thickness), which is coated in a thin metal interlayer (10-25  $\mu\text{m}$ ) and encapsulated by two AL6061-T6 aluminum cylinders. The cylindrical shape allows an effective cooling and gives the target a high mechanical stability against potential critical swelling. The target contains approximately 20 g of uranium with an enrichment of 20%. A schematic and dimensions of the target are shown in [Figure 10](#).

The target is manufactured in several steps, which are illustrated in [Figure 11](#). First, the uranium foil is produced and sheared to the necessary dimensions. Second, the uranium foil is coated by electroplating or wrapped into a thin foil of metal, which serves as recoil barrier (e.g. nickel). Third, the coated foil is wrapped around an indentation on the inner aluminum tube and then the inner tube is slipped into the outer aluminum tube. Fourth, the inner tube is mechanically widened to guarantee a good thermal contact between the uranium and the aluminum cladding. And last, the two aluminum cylinders are welded shut at both ends to safely encapsulate the fission products [27].

Due to the high density of uranium metal compared to dispersed uranium or uranium alloy, the total uranium loading of this target is significantly higher compared to conventional HEU targets. Therefore, an equivalent yield to HEU targets can be produced.

The interlayer serves as a recoil barrier, which stops energetic fission products from entering the aluminum cladding. In this way, a bonding of the uranium and the aluminum cladding is prevented. Hence, the target can easily be disassembled after irradiation and the uranium foil can be removed. The cladding material can then be disposed separately as radioactive solid waste, whereas the uranium foil is chemically processed. Thus, the amount of liquid highly radioactive waste is significantly reduced compared to conventional targets, where the whole target has to be dissolved for further processing. This reduces both processing time and



processing costs. According to [28] dissolution time (including disassembly) and processing liquid are reduced by a half compared to current HEU targets.

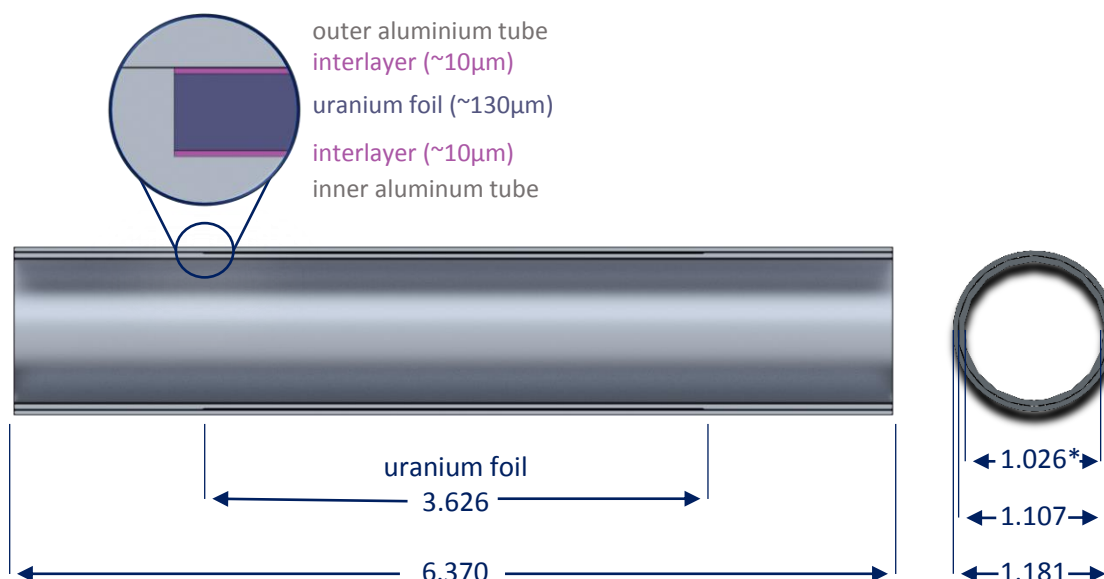


**Figure 10: The cylindrical LEU foil target.** The target consists of two coaxial aluminum tubes. In an indentation on the inner tube is a sandwich of a uranium foil wrapped or coated in an interlayer material. To guarantee a good thermal contact between the aluminum and the uranium, the inner tube is widened after assembly. To ensure a safe encapsulation of the fission products, both tubes are welded together on both ends. All given dimensions in the drawings are in inches. The diameter marked by the asterisk \* is the inner diameter before the widening of the inner tube. [29]

The feasibility of the cylindrical foil target was proven by irradiation tests in the Indonesian RSG-GAS reactor [26]. Hereby targets with Al and Zr tubes and recoil barriers made of Ni, Zn and Al were irradiated and subsequently disassembled. The targets have shown a good irradiation performance. There was no evidence of heat-transfer problems or significant mechanical distortion. The irradiated foils did not bond to the aluminum cladding and could easily be removed afterwards. Since the zirconium targets do not show any significant advantage over the aluminum targets, the usage of aluminum is preferred due to the lower costs. The material choice for the interlayer has to be made in respect to the compatibility to the subsequent chemical processing of the target. At present day, the way of processing is not decided. Therefore, the interlayer material is still a subject to discussion.

It was shown in the early stage of the target design that the LEU foil target is in principle compatible to an alkaline as well as an acidic process. However, this involves greater changes in the established chemical processes of the major  $^{99}\text{Mo}$  producers and, thus, high investments. Therefore, much effort was put into fitting the LEU foil target into the established purification processes. In [30] an alkaline and an acidic processing of the LEU foil are described, which can be fed into the established  $^{99}\text{Mo}$  purification procedures. Both processes were demonstrated with low-burnup LEU foils. Thereto, the foils were irradiated for 10 minutes in a neutron flux of  $10^{11} \frac{n}{\text{cm}^2\text{s}}$  and cooled for several hours.

For the acidic process, targets with a nickel interlayer were used. The LEU foil including the Ni was dissolved in  $\text{HNO}_3$  and then passed over titania columns to adsorb the molybdenum. In a next step, the molybdenum was washed out by NaOH to gain a liquid, which can be fed to established  $^{99}\text{Mo}$  purification procedures.

The targets used for the alkaline process, consisted of a LEU foil with an aluminum interlayer. In a first step, the aluminum interlayer was dissolved in NaOH. Subsequently, the uranium was

liquefied in  $\text{NaHCO}_3$  by an electrochemical process. The uranium and the fission products were then precipitated by  $\text{CaO}$  and filtered. The remaining alkaline  $^{99}\text{Mo}$  solution is compatible with current purification processes.

It showed that both processes were able to recover  $>90\%$  of the  $^{99}\text{Mo}$ . In future experiments high-burnup tests are to be performed and the hot-cell compatibility of the equipment needs to be improved.

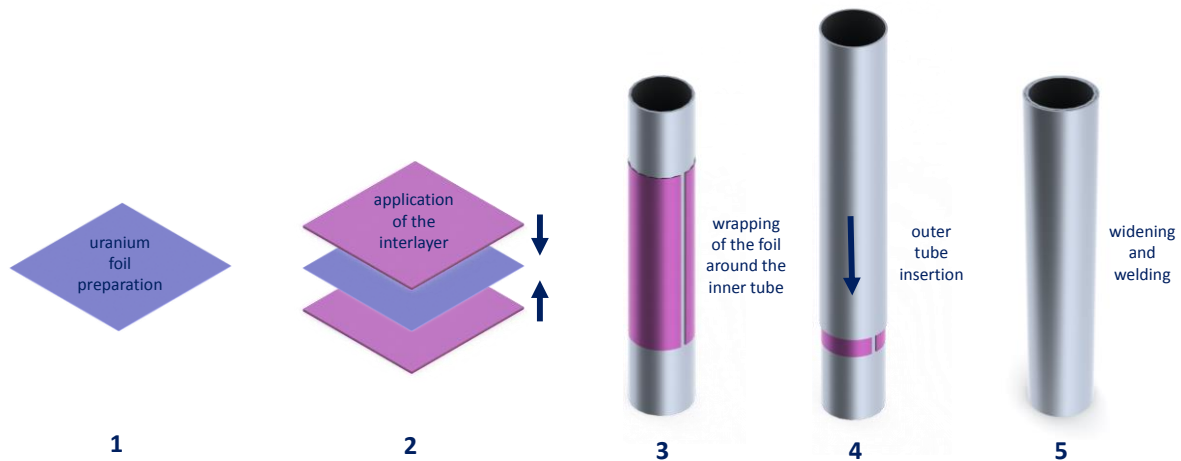


**Figure 11: Irradiation target manufacturing with a prepared uranium foil.** (1) The uranium foil is manufactured. (2) The interlayer is applied to the uranium foil. (3) The covered uranium foil is placed in an indentation on the inner aluminum tube. (4) The inner tube is inserted in the outer tube. (5) The inner aluminum tube is widened.

## 1.5 TARGET MANUFACTURING BY SPUTTERING AND AIM OF THIS THESIS

One major challenge in the production of these targets is the manufacturing of thin uranium foils with a sufficient quality. Currently, two ways of producing the uranium foils exist: hot- and cold-rolling by Y-12 and cooling-roll casting by KAERI. The rolling process investigated by Y-12 National Security Complex includes several steps: uranium coupon cutting, cleaning and polishing of the coupons, hot-rolling, cold-rolling, annealing and shearing [31]. The sum amount of these different steps make this process very labor-intensive and lowers the uranium usage efficiency. In contrast, KAERI's cooling-roll casting process is more time and labor efficient. In this process molten uranium is dripped onto a cooled roll rotating with high speed. The uranium rapidly cools down and forms a thin foil. Disadvantages of this method are a low surface quality and an inhomogeneous thickness of the produced foils. [32]

In this work an alternative manufacturing process for the cylindrical LEU targets was developed. To avoid the difficulties of pre-producing a thin uranium foil, the recoil barriers as well as the uranium foil are directly coated on the inside of the outer aluminum cylinder.

The coating process is done using a form of physical vapor deposition (PVD), referred to as *sputtering*. Thereby, the coating material (*sputter target* or *target*) is eroded by a bombardment with argon ions, which are produced in a low pressure plasma. The eroded (*sputtered*) atoms turn into gas phase and form a foil by condensation on the outer aluminum tube. The manufacturing principle is shown in [Figure 12](#).

The main advantage of the PVD process compared to the conventional processes is that it makes pre-producing the uranium foil obsolete. This avoids the above mentioned difficulties connected to the hot- and cold-rolling and the cooling-roll casting process.

The necessary sputter targets, which consist of uranium or the interlayer material, have a simple geometry and can be produced by casting. Residues of used sputter targets can easily be recycled and used for the production of a new targets. Therefore, it is expected that this process reduces the scrap material significantly compared to the conventional processes.

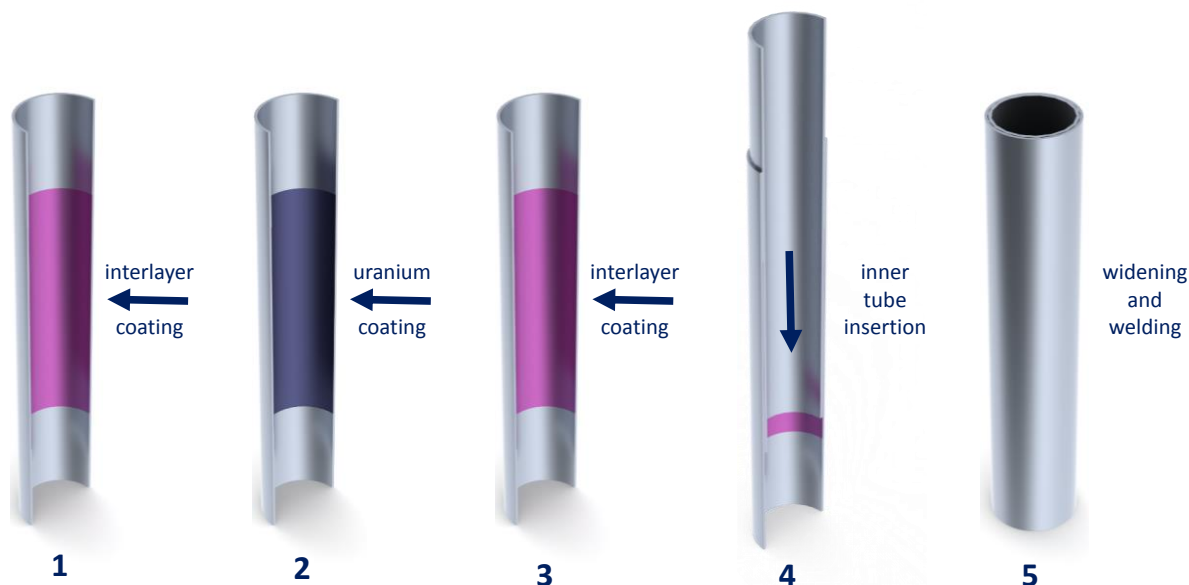


**Figure 12: Irradiation target manufacturing by PVD coating.** (1) The first recoil barrier is applied to the outer tube. (2) The uranium foil is grown by PVD coating. (3) The second recoil barrier is applied. (4) The inner aluminum tube is inserted. (5) The inner aluminum tube is widened.

For a higher production volume, a parallel production of several irradiation targets is easy to realize. Since most of the expensive components (e.g. vacuum systems) can be used for several production units simultaneously, this can be achieved with low extra costs.

Furthermore, the PVD process is highly flexible, since it allows an easy adjustment of the foil's thickness, the dimensions of the irradiation target or the material of the interlayer. Compared to the rolling process, there are no limitations to the thickness of the foils.

It is the aim of this work to develop, build and characterize a prototype sputter reactor to demonstrate its feasibility for irradiation target production. Requirements are:

- the production of a self-supporting uranium foil with a homogenous thickness
- the controllability of the adhesion of the foil to the aluminum tube
- a high deposition rate, in order to achieve reasonable manufacturing times
- the integration into a glove box to allow a safe handling of the uranium
- the demonstration that the irradiation target can be assembled

In the next chapter of this thesis the relevant theoretical background of the sputter process is described. This involves a description of the low pressure plasma environment, the particle ejection, the layer growth of the sputtered material and the technical realization of the sputter process. Chapter 3 first gives a short overview of an experimental set-up, which was built in order to gain experience for the final prototype reactor. This reactor is then describes in-detail. The parametrization of the prototype device and the examination of the resulting layers are presented in chapter 4. In the last chapter the assembly of the target is investigated.



## 2 THEORETICAL BACKGROUND

The sputter process or simply sputtering describes the erosion of a material, *the target*, by bombardment of energetic atomic-sized particles. Thereby, surface near-atoms are ejected by momentum and energy transfer [33]. The deposition of those atoms on another surface, *the substrate*, is called sputter deposition. This effect was first observed in the 19th century in form of metallic coatings in the region of the negative electrode of glow discharge tubes. The first descriptions of this effect was done by William Grove in 1858 [34] and Julius Plücker in 1858 [35]. Since then, this technique was used for a magnitude of applications, e.g. production of mirrors [36], application of low-emissivity coatings on glass, production of compact discs or hardening of tools by nitride-coatings [37]. During the years a variety of types of sputter techniques were developed.

A conventional sputter setup consists of a target, a substrate and a source of ions. The ions are accelerated by an electric field towards the target, where they knock out atoms from its surface. These sputtered atoms can condense on the substrate and form the desired layer. In a direct current (dc) sputter device the source of ions is a low pressure plasma. This plasma is usually initiated by the same electric field as it is used for the acceleration of the ions. In a dc magnetron sputter device, which is used in the following work, the plasma is additionally confined by a magnetic field, what leads to a significantly higher deposition rate. [Figure 13](#) gives a quick overlook over the basic principle of dc sputtering.

The following chapter will describe the dc sputter process and its technical realization in more detail to enable the reader to understand the subsequent considerations. However, there is a big variety of different sputter techniques, like reactive sputtering, radio frequency sputtering or pulsed power magnetron sputtering. It is not aim of this work to give a comprehensive description of all these sputter techniques. For an in-detail description reference is made to [38].

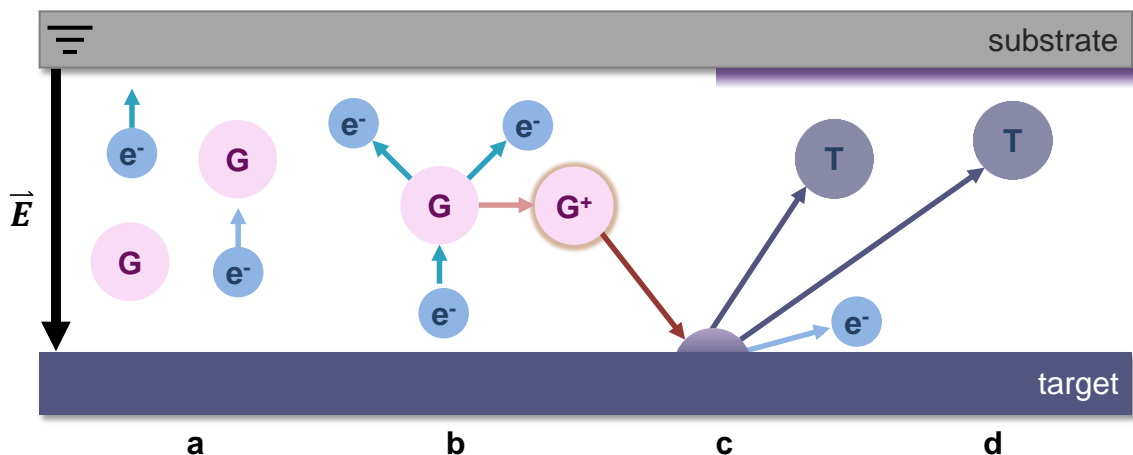


**Figure 13: Basic principle of dc sputtering.** a) Electrons in a low-pressure atmosphere are accelerated by an electric field. b) Having enough kinetic energy, these electrons can ionize the gas atoms (G). c) Positively ionized gas atoms ( $G^+$ ) are accelerated by the electric field towards the sputter target, where they can knock out surface atoms (T). d) These atoms condense on the substrate and form a layer. [39]

## 2.1 LOW PRESSURE PLASMA

A plasma is matter, which is so highly ionized that the dynamical behavior of free charges dominates its behavior [40]. In general, a plasma is an ionized gas with a certain degree of ionization. The degree of ionization is defined by the density ratio of ionized species to the sum of ionized and neutral species [41]. To sustain a plasma, a continuous energy supply is necessary to compensate energy losses, e.g. due to radiation. There is a variety of ways how to ignite and sustain a plasma. A plasma can for example be created by heating a gas or by applying strong electromagnetic fields. A common way to ignite a plasma, is the application of a static electric field on two opposing electrodes in a low pressure atmosphere. This plasma is called a dc glow discharge. The energy, which is necessary to sustain the plasma is induced by the power supply generating the electric field. This kind of low pressure plasma is used in dc sputter devices and, therefore, will be explained in the following.

### 2.1.1 IONIZATION

In thermal equilibrium, the degree of ionization of a gas is below 0.1% [42]. This percentage is caused by thermal ionization of the gas atoms or molecules. In a plasma the degree of ionization is significantly higher. It is sustained by induced continuous ionizations of gas atoms or molecules. Ionization can be caused by several processes, like atom-atom collision, radiation or surface ionization. However, the most important process in case of the glow discharge is the ionization of the gas particles by electrons, e.g.:



When an electron hits an atom or molecule, energy is transferred and the outer-shell electrons are elevated to a higher energy level. If the transferred energy exceeds the bonding energy of the outer-shell electron, the atom or molecule gets ionized. The necessary energy is called the ionization energy. Examples for different atoms and ionization states are given in [Table 3](#).

**Table 3: Ionization energies of the non-radioactive noble gases.** The ionization energies of the different ionization states are given in eV. [43]

Element	X <sup>+</sup>	X <sup>++</sup>	X <sup>+++</sup>	X <sup>++++</sup>
Helium	24.59	54.42	-	-
Neon	21.56	40.96	63.42	97.19
Argon	15.76	27.63	40.74	59.58
Krypton	14.00	24.36	35.67	50.85
Xenon	12.13	20.98	31.05	42.20

The de-excitation of outer shell electrons leads to an emission of photons in a characteristic wavelength. Characteristic colors are e.g. purple for argon, green for copper, pink for nitrogen and light-blue for oxygen [44]. The detection of characteristic radiation can be used to monitor gas species in the plasma. In this way, it is possible to observe the plasma chemistry. For example, impurities caused by leaks or outgassing materials can be detected.

The probability of an ionization induced by an electron collision is given by the ionization cross-section. This cross-section depends on the gas species and the electron energy (see [Figure 14](#)). For the noble gases, the cross-section has a maximum at approximately 100 eV. Therefore, dc glow discharge devices are usually operated at a voltage of several hundred volts.

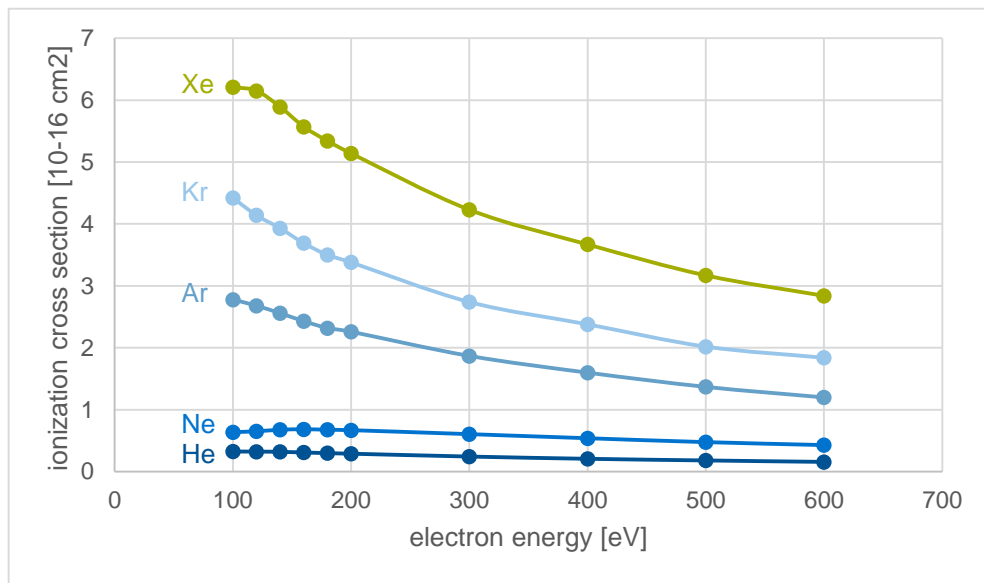


**Figure 14: Ionization cross section.** The ionization cross-section is a measure for the ionization probability and has a big influence on the degree of ionization of a plasma. For the noble gases this ionization cross-section has a maximum at around 100eV. At higher energies the ionization cross-section decreases and the electrons can pass through the gas easily. [45]

Main source of electrons, which are necessary to sustain a plasma, is their release in ionizing collisions and the emission from surfaces, which are bombarded by ions or electrons. Latter ones are called secondary electrons.

### 2.1.2 DC PLASMA DISCHARGE

Depending on its current-voltage behavior, the dc plasma discharge is classified in different regions. In a dc sputter device, the abnormal glow discharge region is used. This type of plasma discharge is characterized by the fact that the whole cathode is covered by a bright spot and the current density on the target is proportional to the applied voltage and pressure [46]. A schematic of such a glow discharge is shown in [Figure 15](#).

The negatively charged cathode attracts positively charged ions from the plasma. These ions are accelerated across the cathode fall region to imping on the cathode surface. The cathode fall region is a region close to the cathode surface, where most of the electric potential drops. This effect is caused by a strong concentration of ions in the negative glow region. The rest of the discharge zone shows an almost equal potential. The accelerated ions can directly reach the target surface or become neutralized. In this way, ions and energetic neutrals reach the target surface and eject both neutral target atoms and secondary electrons. The ejected electrons are due to their negative charge accelerate towards the anode. On their way they experience inelastic collisions with the sputter gas, cause ionization and release new electrons. In this way the dc plasma discharge is sustained in an equilibrium state. A change in the discharge parameters, like the applied voltage, gas type or the gas pressure, lead to a new equilibrium state.

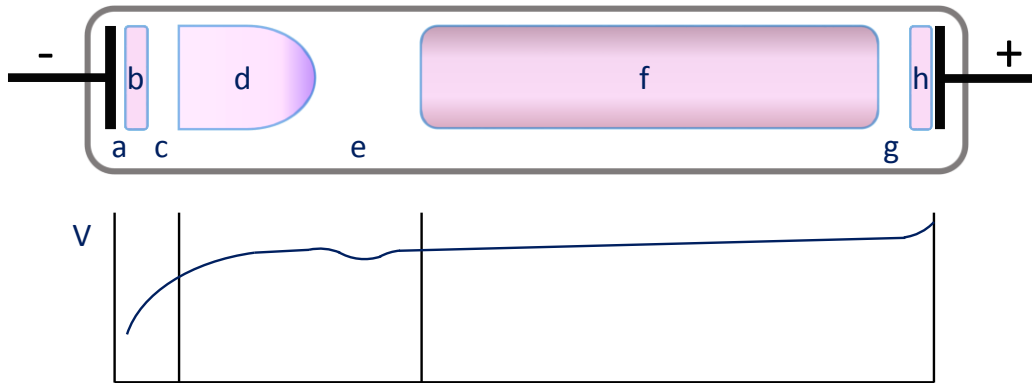


**Figure 15: Dc glow discharge inside a vacuum tube and its electric potential.** The glow discharge can be separated into five optically visible main regions: a) the Aston dark space, b) the cathode glow, c) the cathode dark space, d) the negative glow, e) the Faraday dark space, f) the positive column, g) the anode dark space and h) the anode glow. Close to the cathode a deep potential drop occurs, which is caused by a high density of positive ions on the border between region c) and d). The electrons ejected from the cathode gain most of their energy in this region and cause an intensive ionization in region d). Its glowing is caused by recombinations of ions and electrons. The positive column f) is characterized by a high and constant density of electrons and ions. The potential in this region is nearly constant. Its glowing is caused by the excitation of the gas atoms. [47]

However, a dc discharge can just be sustained if the secondary electrons create a sufficient amount of ions. Therefore, the space between cathode and anode cannot be too short. This effect is used to suppress a plasma burning in unwanted regions of the target by surrounding this regions with a grounded conductor in a certain distance. This kind of plasma shielding is called dark field shielding. The minimum distance, which is necessary to suppress a plasma, can be estimated by the mean free path in the sputter gas at the required operation pressure.

The secondary electron emission of a surface depends on its temperature and the material composition. A higher emission occurs at hotspots or contaminations on the target surface, especially at oxides. This higher electron emission can lead to electric arcs. Because of surface oxides, arcs appear mainly in the beginning when using fresh sputter targets. To a certain extent arcs can be suppressed by power supplies with a built-in arc management.

## 2.2 PARTICLE EJECTION

### 2.2.1 EJECTION MECHANISM

The leading mechanism of the sputter process is the momentum transfer. The kinetic energy of the impinging ions distributes in a limited volume of the target surface region by a sequence of quasi-elastic collisions between ions and atoms or atoms and atoms. This leads to a collision cascade, which transfers the energy either into the bulk of the target material or back to the surface. If the energy transferred to a surface atom is higher than its surface binding energy, the surface atom is ejected from the target. The rest of the energy is stored in the surface region and near surface region in form of heat and displacements in the lattice. The impinging particle can either be implanted into the surface or be reflected from the surface as energetic neutrals. In systems with a short target to substrate distance and/or low pressure these neutrals can hit the substrate surface without losing their energy. The release of this energy on the substrate strongly influences the surface layer.



The energy transfer of the impinging atom to the target atoms can be described using the elastic collision of hard spheres. The transferred energy  $E_t$  is given by:

$$E_t = E_i \frac{4M_i M_t}{(M_i + M_t)^2} \cos^2(\vartheta) \quad (4)$$

where  $E_i$  is the energy and  $M_i$  the mass of the impinging particle,  $M_t$  the mass of the target atom and  $\vartheta$  the angle of impact (related to the surface normal). A maximum of energy is transferred when the mass of the impinging ion is equal the target atom. Therefore, the sputter gas is supposed to be chosen according to the target material to achieve a high sputter yield. However, due to chemical considerations, the choice of gasses is limited to noble gases in order to deposited pure materials by sputtering. In most cases, argon is used as sputter gas due to its low costs.

The minimum energy of the impinging particles, which is needed to achieve sputtering, is material dependent and related to its enthalpy of sublimation. Below this threshold no sputtering occurs. **Table 4** shows the energy threshold  $E_s$  of argon and krypton on several selected materials. As one can see, these materials do not show any significant differences since all energy thresholds are around 20 eV. Therefore, no restriction in the choice of target materials is set in respect to the threshold energy when using a standard dc sputter device with a voltage of several hundred volts.

**Table 4: Energy threshold  $E_s$ .** The necessary kinetic energy of argon and krypton as sputter gases for sputtering several materials is given in eV. [48]

Target material	Argon	Krypton
Al	13	15
Ti	20	17
Fe	20	25
Ni	21	25
Cu	17	16
Zr	22	18
Mo	24	28
U	23	25

### 2.2.2 SPUTTER YIELD

The efficiency of the sputter process is described by the sputter yield  $S$ .  $S$  is given by the ratio of the ejected atoms to the impinging particles. The sputter yield depends on a variety of parameters, like the mass ratio of the impinging particle and the target atom, the energy of the impinging particle and the angle of impact. The temperature of the target has, up to 80% of its melting point, a negligible influence on the sputter yield.

The general energy dependency of the sputter yield shown in **Figure 16**. Below the threshold energy  $E_s$  no sputtering occurs. With rising energy of the bombarding particles, the yield increases. A peak of the sputter yield is reached at approximately 10 keV.

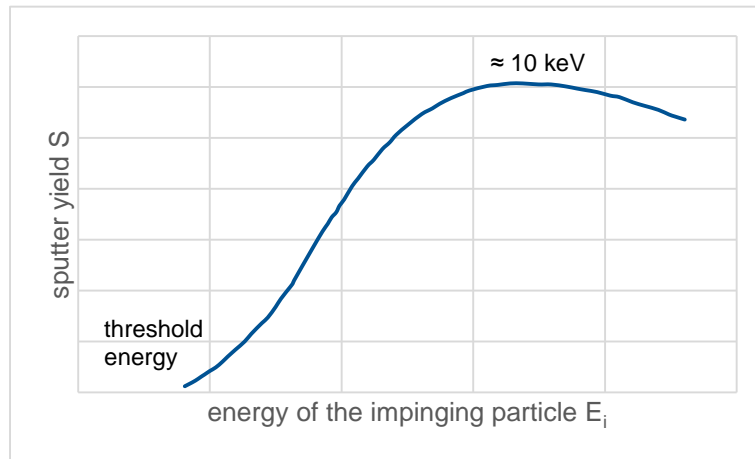


Figure 16: General energy dependency of the sputter yield. [49]

Figure 17 shows the angle of impact dependency on the sputter yield for several polycrystalline materials. Up to an angle of approximately 60°, yield is roughly given by

$$S = S_0 / \cos(\vartheta) \tag{5}$$

where  $\vartheta$  is the angle of the impinging particle to the surface normal and  $S_0$  is the sputter yield at an angle of  $\vartheta=0^\circ$ . Up to an angle of approximately 75°, the sputter yield increases due to an increased energy deposition in the surface. Above this maximum, the yield decreases caused by an increased reflection of the impinging particles.

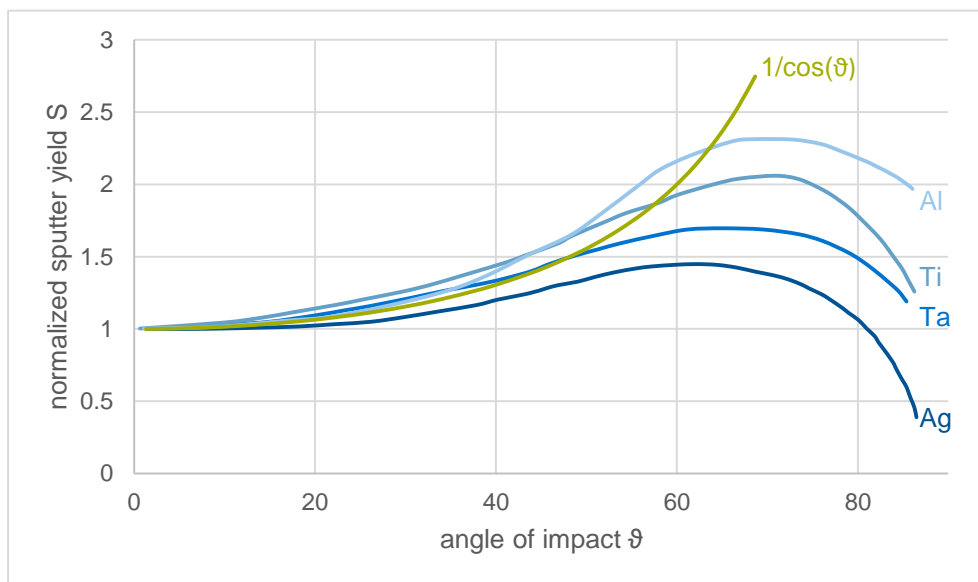


Figure 17: Angle of impact dependency on the sputter yield for different target materials sputtered by 1.05 keV Ar ions. The sputter yield has a maximum at approximately 70 – 80°. This is caused by a growing energy deposition in the surface region at higher impact angles. However, above this maximum the reflection of the impinging particles is growing, which leads to a decrease of the sputter yield. [50]

Table 5 shows the sputter yield of several selected sputter gas and target material combinations at an angle of impact of 0° and a particle energy of 500 eV. Additionally, the product of the

sputter yield and the atomic mass of the sputter target material is shown. Under the assumption that flux and energy of the impinging particles is independent of the target material, this value gives a first guess, which ratio of sputter rates can be expected. The sputter rate is defined as the eroded mass per time. As one can see, high sputter rates can be achieved with uranium and copper as target materials.

**Table 5: Examples of sputter yields.** The given numbers show calculated sputter yield at  $\vartheta=0^\circ$  and  $E=500$  eV. These sputter yields only give a rough idea about the achievable deposition rate, since the deposition rate strongly depends on the sputter device. [51]

Target material	Argon		Krypton	
	$\frac{\#_{\text{ejected}}}{\#_{\text{impinging}}}$	$\frac{\#_{\text{ejected}}}{\#_{\text{impinging}}} m_{\text{target}}[\text{u}]$	$\frac{\#_{\text{ejected}}}{\#_{\text{impinging}}}$	$\frac{\#_{\text{ejected}}}{\#_{\text{impinging}}} m_{\text{target}}[\text{u}]$
<b>Al</b>	0.986	27	0.822	22
<b>Ti</b>	0.469	22	0.467	22
<b>Fe</b>	1.117	62	1.202	67
<b>Ni</b>	1.098	64	1.199	70
<b>Cu</b>	1.897	121	2.183	139
<b>Zr</b>	0.515	47	0.640	58
<b>Mo</b>	0.553	53	0.695	67
<b>U</b>	0.742	177	1.214	289

### 2.2.3 TRANSPORT OF THE SPUTTERED MATERIAL

When a target atom is ejected from the target surface, it is ejected with a certain angle to the surface normal. For a perpendicular bombardment of the target, the distribution of this ejection angle  $\omega$  can be approximated by a cosine distribution.

$$\frac{dS}{d\omega} \sim \cos^n(\omega) \quad (6)$$

where  $n$  is a dimensionless fitting parameter. For high energies of the impinging particles ( $>1$  keV), the parameter  $n$  is greater than 1. For lower energies it is usually below 1 [52].

Under not-normal impact angles, the distribution is deformed in the forward direction. This effect, is small at higher energies compared to the bombardment with low energy particles. **Figure 18** gives an example of sputtered tungsten with different impact angles and particle energies. The impact angles are mainly given by the shape of the electric field, which is used to accelerate the sputter gas ions.

Another important factor, which influences the angle distribution, is the ion species and the target material. The probability for an emission in the direction of the target normal depends significantly, on the energy, which is necessary for the target atoms to leave the surface. At low energy thresholds, the emission in normal direction is reduced and the emission profile assumes a torus-like shape.

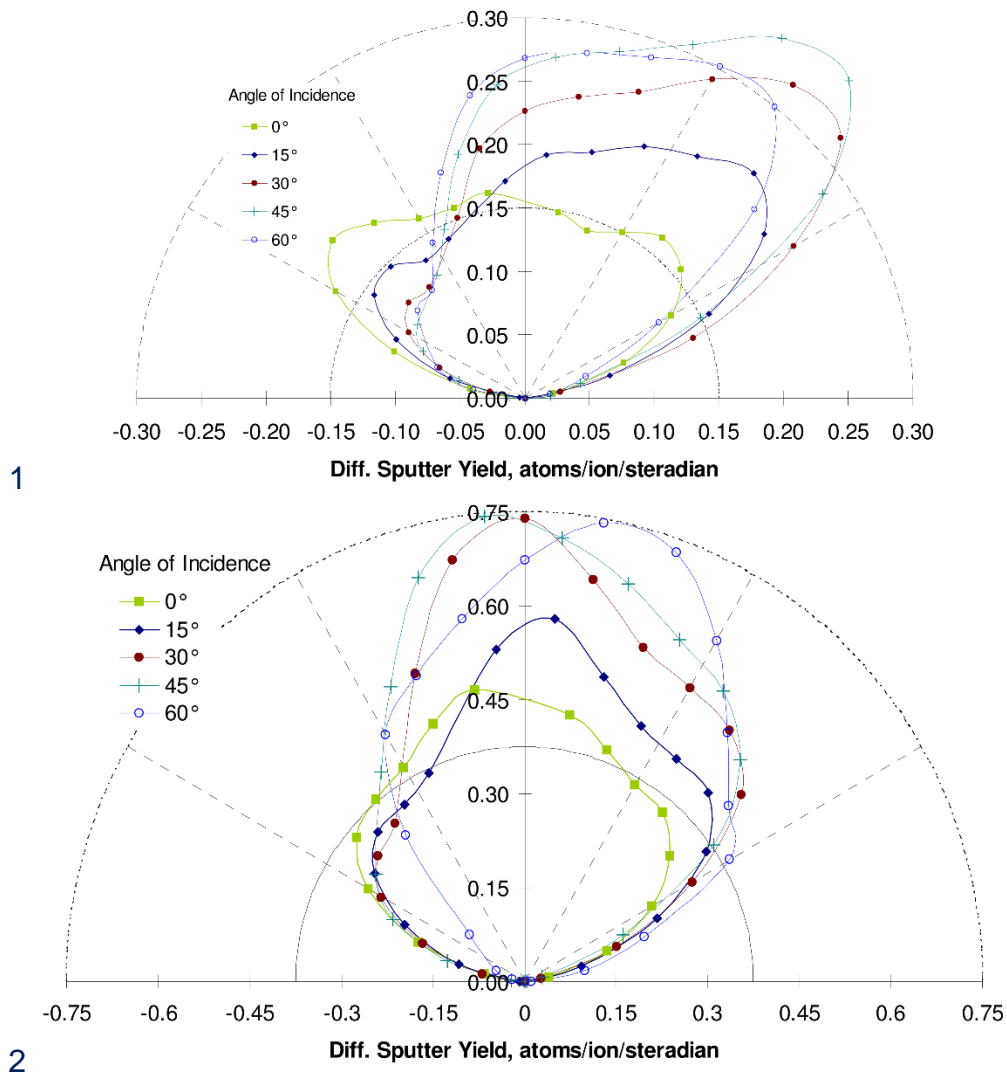


**Figure 18: Differential sputter yield.** The two figures show the influence of the incidence angle and the energy of the impinging particle on the differential sputter yield. The values show tungsten sputtered with 500eV (1) and 1500eV (2)  $Kr^+$  ions. The particles impinging from the left side with the given angle in respect to surface normal. Especially at a low particle energy, the sputter distribution is strongly deformed in the forward direction. [53]

After being ejected from the surface, the target atoms traverse through the space surrounding the target. Under high vacuum conditions, the atoms move directly to the opposite surface. However, under normal process conditions, which are in a pressure range from 0.01 to 0.1 mbar the sputtered atoms can interact with the sputter gas. Thereby, they undergo elastic collisions with the gas atoms. This process both alters the flux distribution and the energy of the target atoms. As detailed in the chapter 2.4, this energy has a significant influence on the structure of the layer growth.

The alteration of the flux leads to a coating of areas that are out of line of sight of the target and also alters the angle of incident on the substrate surface. The latter effect has an influence on the characteristic of the layer growth. As demonstrated in [Figure 19](#), an initially normal flux (image 1) is altered at higher pressure (image 2) to a non-uniform flux. Caused by this effect, geometrically shadowed areas can better be coated at higher pressure.

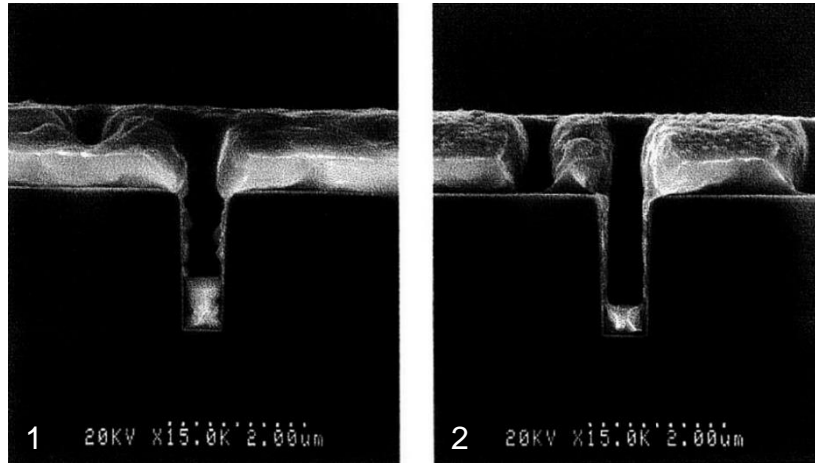


**Figure 19: Pressure dependency on the sputtered atom flux.** The SEM images show sputter deposited copper on a surface with submicron contact holes. Case 1) is performed at a pressure of  $1 \cdot 10^{-5}$  Torr and case 2) is performed at  $1 \cdot 10^{-3}$  Torr. Due to lower scattering in case 1), the copper flux impinges mostly normal to the surface and, therefore, leads to a higher deposition in the contact hole. In contrast, the higher pressure in case 2) leads to a non-uniform flux and therefore to a higher shadowing effect. [54]

The average length a sputtered atom travels before it collides with a gas atom can be approximated by the mean free path of the sputter gas

$$l = \frac{k_B T}{\sqrt{2} \pi d^2 p} \quad (7)$$

where  $k_B$  is the Boltzmann constant,  $T$  the temperature,  $d$  the diameter of the gas particles and  $p$  the pressure.

Figure 20 shows the calculated values for argon using a temperature of  $T=300$  K and a diameter of  $3.82 \cdot 10^{-8}$  cm [55]. As one can see, above a pressure of approximately 0.007 mbar the mean free path in argon is reduced to a value below 10 mm. Given the inner diameter of the substrate cylinder of 14.5 mm and a typical pressure range from 0.01 to 0.1 mbar for sputtering, it is expected that the pressure will have an influence on the flux distribution and energy of the sputtered atoms.

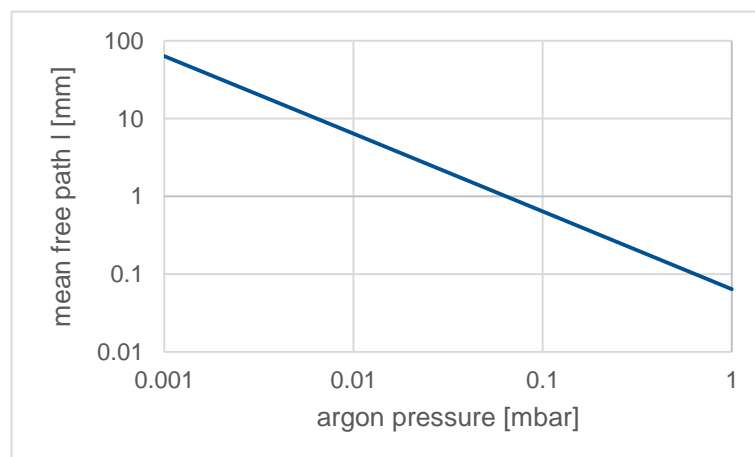


**Figure 20: Mean free path  $l$  of argon.**

Furthermore, a lower mean free path also leads to a higher residence time of the sputtered atoms in the plasma. As a consequence the ejected atoms, which are generally neutral when they leave the target surface, are ionized and accelerated back to the target by the applied electric field, what reduces the deposition rate significantly. This effect can optically be seen in the plasma color. When ionization of the target atoms occurs, the characteristic light emission of this material can be detected.

### 2.2.4 EMISSION CHARACTERISTIC OF A SPUTTER TARGET

In order to predict the shape of the deposited layers, it is important to know the emission characteristic of a sputter source. In this context the emission characteristic is defined as the distribution of the deposited material on the substrate caused by the sputter erosion of a not moving sputter target. This characteristic is defined by the superposition of all the single differential sputter yields over the whole target surface and the transport of the sputtered material. As seen in the previous chapters, these properties depend on the target material, the energy of the bombarding species, the pressure of the sputter gas and the shape of the electric field. In the sputter device built in the context of this work the gas pressure was fixed to a certain value, the shape of the electric field is mainly given by the geometry of the device and the energy of the bombarding particles only varies in a very limited range. This leaves the target material as last free parameter for the emission characteristic of the sputter target. Therefore, it needs to be determined for each used target material separately.

## 2.3 SPUTTER TARGET

### 2.3.1 TARGET SHAPE AND TARGET COOLING

Sputter targets can have a variety of different shapes according to their application. In many cases, it is of advantage to match the shape of the target to the shape of the substrate. For example brick like sputter targets are used for the coating of flat surfaces like metal plates. In this work a rod shaped target is used to coat the inner wall of a cylinder. The shape of the target brings several consequences to the construction of the sputter reactor. This includes for example the way the magnetic field is applied in a dc magnetron device or how the target cooling is realized.

During sputtering the shape of the target undergoes changes. For example, erosion ditches appear. In dc magnetron devices, this effect is mainly determined by the shape of the magnetic field. The changes in surface have a self-influencing effect, since a changed geometry of the target surface also influences the electric field and therefore the ion bombardment on the surface. The target utilization can strongly be influenced by the shape of the magnetic field.

An active cooling of the target is especially necessary in sputter set-ups with a high power compared to the target surface area. Normally, target cooling is solved by a copper cooling element, which is connected to the target. This connection can either be realized by mechanical means, like clamping or bolting, or by bonding, like soldering. In general, bonding provides the better thermal contact, however this technique is not always applicable due to other considerations, like the target material, the target shape or the costs. The target cooling is a vital element in the reliable operation of a sputter device and has to be monitored. A lack of cooling can lead to a partial or complete meltdown of the target material. As a consequence, the target material, the substrate or even the sputter device can be damaged.

### 2.3.2 TARGET MATERIAL

One important factor of the quality of a target is its density. A density below 95% shows interconnected porosities, which create virtual leaks in the vacuum system. Outgassing substances, like water, oxygen or carbon-hydrides, can change the process parameters. This effect is hard to control and make a good reproducibility of the sputter process difficult.

Another important factor is the purity of the target material, since the deposited layer normally shows the same material composition as the target material. Therefore, the purity of the target

is supposed to be as high as for the desired substrate coating. Due to the high costs of highly pure materials, it is advisable to keep the purity as low as necessary. One way to eliminate surface contaminations from the target, like surface oxidation, is to pre-sputter the target before the actual substrate is coated. This can either be done by shielding the target with a shutter before coating or by inserting the substrate after pre-sputtering.

### 2.4 LAYER GROWTH

The growth of the deposited layers can be separated in three stages: the condensation of the sputtered atoms on the surface, the formation of an interlayer between the surface and the deposited layer and the formation of the deposited layer itself. These processes depend on a variety of external parameters, like the substrate surface condition (roughness, contaminations, shape) and the process parameters (deposition rate, temperature, angle of incidence). By controlling these parameters, the properties of the resulting layers can strongly be influenced.

#### 2.4.1 CONDENSATION

When an atom hits a surface, it can either be reflected, directly condense on its impact location or adhere on the surface but keep a certain mobility over the surface. In the latter case, the atom is called adatom. The mobility of an adatom on a surface depends on its energy, the substrate temperature and the surface-atom interactions. After a residence time it can either re-evaporate or lose its kinetic energy and condense on the surface. The bonding mechanism for condensation can either be metallic bonding or electrostatic bonding. The kinetic energy of adatoms is lost by chemical reactions with the surface, collisions with other mobile adatoms, collision with adsorbed atoms or by finding nucleation sites (like impurities or lattice defects).

The initial nucleation density (number of nuclei per area) is an important factor for the formation of the layer. A high nucleation density favors the formation of a dense layer with a good adhesion to the underlying surface. Since the mobile adatoms may nucleate by collision with other mobile adatoms, the deposition rate (the number of impinging atoms per time) is influencing the nucleation density. Therefore, a higher adhesion and denser layers can be obtained by applying a higher deposition rate. Another way to increase the nucleation density is the bombardment of the surface with energetic particles to produce lattice defects.

A homogeneity of the nucleation density favors homogenous layer properties throughout the surface. It can be improved by a low surface roughness and a high surface temperature. With a higher surface temperature, the adatoms have a better mobility, what allows them to even out inhomogeneities in the surface's composition. The substrate temperature can on the one hand be controlled by external heating or cooling and on the other hand the surface temperature is strongly influenced by the deposition rate and the energy of the impinging atoms. Also radiation and surface recombination of a nearby plasma influence the surface temperature. This is especially the case in a magnetron sputter device with a low target to substrate distance.

#### 2.4.2 INTERFACE

The interface between the growing layer and the original surface can either be in the form of an abrupt interface or a transition layer between the two materials. The transition layer can be formed by diffusion, the formation of chemical compounds, physical mixing or recoil implantation. Whereas, at an abrupt interface the material abruptly changes from the substrate material to the layer material, at a transition layer the material composition gradually changes.

An abrupt interface is formed when there is a low bulk diffusion in the substrate material, no solubility or chemical reaction between the layer material and the bulk material, a low deposition temperature or surface contamination. In this case the adhesion of the layer is generally low. On the contrary, when forming a diffusion layer, the adhesion tends to be higher.

The interface properties can be controlled by adjusting the substrate temperature, cleaning the surface or introducing energy into the surface by bombardment with energetic particles.

### 2.4.3 DEPOSITED LAYER

The deposited layer on the substrate grow by successive nucleation of atoms on previous deposited material. Layers deposited atom-by-atom, like sputter coating, generally grow in a columnar structure. Existing structures on a surface, either already deposited material or surface roughness, agglomerate material on elevated points and shadow deeper points. By this mechanism polycrystalline or amorphous columns start to grow. The shadowing effect depends strongly on the angle of the incidence flux. A flux, which is not normal to the surface, leads to a not normal column growth and a lower material density of the deposited layer.

The form of the columnar growth mainly depends on the mobility of the adatoms. In a given system (materials, deposition technique), this mobility can be controlled by the substrate temperature and the inert gas pressure. The gas pressure is influencing the adatoms in two ways. First, a high gas pressure reduces the speed of the impinging atoms, since they undergo scattering on their way from the sputter source to the substrate. And second, a higher gas pressure also leads to an increased adsorption of gas atoms on the surface reducing the adatoms mobility by an increased number of collisions.

In 1977 John Thornton introduced a structure zone diagram (Figure 21), which is showing the different types of columnar growth (zones) in dependency of the gas pressure and the substrate temperature.

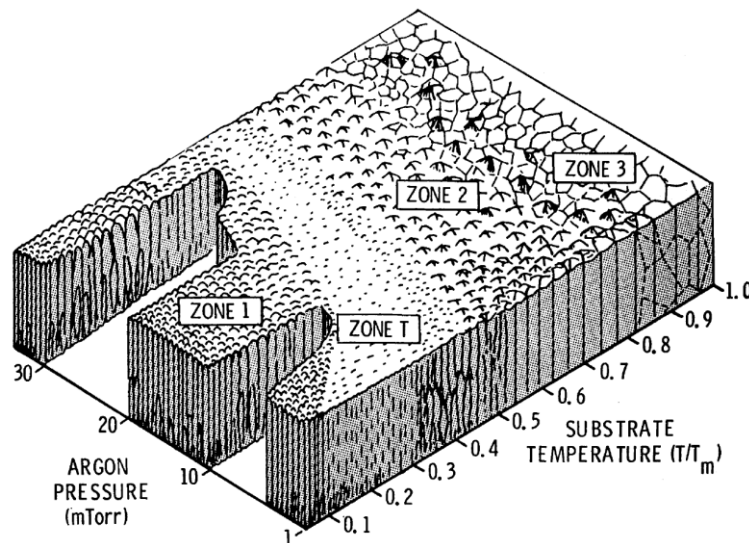


**Figure 21: Structure zone diagram according to Thornton [56].** The structure zone diagram shows the different forms of layer growth depending on the inert gas pressure and the homologous temperature. The homologous temperature is the absolute substrate temperature relative to the melting temperature of the deposited material. In zone 1 the mobility of the adatoms is low. Therefore, their energy is too low to overcome the geometrical shadowing of surface structures. As a result, a layer with a strong columnar character, a low density and large voids between the columns is formed. Zone T is a transition zone between zone 1 and zone 2. It features a fibrous crystal structure and a higher density than zone 1. In zone 2 the adatoms diffusion on the surface is the dominating factor. In this zone the columnar boundaries are densified, however their basic morphology remains. Zone 3 is governed by bulk diffusion, which allows recrystallization, grain growth and densification. The recrystallization leads to random grain orientation and a reduction of the columnar orientation. [40]



It should be noted that this model has no general application since the zones boundaries are also influenced by other initial parameters, like target current, voltage, pressure, substrate distance from target etc. A more general approach is given in [57]. In this model the substrate temperature is exchanged by a more generalized temperature, which additionally includes a temperature shift caused by the potential energy of atoms arriving on the surface. Also the energy introduced by reflected neutrals is considered. The pressure is generalized by a normalized energy describing displacement and heating effects caused by the kinetic energy of the bombarding atoms.

## 2.5 TECHNICAL REALIZATION

Sputter deposition can be realized in a large variety of different set-ups. In the following, two important types are described to explain the considerations made to realize a cylindrical sputter device.

To control the deposition process, following parameters are usually monitored and controlled:

- Voltage, current and power of the high voltage power source
- Gas pressure
- Substrate temperature
- Magnetic field

### 2.5.1 DC SPUTTERING

Dc sputtering is the most common form used for sputter deposition. [Figure 22](#) shows a schematic of a basic dc sputter reactor.

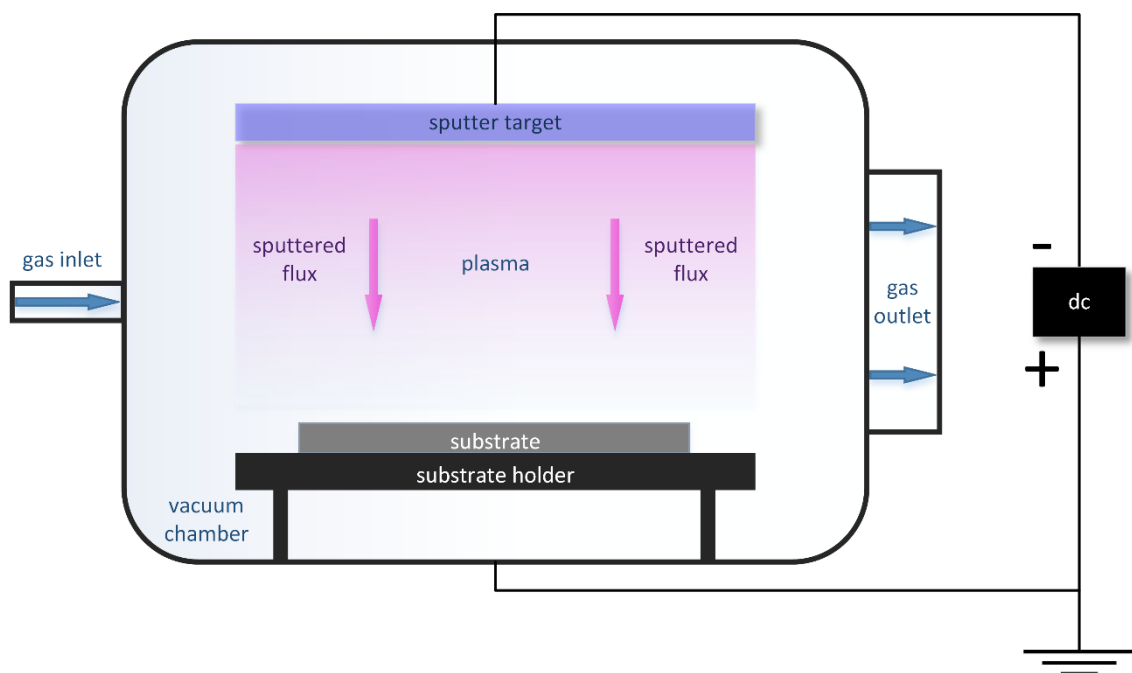


*Figure 22: Schematic of a dc sputter device.*

It features two opposing electrodes inside a vacuum chamber. One electrode, the cathode, is connected to the negative outlet of a high voltage power source. The counter-pole, the anode, is connected to the ground. The cathode is equal to the sputter target, whereas the anode often is, but does not have to be, connected to the substrate. In a normal process cycle, first the vacuum chamber is evacuated to minimize the contamination of the process atmosphere

by impurities, like oxygen, nitrogen or humidity. Afterwards the chamber is filled with the process gas, like argon or krypton, to a pressure of 0.01 - 0.1 mbar. By activating the high voltage power source an abnormal glow discharge is ignited. Within the plasma, positively charged gas ions are generated and accelerated onto the negatively charged sputter target, where they evaporate the target material. The ejected target atoms then either fly on a direct line towards the opposing surface or undergo scattering in the gas atmosphere. In this way, the sputter source has an evaporation profile, which depends on the gas pressure. The target atoms, which impinge on the substrate, form the desired layer.

To influence the properties of the growing layer, most sputter devices are equipped with a substrate heating and/or cooling, which allows regulating the substrate's temperature. To improve the properties of the sputtered layer it is also possible to use the chamber walls as an anode and give the substrate a low negative bias. Thus, a certain percentage of the gas ions impinge on the substrate, induce energy and thereby increase the mobility of the adatoms.

Dc sputtering works with all electrically conductive target materials. When using non-conductive target materials, the positive charge, which is induced by the positively charged gas ions, cannot be discharged and the electric field between the target surface and the anode decreases until it prohibits the sputter process to continue. This effect can also happen when a reactive sputter gas forms a non-conductive layer on the target material.

### 2.5.2 DC MAGNETRON SPUTTERING

An established way to improve the deposition rate of dc sputtering is dc magnetron sputtering. In this method, the electric field is superposed by a magnetic field (see [Figure 23](#)).

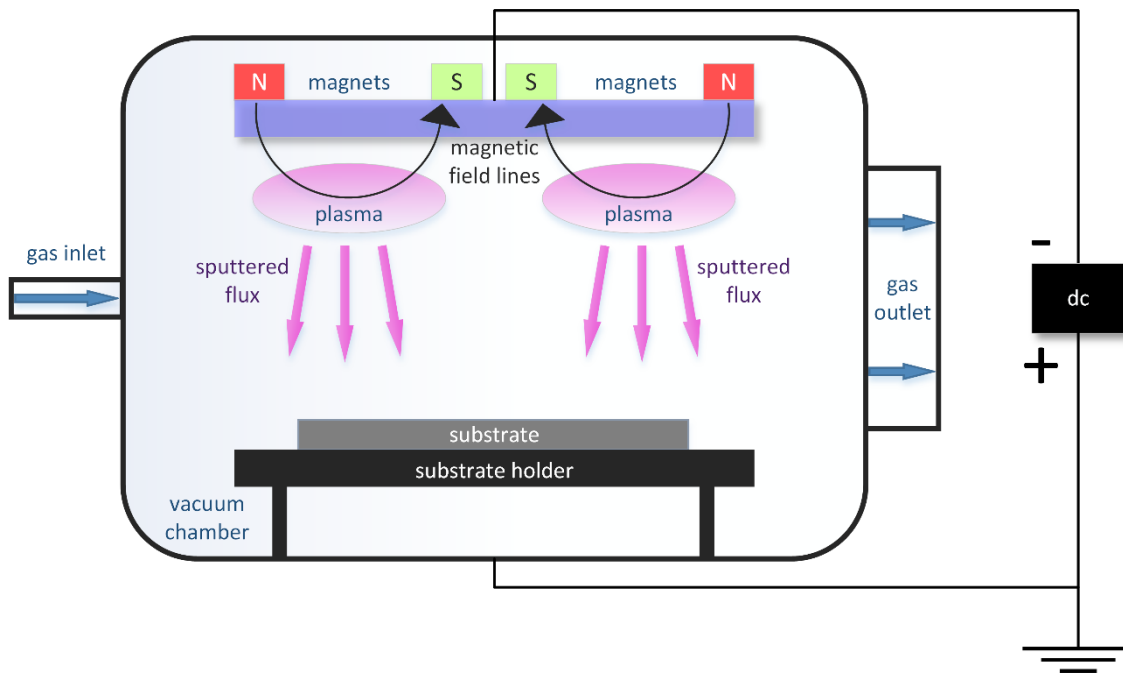


*Figure 23: Schematic of a dc magnetron sputter device.*

The magnetic field is used to influence the movement of the electrons. The electrons will move in form of a spiral around the magnetic field lines. The radius and the frequency of this motion depends on the magnetic field strength. Additionally, there is a movement perpendicular to both the electric and the magnetic field lines. The field lines can be shaped in such a way that the electrons circulate on a closed path above the target surface. In this way, the electron density is much higher compared to a regular dc sputter device, where the electrons are simply

accelerated away from the cathode. This increased electron density leads to a higher ionization of the gas atoms and therefore to a higher plasma density, which improves the deposition rate significantly. Also, the necessary voltage to sustain the plasma discharge is reduced from approximately 700V to 300V (depending on the sputter set-up and the given parameters). As a consequence the arc rate is reduced and the deposition process becomes more stable.

The magnetic field can either be generated by permanent magnets or electro magnets. A typical material for permanent magnets is neodymium-iron-boron (NdFeB) alloy. The main advantages of these magnets are their high magnetic flux density and their small size. This allows the construction of very compact sputter sources. However, their maximum operation temperature is usually at approximately 80°C. Therefore, a sufficient cooling has to be guaranteed at all time. In contrast, electro magnets avoid this problem. However, to reach a comparable magnetic flux density as permanent magnets, high electric currents are necessary. Also magnetic field coils maybe difficult to integrate in the sputter set-up. Advantages of the electro magnets are their increased insensitivity to high temperatures and the controllability of the magnetic field. The decision for one type of magnets depends on the specific requirements of the sputter system.

The most common dc magnetron sputter set-up is the planar type, where permanent magnets are arranged underneath a planar sputter target (see [Figure 24](#)). Here, the electrons are trapped along a closed path above the surface of the target, the so-called *race track*.

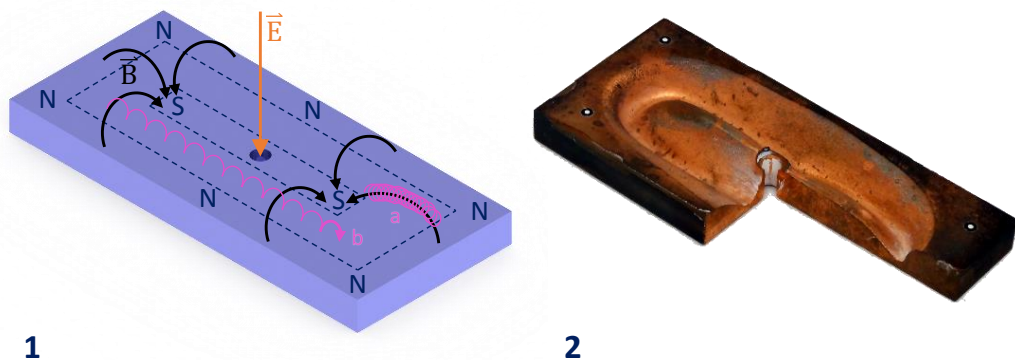


**Figure 24: Electron drift and sputter erosion of a planar magnetron device.** 1) The magnetic field  $\vec{B}$  and the electric field  $\vec{E}$  force the electrons on spiral paths around the magnetic field lines (a). Additionally, the electrons experience a drift in the  $\vec{E} \times \vec{B}$  direction (b). This leads to the formation of a so-called racetrack, a closed path around the target surface with a very high electron density. Due to the high ionization rate of these electrons, a characteristic erosion profile along this racetrack is formed. A used copper target of a planar magnetron is shown in 2). [58]

### 2.5.3 CYLINDRICAL MAGNETRON DEVICE

In the context of this work, a so-called *cylindrical magnetron sputter set-up* is used. Different types of cylindrical magnetrons are described in [59]. The current work will focus on the configurations shown in [Figure 25](#). In these arrangements the sputter target consist of a cylinder, which is located coaxial in the center of the cylindrical substrate. The electric field is applied between the target and the surrounding substrate, whereas the magnetic field is generated in axial direction by a magnetic coil around the substrate. Configuration 2 additionally has electron deflecting surfaces on both ends.

The trajectory of electrons is influenced by the electric and the magnetic field. The radially applied electric field  $\vec{E}$  leads to an acceleration of the electrons in radial direction towards the

substrate and an acceleration of the sputter gas ions towards the target. The acceleration  $\vec{a}$  of the electron is given by

$$\vec{a} = \frac{e}{m_e} \vec{E} \quad (8)$$

where  $m_e$  is the mass and  $e$  the charge of the electron.

By adding a magnetic field  $\vec{B}$  the electrons additionally experience a force perpendicular to the magnetic field and their velocity  $\vec{v}$ , the Lorentz force. The total acceleration of the electron is given by

$$\vec{a} = \frac{e}{m_e} (\vec{E} + \vec{v} \times \vec{B}) \quad (9)$$

In contrast, the influence of the magnetic field on the sputter gas ions can be neglected because of their high mass.

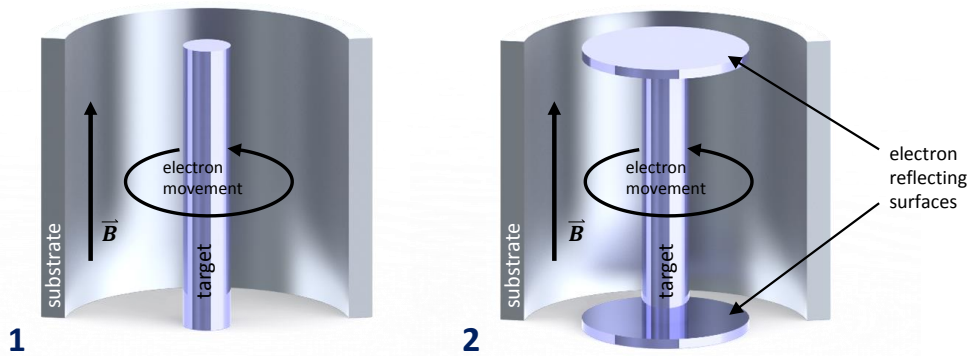


**Figure 25: Cylindrical magnetron configurations.** 1) A negatively charged target is placed coaxial to a grounded cylindrical substrate. A magnetic field is applied in the axial direction. The electric and the magnetic field lead to an electron movement around the target. In a simple magnetron configuration (1) an additionally movement of the electrons in axial direction leads to the loss of electrons on both ends. This can be hindered by electron reflecting surfaces (2).

The main source of electrons sustaining the plasma discharge in the cylindrical magnetron are the secondary electrons, which are ejected from the target surface during ion bombardment. Since these electrons are usually ejected with a low energy of several eV compared to an applied voltage of several hundred V, the ejection energy can be neglected and the kinetic energy of the electron mainly depends on its radial distance to the target surface. Assuming a uniform electric field the electrons would be forced on a cycloidal path in the  $\vec{B}$ -plane according to equation (9). The radius of this cycloid path is given by the Larmor radius

$$r_L = \frac{m v_{\perp}}{e |\vec{B}|} \quad (10)$$

where  $v_{\perp}$  is the electrons speed perpendicular to the magnetic field. Due to the not uniform electric field in a cylindrical magnetron, a cycloidal-like path with a slightly altered radius is formed. However, this radius is similar to the Larmor Radius with the speed, which is gained after the acceleration by the potential drop close to the cathode surface (see chapter 2.1). Undisturbed, this path leads away from the target surface to a turning point and then returns back to the target surface. To cause an ionization, the electrons have to reach a minimum energy, which is given in the negative glow region (see chapter 2.1). Therefore, the magnetic field has to be within certain limits. On the one hand, a magnetic field, which is too high, hinders

the electrons from gaining enough kinetic energy to ionize gas atoms. On the other hand, in a too low magnetic field the electrons reach the anode wall without being returned. This leads to a low residence time in the gas volume and therefore to a low ionization probability. Electrons, which cause ionization of the sputter gas, lose momentum and cannot overcome the electric field to return to the target surface. These electrons are trapped on a cycloidal-like path around the target (see [Figure 26](#)), what leads to a high ionization density.

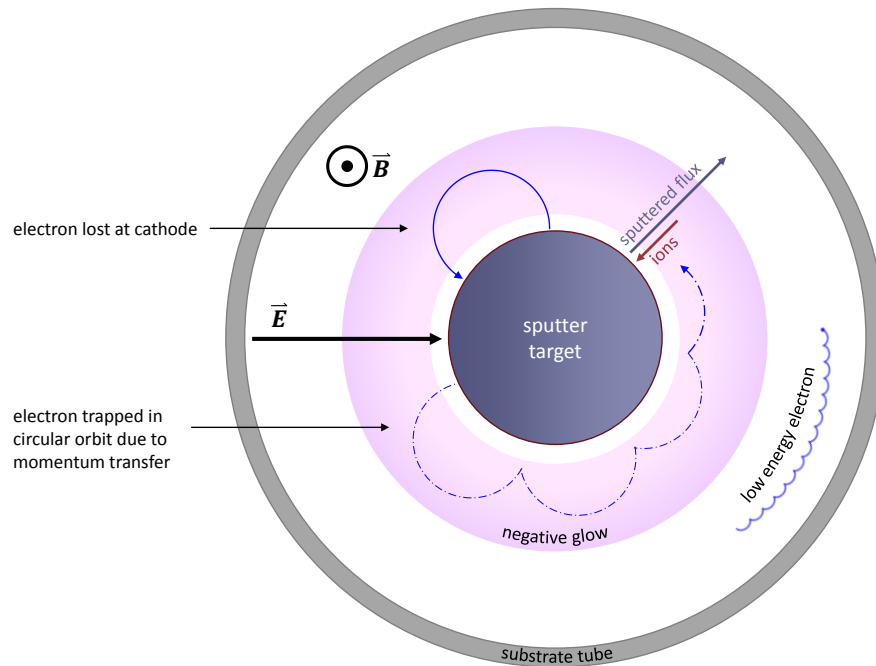


**Figure 26: Electron transport processes in a cylindrical magnetron device.** The section drawing of the  $\vec{B}$ -plane in a cylindrical magnetron device shows the paths of different representing electrons in the sputter process. Secondary electrons ejected from the target surface describe a cycloidal-like path with a radius, which is dependent on the magnetic field. When these electrons lose momentum on their trajectory they get trapped on a circular orbit around the target. Low energy electrons, which are generated in ionization processes in the outer region, also follow a circular orbit around the target.

Additionally to the movement in the  $\vec{B}$ -plane, the electrons can move in an axial direction. This is caused by an axial component of the electric field. This component is induced by the electric space charge in the plasma region. In simple cylindrical magnetrons ([Figure 25](#), set-up 1) this leads to a loss of electrons at both ends of the sputter target. Therefore, the performance of such set-ups is usually low. This can be improved by placing electron reflecting surfaces on both ends of the target to trap the electrons in the target area ([Figure 25](#), set-up 2). The electron reflecting surface can either be made of a conducting material (e.g. the target material) connected to the negative voltage of the target or in form of an isolating material. When the isolator is in contact with the plasma electrons, this leads to a build-up of a negative potential and therefore a repulsive force.



### 3 INSTRUMENTATION

To realize the manufacturing of cylindrical irradiation targets by sputtering, two cylindrical magnetron devices were built. A first elementary set-up was constructed in order to study basic operation parameters and conceptual considerations. Points of interest were, among others, the generation of the required magnetic field, the testing of suitable materials and the development of preparation methods for further analysis of the sputtered test samples. The first experimental device is equipped with a fixed, not moving, sputter target, whose length covers the length of the area to be coated. In the following, this set-up is referred to as fixed target set-up (FTS). Based on the gained knowledge a second prototype sputter reactor was developed. This reactor features a moving sputter target, which allows the production of coatings with a homogenous thickness. Additionally, this reactor was integrated in a glove box to allow a safe handling of nuclear material. This set-up is referred to as moving target set-up (MTS).

In the beginning of the following chapter a compact overview over the fixed target set-up is given. Its concept and realization is explained and the gained results are presented. For a more detailed description of the FTS reference is made to [39]. In the following chapters, the moving target set-up as well as its controlling and monitoring systems are described in detail.

#### 3.1 PREDEVELOPMENT: FIXED TARGET SET-UP

A schematic drawing of the fixed target set-up and its process diagram are shown in [Figure 27](#) and [Figure 28](#).

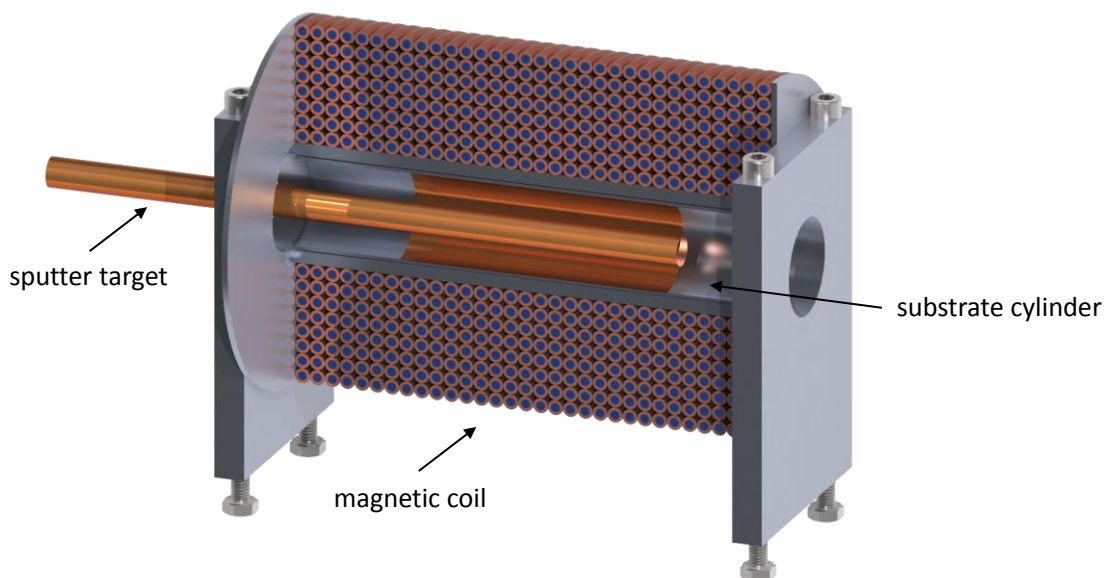


**Figure 27: Fixed target set-up.** The FTS consists of a not movable sputter target, which is located in the center of the substrate cylinder. The substrate cylinder is placed in a substrate carrier tube, which is surrounded by a magnetic coil. The coil is wound of an isolated copper pipe and is cooled by water flowing through the pipe. [39]

The substrate cylinder is located inside a magnetic coil with a length of 160mm, which is made of an isolated copper pipe wound in eight layers around a substrate carrier tube. The usage of a pipe instead of a solid wire allows an effective cooling by passing water directly through the magnetic coil. The heat dissipation of the coil allows a maximum electric current of

approximately 40 A resulting in a maximum magnetic field intensity of 85 mT in axial direction located at the center of the coil. The sputter target is in form of a rod with a diameter of 6 or 10 mm, which is mounted along the central axis of the sputter cylinder. The length of this target rod exceeds the length of the area, which is supposed to be coated. To fixate the target rod and to cover the ends of the substrate cylinder from unwanted coating, target fixations in different materials and shapes were investigated (see Figure 29).

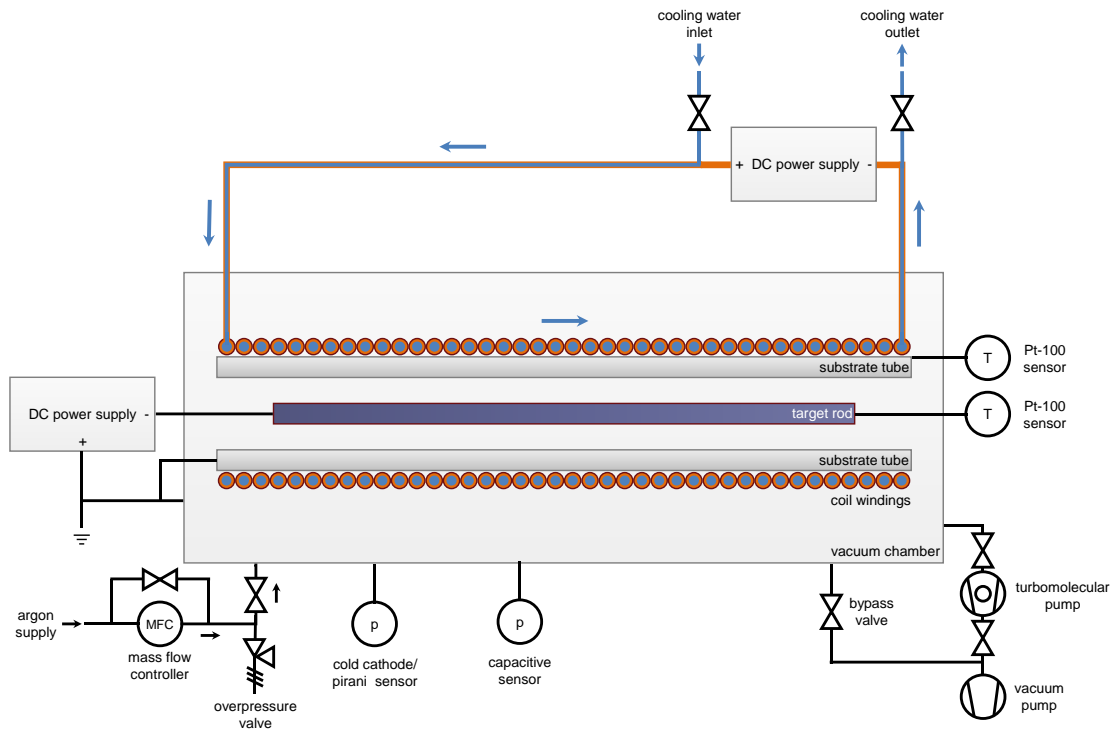


**Figure 28: Schematic of the FTS.** The FTS is placed in a vacuum chamber. The chamber is equipped with a pumping system and an argon gas supply. The gas pressure is controlled by regulating the gas inflow by a mass flow controller while pumping at a constant rate. The gas pressure is measured by two sensors: a cold cathode/pirani sensor for a rough measurement in a wide pressure range and a capacitive sensor for a more precise measurement in the range of the sputter process. The magnetic field is generated by a coil powered by a high current power supply. The generated heat is removed by cooling water flowing through the copper coil pipe. The sputter target is connected to a high voltage supply in order to ignite the plasma discharge. To guarantee a safe operation the temperature of the sputter target and the magnetic coil is monitored by two Pt-100 sensors. [39]

To generate a suitable process atmosphere, the assembly is placed in a vacuum chamber, which is equipped with a roughing pump, a turbo molecular pump and a mass flow controller to regulate the sputter gas inflow. As a sputter gas, argon is used. To establish a process atmosphere, first the chamber is evacuated to a pressure of roughly  $10^{-6}$  mbar to remove residues, which could disturb the coating process. Afterwards the pumping speed is reduced by an adjustable gate valve and argon is injected to establish the desired pressure in a dynamic equilibrium. Typical sputter pressures are between  $5 \cdot 10^{-3}$  and  $1 \cdot 10^{-1}$  mbar. The coating process is started by applying a negative voltage to the sputter target. Due to the lack of an active cooling of the sputter target the sputter power was limited to 50 W. Typically at a pressure of  $5 \cdot 10^{-2}$  mbar and a magnetic field of 50 mT, a sputter power of 50 W is established at a voltage of approximately 500 V. Typical coating times to reach the desired mass of sputtered material were between 24 and 48 h depending on the sputter power. Since all experiments were performed with copper as sputter materials, the reactor did not have to be integrated in a glove box.



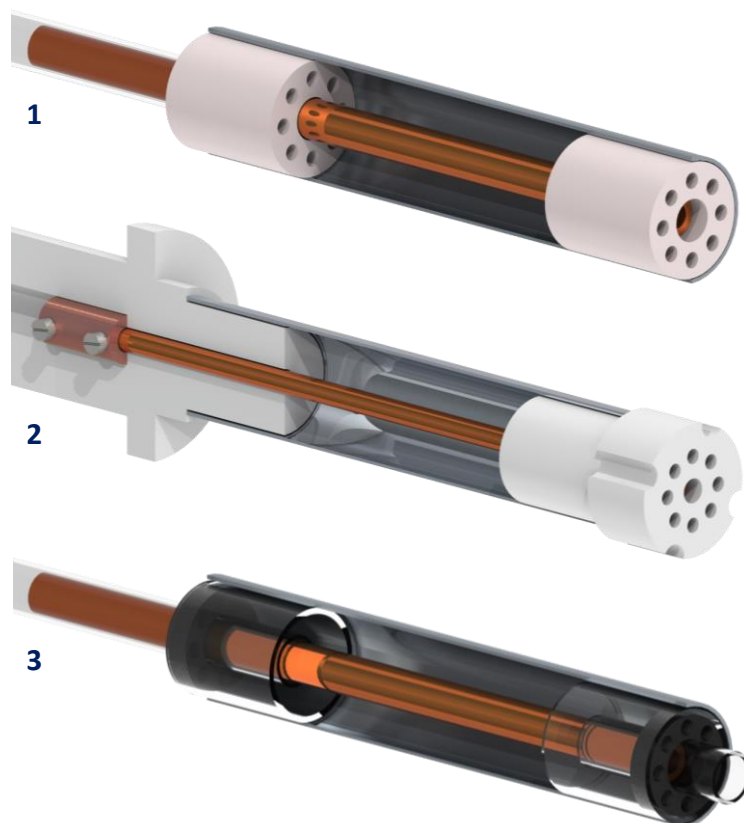


**Figure 29: FTS sputter target fixations.** In order to arrange the sputter target in the center of the substrate tube and to define the area to be coated, different target fixations were investigated. The figure shows three examples made of boron nitride (1), PTFE (2) and an assembly of glass and iron (3). The holes in the target fixation allow the sputter gas to reach the plasma volume. [39]

With this reactor, experiments were made to investigate suitable construction materials, necessary process parameters and the suitability of the magnetic coil and its cooling system. Several coating runs with different target fixations and sputter parameters were performed. The experiments showed an inhomogeneous erosion profile of the sputter target, what led to an inhomogeneity of the thickness of the sputtered layer. One reason of this inhomogeneity was the influence of the target fixation on the plasma behavior. By optimizing the target fixations the erosion profile was homogenized. However, a residual inhomogeneity, which cannot be accepted for an irradiation target production, could not reliably be eliminated.

From the performed experiments several conclusions were drawn, which were used to build the MTS sputter reactor:

- Using a water cooled copper coil is a suitable way to generate the magnetic field for the sputter process. It allows a sufficient magnetic field intensity and can reliably be cooled. To achieve a more homogenous field however, the length of the magnetic coil needs to be increased.
- Boron nitride (BN) proved to be a good material for the application in a sputter device. The material features a high thermal conductivity and durability. It has a low outgassing rate and can, therefore, be used in a vacuum environment. Additionally, it can easily be machined compared to other ceramics. BN also showed a good stability when in

contact with the plasma environment. Therefore, BN is suitable to be used for the target fixations.

- It was not possible to reach a homogenous layer thickness using a one fixed target. Hence, a shorter target with the ability to be moved in the axial direction needs to be used. A shorter and simple target design also allows a target production by casting. This is especially of interest when using uranium. Due to its radioactivity, it is of advantage to avoid production steps, which involve machining.
- In order to achieve acceptable coating times, the sputter power has to be increased significantly, especially, when taking the reduced target size into consideration. Therefore, an active target cooling system needs to be installed.
- With the FTS it was barely possible to control the adhesion of the deposited layer on the substrate. Since the adhesion strongly depends on the substrate temperature, a temperature control for the aluminum cylinder is necessary.

### 3.2 CONCEPT OF THE MOVING TARGET SET-UP

The MTS was constructed using the experience gained with the FTS. In contrast to the experimental FTS, the MTS is built to deposit uranium in order to manufacture irradiation targets. Therefore, special attention was given to make the FTS usable inside a glove box. To achieve this, an easy substrate and sputter target loading system is realized. An overview of the MTS is shown in [Figure 30](#).

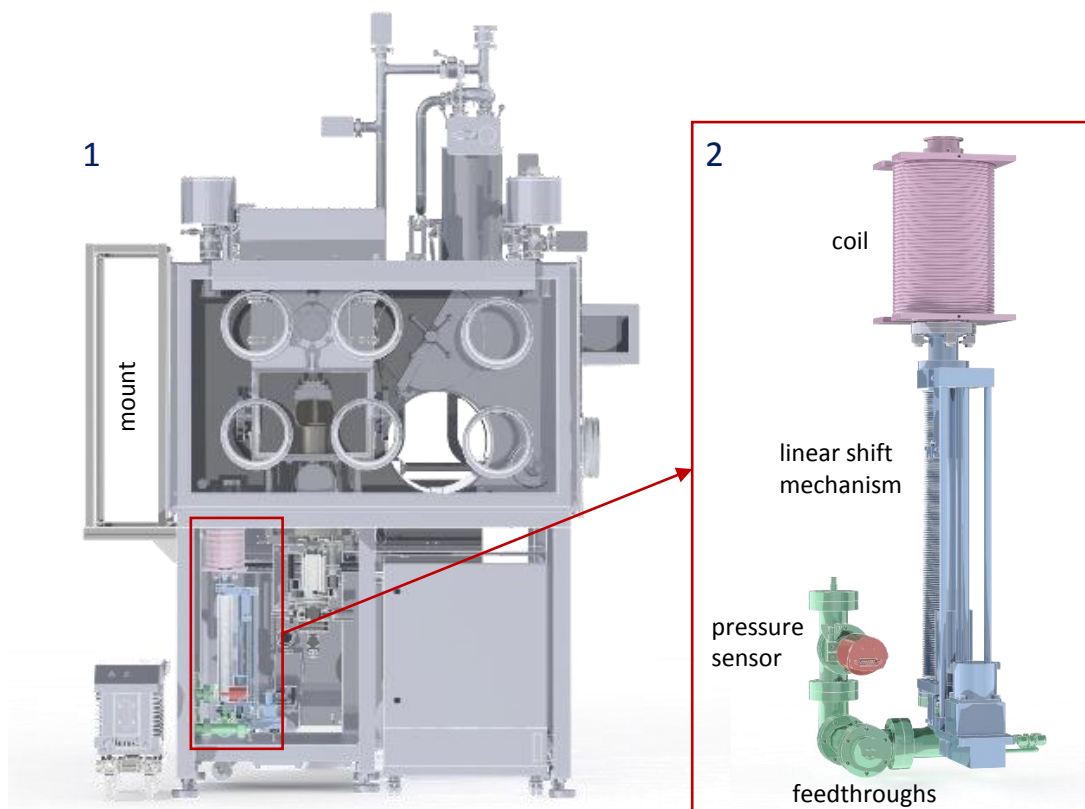


**Figure 30: Overview of the MTS.** 1) Front view of the glove box housing the MTS apparatus. 2) The MTS consists of a magnetic coil, a linear shift mechanism, a support flange with the necessary vacuum feedthroughs and a pressure sensor. A mount on the left side of the glove box is housing all the power supplies and the mass flow controller.

The MTS is connected to a double sided vacuum flange on the bottom of a glove box. On the outside of the glove box, the MTS consists from top to bottom of a magnetic coil, a linear shift mechanism and feedthroughs for cooling water, dc sputter current, thermocouples, sputter gas and a pressure sensor. Inside the glove box, the vacuum flange is connected to a 6-way manifold. This manifold is on one side connected to the vacuum system and on the other side equipped with a ventilation valve. On the top side the manifold has a removable vacuum window. During operation this window is used to observe the plasma discharge with a camera.

For loading and unloading of the substrate and the target, the window and the camera is removed and the linear shift mechanism of the MTS is used to move the mount of the sputter target to a position inside the glove box, where a new target can be inserted. The target mount is made in form of a water cooled copper body (see [Figure 31](#)). This allows an effective cooling of the sputter target and makes high deposition rates possible. The substrate is placed in a copper capsule with a hole in its bottom. This capsule is put over the sputter target. Both the substrate capsule and the sputter target are then moved by the linear shift mechanism down inside the magnetic coil. The substrate capsule comes to a stop on a rest inside the vacuum vessel and, thus, is fixed in the center position of the magnetic coil. With the sputter capsule fixed, the sputter target is able to move in a vertical range of  $\pm 48$  mm from the center position during the coating process. In this way a deposited layer with a homogenous thickness can be achieved.

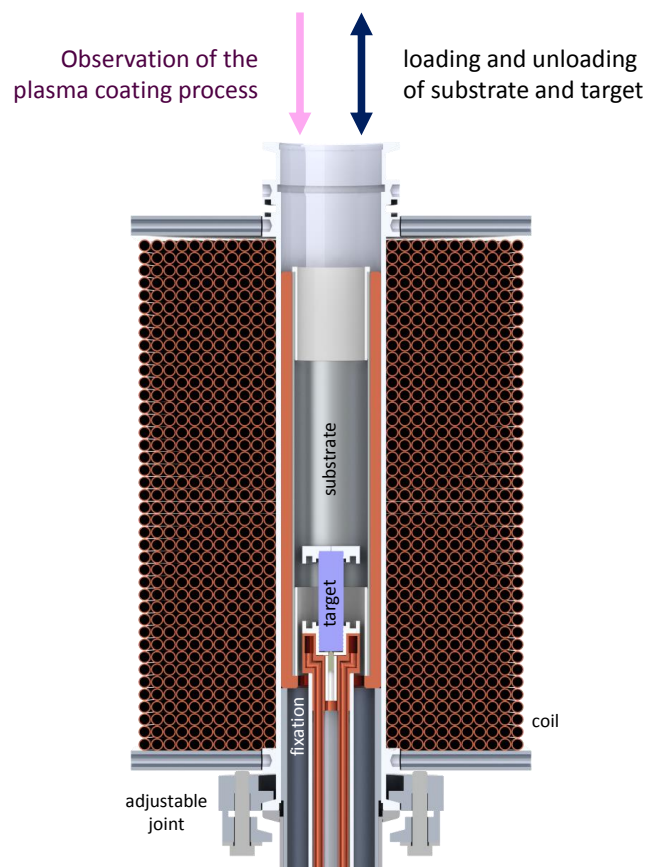


**Figure 31: Cut view of the MTS.** In the center of the magnetic coil, the substrate capsule rests on a fixation. The sputter source is able to freely move in axial direction in a range of  $\pm 46$  mm from the center of the substrate. An adjustable joint allows to compensate manufacturing inaccuracies.

The linear shift mechanism has a maximum stroke of 300 mm. From its lowest position to 96 mm, the linear shift mechanism is used to solely move the sputter target inside the fixed substrate. From 96 mm to 300 mm the mechanism is used to move the target and the substrate to a position inside the glove box, where they can be replaced. The mechanism has an accuracy of  $<20\ \mu\text{m}$  and a maximum speed of 3.4 mm/s.

In this design the magnetic coil is arranged on the outside of the vacuum vessel. On the one hand, this allows an easy access to the coil for maintaining purposes. And on the other hand, it significantly reduces the volume required in the vacuum chamber and the amount of virtual leaks<sup>3</sup>. Therefore, placing the coil on the outside of the vacuum chamber significantly decreases the pumping times and reduces the risk of unwanted contaminations in the process atmosphere.

To control the adhesion and the properties of the deposited foil a temperature control of the substrate is implemented. The ohmic heat of the magnetic coil is used to heat the substrate. To regulate the temperature, the cooling water flow can be regulated at a given electric current by a proportional valve. The proper thermal contact between the magnetic coil and the substrate is realized by the copper capsule used for loading and unloading the substrate.

### 3.3 SUBSTRATE

The original dimensions of the irradiation target design from ANL (see [Figure 10](#)) were adapted to the metric system and slightly altered (see [Table 6](#)). The change in dimension was kept small to guarantee the transferability of the process to the original dimensions. However, machining and acquisition of components was facilitated significantly. Due to the nature of the coating process, the indentation to house the uranium foil is made in the outer aluminum tube; in contrast to the ANL design, where the indentation is made on the inner aluminum tube. Taking into consideration the bigger radius of the indentation, its depth is reduced to achieve a comparable volume. As substrate material aluminum 6061-T6 is used.

*Table 6: Adapted substrate dimensions.*

<b>Dimension</b>	<b>ANL design</b>	<b>TUM design</b>
<b>Outer tube length</b>	6.370 inch (=161.8 mm)	162 mm
<b>Outer tube outer diameter</b>	1.181 inch (=30.0 mm)	31 mm
<b>Outer tube inner diameter</b>	1.107 inch (=28.1 mm)	29 mm
<b>Coating zone length</b>	3.626 inch (=92.1 mm)	92 mm
<b>Indentation depth</b>	0.00625 inch (=159 $\mu\text{m}$ )	150 $\mu\text{m}$

During the coating process, the substrate is placed in a copper capsule. This capsule allows an easy loading and unloading of the substrate cylinder and, additionally, serves as thermal contact of the substrate to the magnetic coil. Copper was chosen as a material due to its high

<sup>3</sup> Virtual leaks are trapped volumes of gas inside the vacuum chamber, which are hard to pump out of the vacuum system.

thermal conductivity and its magnetic properties. To shield the ends of the substrate of unwanted coating, thin cylindrical covers are applied on both ends. The covers are either made of glass or aluminum. An assembled target capsule is shown in [Figure 32](#).

All parts are held in place by gravity, so no adhesion has to be applied. The thermal contact between the substrate and the copper capsule and the copper capsule and the walls of the vacuum vessel was enhanced by coating the surfaces with graphite spray.

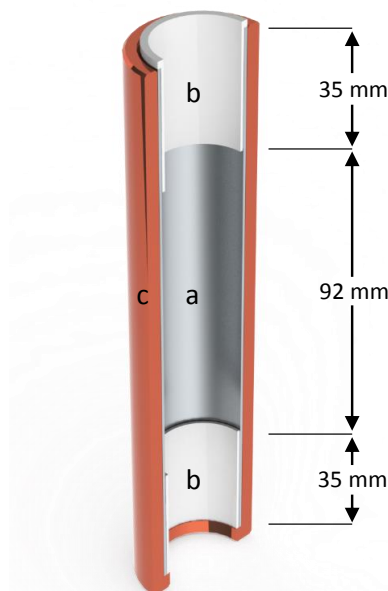


**Figure 32: Substrate capsule of the MTS.**

*The substrate (a) is housed in a copper capsule (c). This allows an easy loading and unloading of the substrate and provides a good thermal contact to the magnetic coil surrounding the vacuum vessel. Two deposition shields (b) avoid the coating of the end parts of the substrate.*

### 3.4 SPUTTER SOURCE

The sputter source of the MTS consists of a vertically mounted sputter target in pin shape. The target is connected to a heat sink on its lower end. To electrically isolate the target from the heat sink, a ceramic socket is used. This socket features an electrical connector on its bottom. On both ends of the target pin reflecting surfaces made of an isolator are attached. [Figure 33](#) shows a cut view of the MTS sputter source.

The sputter target has a length of 40 mm and a diameter of 10 mm. Using approximately 10 mm for the thermal connection to the heat sink, 30 mm of the target are exposed to the sputter process. This length was chosen since experiments with the FTS showed a maximum of the erosion rate within 15 mm of the electron reflecting surfaces. The diameter of the target was chosen to provide approximately two times the volume necessary to coat one irradiation target. The extra volume is supposed to prevent the target from breaking apart at high sputter burn-ups. The simple shape of the targets allows their production by casting. Thus, the unused target material can be recycled after the coating run.

The heat sink of the sputter source consists of a water cooled copper ring. The copper ring is fed with cooling water by two 4x0.5 mm copper pipes. These pipes are connected to the cooling

water system of the laboratory by a vacuum feedthrough in the lower section of the MTS. To monitor the temperature of the sputter source, the heat sink is equipped with two type K thermocouples.

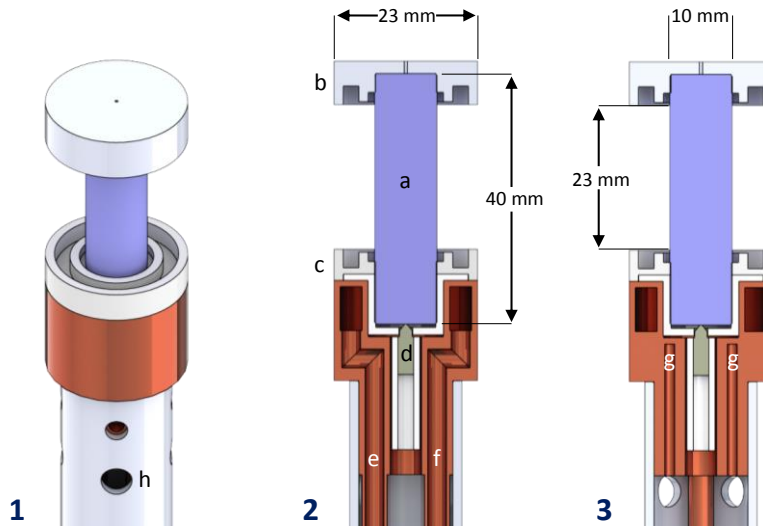


**Figure 33: Sputter source of the MTS.** The sputter source consists of a cylindrical sputter target (a), which is mounted in a ceramic socket in a copper heat sink. The heat sink is cooled by a cooling water flow provided through an inflow (e) and an outflow (f). The temperature of the heat sink is monitored by two type K thermocouples mounted inside the copper body (g). The target is connected to a high voltage power supply by a tungsten pin (d). During the evaporation the plasma is encapsulated by two ceramic electron reflecting surfaces (b) and (c). The sputter gas is provided to the process chamber via four holes in the support shaft (h).

The heat sink surrounds a ceramic socket holding the sputter target. To improve the thermal contact between the heat sink, the ceramic socket and the target, heat conductive paste is applied on the matching surfaces. Good results were gained using Keratherm KP98 Thermal Grease.

As ceramic material HeBoSint<sup>®</sup> O140 and AlN 180 were investigated. HeBoSint<sup>®</sup> O140 is a sintered ceramic material based on boron nitride. AlN 180 is based on aluminum nitride. **Table 7** shows important material parameters of the two ceramics. AlN180 features the advantage of a much higher thermal conductivity compared to HeBoSint<sup>®</sup> O140. However, AlN180 is also very brittle and hard to machine. Experiments showed that both materials have sufficient material properties to be used in PVD devices. These properties are a sufficiently high thermal conductivity, a compatibility to the vacuum environment and a high dielectric strength. In the experimental coating runs, HeBoSint<sup>®</sup> O140 was preferred over AlN180 due to its significantly better machinability. This allowed to easily adjust the ceramic components according to changing tolerances of the target materials. However, when producing irradiation targets, boron might be avoided, because of its high neutron capture cross-section. In this case AlN180 is a suitable alternative.

The electron reflecting surfaces are manufactured of the same ceramics as the ceramic socket. Also here, both materials performed well and HeBoSint<sup>®</sup> O140 was chosen as the standard material for the experiments. The lower electron reflecting surface is in form of a ring, which covers the heat sink from being coated. The upper electron reflecting surface is manufactured as a cap, which is put on the top of the target pin.

**Table 7: Properties of AlN and BN.** If applicable, all values are at 20°C. [60, 61]

Material property	HeBoSint® O140	AlN 180
Density	2.9 g/cm <sup>3</sup>	3.31 g/cm <sup>3</sup>
Thermal conductivity	24 W/mK	180 W/mK
Specific heat capacity	600 J/kgK	738 J/kgK
Maximum operating temperatures	>1000°C	>1000°C
Elastic modulus	45 GPa	310 GPa

The design of the electron reflecting surfaces underwent three iterations, which are shown in [Figure 34](#). In the final design, both reflecting surfaces feature circular indentations and increments. The increments provide shadowing of the sputtered material. The shadowed areas together with the sharp edges in this profile prevent a conductivity from the sputter target to the copper heat sink. Experiments performed with flat electron reflecting surfaces showed heavy arcing or even short circuits after a short sputter time. To eliminate virtual leaks between the target and the upper cap, a small pinhole was drilled in the center of the upper cap.

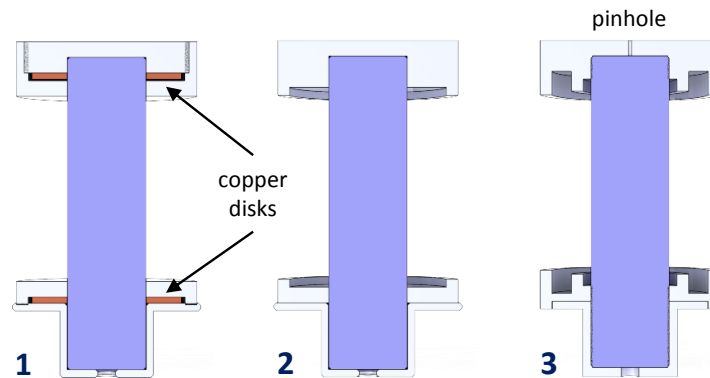


**Figure 34: Designs of the electron reflecting surfaces.** In a first attempt (1), copper disks were installed. The purpose of these disk was to prevent end losses of the plasma by electrostatically trapping the electrons in the plasma volume. However, it showed that even without the copper rings a similar effect was reached by the build-up of negative charges on the insulating ceramic surfaces. Since it was difficult to ensure a proper electrical contact between the target and the ring, this element was dropped in the second iteration (2). Also a small increment at the end of the ceramic parts was introduced. In this way, arcing could be avoided, which occurred after some hours of sputtering when using design 1. In a third iteration step (3), this increment was made higher and a second one was introduced to enforce the geometric shielding effect. In addition, the lower electron reflecting surface now also covers the ceramic socket. In this way, the socket does not need to be cleaned after every coating run. The upper cap, now features a small pinhole to avoid virtual leaks.

The sputter target is electrically connected to the dc power supply by a metallic pin on the bottom of the ceramic socket. The pin is housed in an AlN tube, where it is connected by

soldering to a shielded high-voltage cable. The ceramic tube is in good thermal contact to the heat sink in order to prevent the solder joint from overheating. Furthermore, the pin is sharpened on the top to minimize the contact area to the target and the heat transfer to the solder joint. The metal pin is made of tungsten due to its high melting point of 3370°C and its low specific electrical resistance of  $5.28 \cdot 10^{-2} \frac{\Omega \cdot \text{mm}^2}{\text{m}}$  [62]. The high-voltage cable is connected to a Hüttinger TruPlasma DC 3002 high-voltage power source through a coaxial vacuum feed-through. The TruPlasma power source is able to provide a maximum sputter voltage of 800 V and a maximum power of 2000 W. It is equipped with an arc management system, which reduces the residual energy of an occurring arc.

### 3.5 VACUUM AND GAS SUPPLY SYSTEM

To establish a suitable process atmosphere, the MTS sputter reactor is equipped with a vacuum and gas supply system. A simplified drawing of the system is shown in [Figure 35](#).

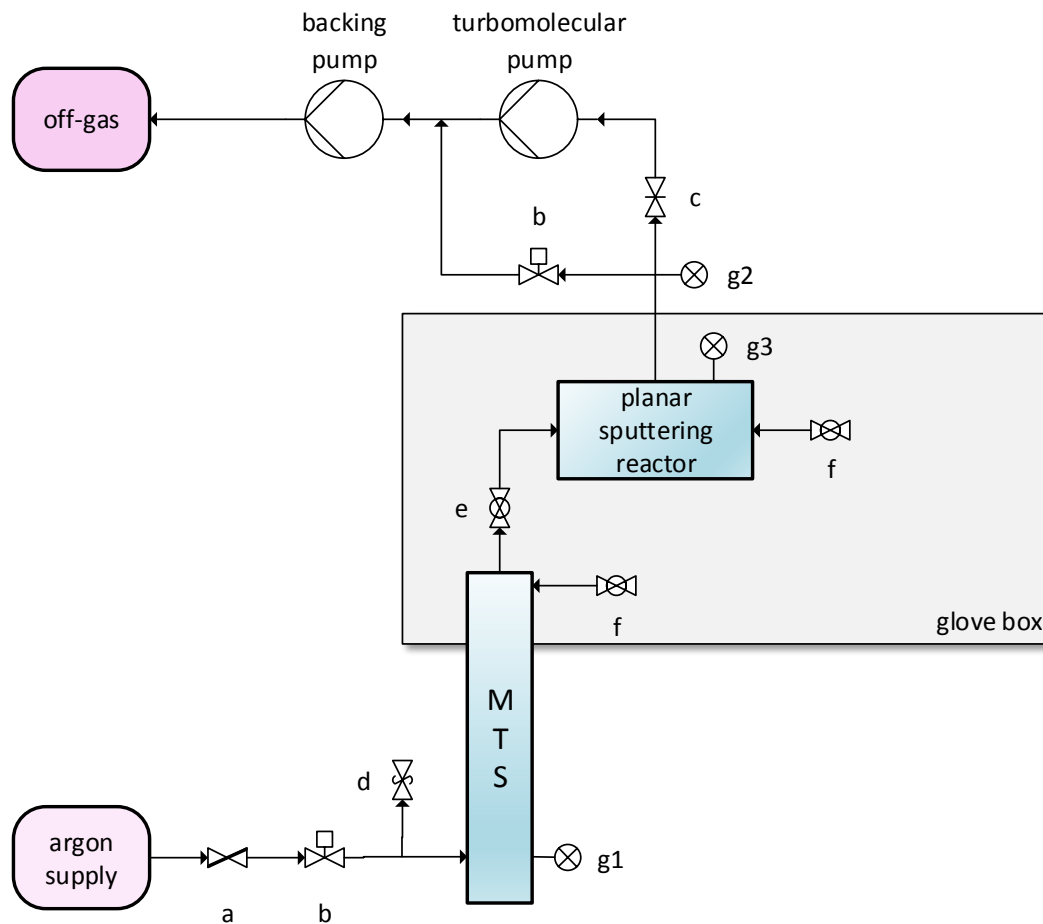


**Figure 35: Vacuum and gas supply system of the MTS.** The operating pressure in the MTS reactor is established in form of a dynamic equilibrium. The system features a mass flow controller (a), magnetic operated valves (b), a gate valve (c), an overpressure valve (d), a manually operated valve (e), ventilation valves (f) and three pressure sensors (g).

The vacuum system consists of a two staged pumping system using an Oerlikon TRIVAC D65B backing pump and an Oerlikon MAG W 1300 turbomolecular pump. Before starting the turbomolecular pump, the backing pump is used to establish a prevacuum. This pumping process is done through a valve bypassing the turbomolecular pump. This avoids mechanically



damaging the sensible turbomolecular pump by macroscopic particles carried by the viscous gas flow, which is present at higher pressures. After establishing a prevacuum of approximately  $10^{-2}$  mbar, the bypass valve is closed and a gate valve separating the turbomolecular pump and the vacuum chamber is opened. Then, the turbomolecular pump is started to establish high vacuum conditions. The high vacuum is used to remove unwanted residues from the process atmosphere. Residues are mainly reactive gasses like oxygen or nitrogen, humidity or organic residues from cleaning substances like acetone. After reaching a basic vacuum of approximately  $10^{-6}$  mbar, the process atmosphere can be established by injecting the highly pure sputter gas. In the following experiments argon with a purity of >99.998% provided by Linde AG was used.

The process atmosphere is established in form of a dynamic equilibrium. This means that the pressure is controlled by continuously injecting gas while pumping. The sputter gas is injected by a Bronkhorst mass flow controller capable of controlling the gas inflow between 0 and 300 sccm. Using a dynamic equilibrium features several advantages. The pressure can very easily and precisely be controlled since the pressure directly depends on the gas inflow, which is well controllable. Another advantage is the continuous replacement of the process atmosphere. This prevents a build-up of gasses, which could negatively influence the sputter process. This may be caused by leaks, virtual leaks or reactions of the plasma with other materials. To reduce the inflow and, therefore, the volume of used gas, the pumping speed of the vacuum system is reduced by setting the gate valve to an intermediate position.

The pressure in the process chamber is monitored by three pressure sensors. An Oerlikon PENNINGVAC PTR 90 is used to observe the full pressure range of  $5 \cdot 10^{-9}$  to 1000 mbar. This sensor uses a Pirani gauge for the higher pressure range and a cold cathode gauge for the lower pressure range. It is characterized by a low precision of  $\pm 30\%$  in a range from  $1 \cdot 10^{-8}$  to 100 mbar. Therefore, it is just used to monitor the initial pumping process meant to remove residues from the process chamber. To monitor the pressure more precisely in a range from  $10^{-3}$  to  $10^{-1}$  mbar, which is the relevant pressure range for the coating process, two Oerlikon CERAVAC CTR 100 sensors are used. The sensors use a capacitive measurement principle, which features a higher precision of  $<1\%$  and is not dependent on the type of gas. One sensor is located at the bottom of the FTS in close proximity to the gas inlet (CTR 100 bottom). It has a range from  $10^{-4}$  to 1 mbar. The other sensor is located inside the glove box close to the pumping outlet of the system (CTR 100 top). This sensor offers a range from  $10^{-5}$  to  $10^{-1}$  mbar. The different pressure ranges take an expected pressure drop from gas inlet to pumping outlet into consideration. **Figure 36** presents the dependency on the different pressure readings of the gas inflow in the MTS reactor. As one can see, the CTR 100 bottom and CTR 100 top sensor differ in two orders of magnitudes. This shows a strong pressure gradient along the MTS system.

After the deposition process, the process chamber is ventilated using the argon atmosphere of the glove box. This atmosphere is continuously purified to  $\text{H}_2\text{O}$  and  $\text{O}_2$  levels of  $<0.1$  ppm. On the one hand, using this purified atmosphere, prevents the coated substrates and remaining target material from oxidization. On the other hand, it inhibits the contamination of the sputter system with oxygen or humidity and reduces the necessary pumping times significantly.

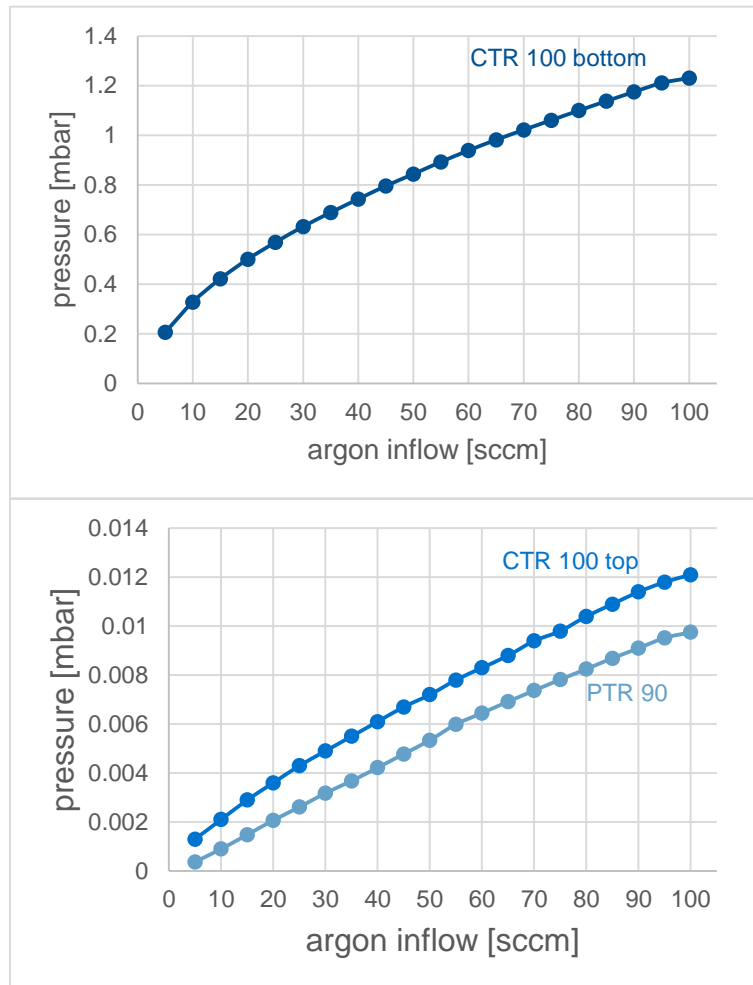


**Figure 36: Inflow-pressure-diagram of the MTS.** The diagrams show the measured dependency of the system pressures on the gas inflow. This measurement was performed using argon having the linear shift mechanism in the lowest position.

### 3.6 MAGNETIC COIL

Like the magnetic coil of the FTS, the MTS coil is wound in several layers of a copper pipe, which allows an efficient cooling by passing cooling water directly through the coil. The FTS coil had a length of 160 mm, 8 layers and an inner diameter of 40 mm. This geometry results in a magnetic field on the central axis of the coil, which is approximately 9% weaker at the ends of the coating zone compared to the center. This inhomogeneity was identified as one possible reason for the inhomogeneous erosion profile of the sputter target, which was one of the main flaws in the FTS concept.

Therefore, it was one design goal for the MTS coil to increase the coil's length significantly to reach a more homogenous magnetic field. Furthermore, a maximum magnetic field intensity of 100mT should be reached, while ensuring the heat dissipation of the coil. Variable parameters of the coil are its length, its inner diameter, the number of winding layers and the dimension of the copper pipe. However, the coil's length and inner diameter were defined by external constraints. The geometric conditions of the glove box just allowed a maximum length of 205 mm. The coil's inner diameter of 44 mm was defined by the standard dimensions of the vacuum vessel, which was used as center of the coil.

For the copper pipe the same dimensions as for the FTS were used. The pipe has an outer diameter of 4 mm and a wall thickness of 0.5 mm. This dimensions proved to be a good compromise between cooling water throughput, electric conductivity, outer dimensions and workability. To electrically isolate the copper pipe, a heat shrinkable tubing was used. This increases the pipe's outer diameter to 5 mm, what results in a total number of 41 windings per layer.

These considerations left the number of winding layers as last variable parameter for the geometry of the coil. This variable was chosen as a compromise between a good heat dissipation of the coil and the field homogeneity.

The magnetic field in axial direction of one layer at the central axis of the coil is given by

$$B_z^{layer}(z, r) = \frac{\mu IN}{2l} \left[ \frac{\frac{l}{2} - z}{\sqrt{(\frac{l}{2} - z)^2 + r^2}} + \frac{\frac{l}{2} + z}{\sqrt{(\frac{l}{2} + z)^2 + r^2}} \right] \quad (11)$$

where  $\mu$  is the magnetic permeability,  $I$  the electric current,  $N$  the number of windings per layer,  $l$  the length of the coil,  $r$  the radius of the layer and  $z$  the position along the central axis of the coil (measured from its center). The field of the whole coil can be calculated by

$$B_z^{coil}(z) = \sum_{i=0}^{L-1} B_z^{layer}(z, r_0 + id) \quad (12)$$

where  $r_0$  is the radius of the inner layer,  $L$  the number of winding layers and  $d$  the layer thickness. Increasing the number of layers  $L$  leads to a higher inhomogeneity of the field due to the increasing radius of the outer layer. However, less layers have to be compensated by a higher electric current. The electric current leads to an ohmic heating of the coil, according to

$$P = I^2 R \quad (13)$$

where  $R$  is the electrical resistance of the copper pipe. The resistance depends directly on the length of the copper pipe and, therefore, on the number of layers. Due to the quadratic influence of the electric current on the ohmic heating, the limiting factor of the coil's heat dissipation is the electric current. As a good compromise,  $N$  was set to 11. This value, results in a current of approximately 40 A to reach a maximum magnetic field intensity of 100 mT. With a coil resistance of approximately 0.5  $\Omega$ , the created ohmic heat is approximately 800 W.

**Figure 37** shows a comparison of the calculated magnetic field intensity in axial direction by formula (12) and measured values. To measure the magnetic field, a sputter target was prepared with a central drill hole housing the measuring tip of a Hall probe. In this way, the measuring point was located on the central axis of the coil and in the middle between the two electron reflecting surfaces. As one can see, the measured and the calculated values are in good accordance. The field inhomogeneity, the difference between the center and the end of the coating zone, was reduced to 6%. A further reduction could not be realized due to the limited building space. Therefore, an active compensation of the magnetic field is necessary to reach similar coating conditions in every position of the sputter source. This feature is explained in detail in chapter 4.2.

As a dc power supply to generate the magnetic field, a HEIDEN power PS 8080 120U is used. The power supply is capable of delivering a maximum current of 120 A up to a power of 3 kW. The current can be set with an accuracy of 100 mA.

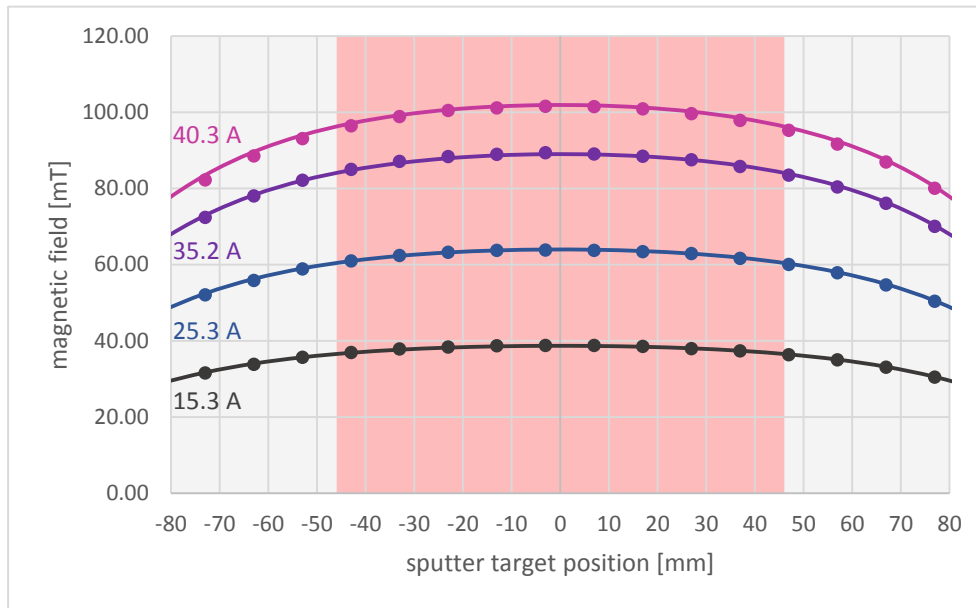


**Figure 37: Magnetic field of the MTS.** The diagram shows a comparison of the measured (dots) and calculated (line) magnetic field in axial direction along the central axis of the coil. The pink area from -46 mm to 46 mm indicates the actual coating zone.

### 3.7 COOLING UND TEMPERATURE CONTROL

To allow a strong magnetic field, a high sputter rate and a reliable operation, the MTS apparatus is equipped with a cooling and temperature control system. The cooling water circuit is embedded in a laboratory-wide cooling system. This cooling system is in form of a closed loop using a heat exchanger as a heat sink. In case of an error, this configuration avoids the release of any contamination to the environment. The laboratory cooling system is able to provide a pressure difference of 6 bar to the in- and outlet of the MTS apparatus. The provided cooling water has a temperature of approximately 16°C. A simplified drawing of the cooling circuit is shown in [Figure 38](#).

The cooling water is used to cool the magnetic coil and the sputter source. The magnetic coil is separated into three winding. One outer winding, which covers the layers 2 to 11 (from in- to outside) of the magnetic coil and two inner windings, which form layer 1. The inner windings are wound in form of a double helix, as shown in [Figure 39](#). The cooling water of the sputter source and the outer winding are both directly connected to the cooling water system and cannot electronically be regulated. The flow through the two inner windings however, is controlled by a proportional valve. This valve allows to adjust the cooling water flow from 0 to 100%. Due to safety considerations the minimum flow is set to 5%.

Under normal operation (magnetic field 85 mT) approximately 750 W of ohmic heat are released in the magnetic coil. At a flow of 0.15 l/min through the outer winding, a heat-up of approximately 45°C occurs. This results in a cooling power of approximately 470 W of the outer winding. The remaining 330 W can be used to increase the temperature of the inside of the magnetic coil. Hence, the coil temperature can be controlled by adjusting the additional cooling of the inner windings. A good thermal contact of the coil and the aluminum vacuum vessel was established by tight winding and the application of heat conductive paste at the interlayer. Due to the good thermal contact of the substrate capsule to the substrate and the vacuum vessel, the substrate temperature can be controlled by the cooling water flow of the inner windings. To achieve a uniform heating or cooling of the substrate, two windings with an opposite flow direction are used. This arrangement significantly reduces an axial temperature gradient.

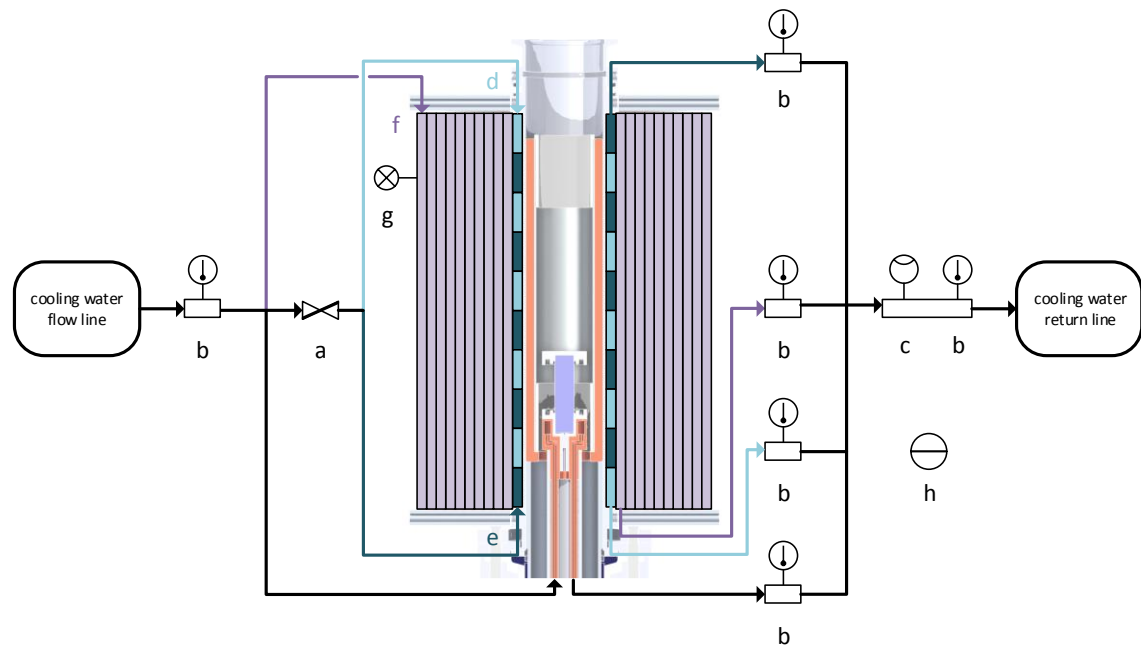


**Figure 38: Cooling system of the MTS.** The cooling water flow line of the MTS is split in three separated cooling lines: one to supply the sputter source and two to supply the magnetic coil. The outer layers of the coil (f) are cooled directly with a flow direction from the outer layer to the inner layer. In this way, a temperature gradient from the outer layer to the inner layer builds up, which allows a better heating of the substrate in the center of the magnetic coil. The substrate temperature is regulated by the cooling water flow through the two inner windings (d) and (e), which is controlled by a proportional valve (a). The cooling water system is monitored by thermocouples directly measuring the water temperature (b), a flow meter (c) and temperature sensors (g) between the layers of the magnetic coil.

The temperature control is realized by a PID-controller. The actual temperature is measured by two foil-type Pt-100 temperature sensors, which are located between the inner windings of the magnetic coil and the vacuum vessel in its center. The temperature sensors have a length of approximately 10 cm and a width of 1 cm. Their long side is arranged in axial direction to give the average temperature in the substrate region. Similar sensors are placed between layer 1 and 2 and layer 4 and 5 to monitor the coil's internal temperature for safe operation. In the future context the average temperature reading of the two inner sensors is referred to as measured or externally applied substrate temperature. The actual substrate temperature cannot be monitored during operation, since it additionally depends on the sputter power and the gas pressure. However, it showed that the readings of the two inner temperature sensors are a reliable value to characterize the coating process. The temperature control allows a safe adjustment of the temperature from 20°C to 90°C.

Additional thermocouples, which directly measure the temperature of the cooling water, are installed in the cooling water flow line and in each return line. Furthermore, the system is equipped with a flow meter and a leakage detector. These sensors are automatically monitored at all times. If a sensor exceeds its allowed value or detects a leakage, the deposition process is immediately shut down and the MTS apparatus turns into a safe condition. This includes the shutdown of all power supplies, an interruption of the cooling water supply and an alarm message to the experimenter.

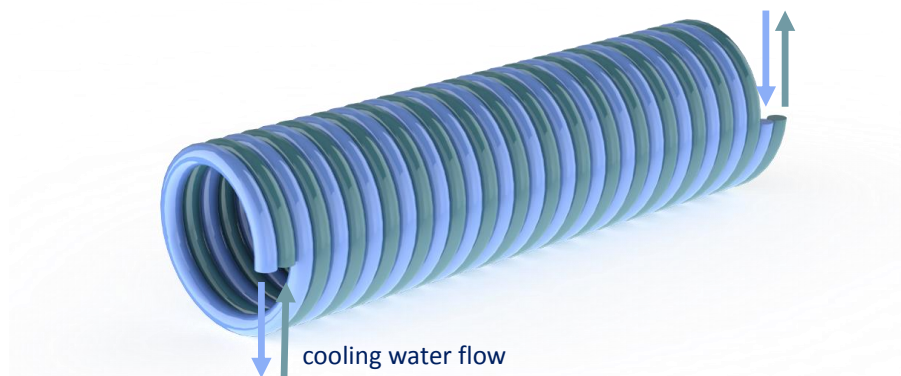


**Figure 39: Inner layer of the magnetic coil.** The inner layer of the magnetic coil consists of two copper pipes wound in form of a double helix. The cooling water flow through these pipes is in opposite direction in order to receive an even substrate temperature across the substrate length.

### 3.8 PLC CONTROL

The MTS apparatus is equipped with a central programmable logic controller (PLC), which is used to control the deposition process and guarantee a safe operation. The Beckhoff PLC has an operation cycle of 30ms and continuously monitors the following values:

- Power, voltage, current and arc rate of the high-voltage supply for the plasma discharge
- Power, voltage and current of the high-current supply for the magnetic field
- Pressure of PTR 90, CTR 100 top and CTR 100 bottom
- Position and speed of the linear shift mechanism
- Status of the gas valves and pumps
- Gas inflow
- Temperatures, flow rate and pressure of the cooling water supply
- Temperatures of the magnetic coil and the sputter source
- Status of the glove box

To actuate the deposition process, following parameters are controlled:

- Power, voltage and current of the high-voltage supply for the plasma discharge
- Power and current of the high-current supply for the magnetic field
- Movement of the linear shift mechanism
- Status of the gas valves and pumps
- Sputter gas inflow
- Status of the cooling water valves
- Cooling water flow through the inner windings of the magnetic coil

Since the coating of one irradiation target takes several hours, it is necessary to realize a reliable, safe and autonomous operation of the MTS. Therefore, a variety of safety measures were implemented. The PLC is constantly monitoring critical system parameters, like cooling water temperatures, cooling water flow, gas pressures or component temperatures. If the system detects abnormal values, the sputter process is interrupted and all components are shut down. Additionally to this implemented safety routine, a separate emergency shutdown system is installed. This system features leakage detectors, emergency shut-down buttons and it monitors the status of the glove boxes and the cooling water pump. In case of an error, this system is also able to shut down the MTS apparatus. In either case the MTS is transferred into a safe condition and the experimenter is informed about the occurrence and the cause of the error.

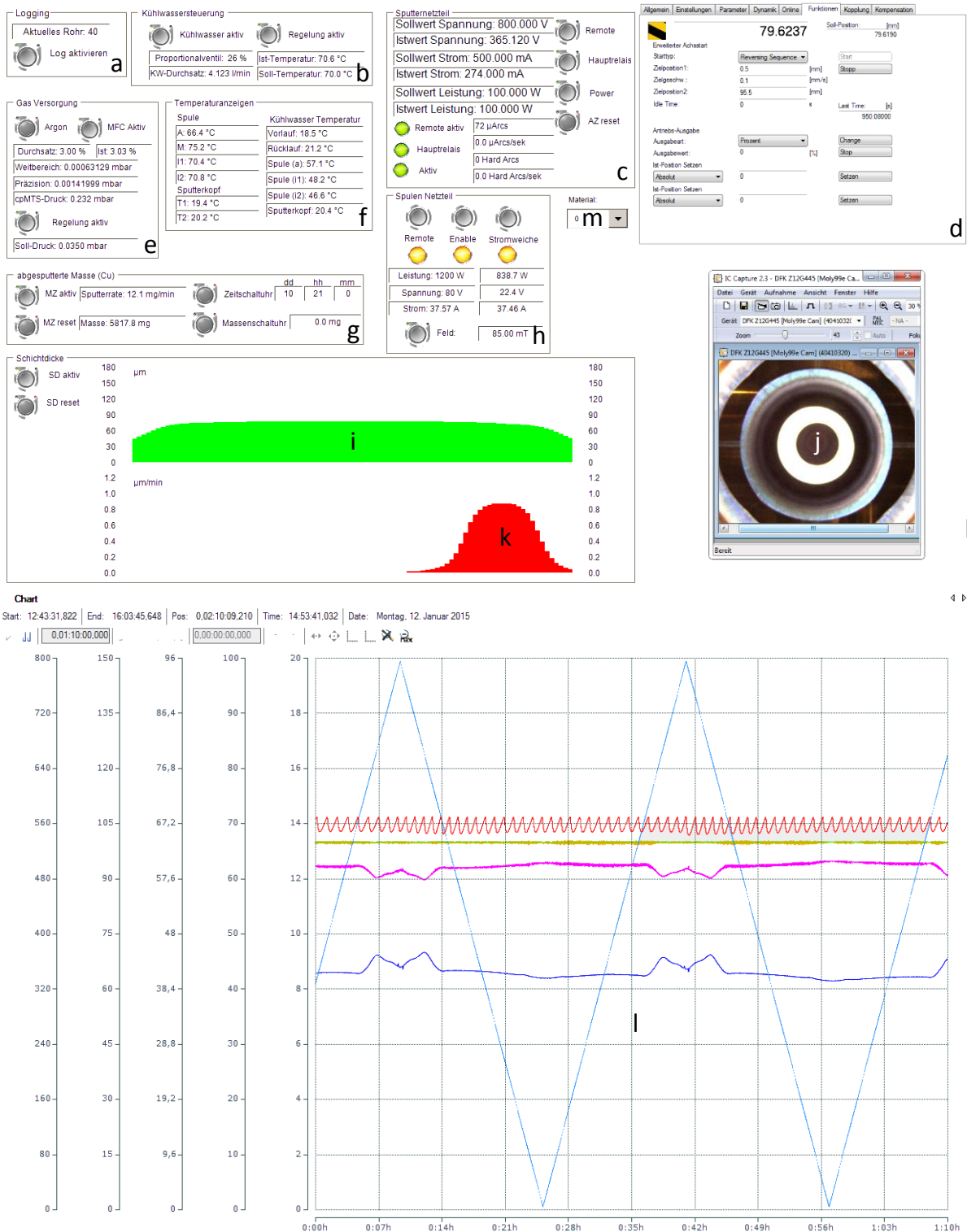


**Figure 40: Control interface of the MTS.** The control interface consists of different controlling and monitoring panels for logging (a), substrate temperature (b), sputter power supply (c), linear shift mechanism (d), gas supply (e), cooling water temperature (f), end conditions for the sputter process (g), magnetic field (h), calculated real-time layer thickness profile (i), plasma monitor (j), calculated real-time emission profile (k), plot (l) and material selection (m).

To allow an autonomous operation, the PLC is programmed with several controllers and algorithms:

- PID controller to regulate the substrate temperature by controlling the cooling water flow
- Controller to regulate the pressure in the coating zone taking into consideration the position of the linear shift mechanism
- Routine to calculate the deposition rate from the sputter voltage and sputter current
- Controller to regulate the magnetic field depending on the position of the linear shift mechanism
- Algorithm to automatically calculate the deposition layer thickness profile
- Controller to realize different moving profiles of the linear shift mechanism
- Logging of all parameters

The MTS is controlled either on a local or remote PC via the control interface, which is shown in [Figure 40](#). It allows the user to enter all important process parameters and the desired coating time, layer thickness or deposited mass. When one of these values is reached, the MTS automatically turns off the coating process and slowly cools down the substrate. When room temperature is reached, the vacuum system is ventilated and substrate and target can be removed. To observe the coating process, the interface shows all important parameters, a camera image observing the plasma and a real time plot. This plot shows sputter voltage, sputter power, substrate temperature, pressure, target position and the calculated deposition rate. Additionally, a real time thickness profile is displayed, which is calculated from the target movement, the sputter voltage and the sputter current.

### 3.9 GLOVE BOX INTEGRATION

The working principle of the MTS apparatus is to evaporate materials in order to form layers on the cylindrical substrate. Evaporating radioactive and/or harmful materials, like uranium or nickel, makes a safe enclosure mandatory. Therefore, the MTS was integrated in a glove box system (see [Figure 41](#)). The glove box system consists of two different glove boxes: the sputter glove box and the chemistry glove box.

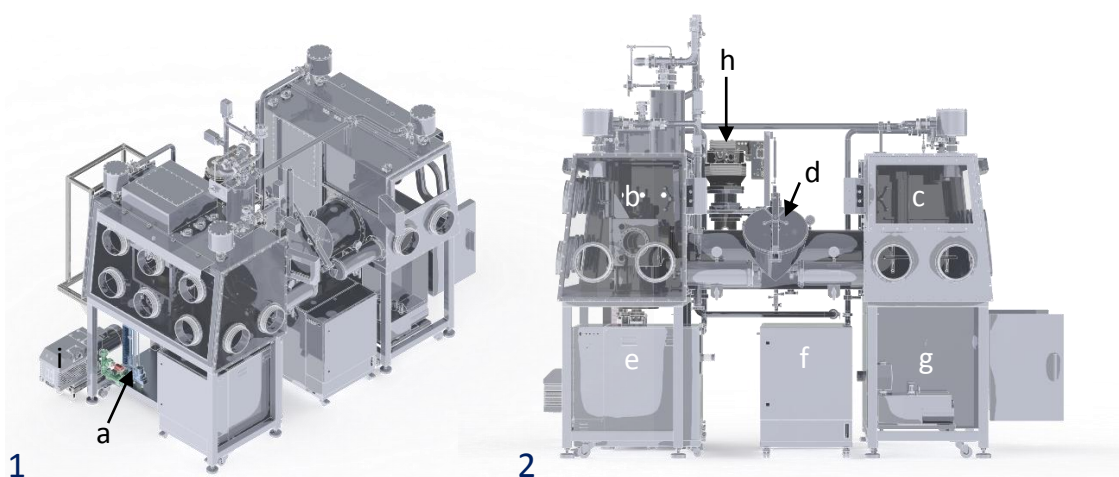


**Figure 41: Glove box system.** The glove box system, which houses the MTS reactor (a), consists of a sputter glove box (b) and a chemistry glove box (c). Both glove boxes are connected by a T-shaped antechamber (d) and have separated gas purification systems (e) and (f). From the chemistry cabinet (g) chemicals can be taped inside the chemistry glove box. The turbomolecular pump (h) is mounted on the back of the sputter glove box and directly connected to the vacuum chamber of the experimental planar reactor. For easy maintenance, the backing pump (i) is installed on a rolling base next to the sputter glove box.



The sputter glove box houses two sputter reactors, the MTS and an experimental reactor for planar sputter targets. To optimize costs and minimize installation space, both reactors share the same infrastructure (power supplies, vacuum and gas system, PLC, cooling water supply). From the MTS just the 6-way manifold is located inside the glove box. It is connected to the experimental sputter reactor by a vacuum hose (see [Figure 35](#)). On the topside the manifold is equipped with a window, which is easy to remove to load and unload target and substrate. When closed, it allows an optical observation of the coating process. To facilitate an easy handling of the MTS inside the glove box, substrate capsule and the target assembly (target, electron reflecting surfaces and ceramic socket) can be assembled separately. The target assembly is then simply plugged into the heat sink and the substrate capsule slid inside the manifold. The inside of the glove box is shown in [Figure 42](#).

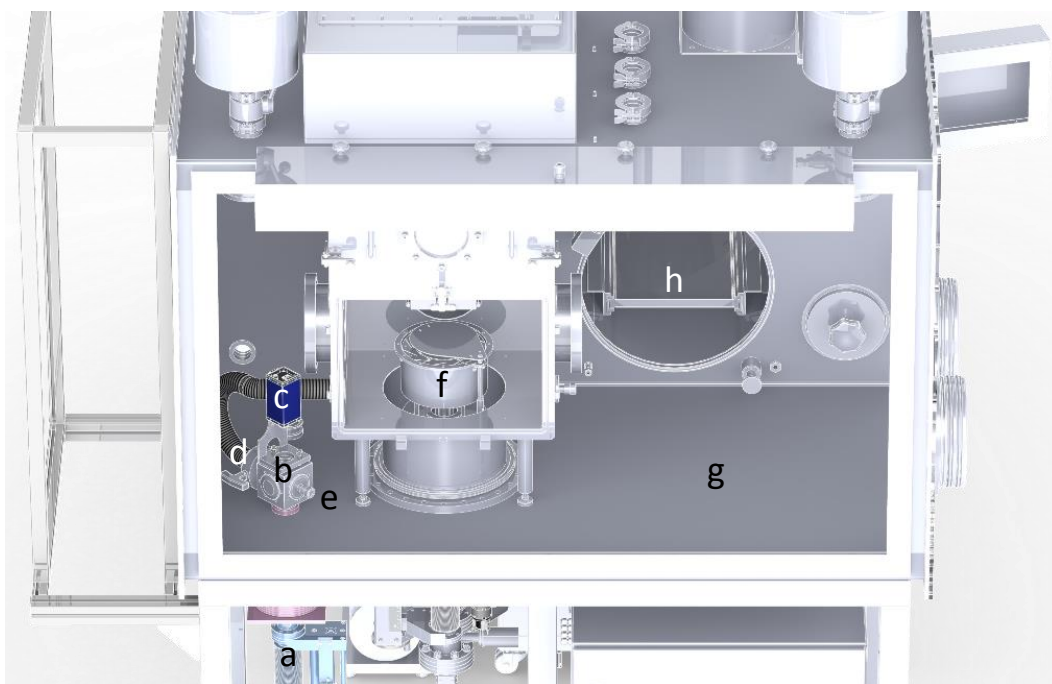


**Figure 42: Workspace in the MTS glove box.** The MTS (a) can be accessed from inside the glove box by the 6-way manifold (b). The manifold is equipped with a ventilation valve (e) and a hand valve (d). The hand valve is used to separate the MTS from the vacuum system (pumps etc.), which is also used by another experimental PVD reactor (f). To load and unload the sputter target and the substrate, the manifold has a removable vacuum window on its top. During the coating process this window is used to observe the plasma with a camera (c). The target assembly and the substrate assembly can be put together on the free workspace (g). The components can be cleaned in an inert gas atmosphere in the chemistry glove box, which is connected through a T-shaped antechamber (h).

The sputter glove box is equipped with a gas purification system, which guarantees a highly pure argon atmosphere. Therefore, the atmosphere is continuously passed through adhesion filters reducing the oxygen and water levels to <0.1 ppm. The argon atmosphere prevents oxidation of the sputter targets and the coated substrates. Therefore, targets and substrates can be stored in the glove box, to avoid changes in their chemical composition. When the sputter reactor is loaded or unloaded, it is ventilated with the glove box atmosphere. This significantly reduces gaseous impurities in the process atmosphere and, therefore, prevents a pollution of the coated layers and the sputter targets. In this way, a build-up of oxygen in the sputter targets can be avoided when recycling them by re-melting and casting to new target pins.

The chemistry glove box is also equipped with a gas purification system, but it features an additional solvent filter and specially coated active coal. This permits a pure argon atmosphere

even when working with organic solvents, acids or bases. Inside the box following chemicals are provided by taps:

- Distilled water
- Isopropanol
- Ethanol
- Ammonia
- Nitric acid
- Hydrogen peroxide
- Sodium hydroxide

These chemicals are stored in a chemical cabinet underneath the chemistry glove box.

The glove box is used to clean samples and prepare them after coating for further analysis. Therefore, the samples can be impregnated in a resin to fix the produced coating. The samples can then be cut and polished to allow microscopic examinations.

Both glove boxes are connected by a T-shaped antechamber. This antechamber allows the transfer of items into the boxes and from one box to the other. It also separates the two atmospheres, preventing cross-contaminations between the two boxes. Additionally, the two glove boxes are equipped with smaller antechambers allowing an easy transfer of samples.

### 3.10 COATING PROCEDURE

For a typical coating run the following procedure is performed:

1. Cleaning of the sputter target surface with a solvent (isopropanol or acetone)
2. Application of the electron reflecting surfaces and the ceramic socket to the target
3. Application of heat conductive paste
4. Mounting of the target assembly to the heat sink (see [Figure 33](#)) (Linear shift mechanism in the upper position)
5. Cleaning of the substrate:
  - a. Cleaning with a brush, soap and water to remove oil and dirt from machining
  - b. Cleaning with a solvent (isopropanol or acetone) to remove aqueous residues
6. (optional) Coating of the inner wall of the substrate with graphite spray:
  - a. Application of the graphite spray
  - b. Baking out the substrate for up to 1 h at 100°C to remove soluble residues
7. Assembly of the substrate, the coating shields and the substrate capsule (see [Figure 32](#))
8. Insertion of the sputter capsule into the MTS
9. Activation of the linear shift mechanism to lower the substrate and the sputter target into the center of the magnetic coil
10. Closing of the vacuum chamber and installing the camera on top to be able to observe the process
11. Pumping down to a basic vacuum of  $10^{-6}$  mbar (optionally, the substrate can be heated up to 90°C to remove humidity during the pumping process)
12. Setting the coating parameter:
  - a. Sputter power (0-150 W)
  - b. Substrate temperature (20-90°C)
  - c. Movement of the sputter source
  - d. Pressure ( $10^{-3}$ - $10^{-1}$  mbar)
  - e. Magnetic field (0 – 100 mT)
  - f. End condition (layer thickness, deposited mass or sputter time)
13. Start Logging
14. Start procedure

When the end condition is reached, the coating process is stopped and the substrate is slowly cooled to room temperature. Subsequently, the chamber is ventilated. Substrate and target

can then either be removed or the target can be replaced and the procedure repeated to produce a multi-layer system.

The electron reflecting surfaces and the coating shields can be re-used for several coating runs. To prevent any cross-contamination, one set was used for one target material. One way to remove the deposited material is the chemical dissolution of the material. Nitric acid showed good results in removing copper from the components without attacking the aluminum or the ceramic material. To chemically remove aluminum from the electron reflecting surfaces, sodium hydroxide was used. This is a convenient and quick way to clean the components from inexpensive material. However, in case of expensive material, the material can also be removed mechanically. The resulting layer can, after several coating runs, be removed using a forceps. Then the material can be recycled by melting and casting to new target pins.



## 4 DEPOSITION RESULTS

---

The results gained with the MTS sputter reactor are presented in the following chapter.

The chapter details the influence of different sputter parameters and materials on the sputter process. The emission profile of the sputter source and the sputter rate were determined depending on the sputter power and material. Based on these results, the thickness profile of the layer can be predicted based on the movement of the sputter source and the measured sputter parameters. To allow a homogenous thickness of the deposited layers, the magnetic field and the pressure distribution in the coating area were determined and inhomogeneities electronically compensated.

One-layer and multi-layer systems of copper, uranium and aluminum were deposited and further analyzed. By adjusting the sputter parameter and/or the application of a graphite interlayer, the adhesion of the layers to the aluminum cylinder could be controlled and self-supporting, easily removable foils were produced.

To demonstrate the recycling of used target pins, casting experiments with uranium were performed. It showed that pins in the desired shape and density can be cast in an arc melting furnace. The resulting pins were successfully used as sputter targets.

### 4.1 MATERIALS

#### 4.1.1 SURROGATE MATERIAL

The usage of radioactive uranium as sputter target leads to a significant complication of the experimental procedures. The radioactivity requires a safe handling in dedicated machinery with special precautions. To avoid these problems and to allow the characterization and optimization of the sputter reactor in a reasonable amount of time with reasonable costs, a non-radioactive and easy-to-handle surrogate material was used for most of the experiments. The surrogate material needs to fulfill different requirements in order to allow a comparability of the results to the sputter process of uranium.

One important criterion is the melting point of the material, since the melting point strongly influences the layer growth. As shown in chapter 2.4, the substrate temperature in relation to the melting temperature of the deposited material defines the type of layer growth. The type of layer growth is important to the density and the structural strength of the resulting layer. Therefore, the choice for the surrogate material was limited to materials within a range of  $\pm 100$  K of the melting point of uranium.

A second important criterion is the magnetic behavior of the material. Metallic uranium is paramagnetic with a relative magnetic permeability of  $\mu_r = 1 + 4.2 \cdot 10^{-4}$ . In contrast to ferromagnetic materials, para- and diamagnetic materials normally feature a relative magnetic permeability close to 1 (vacuum). In these materials no significant alteration of the externally applied magnetic field in the sputter reactor is expected. Therefore, the choice of material was limited to para- and diamagnetic materials.

Given these prerequisites, only gold and copper are eligible as surrogate materials for uranium. Important properties of all three materials are shown in [Table 8](#). Despite the almost perfect properties of gold, like its density, magnetism and melting point, it was ruled out due to its high costs. Therefore, all surrogate tests were performed with copper. Additionally to the previous mentioned properties, copper is cheap and easily available. Due to its yellowish color, it is optically easy to distinguish from aluminum. This makes quick optical and microscopic inspections of the sputtered layers easier. Furthermore, copper has a very high sputter rate (see [Table 5](#)), what reduces the required coating time.

For the experiments, the standard alloy CW004A was used. It features a purity of  $\geq 99.9\%$  [63].

**Table 8: Important material properties of copper, gold and uranium.** If applicable, data are valid for a temperature of 20°C [64].

Material property	Copper	Gold	Uranium
Atomic mass	64	197	238
Density	8.93 g/cm <sup>3</sup>	19.32 g/cm <sup>3</sup>	19.07 g/cm <sup>3</sup>
Relative magnetic permeability $\mu_r$	$1-9.0 \cdot 10^{-6}$	$1-3.4 \cdot 10^{-5}$	$1+4.2 \cdot 10^{-4}$
Electrical resistivity	$1.7 \cdot 10^{-8}$ $\Omega\text{m}$	$2.2 \cdot 10^{-8}$ $\Omega\text{m}$	$3.0 \cdot 10^{-7}$ $\Omega\text{m}$
Specific heat capacity	0.385 J/gK	0.128 J/gK	0.116 J/gK
Thermal conductivity	385 W/mK	301 W/mK	26.8 W/mK
Melting point	1083.4°C	1064.43°C	1132.3°C

#### 4.1.2 URANIUM

The uranium sputter targets used in these experiments were fabricated out of stock material by arc-melting and casting. The stock material is metallic depleted uranium in form of bars. The bars had a dimension of approximately 15 mm  $\times$  15 mm  $\times$  45 mm and a weight of approximately 200 g. Seven sputter targets, each approximately 54 g, were manufactured out of two bars. The surface of the uranium bars was highly oxidized, which could be seen on their black color. To manufacture sputter targets, following procedure was followed (see [Figure 43](#)):

1. Each bar was cut into three pieces by a separating disk.
2. The oxidized surface was removed by storing the uranium in nitric acid (HNO<sub>3</sub>) for approximately 10 minutes.
3. The acid was removed by cleaning the pieces in distilled water.
4. The pieces were finally cleaned with acetone.
5. The clean pieces were melted in an arc-melting device.
6. The molten uranium was directly poured in a water cooled copper crucible with a length of 40 mm and a diameter of 10 mm.
7. Protruding material on the uranium cast was removed by a separating disk.
8. The resulting pin is again cleaned by HNO<sub>3</sub>, H<sub>2</sub>O dist. and acetone.

The overall mass utilization of this procedure was approximately 94.8%. The main mass loss appears when cutting the uranium by the separating disc. The material utilization could be increased by using an alternative separation method like a diamond wire saw. However, this would also significantly increase the preparation time.

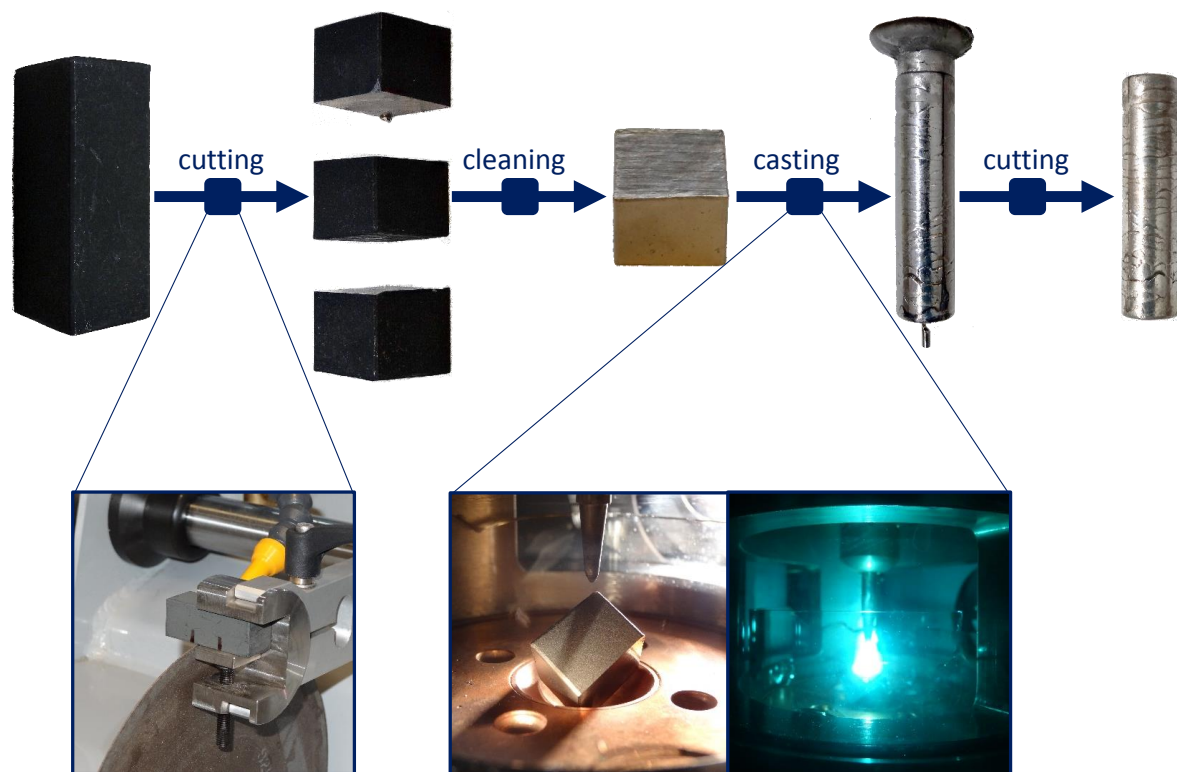


**Figure 43: Pin casting.** Bars of depleted uranium are cut into three pieces. These pieces are cleaned by nitric acid and then cast to uranium pins. These pins are then correctly shaped by removing the upper and lower end.

By the presented procedure, pins with a high density of 98.8% in average were produced. Detailed information about the different casts are given in [Table 9](#). The difference between the measured geometry and the mass/density is caused by an open porosity, which is visible in form of small indentations on the surface of the pins. All pins were mechanically stable, which means no significant cold shuts were present. Cold shuts happen when two streams of metal are too cold to properly fuse together [65]. This could happen, when the casting process is not performed in a continuous manner. Then liquid material comes in contact with already solidified material. In this case, the resulting boundaries have a very low mechanical strength and can easily be broken apart.

The surface of the cast pins had a silver color, which indicates a low oxidation. It showed small indentations, which have a “zebra” like texture. These indentations are caused by the quick solidification during casting. These indentation could likely be reduced by a higher crucible temperature and/or a quicker casting of the material. However, both variants could not be realized with the available arc-melting device. However, it is assumed that the achieved surface quality is sufficient for the sputter process.

By the same process, also nickel pins were cast. These pins were produced of nickel with a purity of 99.5% provided by Alfa Aesar. However, the nickel pins showed in general a worse quality compared to the uranium pins. Due to the higher melting point of nickel, the cast solidified quicker. Therefore, the formation of cold shuts became an issue. [Figure 68](#) shows a used nickel target. Defects caused by the solidification process are clearly visible.

**Table 9: Cast uranium pins.** The densities were determined using the Archimedes' principle.

Pin #	Mass [g]	Diameter [mm]	Length [mm]	Density [%]
1	53.936	9.7	39.4	98.4
2	54.888	9.7	39.4	98.8
3	54.163	9.7	39.4	98.8
4	54.265	9.7	39.5	98.9
5	54.206	9.7	39.5	99.0
6	54.146	9.7	39.2	98.9
7	54.559	9.7	39.4	98.9
∅	54.371	9.7	39.4	98.8

#### 4.1.3 INTERLAYER MATERIAL

A major design goal of the cylindrical LEU target is the separability of the uranium foil from its cladding after irradiation. However, early irradiation tests using blank uranium foils in an aluminum cladding showed a strong interdiffusion between uranium and aluminum under irradiation. This interdiffusion is mainly caused by the highly energetic fragments released in the nuclear fission. These fragments interact with the surrounding matter by energy transfer due to elastic collisions with surrounding lattice atoms, inelastic collisions with the electrons in the solid and inelastic collisions with the nuclei of the solid. A detailed description of the interaction mechanism is given in [66]. The energy, which is deposited in the solid, enhances diffusion processes. At interfaces between two solids, this radiation enhanced diffusion leads to an intermixing and alloying of the materials. The resulting interdiffusion layer causes the uranium foil to bond to the cladding material and, thus, prevents the desired separability.

It showed that this bonding can successfully be prevented by introducing an interlayer between the uranium and the cladding. In this case, the released fission fragments cause a bonding between the uranium and the interlayer, however prevent a bonding between the interlayer and the aluminum cladding. An upper bound for the necessary interlayer thickness can be approximated by the penetration depth of the fragments in the interlayer material. This value can be determined by computer simulations using *SRIM* [67]. *SRIM* is a software, which simulates the different interaction mechanism between highly energetic ions and matter. This simulation is performed in a statistical manner by simulating a multitude of ions. Among other values, the program determines the trajectories and the energy losses of the ions by different mechanism. To simulate the interaction between the irradiated uranium and the interlayer materials, two representative ions are used. Taking into consideration the characteristic shape of the fission fragment distribution (see [Figure 4](#)), one ion is used from each peak: niobium with a mass number of 93 and iodine with a mass number of 127. Both ions are simulated with an energy of 80 MeV, which is a typical value for a fission fragment. [Figure 44](#) shows the simulation results for a selection of interface materials: Al, Ni and Zr. The plots show the distribution of the fission fragments at a certain penetration depth. From this distribution then the average penetration depth is calculated. As one can see, this depth depends strongly on the interlayer material.



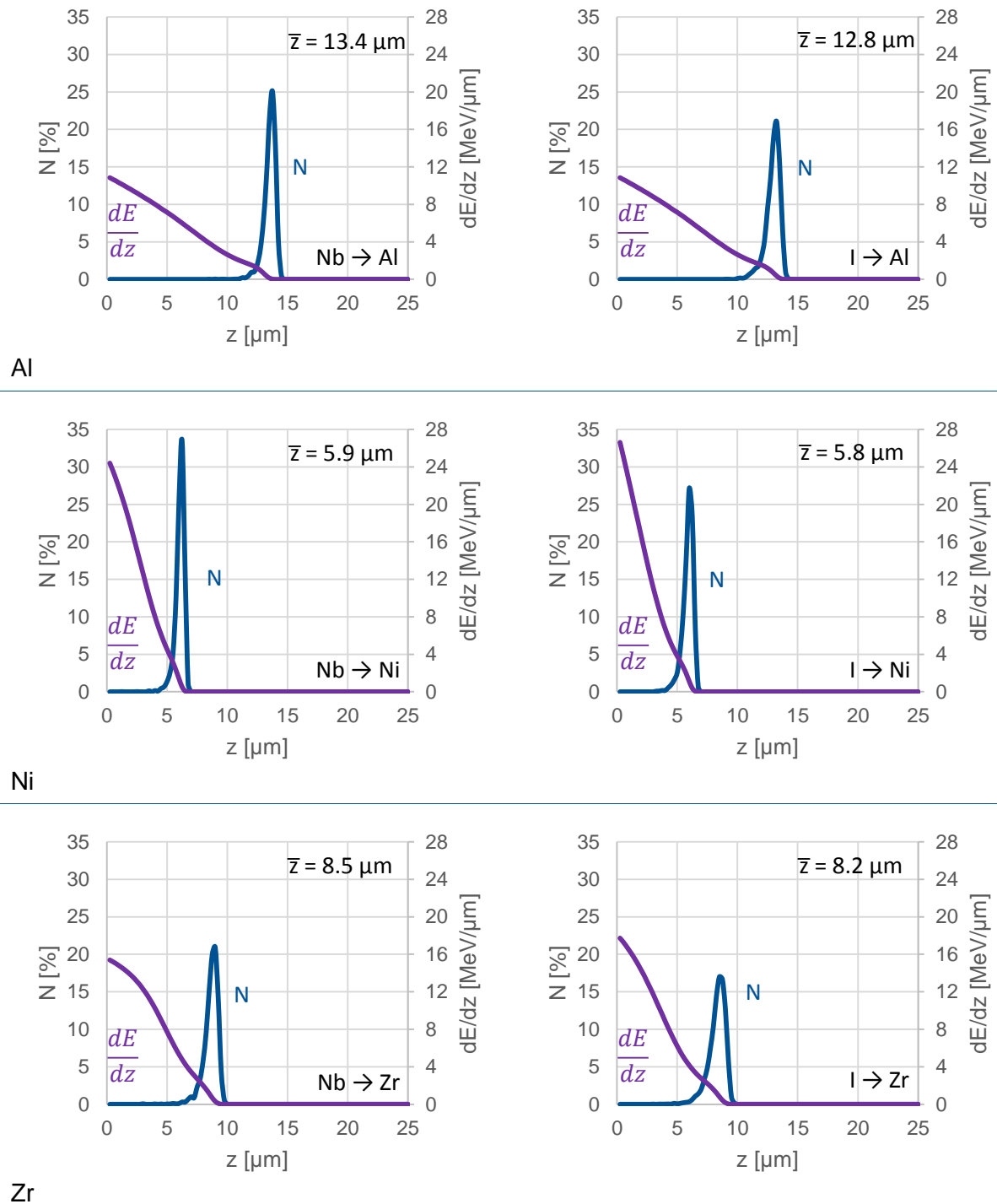


**Figure 44: SRIM simulations.** The plots show the distribution and the energy loss of niobium and iodine ions entering various interlayer materials with an energy of 80 MeV. All simulations were performed with the software SRIM using a total number of 5000 ions for each simulation.

The plots also show the energy loss  $\frac{dE}{dz}$  of the ion along its path through the interlayer. The given value is the energy loss by electronic interaction of the surrounding solid. Since electronic interaction accounts for more than 95% of the total energy loss, this value represents well the energy distribution in the interlayer. According to these results, most of the radiation enhanced diffusion is to be expected at the interface to the uranium layer. Therefore, even a thinner interlayer might be sufficient to allow a separability of the target.

An even further decrease of the interlayer thickness could be reached by choosing a suitable interlayer material. As shown in [68], an important parameter for the intermixing of two materials is their mixing enthalpy. A high mixing enthalpy suppresses the radiation enhanced diffusion. Therefore, choosing a material with a high mixing enthalpy to aluminum or uranium could decrease the interdiffusion to a level, which allows a separability of the layers. Using a thinner interlayer material, would reduce the amount of material, which needs to be dissolved during the reprocessing of the target. This has a positive effect on both the processing time and the amount of highly radioactive waste. However, this issue would require a detailed investigation in according irradiation tests.

Additionally to the necessary thickness, the used interlayer material has to fulfill following requirements:

- low thermal neutron absorption cross-section to minimize the loss of neutron flux
- no long-lived activation products
- chemical compatibility to the  $^{99}\text{Mo}$ -extraction process

Irradiation tests were performed using nickel and zinc as interlayer materials due to their solubility in nitric acid to make it compatible to the acidic extraction process. For the compatibility with the alkaline process, aluminum was tested due to its solubility in sodium hydroxide. These interlayers were either wrapped in form of a foil around the uranium or directly electroplated on the uranium foil. All of those materials performed successful and allowed a disassembly of the target after irradiation [69].

However, also other materials could be considered. Taking into account the interdiffusion of the materials, possible interlayer materials are zirconium, titanium or niobium.

In the following coating experiments, the possible interlayer materials aluminum, nickel and zirconium were tested. Those three materials show significantly different material properties and can, therefore, show up the possibilities and limitations of the presented coating apparatus. Zirconium, on the one hand, has a very high melting temperature ( $T_M=1857^\circ\text{C}$ ) compared to uranium and aluminum. As detailed in chapter 2.4, the melting point has a strong effect on the layer growth and the layer properties. Nickel, on the other hand, is ferromagnetic. Therefore, the material alters the magnetic field in the coating device and, thus, changes the plasma behavior.

## 4.2 SPUTTER PARAMETERS

Before optimizing the coating procedure (sputter source movement, substrate temperature), the optimal plasma parameters (magnetic field, pressure and sputter power) were determined to guarantee a stable and reliable coating process.

### 4.2.1 MAGNETIC FIELD

The optimal magnetic field in the coating zone was chosen as a compromise between the heat dissipation of the magnetic coil and its ability to sustain a stable plasma.

The magnetic field depends on the electric current applied by the high-current power supply. **Figure 45** shows the dependency of the magnetic field intensity in axial direction in the center of the coil on the electric current and the electric power. The magnetic field intensity was measured by a Hall probe inside the center of a prepared copper target. As predicted by equation (11), the electric current is directly proportional to the magnetic field intensity. According to

$$P = RI^2 \quad (14)$$

the electric power  $P$  shows an almost quadratic dependency on the electric current  $I$  and, therefore, on the magnetic field intensity. A slight deviation of the quadratic behavior is caused by the temperature and, therefore, current dependency of the ohmic resistance  $R$  of the magnetic coil.

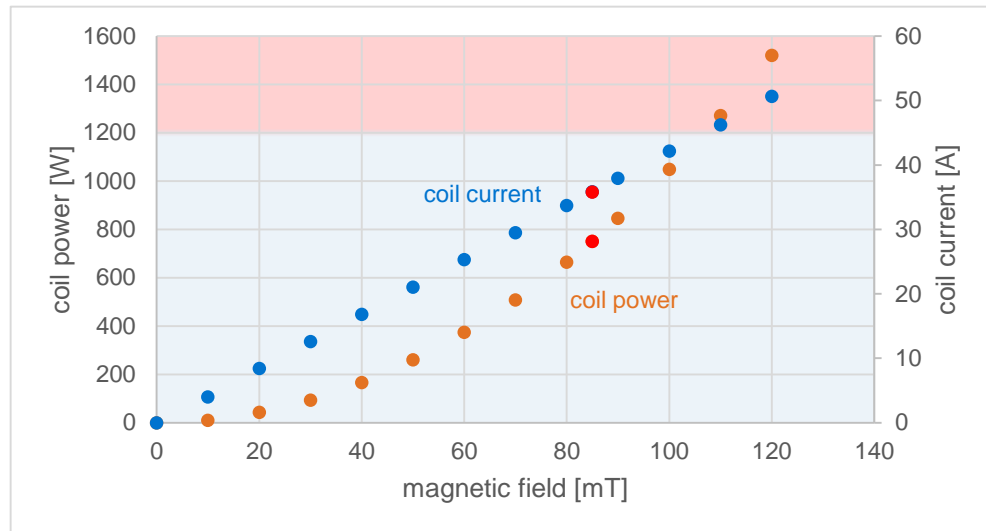


**Figure 45: Magnetic field dependency of the coil's electrical current and power.** The values were measured in the center position of the coil. The red area indicates power values of more than 1200 W. Due to safety considerations, the power supply output was limited to this value and in most experiments the normal operation was set to 85 mT, resulting in a power of approximately 750 W (red marker).

Due to safety considerations, the electric power of the high-current power supply is limited to 1200 W. With this value, the coil's temperature stays below 95°C, assuming a minimal cooling water supply. For normal operation, a maximum magnetic field of 85 mT in the center of the coil was chosen. At this value, the electric power is approximately 750 W. On the one hand, this power is sufficient to heat up the substrate to approximately 90°C. And on the other hand, it keeps enough reserves to compensate for a reduction of the magnetic field at the ends of the coating zone by increasing the electric current.

Figure 46 shows the dependency of the magnetic field intensity on the sputter parameters: sputter voltage, sputter power and sputter current. The measurements were performed with a copper target at a pressure of 0.035 mbar at the center position of the magnetic coil. To eliminate any effects caused by surface impurities of the copper target, the measurements were performed after approximately 1 hour of sputtering at a sputter power of 100 W and a magnetic field of 85 mT. Each measurement was taken approximately 10 minutes after changing the magnetic field, to allow the system to adopt to a new equilibrium state. The plot shows the mean values of 60 measurements recorded every 2 seconds. For the sputter current, also the maximum deviations of the mean values are plotted in form of error bars. They give an indication about the stability of the plasma. The system is limited by the maximum voltage of the power supply (800 V) and a preset sputter power of 100 W. This value is the desired power for a continuous sputter process.

With this settings, a plasma was ignited when applying a magnetic field above 15 mT. Up to approximately 55 mT, the field is not sufficient to establish the required sputter power of 100 W due to the voltage limitation. In this region, a plasma with an unstable behavior was established. The instability is caused by the high voltage.

With increasing magnetic field, the plasma resistance decreases. This is caused by a more efficient trap of the electrons in the system, which results in a higher ionization of the sputter gas. This decrease in the plasma resistance leads to an increasing sputter current and sputter power. Above 55 mT, a sputter power of 100 W is reached and the sputter voltage drops with increasing magnetic field. Due to the lower sputter voltage, the plasma is more stable at higher magnetic fields. Therefore, the magnetic field should be as high as possible to guarantee a stable coating process.

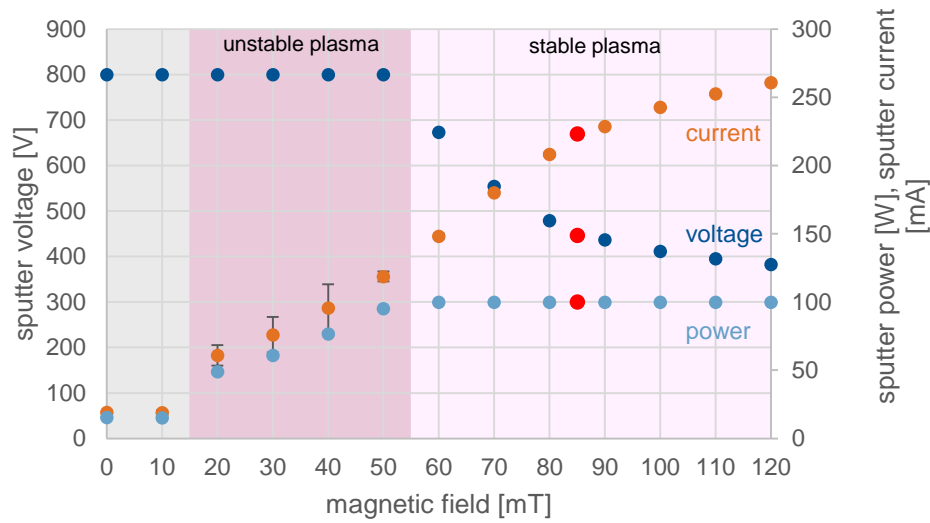


**Figure 46: Magnetic field dependency of the plasma parameters.** The values were measured with a copper target at a pressure of 0.035 mbar in the center position of the coil. The sputter power supply was limited to a maximum power output of 100 W and a maximum voltage of 800 V. The grey area indicates the field values, where no plasma could be ignited. In this region the power supply showed a certain offset in the electrical current. The dark purple area shows the magnetic field values where a plasma was ignited, but rather unstable. This instability could be seen by a fluctuating sputter current and voltage. The fluctuation in the current is indicated by error bars. The light purple area shows the region where a stable plasma was ignited. The red marker indicates the operation point for most experiments at 85 mT.

As a compromise between the thermal restrictions and the influence on the plasma behavior, the standard magnetic field was set to 85 mT (red marker). It allows a safe operation, establishes the possibility to heat up the substrate and facilitates a stable plasma condition. If not stated otherwise, the following experiments are performed with this value.

### Electronic compensation

As shown in Figure 37, the magnetic field in axial direction depends on the position inside the magnetic coil. This would lead to a dependency of the plasma properties on the position of the sputter source. To achieve a homogenous coating process, an electronic compensation of the magnetic field was implemented in the PLC. This compensation automatically adjusts the coil current to the position of the sputter source and, in this way, provides a constant axial field over the length of the coating zone.

The equation used for the compensation is based on equation (11). However, compared to equation (12) it is simplified, by replacing the radii of the different layer by one mean radius. The resulting equation for the electric current  $I$  is

$$I = \frac{2l}{\mu BLN} \left[ \frac{\frac{l}{2} - z}{\sqrt{(\frac{l}{2} - z)^2 + r^2}} + \frac{\frac{l}{2} + z}{\sqrt{(\frac{l}{2} + z)^2 + r^2}} \right]^{-1} \quad (15)$$

where  $B$  is the desired field,  $z$  the position of the sputter source,  $L$  the amount of layers,  $N$  the amount of windings per layer,  $r$  the mean radius and  $l$  the length of the coil.

The parameters  $l$ ,  $r$ ,  $N$  were used to fit the equation to measured values by a least square fitting method. Therefore, the electric current was adjusted to reach a certain magnetic field at a defined position of the sputter source. The magnetic field was measured by a Hall probe in the center position of a prepared copper target. This process was applied for 50 mT, 75 mT and 100 mT in a range of -50 mm to 50 mm of the substrate's center position.

The results of the measurement for a magnetic field of 100 mT and the obtained fit are shown in [Figure 47](#).

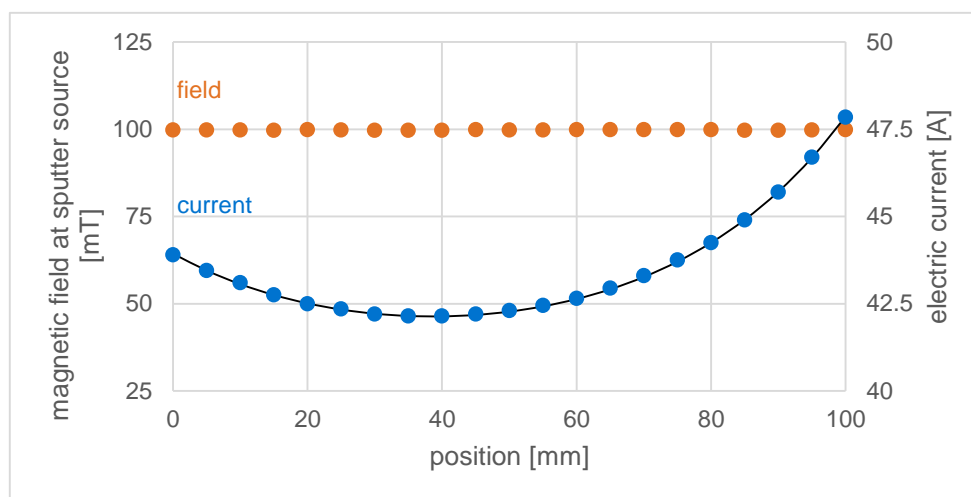


**Figure 47: Magnetic field compensation.** At each position of the sputter source, the electric current of the coil is adjusted to reach a constant magnetic field of 100 mT. The plot shows the measured electric current (blue dots), the fitted function (line) and the resulting field (orange dots) when using the fitted function.

[Table 10](#) shows the resulting fitting parameters. The deviations of the resulting field from the desired magnetic field stays below 1% for all measurements.

**Table 10: Fitting parameters for the magnetic field compensation.**

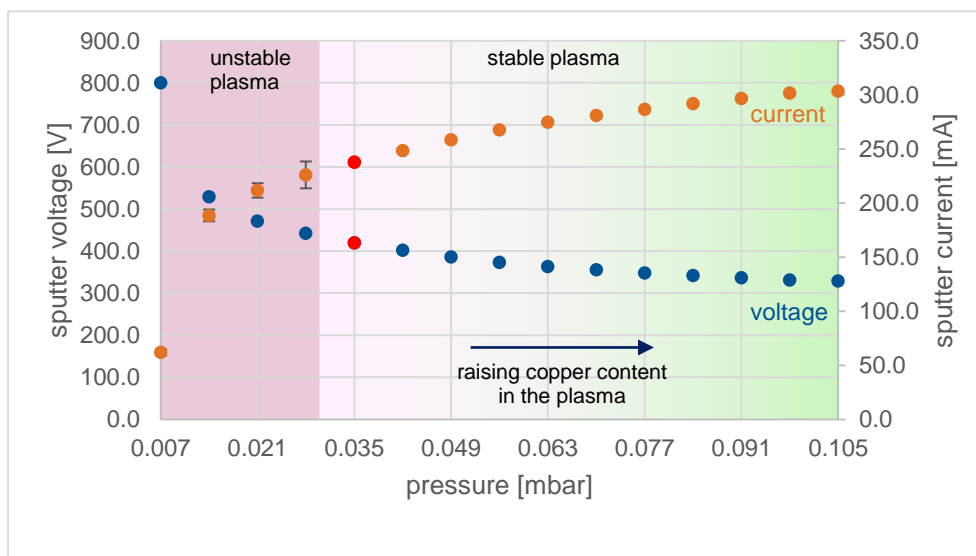
Constant		Simplified fit	Real coil
length	$l$	208.3 mm	205 mm
radius	$r$	57.6 mm	24.5 mm – 74.5 mm
layers	$L$	11	11
windings per layer	$N$	40.9	41

#### 4.2.2 GAS PRESSURE

Another important parameter of the plasma process is the gas pressure inside the process chamber. This parameter was optimized in respect to a stable operation and high deposition rate.

**Figure 48** shows the dependency of the gas pressure on the plasma parameters: sputter voltage, sputter power, sputter current and plasma color. The values were measured using a magnetic field of 85 mT. Apart from that, the same conditions and procedures were used as in the previous chapter. The gas pressure was determined in a separate step directly in the process chamber. Therefore, a THERMOVAC TTR91 pressure sensor was installed inside the vacuum chamber. It was directly mounted to the heat sink of the sputter source. The relation between gas inflow and pressure was determined and used to set the gas pressure in the sputter experiment.




In **Figure 48**, a clear dependency of the sputter parameters and the pressure can be seen. A higher gas pressure leads to a lower plasma resistance and, therefore, a lower sputter voltage. Up to a pressure of 0.03 mbar, the plasma showed an unstable behavior, which is indicated by deviations in the sputter current. Above 0.03 mbar, the plasma was stable in the complete range up to 0.105 mbar. However, in this region the plasma color strongly depends on the gas pressure. At low pressures, the plasma glows purple, which is the typical emission of an argon plasma. With higher pressures, a green color appears, which becomes dominant above 0.05 mbar. This color indicates, the ionization of the eroded copper atoms.



**Figure 48: Pressure dependency of the plasma parameters.** The values were measured with a copper target at a magnetic field of 85 mT in the center position of the coil. The power supply was limited to a maximum power output of 100 W and a maximum voltage of 800 V. The dark purple area shows the magnetic field values where a plasma was ignited but rather unstable. This instability could be seen by a fluctuating sputter current and voltage. The fluctuation in the current is indicated by error bars. The light purple and green area show the region where a stable plasma was ignited. A higher pressure causes a higher ionization of copper in the plasma, what can be seen by a green color in the plasma. The red marker at 85 mT indicates the operation point for most experiments.

When this happens, the ionized copper atoms are accelerated back to the target. This leads to a decrease in the deposition rate. To prove this relation, three long term coating runs with three different pressures were performed. The sputter targets were weighed before and after the coating run to determine the deposition rate. **Table 11** shows the results of these experiments. To eliminate deviations in time and sputter power, the resulting deposition rate is given in mass difference per time and power. As stated in the following chapter, the sputter power scales well with the deposition rate. The table also shows photos of the plasma at the given pressure region. These photos are not taken at the according coating run, but at the experiments used for **Figure 49**. They show well, the color change due to increasing copper ionization.

**Table 11: Influence of the gas pressure on the deposition rate.** The experiments were performed with a magnetic field of 85 mT.

#	Pressure [mbar]	Time [min]	Average power [W]	Mass difference [mg]	Deposition rate [mg/(minW)]	Plasma color
1	$9.0 \cdot 10^{-3}$	467	100	5596	0.12	
2	$3.5 \cdot 10^{-2}$	492	97	5355	0.11	
3	$8.7 \cdot 10^{-2}$	405	90	2207	0.06	

As the results confirm, a high pressure significantly lowers the deposition rate. Since large volumes need to be deposited in order to produce the required foils, the pressure was kept as low as possible to reduce coating times. A pressure of 0.035 mbar turned out to be a good compromise between a stable plasma and a high deposition rate. Therefore, all following experiments were performed with this value if not stated otherwise.

### Electronic compensation

Similar to the magnetic field, it showed that the position of the sputter source influences the gas pressure in the coating zone. This dependency can be seen in [Figure 49](#).

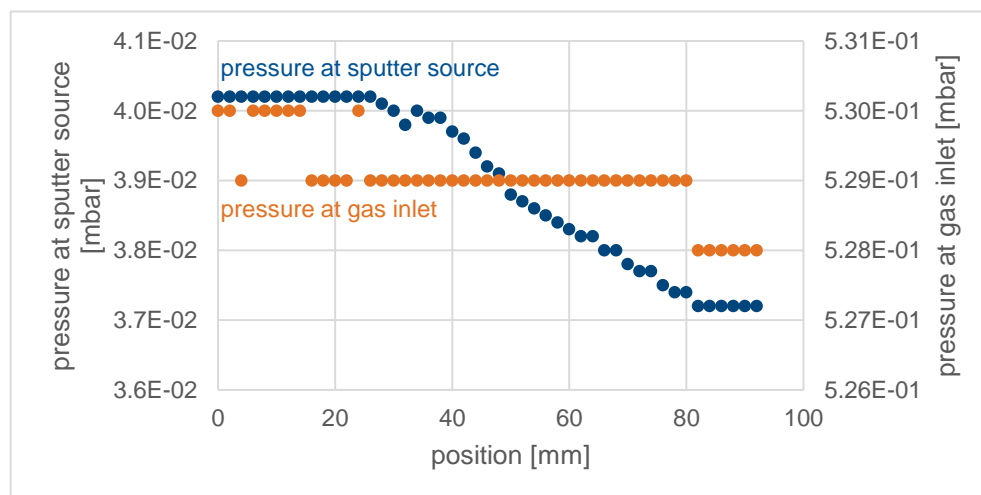


**Figure 49: Gas pressure in the coating zone.** The argon pressure in the coating zone was measured at different positions of the sputter source. The gas inlet was 15.4 sccm. The plot shows the readings of a pressure sensor mounted directly on the heat sink in the coating zone and the CTR 100 bottom sensor close to the gas inlet.

The plot shows the pressure reading of the TTR91 sensor mounted at the position of the sputter source and the CTR 100 bottom sensor mounted close to the gas inlet. As one can see, the pressure at the sputter source decreases with increasing position. This needs to be compensated by an increased gas inflow. The CTR 100 bottom sensor is the closest permanently installed pressure sensor to the coating zone. It would be preferable to use its

readings for the compensation of pressure inhomogeneities. However, the accuracy of this sensor is too low to be used as a control variable to control the actual pressure in the coating zone.

Therefore, analogous to the magnetic field, a function was derived to control the gas inflow  $u$  based on the desired pressure  $p$  and the position  $z$  of the sputter source. Measurements were taken for 0.0125 mbar, 0.025 mbar and 0.040 mbar. Since no analytic equation was found, these values were fitted by a polynomial surface:

$$u = \sum_{i=0}^5 \sum_{j=0}^{\min(5-i,3)} a_{ij} z^i p^j \quad (16)$$

It showed that the measured values could well be described using a degree of 5 for the position and a degree of 3 for the pressure. The fitted parameters are presented in [Table 12](#).

**Table 12: Fitting parameters for the pressure compensation.** The position  $z$  is given in mm, the inflow in sccm and  $p$  in mbar. The parameters  $a_{ij}$  have correspondent units.

$a_{ij}$	$j=0$	$j=1$	$j=2$	$j=3$	$i=4$	$i=5$
$i=0$	$-1.31 \cdot 10^0$	$1.21 \cdot 10^{-2}$	$-5.35 \cdot 10^{-4}$	$1.26 \cdot 10^{-5}$	$-1.72 \cdot 10^{-7}$	$8.54 \cdot 10^{-10}$
$i=1$	$2.63 \cdot 10^2$	$-4.53 \cdot 10^{-1}$	$-8.29 \cdot 10^{-3}$	$6.29 \cdot 10^{-4}$	$-4.13 \cdot 10^{-6}$	
$i=2$	$5.10 \cdot 10^2$	$2.32 \cdot 10^1$	$-3.40 \cdot 10^{-1}$	$-2.41 \cdot 10^{-3}$		
$i=3$	$3.75 \cdot 10^4$	$-5.09 \cdot 10^2$	$1.09 \cdot 10^1$			

The results for a pressure of 0.03 mbar and the obtained fit are shown in [Figure 50](#). The deviation of the resulting and the set pressure stayed below 2.4% for all measurements.

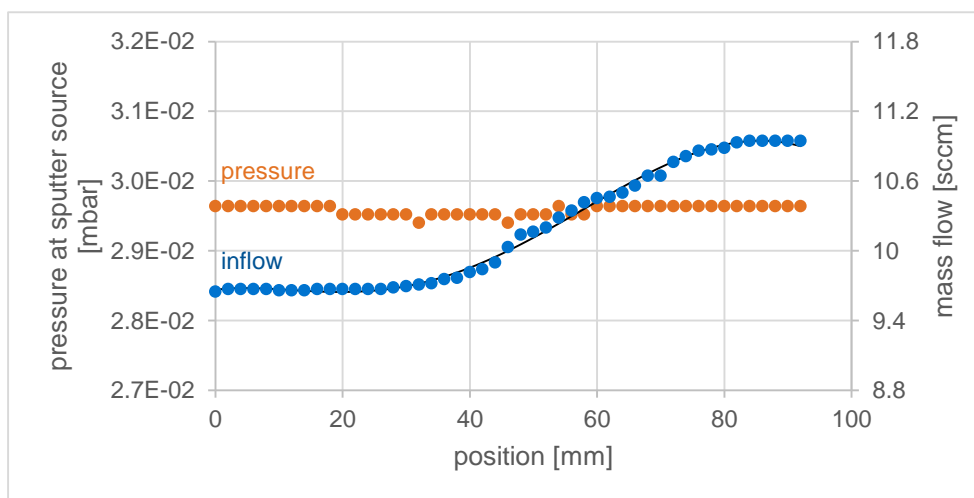


**Figure 50: Pressure compensation.** At each position of the sputtering source, the gas inflow is adjusted to reach a pressure of 0.03 mbar in the sputter zone. The plot shows the measured gas inflow (blue dots), the fitted function (line) and the resulting pressure (orange dots) when using the fitted function.



### 4.2.3 SPUTTER RATE

To be able to predict the thickness of the sputtered layer, it is necessary to know the sputter rate  $R$  in dependency of the process parameters.  $R$  is defined as the eroded target mass per time.

In general, the total eroded mass  $m$  in a sputter run is calculated by

$$m_{tot} = \int_0^T R(t) dt \quad (17)$$

where  $T$  is the duration of the sputter process. In reality, the calculation is performed in discrete time steps given by the sampling rate of the implemented data logger. The sampling time  $t_s$  was set to 2 s. This time constant is short enough to capture all important processes, but long enough to keep the size of the log files within reasonable limits. In the discrete case, equation (17) is changed to

$$m_{calc} = t_s \sum_{i=0}^{T/t_s} R(t_i) \quad (18)$$

The function  $R$  is determined by choosing a suitable parameterized function and fitting measured values  $m_{meas}$  to calculated values  $m_{calc}$  based on the log file of the sputter run. The measured values were obtained by weighing the target before and after each process. The parameters of  $R$ , are optimized by a nonlinear solver using the GRG (Generalized Reduced Gradient) algorithm to minimize the maximum relative mass difference for all considered sputter runs  $j$ :

$$\max_{\forall j} \left( \frac{|m_{calc}^j - m_{meas}^j|}{m_{meas}^j} \right) \stackrel{!}{=} \min \quad (19)$$

To determine  $R$ , 15 different sputter runs were considered. These sputter runs differ in gas pressure, magnetic field, sputter power, sputter times and the position/movement of the sputter source.

In a first attempt, it was assumed that the sputter rate is proportional to the power provided by the dc power supply. Therefore, following ansatz was used

$$R = aP \quad (20)$$

where  $P$  is the applied electric power and  $a$  an arbitrary parameter. This approach is suggested in most literature, e.g. [70]. **Figure 51** shows the total applied energy of the considered sputter processes versus the mass loss of the targets. The measured values are marked with blue dots. The linear relation obtained by equation (20) is shown as a black line. As one can see, this simple assumption gives the general trend. However, certain values strongly divert from the linear relation. The maximum deviation of the calculated values and the measured values was 9.5%. Higher deviations especially appear in coating procedures, where the magnetic field and the pressure strongly deviate from the standard settings ( $B=85$  mT and  $p=0.035$  mbar). As shown in **Figure 46** and **Figure 48**, changes of the pressure or magnetic field lead to a different plasma resistance and, hence, to a different electric current at constant power. Therefore, the linear approach was extended based on [71] to also consider the electric current  $I$ :

$$R = aP \frac{I}{I + b} \quad (21)$$

The results obtained with this equation are shown with purple markers in **Figure 51**. The accordance of the calculated and the measured values significantly improves. In this case the maximum deviation reduces to 3.2%.

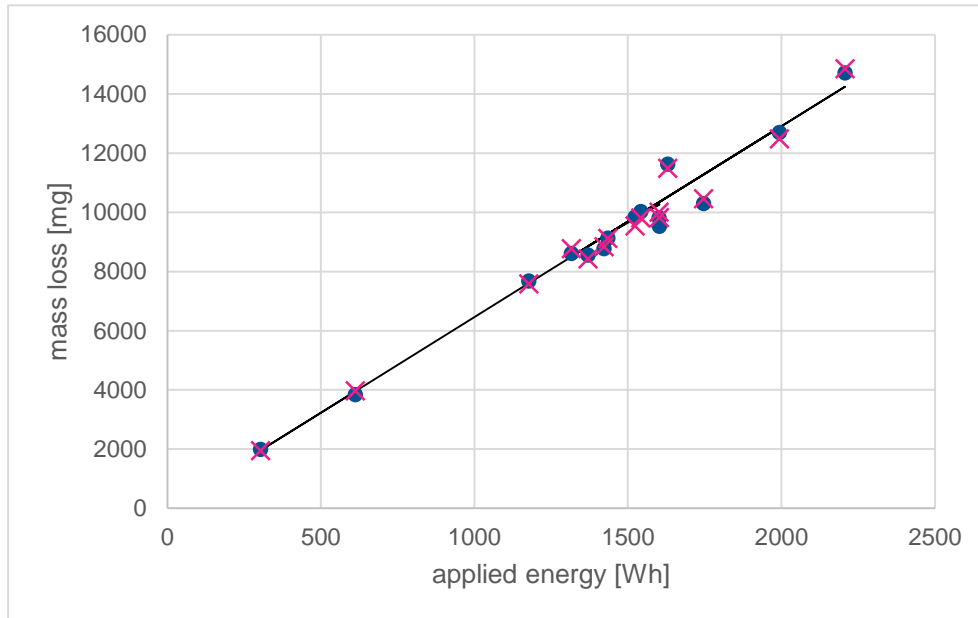


**Figure 51: Dependency of the target mass loss on the sputter parameters.** 15 different sputter runs using argon and copper are plotted with applied electric energy versus mass loss of the sputter target. The plot shows the measured (dots) and calculated values according to equation (20) (line) and (21) (crosses).

It can be concluded that the simple linear approach gives an easy possibility to approximate the sputter rate and the necessary time. For more precise calculations, like the real-time monitoring of the sputter process, equation (21) is used. **Table 13** shows the obtained fitting parameters and accuracy of both approaches. It has to be considered that these values are just valid for sputtering copper with argon ions in the given set-up. For other material combination new parameters have to be determined (see chapter 4.4).

**Table 13: Fitting parameters for the sputter rate of copper with argon ions.**

Equation	$a$ [mg/(W·min)]	$b$ [mA]	$\max\left(\frac{m_{\text{meas}} - m_{\text{calc}}}{m_{\text{meas}}}\right)$
$R = aP$	0.1076	-	9.5%
$R = aP \frac{I}{I + b}$	0.1330	66.356	3.2%

#### 4.2.4 SPUTTER POWER

Due to the almost linear dependency of the sputter rate on the sputter power, a high power is desirable to achieve short coating times. However, the maximum power is limited by the heat dissipation of the sputter source. At high temperatures, the ceramic components tend to crack. With copper as target materials, a stable process can be achieved with sputter powers of up

to 150 W. However, at this power the lifetime of the ceramic components is significantly reduced to a few applications. Whereas, at 100 W no fatigue caused by high temperatures can be observed. Therefore, the sputter power was limited to 125 W, but in most cases 100 W was used.

When sputtering aluminum, additionally its low melting point of 660°C [64] has to be taken into consideration. In this case, the power was limited to 90 W. However, usual coating powers were 80 W to avoid melting of the target.

### 4.3 THICKNESS PROFILE

One major aim of this thesis is to produce homogenous metallic layers on the inside of the substrate cylinder. To measure the thickness profile of the sputtered layers and further analyze the coatings, a preparation technique was developed. This technique involves embedding the layers in an acrylic resin and subsequent polishing. The layers can then be investigated by optical microscopy. To be able to predict and control the layer's thickness profile, an understanding of the coating characteristic of the sputter source and the influence of its movement on the resulting layer profile is necessary. Therefore, an algorithm was developed, which allows to predict the resulting layer thickness from the recorded sputter parameters (power, current, movement). It also calculates the mass loss of the target, the mass, which is actually deposited on the substrate, and, hence, the efficiency of the process. This algorithm was validated by comparing its results to measured thickness profiles and weight measurements.

The algorithm also allows to simulate different movement profiles. The results were used to determine their efficiency and the resulting layer thickness.

#### 4.3.1 SAMPLE PREPARATION

The preparation method used to examine the deposited layers is shown in [Figure 52](#).

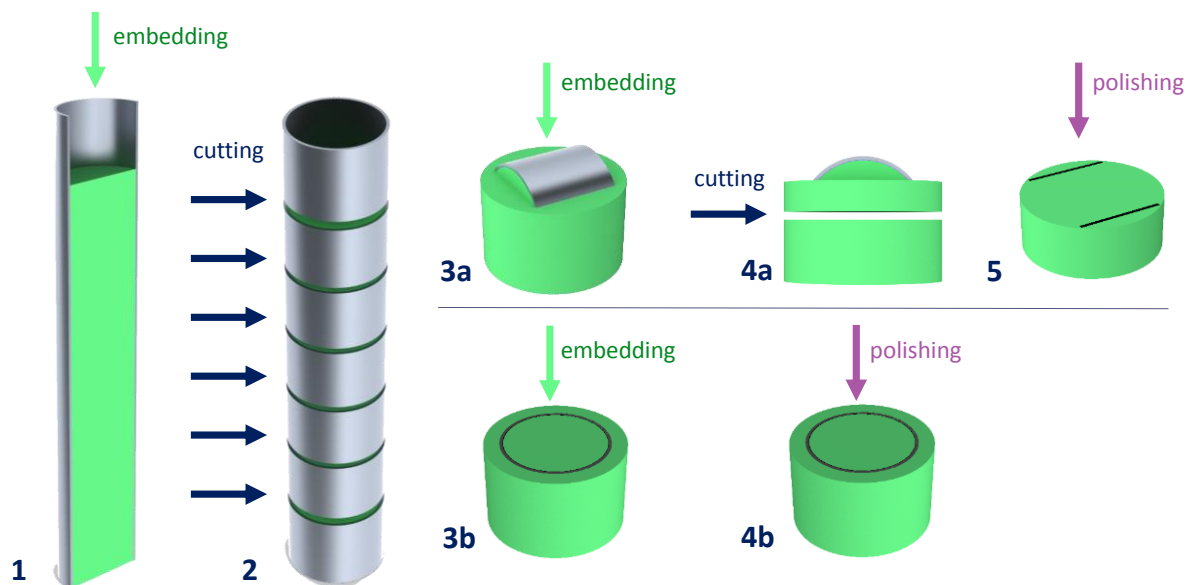


*Figure 52: Sample preparation.*

First, the whole cylinder is filled with an acrylic resin to fixate the deposited layer ([Figure 52](#), 1). Here, it is important that the used resin undergoes no or just minimal shrinkage during hardening. Otherwise the layer can be damaged and the result can be falsified. This property

is rare among the available mounting resins. Good results were obtained with *Struers DuroCit*. However, due to a supply shortage, in later experiments it was switched to *Buehler VariDur 3003*. This resin showed, compared to other resins, a minimal shrinkage, however it was inferior to *Struers DuroCit*.

In a second step, the substrate cylinder is cut in seven pieces (**Figure 52**, 2). The outer two have a length of 26 mm and are disposed since they do not contain any deposited layer. The inner five pieces have a length of 22 mm each. Those pieces are then again embedded in the resin. This is either done in axial direction (**Figure 52**, 3b) or perpendicular to the cylinder axis (**Figure 52**, 3a).

The first ones are directly ground and polished. This delivers a cross section perpendicular to the substrate axis (**Figure 52**, 4b). To prepare an axial cross section of the layer, a second cutting step through the center of the cylinder is necessary (**Figure 52**, 4a). The resulting piece is then ground and polished, in the same way as the perpendicular cross sections.

To measure the layer thickness an optical microscope is used. The accuracy of this method is mainly determined by the angle of the investigated surface to the substrate axis, the focusing of the microscope and possible deformations of the layer caused by the polishing procedure. The error was estimated to a value of approximately 3  $\mu\text{m}$ .

#### 4.3.2 SIMULATION ALGORITHM

The coordinate system used for the simulation algorithm is presented in **Figure 53**.

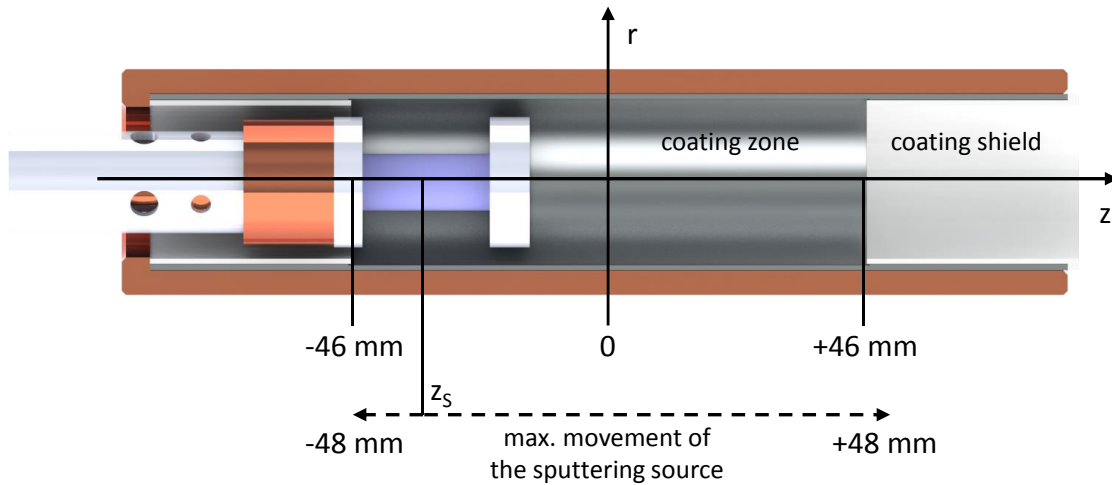


**Figure 53: Coordinate system.** The coordinate system used for the simulation algorithm uses cylindrical coordinates. The z-axis is equal to the central axis of the substrate cylinder and centered at the substrate's center position. The coating zone goes from -46 mm to +46 mm.  $z_s$  marks the central position of the sputter source. The sputter source can freely move from -48 mm to +48 mm.

The layer profile  $F(z)$  is the thickness of the sputtered layer over the axial direction  $z$ . It is calculated by integrating the emission characteristic  $f$  times the sputter rate  $Q$  over the movement of the sputter source  $z_s(t)$ .

$$F(z) = \int_0^T f(z, z_s(t)) Q(z_s(t)) dt \quad (22)$$

Q describes the sputter rate in thickness per time. It depends on the sputter parameters (P, I) at the position  $z_S$  of the sputter source.  $f$  is the coating characteristic of the sputter source. It is the unitless distribution of the deposited layer thickness. Its covered area is defined to be 1:

$$\int_{-\infty}^{\infty} f(z, z_S) dz = 1 \quad (23)$$

The volume of the coated layer, which results from the layer profile  $F(z)$ , is calculated by a cylindrical volume integral. The integration of the radius is performed from  $r_i - F(z)$  to  $r_i$ , where  $r_i$  is the inner radius of the substrate cylinder. The calculation is simplified by neglecting  $F(z)^2$ . This step is justified by the small maximum layer thickness of approximately 0.15 mm compared to the inner radius of the substrate tube of 14.65 mm.

$$\begin{aligned} V &= \int_{-\infty}^{+\infty} \int_0^{2\pi} \int_{r_i - F(z)}^{r_i} r dr d\varphi dz = \pi \int_{-\infty}^{+\infty} (2r_i F(z) - F(z)^2) dz \approx 2\pi r_i \int_{-\infty}^{+\infty} F(z) dz \\ &= 2\pi r_i \int_{-\infty}^{+\infty} \int_0^T f(z, z_S(t)) Q(z_S(t)) dt dz = 2\pi r_i \int_0^T Q(z_S(t)) dt \end{aligned} \quad (24)$$

The independency of the sputtered layer on the angle  $\varphi$  was justified by microscopic investigations of radial cross sections of coated substrate cylinders. For coatings with a thickness above 120  $\mu\text{m}$ , the average inhomogeneity along  $\varphi$  was below 5%. Due to the limited accuracy of the thickness measurement by optical microscopy, it was concluded that no relevant angle dependency of the layer thickness exists.

To connect the calculated volume to the measured sputter rate by mass  $R$ , the mass  $m_{cyl}$ , which is deposited on the substrate cylinder, is calculated. This mass includes not only the mass, which is deposited in the coating zone, but also on the coating shields (see [Figure 53](#)). It is connected to the total eroded mass  $m_{tot}$  (equation (17)) by the coating efficiency  $\varepsilon_C$ . This efficiency factor mainly considers mass losses, which are deposited on the electron reflecting surfaces of the sputter source.

$$\varepsilon_C m_{tot} = \varepsilon_C \int_0^T R(t) dt = m_{cyl} = \rho V = \rho 2\pi r_i \int_0^T Q(z_S(t)) dt \quad (25)$$

By comparing the integrand, following relation between the sputter rate by mass and by thickness can be derived:

$$R(t) = \frac{2\pi\rho r_i}{\varepsilon_C} Q(z_S(t)) \quad (26)$$

Using this relationship and equation (21), the layer thickness  $F(z)$  can be calculated by:

$$F(z) = \frac{\varepsilon_C}{2\pi\rho r_i} \int_0^T f(z, z_S(t)) R(t) dt = \frac{\varepsilon_C}{2\pi\rho r_i} \int_0^T f(z, z_S(t)) aP(t) \frac{I(t)}{I(t) + b} dt \quad (27)$$

In case of a discrete calculation, the equation is transformed to:

$$F(z) = \frac{\varepsilon_C t_S}{2\pi\rho r_i} \sum_{i=0}^{T/t_S} f(z, z_S(t_i)) aP(t_i) \frac{I(t_i)}{I(t_i) + b} \quad (28)$$

To determine the emission characteristic  $f$  of the sputter source, sputter runs with a fixed position of the sputter source were performed. The resulting layers, were prepared according to [Figure 52](#) and the layer thickness was measured using a microscope. The normalized and averaged values for copper are shown in [Figure 54](#).

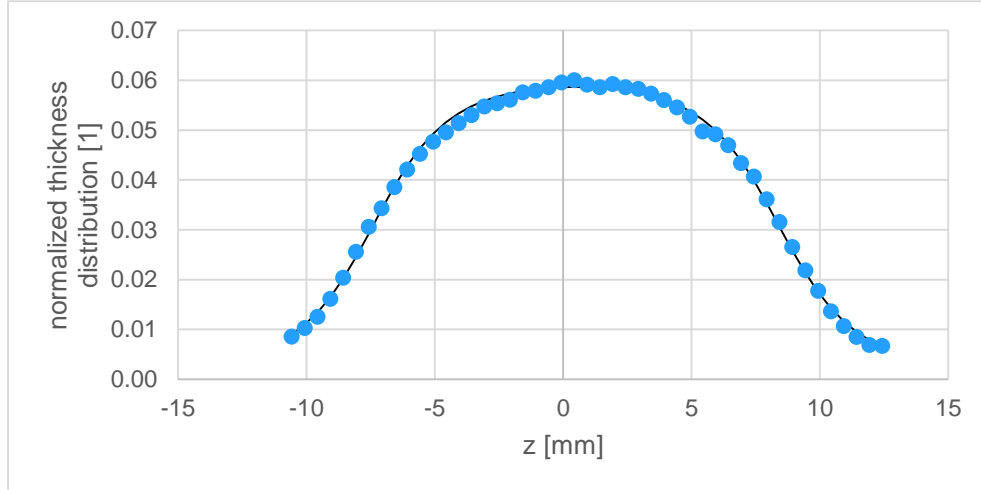


**Figure 54: Emission characteristic of copper under standard operation conditions.** The emission characteristic of the sputter source was determined by measuring the thickness profile of a deposited layer using microscopy. The plot shows the measured values (dots) and the fitted function (line).

A good fit of the measured values was achieved by following formula:

$$f(z, z_S(t)) = \frac{mm}{4c} \left[ \frac{c - (z - z_S(t))}{\sqrt{(c - (z - z_S(t)))^2 + d^2}} + \frac{c + (z - z_S(t))}{\sqrt{(c + (z - z_S(t)))^2 + d^2}} \right] \quad (29)$$

The formula is normalized according to equation (23).

Within a range of -9.5 mm to +9.5 mm from the center of the sputter source, a maximum deviation of 3% between the measured and the fitted value is reached. In the region between -5 mm and 0 mm, a slightly increased deviation to the fitted function can be seen. This indicates a slight asymmetry, which is not covered by equation (29). However, due to the minimal deviation and the therefore minimal effect on the simulation algorithm, this slight asymmetry was ignored. [Table 14](#) shows the obtained fitting parameters. These values are just valid for copper as target material under the standard operating conditions ( $p=0.035$  mbar,  $B=85$  mT). Due to the material dependent angular distribution of the sputtered material (see chapter 2.2), the parameters have to be determined for each target material.

**Table 14: Fitting parameters for the emission characteristic of copper.**

Parameter	Value
<b>c</b>	7.877 mm
<b>d</b>	3.296 mm

The coating efficiency  $\epsilon_C$  was determined by comparing the mass loss of the sputter target to the mass gain of the substrate in coating runs, where the sputter source stayed in the center of the coating zone. In this way, the error caused by material deposited on the outside of the substrate cylinder was minimized. The obtained value for  $\epsilon_C$  is 94.7%.

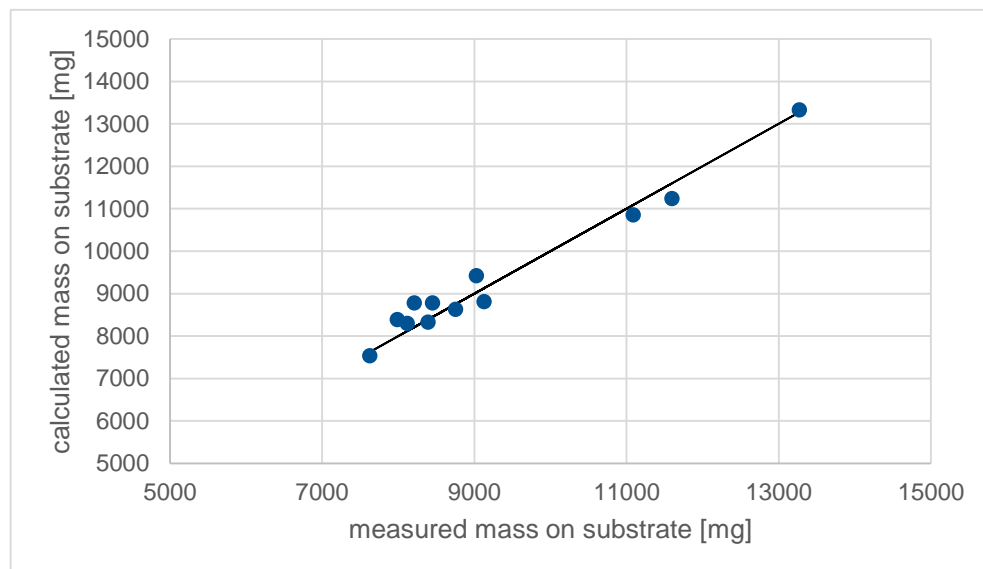
#### 4.3.3 VALIDATION OF THE SIMULATION ALGORITHM

To validate the simulation algorithm, the resulting thickness profile and the calculated mass on the substrate was compared to measured values of a variety of different coating runs.

The mass on the coating zone is calculated by the algorithm using:

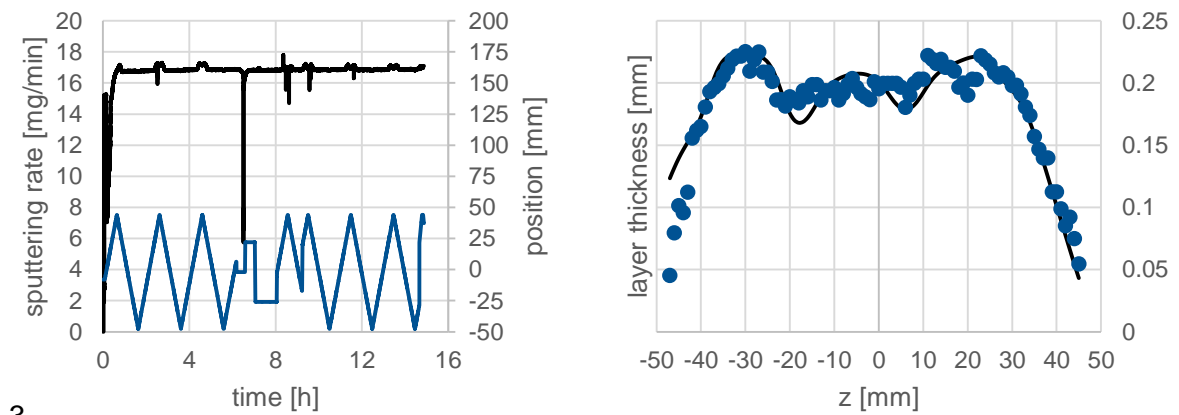
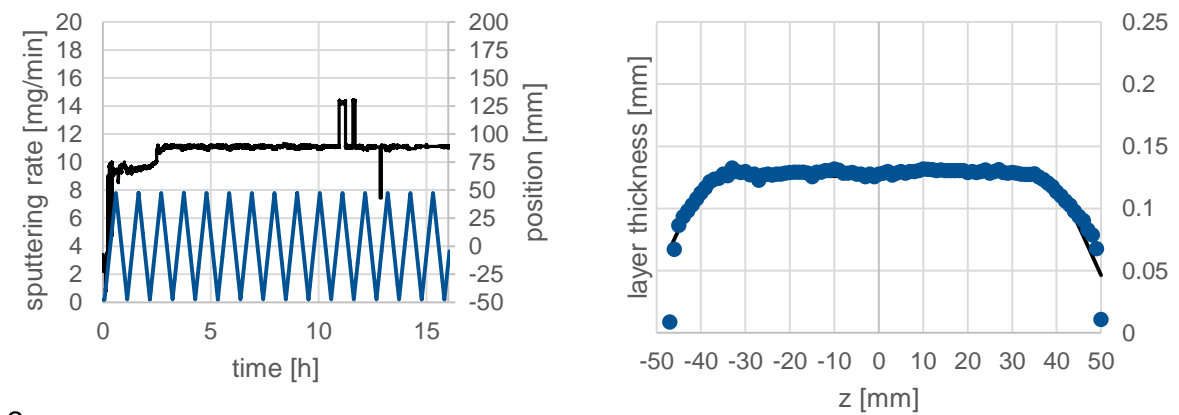
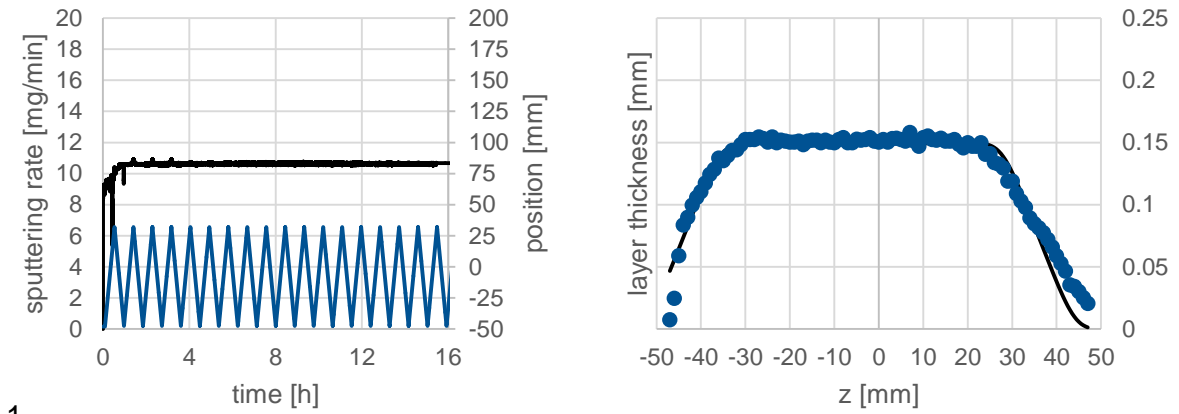
$$m_S = \rho 2\pi r_i \int_{-46 \text{ mm}}^{+46 \text{ mm}} F(z) dz \quad (30)$$

Figure 55 shows the obtained calculated values against the measured mass difference of the substrates before and after coating. The maximum deviation of the calculated and the measured values is 3.2%.



**Figure 55: Mass on substrate.** The plot shows a comparison of the measured mass on substrate (dots) against the values calculated by the simulation algorithm (line).

The calculated thickness profiles for three different coating runs are presented in Figure 56. On the left side, the coating process is displayed by the sputter rate and the position of the sputter source against time. The plot on the right side, shows the calculated thickness profile in comparison with the measured profile. Experiment 1 and 2 were performed with a continuous up and down movement of the sputter source. Except for a short variation in experiment 2, the sputter power was kept constant at 100 W. The resulting layers show a homogenous thickness distribution with steep declines at both ends. In both cases, the calculated thickness profile is in good accordance to the measured values. In contrast to the regular coatings of experiment 1 and 2, coating run 3 showed an irregular behavior both in the movement of the sputter source and the sputter rate. In this coating run, the plasma showed a rather unstable behavior causing arcs and  $\mu$ -arcs. Therefore, the resulting layer shows an irregular thickness profile. However, even given these conditions, the simulation algorithm was able to reproduce the measured values qualitatively.



— sputtering rate  
 — position of the sputtering source  
 ● measured — simulation

**Figure 56: Thickness profiles of sputtered copper layers.** Experiments 1 and 2 were performed with a sputter power of 100 W, a magnetic field of 100 mT and a pressure of 0.035 mbar. In experiment 3 the sputter power was changed to 150 W and the magnetic field to 85 mT.



In summary, it can be concluded that the presented algorithm is able to describe the coating process well. A good accordance was achieved when comparing the measured eroded and deposited mass with the calculated values. The deviation of both values was within a few percent. Furthermore, it showed that the calculated thickness profile fits well to the measured values. This is especially the case, when a homogenous movement is used.

Due to this good accordance, the calculation algorithm offers the possibility to predict the thickness profile and the resulting material efficiency of different movement profiles of the sputter source.

#### 4.3.4 EFFICIENCY

It showed that using an oscillating movement around the center of the coating zone with a constant speed results in a homogenous thickness profile. The maximum oscillation of this movement determines the efficiency of the process, which is defined as

$$\varepsilon_P = \frac{m_S}{m_{tot}} \quad (31)$$

**Figure 57** shows the calculated efficiency over the maximum oscillation of the sputter source as well as the resulting maximum layer thickness, when depositing 20 g of uranium. Up to an oscillation of approximately 35 mm, no significant decrease in efficiency is observed and the coating of the electron reflecting surfaces (given by  $\varepsilon_C$ ) is dominant. Therefore, the maximum efficiency of the process is given by  $1 - \varepsilon_C$ , when the sputter source stays in the center of the coating zone. At higher oscillations, the coating shields get more and more coated and the efficiency decreases.

However, when the mass, which is deposited on the electron reflecting surfaces, reaches a certain thickness, the material can easily be removed. This allows to recycle the material together with the used sputter target. Therefore, the overall material efficiency of the process is likely above 95%.

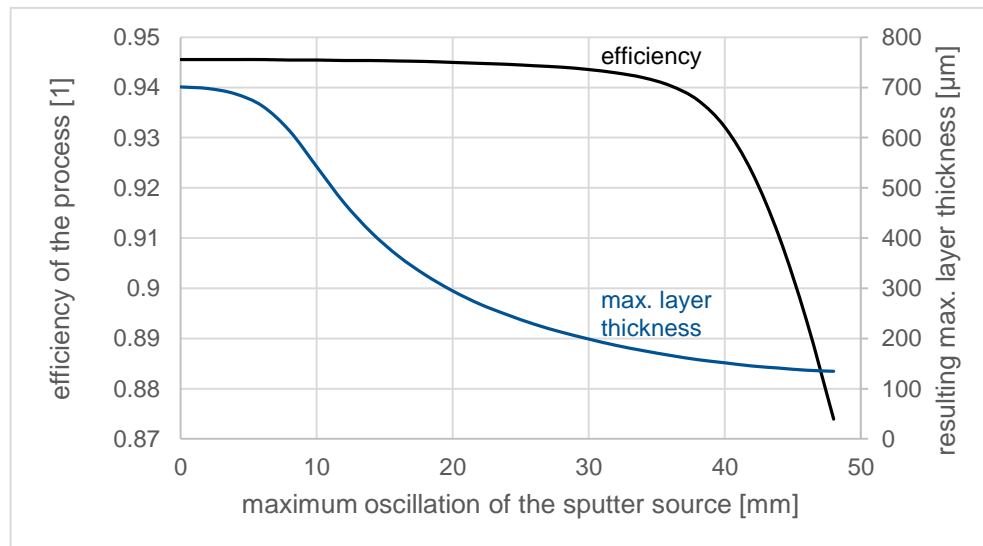


**Figure 57: Efficiency of the sputter process.** With increasing maximum oscillation of the sputter source, the mass efficiency of the coating process decreases due to the increased coating of the coating shields. The maximum efficiency of 94.7% is defined by the coating of the electron reflecting surfaces. The displayed maximum layer thickness is calculated for a total of 20 g uranium in the coating zone. With increasing range of movement the sputtered material is spread over a larger area and, therefore, the maximum layer thickness decreases.

From the manufacturing point of view, it is reasonable to keep the oscillation of the sputter source low to maximize the efficiency of the process. However, for irradiation also the thermal aspects of an increased foil thickness have to be taken into consideration. An oscillation up to 35 mm seems to be a good compromise between a low layer thickness and a high efficiency.

## 4.4 SPUTTER BEHAVIOR

In the following the sputter behavior of different materials is described. Next to uranium, the sputter behavior of copper is presented because it was used as a surrogate material for the parametrization of the PVD apparatus. Nickel and aluminum coatings were performed since their feasibility as interlayer materials was already demonstrated in irradiation tests. Additionally, zirconium was tested in respect to its possible use as interlayer material.

### 4.4.1 COPPER

As copper sputter targets, stock rods with a diameter of 10 mm were used. The rods were trimmed to a length of 40 mm and protruding burrs were removed. A smooth sputter behavior was achieved when the target surface was simply washed using acetone. This treatment was also used for all other target materials. In early coating experiments with copper, the surface was cleaned by using polishing paper and subsequently acetone in an ultrasonic bath. However, after this surface treatment, the sputter behavior was very irregular for several hours.

A typical sputter behavior of copper is shown in [Figure 58](#). In this coating run the sputter source was constantly moving between -47.5 mm and +47.5 mm from the center position of the substrate. In the beginning of the coating run, the sputter power was set to 30 W and the speed of the sputter source to 0.5 mm/s. After 50 minutes the sputter power was increased to 120 W and the speed of the sputter source reduced to 0.1 mm/s. In this way, a self-supporting foil with a low adhesion to the aluminum substrate cylinder could be produced (see chapter 4.5).

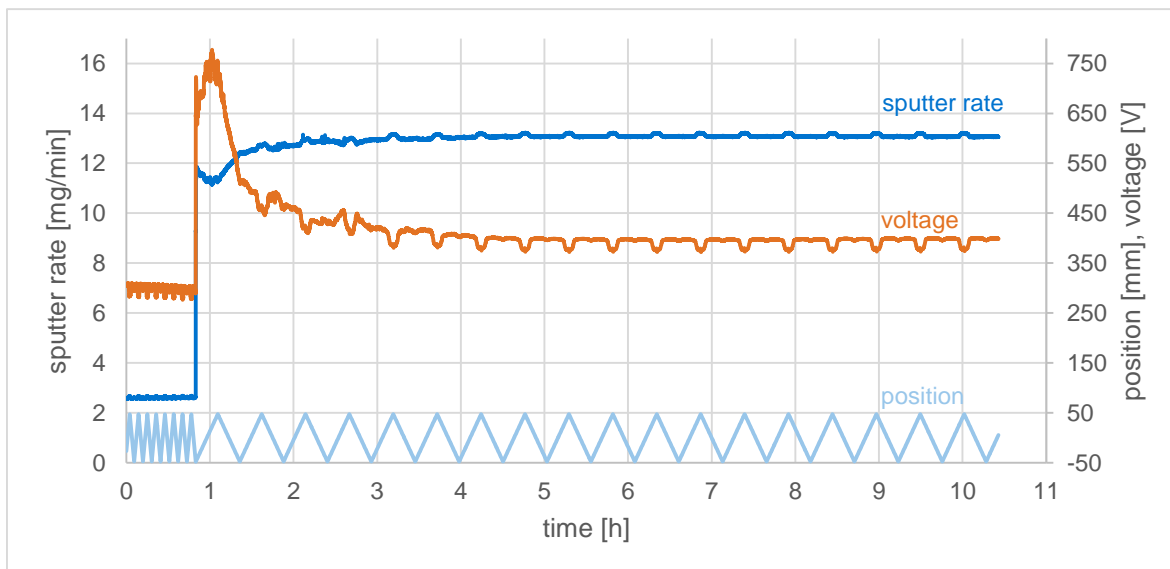


**Figure 58: Typical sputter behavior of copper.** The copper target was sputtered for 10.5 h at a magnetic field of 85 mT. The eroded mass was 7682 g.

At a power of 30 W, the typical voltage is approximately 300 V. A slight decrease of the voltage over time can be seen. When increasing the sputter power to 120 W, the voltage peaks at approximately 750 V and then decreases to 400 V on a time scale below 5 hours. It is assumed that this voltage drop is caused by the coating of the electron reflecting surfaces and, therefore, improved enclosure of the plasma generating electrons.

A typical target burn-up is presented in [Figure 59](#). It emerged that the erosion profile of the sputter target is not radially symmetrical. However, a point reflection through the center between the electron-reflecting surfaces can be found. Since literature suggests a radially symmetric burn-up [72], it is assumed that this asymmetry is caused by a slight tilt in the mounting position. However, despite this asymmetry the circular coating profile proved to be very homogenous with a measured maximum deviation of below 5%.



**Figure 59: Copper target burn-up.** Three different copper targets with different burn-ups are shown: 1)  $0.6 \text{ cm}^3 \approx 5.4 \text{ g}$ , 2)  $1.2 \text{ cm}^3 \approx 10.7 \text{ g}$  and 3)  $1.5 \text{ cm}^3 \approx 13.4 \text{ g}$ .

A typical radial and longitudinal microscopy of a deposited copper layer are shown in [Figure 60](#) and [Figure 61](#). As one can see, the layer features a very homogenous thickness profile. It shows no cracks or other major inhomogeneities. On both ends of the indentation the successful shielding of the outer areas by the coating shields is visible. In the longitudinal microscopy, a wave shaped surface structure of the deposited layer can be seen. This surface profile is the continuation of the substrate's surface profile, which is caused by the machining of the aluminum cylinder. This effect is can be seen in more detail in [Figure 62](#).



**Figure 60: Radial layer profile of deposited copper.**



*Figure 61: Longitudinal layer profile of deposited copper.*

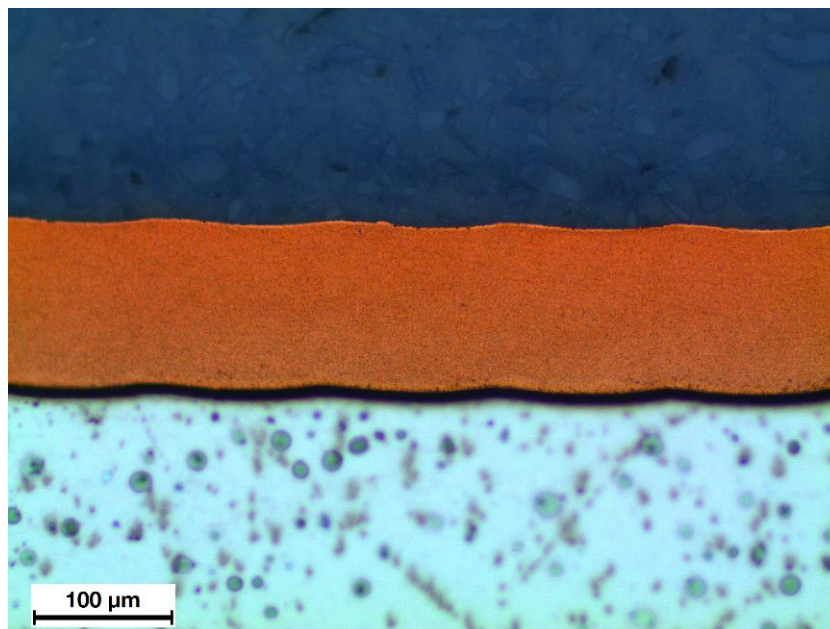


*Figure 62: Longitudinal close-up of a deposited copper layer.*

#### 4.4.2 ALUMINUM

For the aluminum coating experiments, the alloy EN AW-2007 was used. Before sputtering the targets were cleaned by acetone. A typical eroded target is presented in [Figure 63](#). It shows a very similar burn-up profile, including the radial asymmetry and point reflection, as the copper target.



**Figure 63: Aluminum target burn-up.**

But, despite the similar burn-up profile, the emission profile  $f(z, z_s)$  differs from the copper case. [Figure 64](#) shows the measured emission profile and the normalized fit according to equation (29).

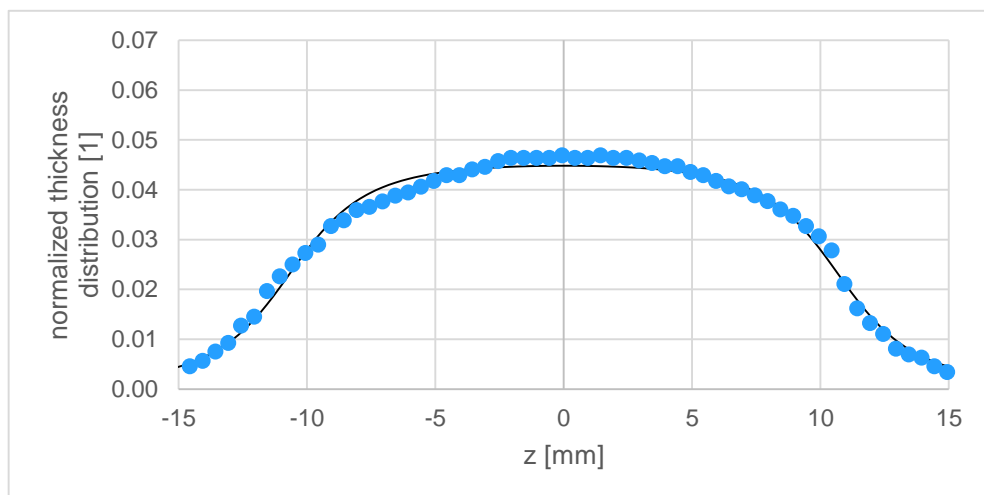


**Figure 64: Emission characteristic of aluminum under standard operation conditions.** The emission characteristic of the sputter source was determined by measuring the thickness profile of a deposited layer using microscopy. The plot shows the measured values (dots) and the fitted function (line).

The emission profile of aluminum can also be described well using equation (29). However, also here a slight asymmetry is seen. The fitting parameters differ from the ones obtained for copper (see [Table 15](#)). Especially parameter  $c$  is significantly larger compared to copper, which results in a broadened profile. This broadening is caused by a different angular distribution of the sputtered target material.

**Table 15: Fitting parameters for the emission characteristic of aluminum.**

Parameter	Value
c	10.677 mm
d	3.233 mm

Also the sputter rate differs substantially. **Table 16** shows the fitting parameters obtained by comparing the calculated values to measured ones. The parameters are based on six coating runs and, therefore, have a much lower statistics than the parameters for copper. Also in this case the maximum deviation from the measured weight difference is significantly reduced when considering the electric current. As indicated by **Table 5**, the sputter rate is lower compared to copper.

**Table 16: Fitting parameters for the sputter rate of aluminum with argon ions.**

Equation	a [mg/(W·min)]	b [mA]	$\max\left(\frac{m_{\text{meas}} - m_{\text{calc}}}{m_{\text{meas}}}\right)$
$R = aP$	0.0188	-	7.0%
$R = aP \frac{I}{I + b}$	0.0520	386.649	1.5%

The sputter process of aluminum showed no relevant difference to the sputtering of copper. A stable plasma could be initiated using the standard settings of 85 mT and 0.035 mbar. However, the sputter power was limited to 90 W due to the low melting point of aluminum.

**Figure 65** shows two typical microscopy images of deposited aluminum. Image 1 shows a layer, which was produced with the sputter source at a constant position. The coating of image 2, in contrast, was produced with the sputter source moving from  $-46$  mm to  $+46$  mm with a speed of 1 mm/s. Deposition 1 shows a regular and homogenous structure, like the copper layers. In contrast, deposition 2 consists of several distinguishable layers. This layer structure shows the influence of the adatom energy on the layer growth. The thicker, brighter layers are deposited with the sputter source at close proximity. This proximity causes a heating of the substrate, which causes a high adatom energy. In contrast, the thin, darker layer is formed by atoms with a lower adatom energy, eroded from the source being at higher distance. This temperature difference causes a different layer growth, as explained in chapter 2.4.

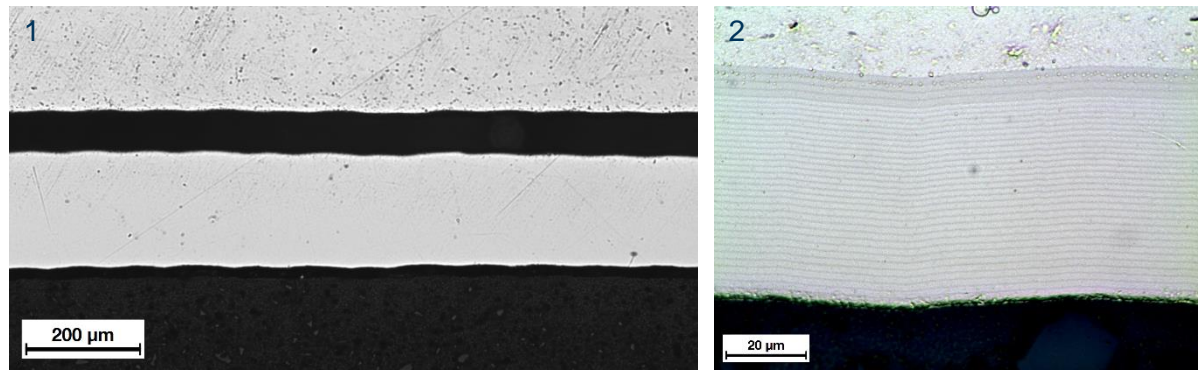


**Figure 65: Deposited aluminum layers.** The presented layers were produced using a fixed (image 1) and a moving (image 2) sputter source. A clear layer structure, which is caused by temperature differences, can be seen in the second case.

As predicted by the theory, the low-energy layers show a lower structural strength compared to the high-energy layer. This can be seen in **Figure 66**, which shows a microscopic image of an aluminum layer deposited with a moving sputter source. In this sample, the layer was damaged by the contracting resin, used for mounting the sample. The force of the contracting resin caused the aluminum layer to rupture at the low-energy layers.

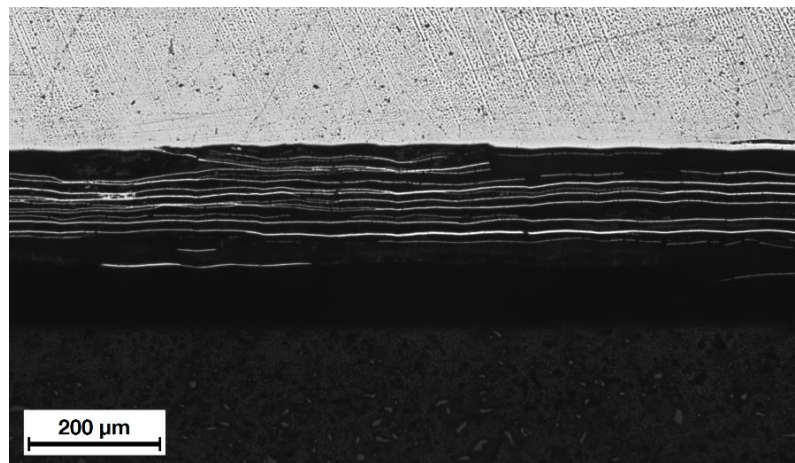


**Figure 66: Ruptured aluminum layer.** A rupture of the aluminum coating occurred due to the contraction of the mounting resin.

This dependency of the adatom energy on the structural strength of the layer can be used to control the adhesion of the deposited layers, as it is detailed in chapter 4.5.

#### 4.4.3 NICKEL

Instead of the other materials investigated in this work, nickel is ferromagnetic. Theory and simulations predict a significant alteration of the magnetic field inside the MTS apparatus. **Figure 67** shows a simulation of the axial component of the magnetic field in case of a non-ferromagnetic target (1) and a ferromagnetic target (2). In case 1 the magnetic field is not influenced by the target rod and shows a distribution according to equation (11) in axial direction. In case 2 however, the field lines are collimated inside the nickel rod. In this way, the magnetic field strength around the rod is significantly reduced. The reduction of the magnetic field around the target rod primarily depends on its magnetic permeability.

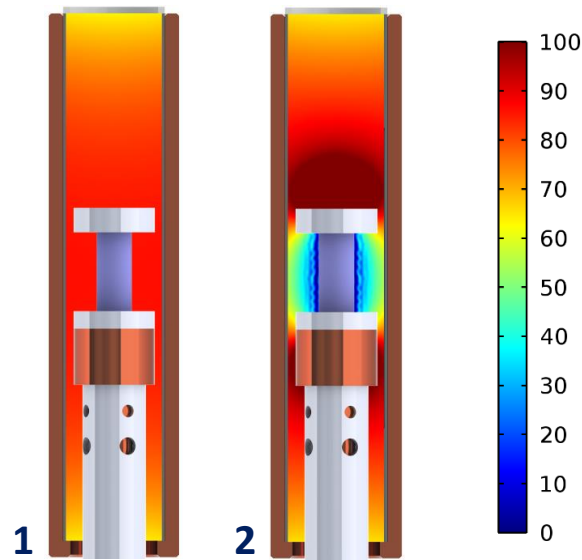


**Figure 67: Axial component of the magnetic field  $B$ .** Image 1 shows the axial component of the magnetic field when using a non-ferromagnetic target. In case 2, a ferromagnetic nickel target was assumed. The values are given in mT. The simulations were performed using the finite element analysis software COMSOL Multiphysics [73].

In case of a too high magnetic permeability, the field around the target rod is not sufficient to trap the electrons in an orbit around the sputter target and no plasma can be ignited under normal operating conditions. This effect was observed, when using commercially available nickel rods with a purity of 99.99% delivered by Goodfellow. However, when using nickel rods, which were produced by casting as described in chapter 4.1, a plasma could be ignited under normal operating conditions. This indicates a change in the magnetic behavior of the material caused by the casting process. With these targets it was possible to deposit layers to the aluminum substrate. However, the erosion profile of these targets was different to the non-ferromagnetic targets. They showed a higher burn-up in the upper part of the target rod (see [Figure 68](#)).



**Figure 68: Nickel target burn-up.** The burn-up profile of a cast nickel target shows a strong erosion on the upper half and almost no erosion in the lower part. The indentation in the lower part is a defect, which occurred due to a too rapid cooling during the casting process.

This phenomenon was explained by the Curie-Temperature. The upper end showed a visible glowing during sputtering. This indicates a temperature above  $500^{\circ}\text{C}$ , which exceeds the Curie-Temperature of nickel ( $T_c=360^{\circ}\text{C}$ ). In the bottom of the target, the temperature is supposed to be significantly lower due to the water cooling. Therefore, the nickel rod loses its



ferromagnetic property in the upper part, which leads to an increase of the magnetic field around the rod in this section. Due to this behavior, the plasma conditions are dependent on the heat contact to the heat sink. This, together with the changes of the magnetic behavior caused by the casting process, could not be reproduced reliably. Therefore, no further coating experiments were performed and the sputter parameters were not calculated.

To avoid these problems, it would be necessary to keep the target at a temperature above its Curie-Temperature. To do so, an improved target temperature control needs to be installed. However, this could not be realized with the current set-up. Another possibility to apply a nickel interlayer could be realized by using a non-ferromagnetic nickel alloy. In this case, however, it needs to be assured that the used alloy elements are compatible to the irradiation of the target.

#### 4.4.4 ZIRCONIUM

The raw material for the zirconium experiments was provided by Goodfellow and featured a purity of 99.2%. The zirconium contained more than 0.2% hafnium. Due to the high neutron cross-section of hafnium, this material is not suitable for the usage in a nuclear reactor. For the sputter experiments however, the hafnium is not supposed to be a constriction.

The zirconium showed, compared to copper, no significant difference in its sputter behavior. A stable plasma could be ignited at the standard conditions (85 mT, 0.035 mbar) and sputter powers of up to 120 W were applied. The process showed a smooth behavior with a low arc rate. The parameters derived to calculate the sputter rate are shown in [Table 17](#).

*Table 17: Fitting parameters for the sputter rate of zirconium with argon ions.*

Equation	$a$ [mg/(W·min)]	$b$ [mA]	$\max\left(\frac{m_{\text{meas}} - m_{\text{calc}}}{m_{\text{meas}}}\right)$
$R = aP$	0.0465	-	10.5%
$R = aP \frac{I}{I + b}$	0.0542	57.518	5.2%

Various experiments with different substrate temperatures and sputter powers were performed. In each case, the sputtered zirconium layers showed a low mechanical strength and bad adhesion to the aluminum substrate. Thus, the coated layer started to flake off during the coating process. This effect could be reduced at high substrate temperatures ( $\approx 80^\circ\text{C}$ ) and sputter powers (120 W), but not totally eliminated.

As an example, [Figure 69](#) shows the photography of a substrate cylinder, which was coated with zirconium and directly following with copper. On the image, the flaking of the zirconium is clearly visible. It is assumed that the low mechanical strength of the deposited layer is caused by the high melting point of zirconium ( $T_M=1857^\circ\text{C}$ ) and, therefore, low homologous temperature during coating. This problem could likely be eliminated by raising the substrate temperature. In the present set-up, the external substrate heating is limited by the boiling point of the cooling water and it was, due to safety reasons, not possible to apply an external temperature of more than  $90^\circ\text{C}$ . To further raise the substrate temperature, an additional heating system needs to be installed, which operates independently from the cooling water supply.



**Figure 69: Copper on a zirconium layer.** View inside a substrate cylinder after applying a copper layer on a previously sputtered zirconium layer.

Another effect, which became present when using zirconium, was a flaking of the layer caused by its oxidation. **Figure 70** shows a substrate cylinder approximately 20 minutes after exposure to air. As one can see, a large part of the zirconium layer fell off. The resulting flakes are shown on the right. The flaking of the layer starts almost instantaneously after exposure to air. The flakes came off energetically, what indicates a high stress in the deposited layer. Therefore, it is assumed that the effect is reduced when applying a higher substrate temperature during the coating process. However, even in this case, it is advisable to perform the target assembly inside a protective atmosphere when using zirconium as interlayer material. In this way, the probability of damaging the interlayer is significantly reduced.



**Figure 70: Flaking of zirconium layers on air.** View inside a substrate cylinder coated with zirconium approximately 20 minutes after exposure to air (image 1). The coating comes off in form of small flakes (image 2) due to the oxidation of the layer.

Due to the described difficulties in achieving a proper zirconium coating in the given sputter set-up, the geometric emission profile could not be determined.

#### 4.4.5 URANIUM

For the following coating experiments, the uranium pins described in chapter 4.1.2 were used. Despite the fact that these pins were cast and did not show a perfect surface quality, no significant difference to the sputter behavior of machined target pins was observed. After a start-up phase of typically 30 minutes, a constant sputtering behavior was reached (see [Figure 73](#)). No unusual arcing or other negative effects caused by the surface could be observed. [Figure 71](#) shows a typical uranium target after a burn-up of approximately 18 g. The figure confirms a high density in the center of the material. Due to the lower thermal conductivity of uranium compared to copper, the sputter power was limited to 90 W. However, [Figure 71](#) shows a different surface structure at the upper end of the target, which indicates a high temperature difference in axial direction.



*Figure 71: Uranium target burn-up.*

Based on sputter runs with seven uranium pins, the fitting parameters for the sputter rate were determined. The sputter rate could well be described using equation (21). In contrast, using equation (20) results in a higher deviation from the measured sputtering rate. However, its simple linearity to the sputter power can be used to quickly determine, the necessary sputtering time for depositing a certain uranium mass. In case of a typical irradiation target, the desired mass is 20 g. Assuming a sputter power of 90 W, this results in a necessary sputter time of approximately 24 h. This value is valid for the current set-up using argon as sputter gas. To decrease the necessary time, krypton could be used. [Table 5](#), indicates an increase of the sputter rate by a factor 1.6 compared to argon. Another option to further enhance the sputter rate, is the application of an improved cooling system, e.g. by a double-sided heat sink. Using both measures, a sputter time of approximately 8 h seems realistic.

*Table 18: Fitting parameters for the sputter rate of uranium with argon ions.*

Equation	$a$ [mg/(W·min)]	$b$ [mA]	$\max\left(\frac{m_{\text{meas}} - m_{\text{calc}}}{m_{\text{meas}}}\right)$
$R = aP$	0.1527	-	6.6%
$R = aP \frac{I}{I + b}$	0.1203	-50.991	1.6%

The emission characteristic of a uranium target is shown in [Figure 72](#). To measure this profile, a layer with a maximum thickness of 250  $\mu\text{m}$  was deposited using standard conditions (85 mT, 0.035 mbar), a sputter power of 90 W and a not moving sputter source. Afterwards, the layer was prepared according to [Figure 52](#) and the thickness profile measured using an optical microscope. [Figure 72](#) shows both the normalized measured values and the fitted emission function using equation (29). The fitting parameters used are given in [Table 19](#). As one can see, equation (29) is well suited to describe the emission of the uranium target.

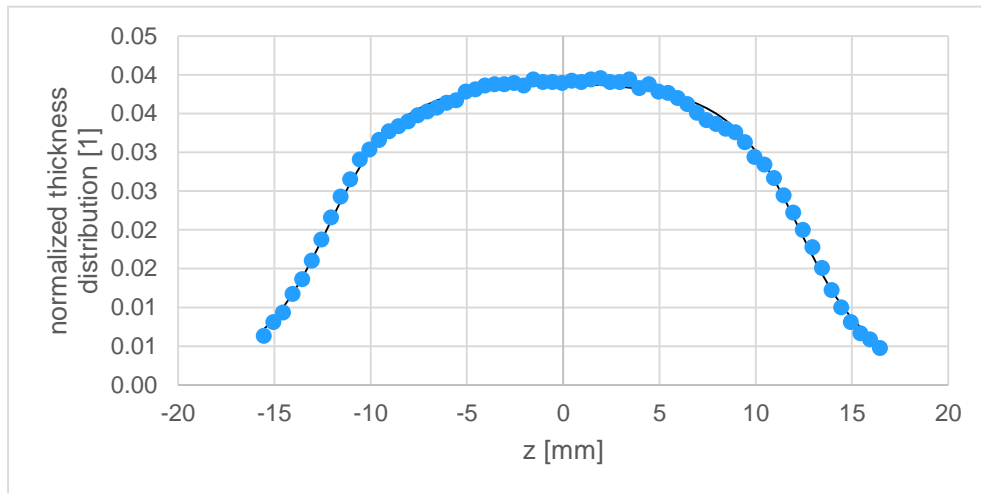


**Figure 72: Emission characteristic of uranium under standard operation conditions.** The emission characteristic of the sputter source was determined by measuring the thickness profile of a deposited layer using microscopy. The plot shows the measured values (dots) and the fitted function (line).

**Table 19: Fitting parameters for the emission characteristic of uranium.**

Parameter	Value
c	12.258 mm
d	3.976 mm

This emission profile was used to perform a thickness simulation according to chapter 4.3.2. The sputter parameters and the position of the sputter source used by the algorithm are presented in Figure 73, a. The resulting calculated thickness profile is as well as measured values are shown in (b). Aside from a slight deviation in the range from -40 to -35 mm, both profiles are in very good accordance in terms of layer thickness and shape. In this plot, also the homogeneity of the deposited layers can be seen. In the section from -30 to +30 mm, the maximum measured difference to the mean value of 109.8  $\mu\text{m}$  was 1.7  $\mu\text{m}$ , which is below 1.6%.

The coating efficiency  $\varepsilon_C$  (see equation (25)) was determined for all performed uranium coating tests. The average coating efficiency is approximately 92%.

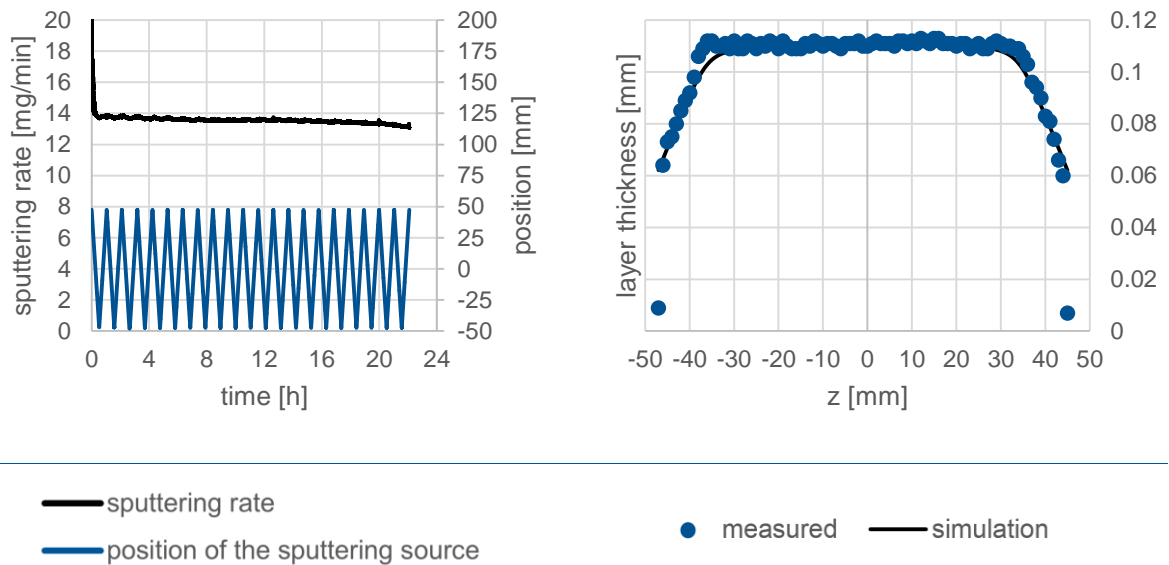


**Figure 73: Thickness profile of a sputtered uranium layer.** The experiment was performed with a sputter power of 90 W, a magnetic field of 85 mT and a pressure of 0.035 mbar. The movement speed of the sputtering source was 0.05 mm/s.

In the following microscopic images of deposited uranium layers are presented. **Figure 74** shows a microscopy of a uranium layer deposited with a substrate temperature of 75°C and a sputter power of 80 W. The layer was coated using a moving sputter source. Therefore, the coat shows a layered structure caused by the appearing temperature difference between the sputter source being close to the observed position and being further away. This sample showed areas as shown in **Figure 74**. Here, the contracting force of the mounting resin caused the coating to crack along the single layers.



**Figure 74: Deposited uranium layer.** The presented layer was produced using a substrate temperature of 75°C and a sputter power of 80 W.

In contrast, **Figure 75** shows a layer coated with a substrate temperature of 90°C and a sputter power of 90 W. The actual temperature difference between the two coating runs is significantly higher than indicated by the given substrate temperatures. This is caused by the higher sputter power and the low substrate to sputter source distance. In the latter case, no cracking of the layer was observed and homogenous layers as presented in **Figure 73** could be produced. This indicates a strong dependency of the layer quality on the temperature during coating.

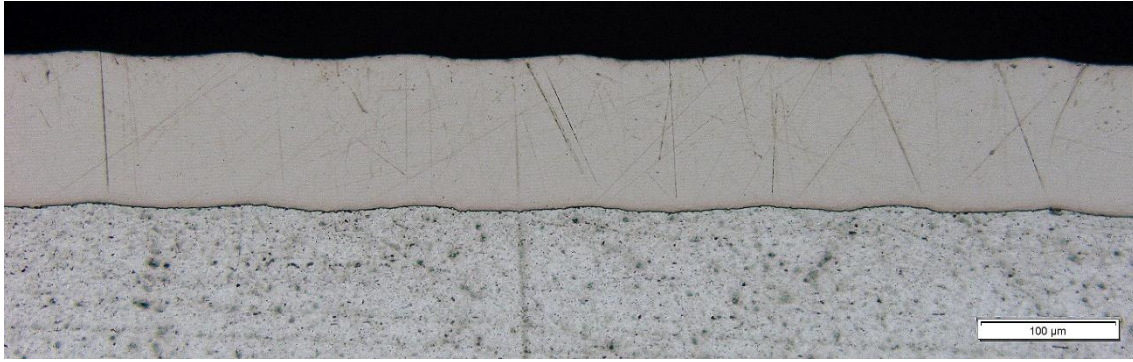


**Figure 75: Deposited uranium layer.** The presented layer was produced using a substrate temperature of 90°C and a sputter power of 90 W.

Using a higher coating temperature, also multilayer foils were produced successfully. **Figure 76** shows a microscopy of an Al-U-Al multilayer. In this case, the substrate temperature was 90°C and the sputter power 90 W. The layer consist of 20 μm aluminum, 140 μm uranium and 5 μm aluminum. The upper aluminum layer was separated from the uranium layer by the contracting force of the mounding resin.



**Figure 76: Al-U-Al multilayer system.** The presented uranium layer was produced using a substrate temperature of 90°C and a sputter power of 90 W.

## 4.5 ADHESION

The adhesion of the deposited layer on the subjacent layer (the aluminum cylinder or a previous sputtered layer) depends on the form of interface between these layers. The interface can either be controlled by the adatom energy or by the application of a thin interlayer between the layers.

As explained in more detail in chapter 2.4, a high adatom energy allows the impinging atoms to stay mobile on the substrate's surface. With this mobility, it is possible for the adatoms to overcome geometric shielding and reach an energetic favorable position. In this way, more dense layers with a good adhesion to the subjacent layer can be achieved. The adatom energy can be controlled by the substrate's temperature and the energy of the impinging atom. Latter can be influenced by the sputter power and the gas pressure. A higher gas pressure reduces the adatom energy due to scattering of the sputtered atoms in the gas phase and the adhesion

of gas atoms on the substrate surface. However, most experiments were performed at the standard pressure of 0.035 mbar, which proved to be ideal to achieve a high sputter rate while having a stable plasma. Therefore, the influence of the gas pressure was not taken into consideration.

The substrate temperature depends both on the controlled heating/cooling by the magnetic coil and the heating caused by the sputter source. Latter is often neglected in literature, because of a target to substrate distance, which is normally above 10 cm. In the present work, the distance is approximately 1 cm and the target is completely surrounded by the substrate. This leads to a heating of the substrate by radiation heating and also a heating of the gas inside the process volume. The target temperature could not be determined by measurement. However, signs of melting occurred when sputtering an aluminum target at 100 W for several hours. This proves a target temperature above 660°C in this case. This number gives a rough idea about the appearing temperatures for the target. However, the actual temperature depends on the thermal conductivity of the sputter target and the heat contact to the heat sink.

A third influencing factor for the substrate temperature is the movement of the sputter source. A slow movement causes a higher residence time over a certain position on the substrate and allows the establishment of a thermal equilibrium and, therefore, a higher substrate temperature.

Another approach to control the layer adhesion is the application of a thin interlayer. Experiments were performed with carbon in form of a graphite spray. Graphite was chosen, since it is both an often used separation layer in mechanical applications and a well-established reactor material. In this experiments the commercially easily available spray CP Graphit-Spray was used. For a later application of the manufactured irradiation targets in an actual nuclear reactor, reactor grade graphite needs to be used. However, the standard graphite spray used in this case is sufficient to show its influence on the adhesion of the sputtered layers. The graphite layer was applied by spraying the graphite directly on the substrate. In a next step, the layer was baked for 1 h at 100°C. In this way, organic binders, in which the graphite is dispersed, are removed. The thickness of the applied layer is approximately 1 µm. This value was roughly estimated by measuring the weight difference of the substrate cylinder before and after spray coating. It was assumed that the graphite is homogeneously distributed over the substrate surface.

In summary, the adhesion of the substrate layer can be influenced by following four parameters: sputter power  $P$ , actively controlled substrate temperature  $T_S$ , the movement of the sputter source  $\dot{z}_S$  and the application of an interlayer. Additionally, the first three parameters also influence the layer properties. According to theory, a higher sputter power, slower movement and a higher substrate temperature should produce a denser and stronger layer with a good adhesion, in contrast to low power, high speed and lower temperature. To test these assumptions, different experiments with copper and aluminum were performed. In these experiments two operation modi with the lower and the upper limits of the apparatus were used:

- *Low energy*:  $T_S=20^\circ\text{C}$ ,  $\dot{z}_S=0.05$  mm/s,  $P=30$  W
- *High energy*:  $T_S=80^\circ\text{C}$ ,  $\dot{z}_S=0.05$  mm/s,  $P=125$  W (Cu) or  $P=80$  W (Al)

For aluminum the maximum power was reduced due to its lower melting point.

Table 20: Adhesion experiments with Cu.

Experiment	Material	$T_s$ [°C]	$P$ [W]	$\dot{z}_s$ [mm/s]	$d$ [μm]	Result
1	copper	20	30	0.1	100	very brittle; bad adhesion; flaking
2	copper	80	125	0.05	100	no debonding; no flaking
3	copper	20	30	0.1	2	no debonding; no flaking
		80	125	0.05	100	
4	copper	20	30	0.1	10	Cu-layer easily separable from the substrate but brittle; remaining Cu on the substrate
		80	125	0.05	100	
5	copper with graphite interlayer	20	30	0.1	3	Cu-layer easily separable from the substrate; not brittle; no remaining Cu on the substrate
		80	125	0.05	70	
6	aluminum (1.)	80	80	0.05	90	first Al layer easily separable from the substrate and the Cu layer; not brittle
	copper	20	30	0.1	4	second Al-layer loosely stuck to the Cu-layer; the resulting Cu-Al-bilayer showed no brittleness
		80	125	0.05	140	
aluminum (2.)	80	80	0.05	150		
7	aluminum (1.)	80	80	0.05	10	Al-Cu-Al-multilayer easily separable from the substrate; both Al-layers stuck loosely to the Cu-layer
	copper	80	125	0.05	150	
	Aluminum (2.)	80	80	0.05	10	

In Table 20 a selection of different experiments is shown to illustrate the influence of the different parameters on the layer adhesion. In the beginning, tests only with copper were performed. A significant difference between the high energy and low energy mode was observed. Copper layers, which were deposited with low energy (case 1), are very brittle. These layers come off easily from the substrate in preferably lamellar shaped pieces. (see Figure 77)





**Figure 77: Copper deposited in the low energy mode.** The deposited layer was very brittle and had a bad adhesion to the aluminum substrate.

The pieces have a curved rectangular shape with a length of up to several centimeters and a width of a few millimeters. They preferably break in a straight line perpendicular to the central axis of the substrate, which indicates a stress along its circumference. Due to the fact that these breaking edges preferably appear when cooling down the substrate after the coating process, it is assumed that this stress is caused by the thermal shrinkage of the deposited layer.

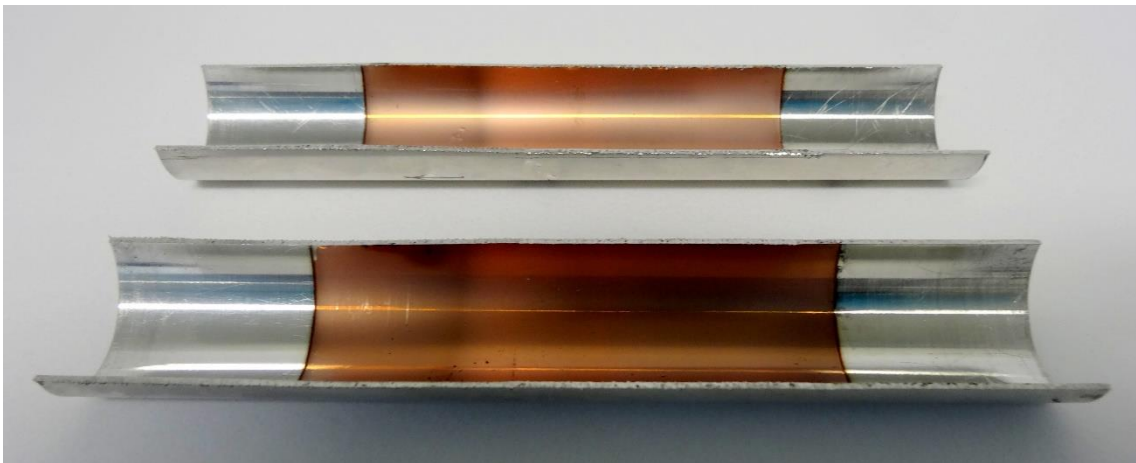


**Figure 78: Copper deposited in the high energy mode.** When using the high energy mode, the deposited layers showed no signs of debonding or brittleness. Their adhesion to the subjacent was strong.

In contrast, copper layers which are deposited in the high energy mode stick well to the subjacent substrate. **Figure 78** shows a layer which is coated using the high energy settings. The layer does not show any signs of debonding. To remove the layer, a high force is necessary. The thermal shrinkage, which causes breaking of the deposited layer in case 1, is supposed to be higher due to the higher deposition temperature. However, it is compensated by a better adhesion and strength of the deposited layer.



**Figure 79: Copper deposited in two stages.** Using a combination of low and high energy mode resulted in a removable copper foil. However, the foil was brittle and some copper remained on the substrate.

These two results were used to produce a foil, which can be removed from the substrate and is at the same time self-supporting. Therefore, first a layer in the low energy mode was applied. After achieving a thickness of approximately  $10\ \mu\text{m}$ , it was changed to the high energy mode (case 3). In this way, a self-supporting and removable foil could successfully be achieved (see [Figure 79](#)). However, the resulting foil was brittle and some copper remained on the substrate. A better result was attained, when introducing a graphite interlayer (case 4, see [Figure 80](#)). The fact that the graphite is visibly removed from the substrate cylinder, shows that debonding happened at the interface between the graphite and the substrate cylinder.

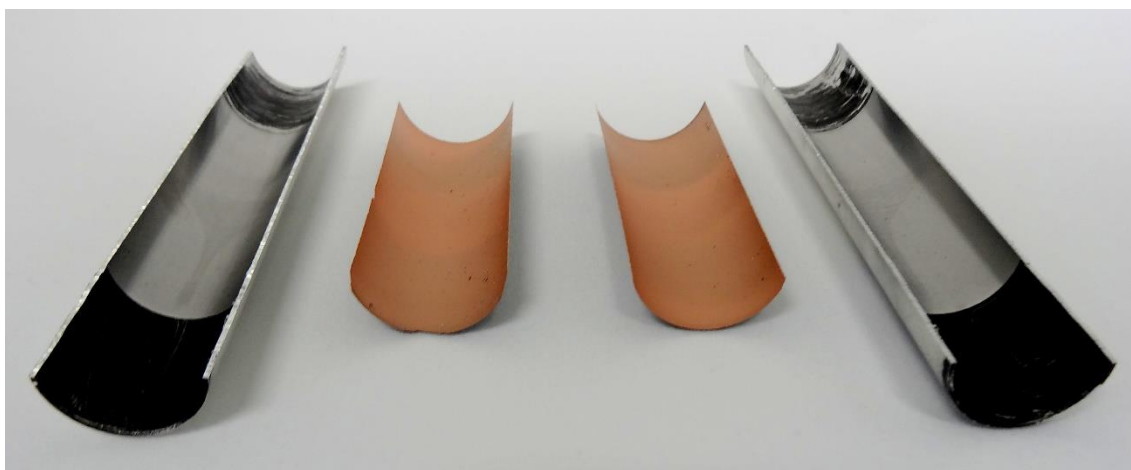


**Figure 80: Copper deposited with a graphite interlayer.** The graphite interlayer successfully prevented the applied copper coating from bonding to the subjacent aluminum substrate.

In a further experiment (case 5), a multilayer system was applied. The system consisted of a copper layer sandwiched into two aluminum layers. Both aluminum layers were applied using the high energy mode. The copper was applied using first the low energy mode and then the high energy mode. [Figure 81](#) shows the obtained result. The substrate cylinder and the outer aluminum layer as well as the outer aluminum layer and the copper layer could easily be separated. However, the copper layer and the inner aluminum layer showed a loose adhesion. The deposited layers show a bending force towards the center of the substrate cylinder. This is likely caused by the thermal stress introduced when cooling the deposited layers after the coating process. A similar result was achieved when reducing the aluminum layer thickness to

approximately 10  $\mu\text{m}$  (case 7). In this case, the copper coating was performed without the low energy mode. As a result, both Al layers stuck loosely to the copper foil. However, the resulting Al-Cu-Al sandwich could easily be removed from the substrate.

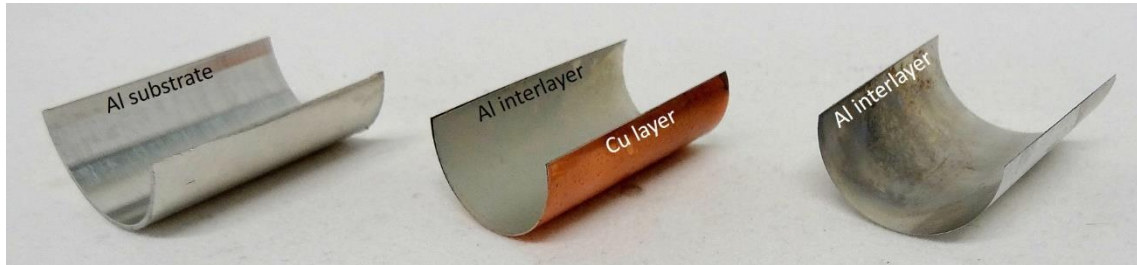


**Figure 81: Al-Cu-Al multilayer system.** When using Aluminum as interlayer material, the Al-Cu-Al sandwich can easily be removed from the Al substrate. The outer Al interlayer showed no adhesion to the copper foil; whereas the inner aluminum was loosely bond to the copper layer.

Based on these results it can be concluded that a high coating temperature is necessary to achieve a mechanically stable and self-supporting foil. According to the theory and the results presented in chapter 4.4, the necessary temperature for a good layer quality depends on the melting point of the material. Furthermore, it could be demonstrated that both an aluminum and a graphite interlayer successfully prevent a bonding of the copper to the substrate. Based on these results, the following experiments with uranium were performed (see [Table 21](#)).

**Table 21: Adhesion experiments with U.**

Experiment	Material	$T_s$ [°C]	$P$ [W]	$\dot{z}_s$ [mm/s]	$d$ [ $\mu\text{m}$ ]	Result
8	aluminum	80	80	0.05	10	Al-U-bilayer easily separable from the substrate; the Al-layer loosely stuck to the Cu-layer; brittle; crumbling after approximately 25 minutes in air
	uranium	80	80	0.05	100	
9	uranium with graphite interlayer	85	80	0.05	100	U-layer easily separable from the substrate; brittle; crumbling after approximately 25 minutes in air
10	aluminum	85	80	0.05	20	first Al-layer loosely stuck to the substrate but easily separable from the U-layer
	uranium	90	90	0.05	140	second Al-layer loosely stuck to the U-layer; the resulting U-Al-bilayer showed no brittleness
	aluminum	85	80	0.05	5	

In a first uranium coating experiment (case 8), an Al-U-bilayer was produced. Both layers were deposited using a substrate temperature of 80°C, a sputter power of 80 W and a sputter source speed of 0.05 mm/s. As shown in [Figure 82](#), the Al-U bilayer could easily be removed from the substrate and the aluminum layer had a good adhesion to the uranium layer. However, the resulting foil was very brittle. After exposure to air of approximately 25 minutes, the foil started to crumble due to the oxidation of the uranium.



**Figure 82: Al-U multilayer system.** When using an aluminum interlayer between the substrate and the uranium layer, a bonding of the foil to the substrate can be prevented.

For the second uranium experiment (case 9), the uranium was deposited using graphite as interlayer material. In this case, the substrate temperature was raised to 85°C. Similar to case 8, the uranium could easily be separated from the substrate (see [Figure 83](#)). However also in this case, the resulting foil was brittle and showed a low resistance to oxidation.

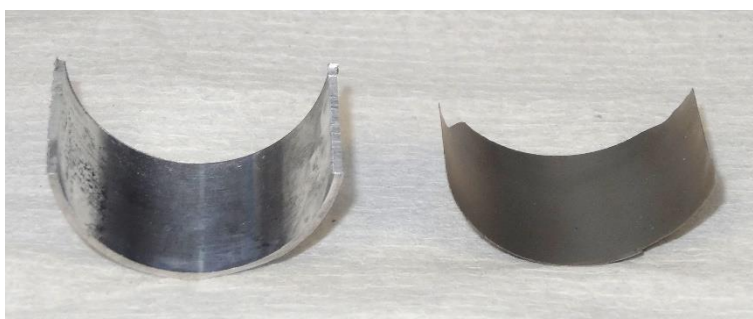


**Figure 83: Uranium deposited with a graphite interlayer.** The graphite interlayer successfully prevented the applied uranium coating from bonding to the adjacent aluminum substrate.

Therefore, the coating temperature was raised even higher in case 10, where an Al-U-Al multilayer system was deposited. For the uranium layer, the sputter power was increased to 90 W and the externally applied temperature to 90°C, what leads to a significant raise of the actual coating temperature. The result of this experiment is shown in [Figure 84](#). The first aluminum is loosely bond to the substrate, whereas it is easily separable from the uranium layer. In contrast, the second aluminum layer is bond to the uranium foil. In this case, the uranium foil showed no signs of brittleness and had a high mechanical strength. Even after an exposure to air of several days, no crumbling due to oxidation appeared.

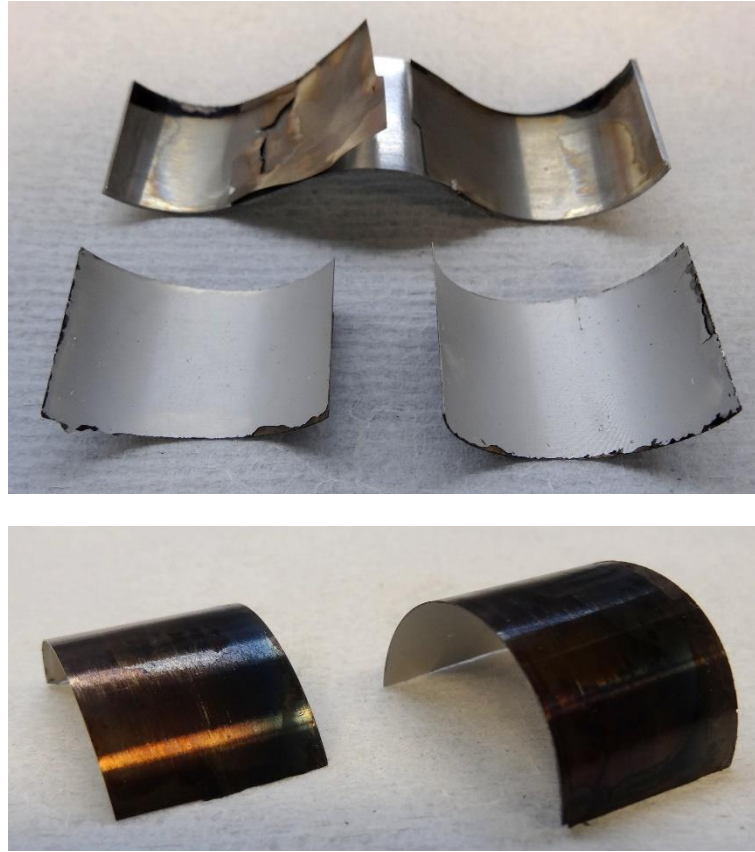


**Figure 84: Al-U-Al multilayer system.** Using aluminum as interlayer material and a high deposition temperature, easily separable and self-supporting foils can be produced. The foils are mechanically stable and do not show crumbling due to oxidation.



## 5 IRRADIATION TARGET ASSEMBLY

Next to the application of the uranium foil and the interlayer material to the outer target cylinder, the assembly of the irradiation target was investigated. After deposition of the foils, the inner aluminum cylinder is inserted and mechanically widened (see [Figure 12](#)). In this way, a good thermal contact between the uranium and the aluminum cylinders is established. This allows the removal of the fission heat, which is generated under irradiation. In the context of this work, two different forming methods were investigated: electromagnetic forming and conventional forming using an axially aligned movable plug.

After forming, the two coaxial cylinders need to be welded in order to safely enclose the produced fission products. To do so several welding techniques are available, e.g. TIG welding, laser welding or electron beam welding. The investigation of a suitable welding technique was not part of this thesis. However, an assembled target was TIG welded in order to proof the general feasibility. [Figure 104](#) shows a fully assembled and welded irradiation target. An in-detail study of the welding process and an investigation of a suitable tightness test have to be performed in a separate work.

### 5.1 BACKGROUND

The deformation of a body is defined as the transformation from its original configuration to a target configuration. Configuration in this context means the relative position of all atoms in the body. Among other reasons, a deformation can be caused by the application of an external force. This external force leads to a certain strain, which induces stress into the body. The relationship between stress and strain is dependent on the material composition of the body and other conditions like the temperature or previous heat treatments of the material. Stress-strain curves display this relationship; they exist for a large variety of materials and material conditions. These diagrams are experimentally determined using tensile testing machines, where a certain stress or strain is applied on a specimen and the according other is measured. [Figure 85](#) shows the engineering stress-strain curve for AL6061-T6 aluminum alloy, as it is used for the aluminum cylinders of the  $^{99}\text{Mo}$  irradiation targets.

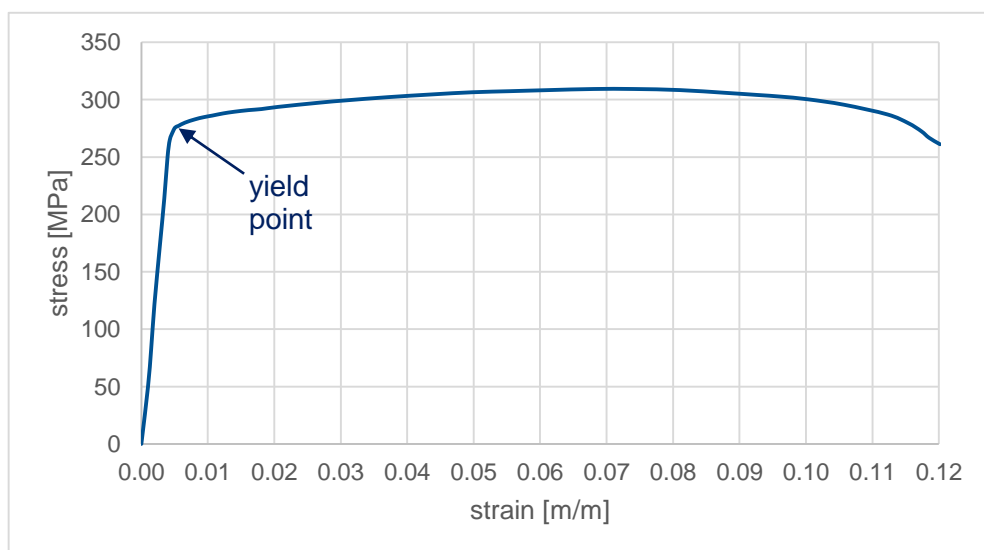


**Figure 85: Engineering stress-strain-curve for AL6061-T6 sheets.** The sheets were tested at room temperature and in longitudinal direction. [74]

In an engineering stress-strain curve, the strain  $e$  is defined as

$$e = \frac{dx}{x_0} \quad (32)$$

and the stress  $S$  as

$$S = \frac{F}{A_0} \quad (33)$$

with  $x_0$  being the original length of the specimen,  $dx$  its change in length,  $A_0$  its original area of the cross-section and  $F$  the applied force. This definition does not take the reduction of the cross-section and the enlargement of the length during the deformation into consideration. This however, can be neglected at low strain values as it is the case in the current application.

As seen in [Figure 85](#), up to the yield point, stress and strain show a very linear relationship. The deformation in this region is called elastic deformation. Any strain in this region will vanish and the specimen will regain its original shape when the applied external force is removed. At higher strains above the yield point, a permanent deformation remains. This is called plastic deformation. Therefore, to reach a certain permanent deformation, both the elastic deformation  $e_{elast.}$  and the desired plastic deformation  $e_{plast.}$  need to be applied:

$$e_{appl.} = e_{elast.} + e_{plast.} \quad (34)$$

As an approximation, this stress and strain model can be used to describe the widening of the inner aluminum cylinder necessary for the assembly of the  $^{99}\text{Mo}$  irradiation target. Using this model the necessary strain to reach the desired deformation can be determined.

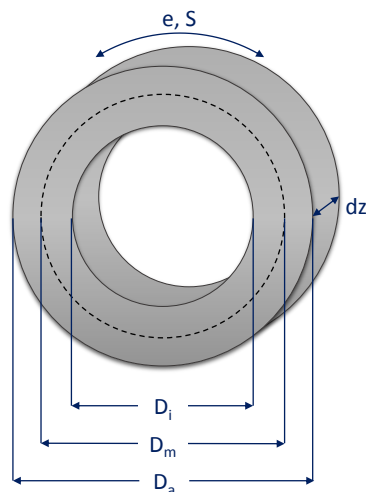


**Figure 86: Geometry used for the deformation model.**

The figure shows a section of aluminum cylinder, which is supposed to be widened. The section is geometrically defined by the outer Diameter  $D_a$ , the inner diameter  $D_i$  and a characteristic diameter  $D_m$ . The length of the section is given by  $dz$ . Both stress  $S$  and strain  $e$  act along the circumference of the cylinder.

To apply this model, the aluminum cylinder is understood as a wound up metal sheet and the strain is defined as the relative change of the circumference at the characteristic diameter  $D_m$ :



$$e = \frac{\pi D_m + \delta x}{\pi D_m} \quad (35)$$

$D_m$  is given by

$$D_m = \sqrt{\frac{D_a^2 + D_i^2}{2}} \quad (36)$$

where  $D_a$  is the outer diameter and  $D_i$  the inner diameter of the cylinder. The definition of  $D_m$  makes sure that the same amount of material is found above and below  $D_m$ .

The stress is defined by

$$S = \frac{F}{(D_a - D_i)dz} \quad (37)$$

with  $dz$  being the axial length of the observed cylinder element. The used geometry is illustrated in [Figure 86](#).

Using the yield point of AL6061-T6, which can be found in [Figure 85](#) at a strain of  $e_{YP}=0.0045$ , the maximum elastic deformation of the inner and the outer aluminum cylinder can be calculated. To calculate the minimum plastic deformation of the inner tube, it was assumed that outer diameter of the inner cylinder has to reach at least the inner diameter of the outer cylinder. To reach this minimum plastic deformation, a minimum total deformation consisting of the maximum elastic deformation and the minimum plastic deformation needs to be applied. The original diameters of the cylinders and the according calculated ones for the various deformations are given in [Table 22](#).

**Table 22: Dimensions of the inner and outer cylinder at various deformations.** To calculate the maximum elastic deformation, the minimum plastic deformation and the minimum total deformation equations (34)-(36) are applied. It was assumed that the cylinders do not undergo any change in length during the deformation process.

Outer cylinder			Inner cylinder			
	original dimension	max. elastic deformation	original dimension	max. elastic deformation	min. plastic deformation	min. total deformation
$D_a$ [mm]	31.00	31.13	28.50	28.62	29.00	29.12
$D_m$ [mm]	30.02	30.15	27.37	27.45	27.85	27.97
$D_i$ [mm]	29.00	29.14	26.20	26.23	26.65	26.77
$dx$ [mm]	-	0.42	-	0.39	1.63	2.02
$e$	-	0.0045 ( $e_{YP}$ )	-	0.0045 ( $e_{YP}$ )	0.019	0.0235

Taking into respect the elastic shrinking, a minimum strain of 0.0235 is necessary for the inner cylinder to match its outer diameter with the inner diameter of the outer cylinder. The maximum outer diameter reached during this deformation is still below the maximum elastic deformation

of the outer cylinder. Therefore, no plastic deformation or remaining stress of the outer cylinder is expected in this case. At a higher deformation of the inner cylinder however, the outer dimensions of the inner cylinder exceeds the inner dimension of the outer cylinder. In this case, the outer cylinder provides a contracting stress on the inner cylinder due to its elastic shrinking. This effect is desirable to increase the stability of the target under irradiation. A higher deformation also allows to compensate any irregularities in the geometry of the target, e.g. the depth of the indentation or the layer thickness. The important parameter for the forming procedure is the average remaining gap between the uranium foil and the aluminum since it defines the dissipation of the fission heat. In the ideal case, the gap should be reduced to zero. However, in reality a certain gap will always remain. To give an example, the Chilean Commission for Nuclear Energy allows a maximum gap thickness of 10 to 30  $\mu\text{m}$  for cylindrical LEU targets [75].

## 5.2 AXIAL HYDRAULIC FORMING

One option to realize the forming of the irradiation target, is the use of a conventional plug forming method. Thereby, a plug with a suitable diameter is pushed through the inner cylinder of the assembled irradiation target. The shape and the maximum diameter of the plug define the deformation of the cylinders. This method of deformation features the advantage of a well-defined process and a high practicability.

### 5.2.1 INSTRUMENTATION

The axial forming device, which was designed within this work, is shown in **Figure 87**, image 1. The device consists of a hydraulic cylinder (a), which pushes a plug through the irradiation target. The target is mounted in a steel capsule (b) and in axial direction fixed by an end stop (c).

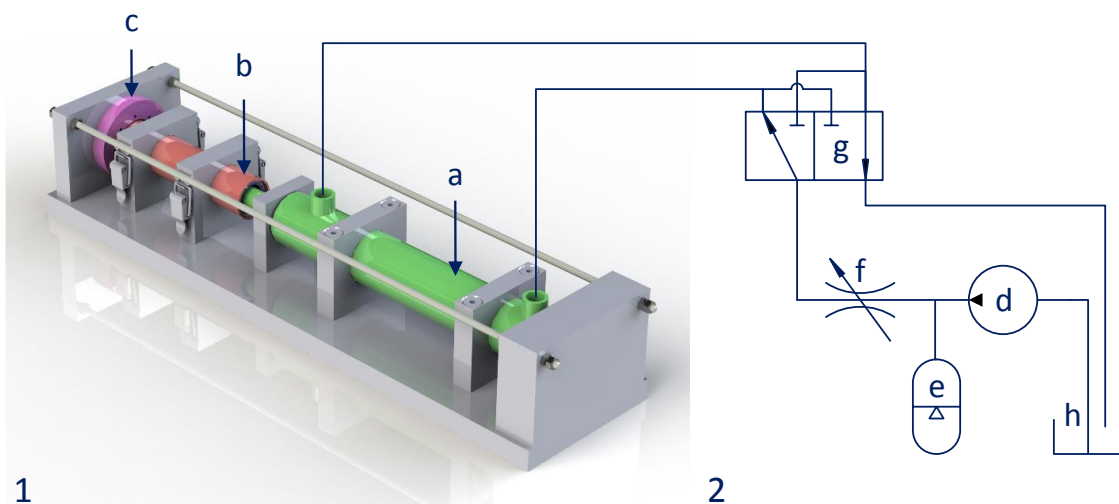


**Figure 87: Overview of the axial hydraulic forming device and its hydraulic system.** The forming device consists of the hydraulic cylinder (a), a steel capsule to fix the target (b), an end stop (c), a hydraulic pump (d), a pressure tank (e), a throttle valve (f), a directional valve (g) and a reservoir (h).

The cylinder is operated by a hydraulic system, which is shown in **Figure 87**, image 2. This system consists of a hand-operated hydraulic pump (d), a pressure tank (e), a throttle valve (f), a 4/3 directional control valve (g) and a reservoir for the hydraulic liquid (h). The hydraulic cylinder is a double acting cylinder with a piston diameter of 50 mm, a maximum stroke of 200 mm and a maximum applicable pressure of 200 bar. To move the cylinder when widening an

irradiation target, first the connection to the cylinder is closed by the directional valve (g) and the pressure tank (e) is filled by operating the hand pump (d). The pressure tank consists of compressible gas volume and is filled with a pressure of approximately 120 bar. After the tank is loaded sufficiently, the directional valve is opened allowing the built-up pressure to move the piston. The adjustable throttle valve (f) regulates the liquid flow and, therefore, controls the speed of the piston.

**Figure 88** shows a detailed view of the axial hydraulic forming device. The figure shows the piston rod (a) pushing a plug (b) through the irradiation target (c). The target is placed in a PTFE cylinder, which is located in a steel cylinder (d). The steel cylinder is fixed to the apparatus, whereas the PTFE cylinder and the target are moveable in axial direction. The function of the PTFE cylinder is to axially align the irradiation target and at the same time allow a certain elastic deformation. An end stop (e) prevents the target from moving in axial direction during the widening procedure. This end stop has a variable radius, which holds the target in the beginning of the widening procedure and opens up at the end of the process to let the plug pass through. This guarantees a uniform movement and prevents any inhomogeneities or damages caused by the stopping and restarting of the plug. After the forming process is finished, the end stop can open further allowing the assembled target to be pushed out by the hydraulic cylinder. For this procedure, a special pushing element is installed instead of the forming plug. This is necessary when the target is stuck to the PTFE cylinder due to high plastic deformation.

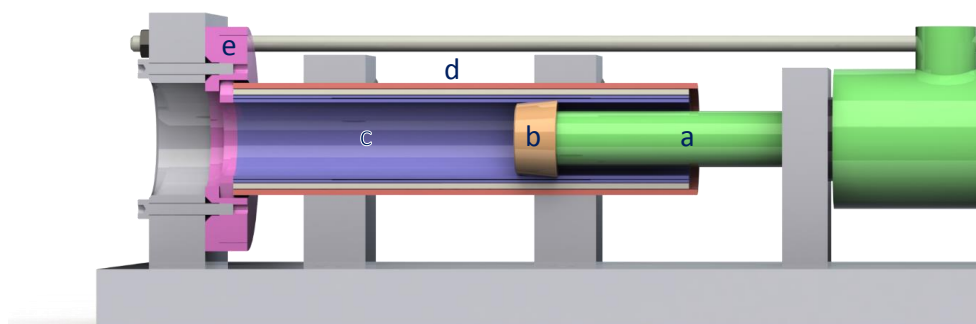


**Figure 88: Detailed view of the axial hydraulic forming device.** The figure shows the piston rod (a), the forming plug (b), the target cylinder (c), the surrounding steel capsule with an PTFE inlay (d) and the end stop with variable radius (e).

As plugs two different geometries were tested, which are shown in **Figure 89**: a conical shape and a spherical shape. The conical plug was made of steel using standard machining equipment. The plug features rounded edges with a radius of 2 mm and a forming surface with an inclination of  $5^\circ$ . It is fixed by a screw to the piston of the hydraulic cylinder. As an alternative, a spherical plug made of hardened steel was investigated. The used spheres are commercially available and are normally used for ball bearings. Therefore, they feature a high precision and at the same time a high cost efficiency. Due to the low costs, the balls can often be renewed, what avoids fluctuations in the production process caused by abrasion of the plug. In contrast to the conical plug, the spherical plug is not fixed to the piston rod. This allows the ball to compensate for manufacturing tolerances of the axial forming device.

In all experiments the plug and the inside of the inner target cylinder were coated with graphite by the application of a graphite spray. In this way, the friction between the plug and the cylinder is lowered, what allows a constant movement of the plug. This is necessary to guarantee a homogenous forming of the target cylinder.

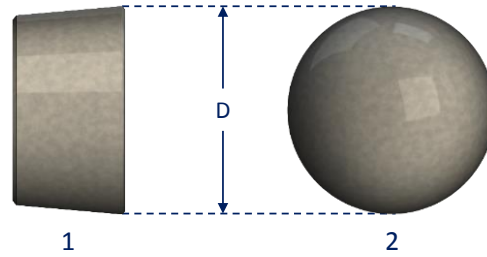


**Figure 89: Plug geometries.** Image 1 shows the conical forming plug. Its forming surface has an inclination of  $5^\circ$ . The edges are rounded with a radius of 2 mm to allow a smooth forming procedure. In image 2 the spherical forming plug is displayed. The used spherical plugs had a G28 quality grading.

### 5.2.2 FORMING PROCEDURE AND ANALYSIS

The experiments to characterize the forming device were performed using a copper layer with a thickness of  $150\ \mu\text{m}$ . If not stated otherwise, most of the presented experiments were performed with pre-produced foils due to a limited coating capacity. Like in the coating tests, copper has the advantage that it is easily distinguishable from aluminum in microscopic pictures. In addition, it is assumed that due to the low thickness of the foil compared to the aluminum cylinders, the difference in mechanical strength of uranium and copper can be neglected.

For the experiments, following forming procedure was followed:

1. Determination of the initial dimensions of the target cylinders by a caliber
2. Coating of the plug and the inner cylinder with graphite
3. Assembly of the target, the PTFE and the steel cylinder
4. Installation of the forming plug
5. Build-up of pressure in the pressure tank
6. Moving the plug through the cylinders by releasing the pressure from the tank
7. Retracting the piston rod
8. If necessary: Installation of the pushing element to push out the target from the PTFE cylinder
9. Optional: Repetition of steps 3 to 8 using different forming plugs
10. Determination of the final dimensions of the target cylinders by a caliber

All forming procedures were performed using a pressure of approximately 120 bar and a piston speed of approximately 200 mm/min.

After the target was successfully formed, the quality of the forming was determined using microscopic examination. Therefore, the assembled target was prepared as described in chapter 4.3.1. Microscopic pictures are taken at each end of the foil and in the middle section. To qualify the forming procedure, the microscopic picture of the middle section is analyzed using an image processing tool. Each pixel of the microscopy is scanned and a gap between the aluminum and the copper foil is recognized by its color. A pixel is identified as gap when the maximum of the single RGB values of a pixel is below  $90^4$ . With this value good results could be achieved (see [Figure 90](#)).

<sup>4</sup> The RGB color code is an additive color code. The color is defined by adding up a red, green and blue component. In this case, the fraction of each color is given on a scale from 0 (0%) and 255 (100%).



**Figure 90: Image processing.** The image processing algorithm detects gaps between the layers by analyzing the RGB color code of each pixel. Image 1 one shows a typical microscopic picture of a deformed target cylinder. In image 2, the gap found by the algorithm is marked in green.

The algorithm then calculates the total area of the gap  $A_{gap}$  and with it the average gap thickness  $\bar{d}$  by

$$\bar{d} = \frac{A_{gap}}{L} \quad (38)$$

where L is the length of the observed interface.

For this measurements images with a magnification factor of 50 were used. This results in a pixel size of approximately  $0.1 \times 0.1 \mu\text{m}^2$ . The average gap thickness obtained by this method show a good accordance to manually measured values. However, the accuracy of this algorithm may not be overrated since it depends on various variables, like the quality of the sample preparation or the quality of the microscopy. Therefore, the given values should be considered as trends instead of accurate numbers.

### 5.2.3 RESULTS

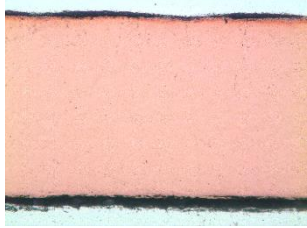
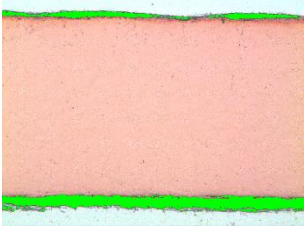
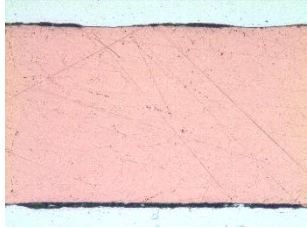
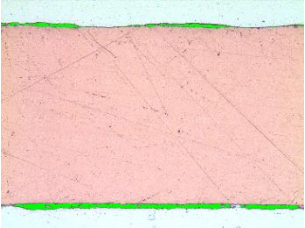
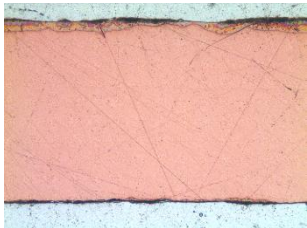
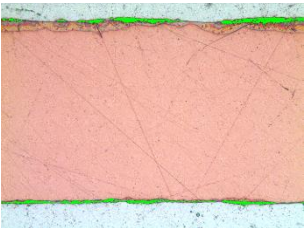
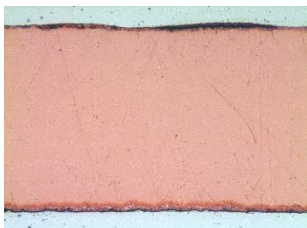
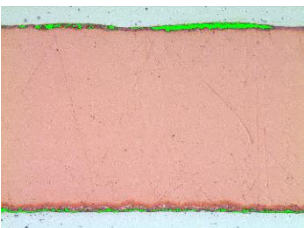
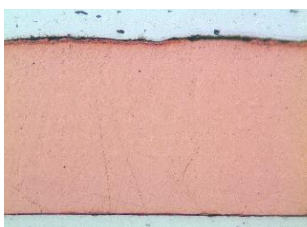
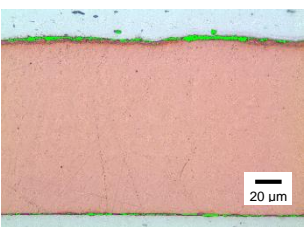
For the forming experiments, four different conical plugs and one spherical plug were used. The sphere had a diameter of 26.988 mm and the conical plugs outer diameters D of 26.58 mm, 26.88 mm, 27.38 mm and 27.88 mm. **Table 23** shows a list of all used plugs, their outer diameters and the measured results after target forming. The diameters of the assembled target are average values measured at various positions along the target. The accuracy of this measurement was approximately 0.05 mm.

**Table 23: Deformation results using plugs 1-5.**

Plug #	Shape	Plug diameter [mm]	Outer diameter of the combined cylinders [mm]	Inner diameter of the combined cylinders [mm]	Calculated average gap thickness [ $\mu\text{m}$ ]
1	conus	26.58	31.0	26.6	10.6
2	conus	26.88	31.2	26.8	3.5
3	sphere	26.988	31.3	26.9	2.7
4	conus	27.38	31.6	27.3	2.4
5	conus	27.88	32.1	27.8	1.6

Except of plug 1, all other plugs lead to an increase of the target's outer diameter. This is in good accordance to the values obtained in **Table 22**. A comparison between the outer diameter

of the plugs and the inner diameter of the assembled target show the elastic shrinking of the cylinders.

Plug	Microscopy	Recognized gap	$\bar{d}$
1			Outside: 2.4 $\mu\text{m}$ Inside: 8.3 $\mu\text{m}$ Sum: 10.7 $\mu\text{m}$
2			Outside: 0.9 $\mu\text{m}$ Inside: 2.6 $\mu\text{m}$ Sum: 3.5 $\mu\text{m}$
3			Outside: 1.5 $\mu\text{m}$ Inside: 1.2 $\mu\text{m}$ Sum: 2.7 $\mu\text{m}$
4			Outside: 0.9 $\mu\text{m}$ Inside: 1.5 $\mu\text{m}$ Sum: 2.4 $\mu\text{m}$
5			Outside: 1.2 $\mu\text{m}$ Inside: 0.4 $\mu\text{m}$ Sum: 1.6 $\mu\text{m}$

**Figure 91: Results of hydraulic forming using plugs 1-5.**

In **Figure 91**, the results of the image processing tool is presented. The table shows the investigated microscopic images, the detected gaps and the calculated gap thicknesses. The gap thickness is given for the gap between the foil and the outer cylinder as well as the gap between the foil and the inner cylinder. Also the sum of both values is presented. As one can see, the total gap thickness shrinks with increased plug diameter. This behavior is to be expected due to the higher plastic deformation of the target cylinders. It also leads to higher contact area between the tubes, which can be seen by the reduction of the green areas.

For the plugs 2-5, the outer gap is roughly constant. This can be explained by the wavelike surface profile of the outer tube, which is dominating the layer contact. This surface profile is caused by the machining of the cylinder.

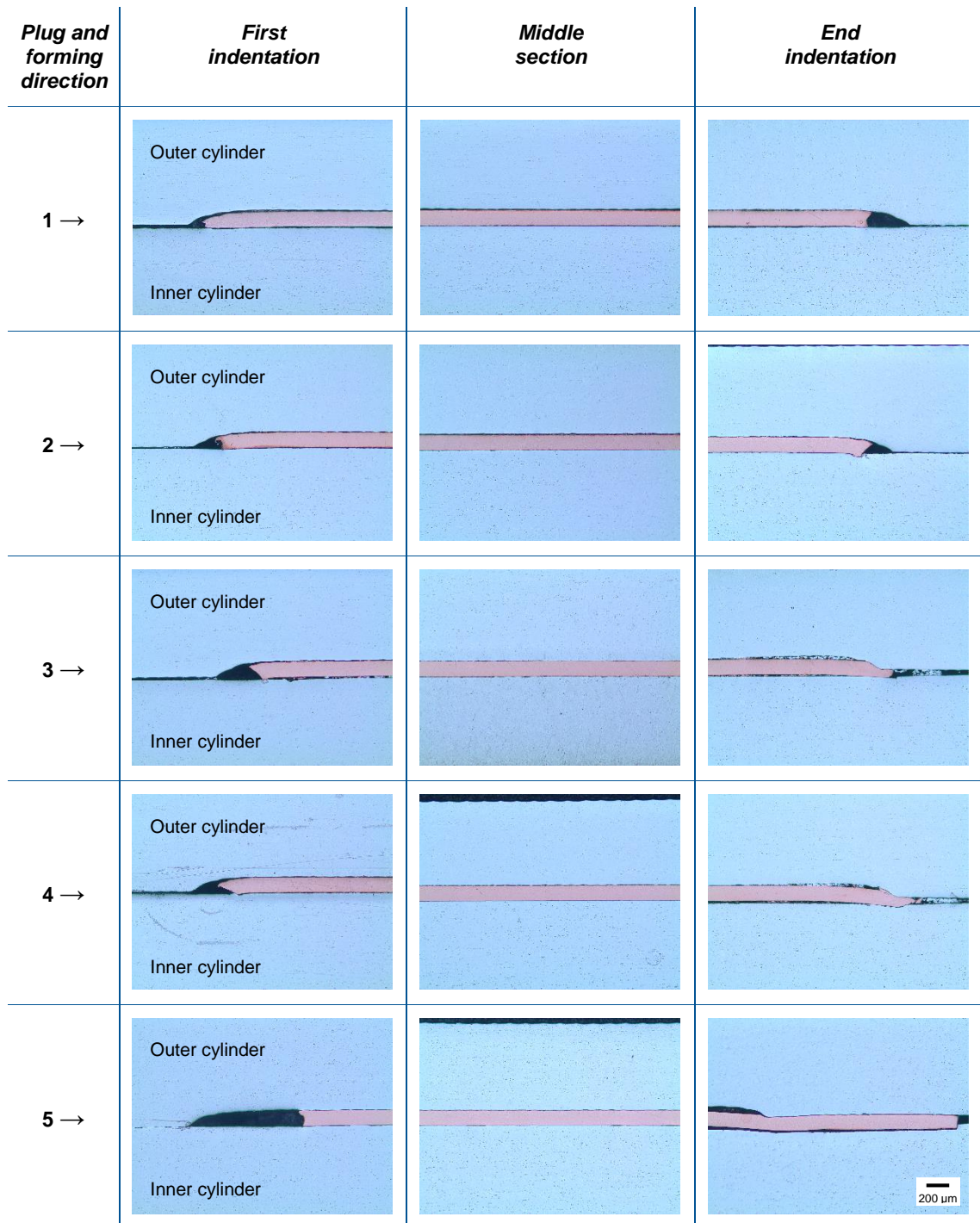


**Figure 92: Results of hydraulic forming using plugs 1-5.**

From this results it can be followed that a large plug diameter is necessary to achieve a good heat contact. However, when using plug 3, 4 or 5, the copper foil is pushed out of the indentation in the outer target cylinder. This can be seen on the microscopic images presented in [Figure 92](#). The displacement of the foil increases with larger plug diameters. This effect could

also be seen optically on the outside of the assembled target in form of a light step on the outer surface. Such a displacement is not acceptable for an irradiation target.

To overcome this problem and avoid the displacement of the foil while guaranteeing a high contact area, the deformation process was optimized. To do so, the target is deformed in three steps with a subsequently increased plug diameter. First, the foil is fixated by using plug 1. Afterwards, the target is widened using plug 2 and subsequently plug 3 and 4 are applied. To counteract a possible displacement of the foil, in each step the deformation direction is altered.

Figure 93 and Figure 94 show a target, which was assembled according to the described procedure. As one can see, by this method the foil can be kept in place and a good contact area can be achieved.

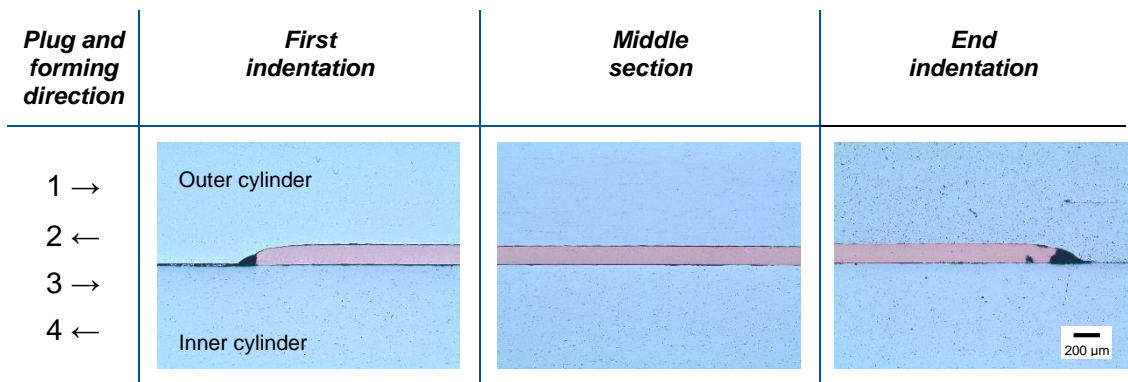


Figure 93: Result of hydraulic forming using the optimized forming procedure.

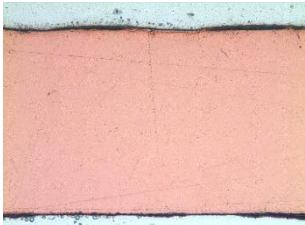
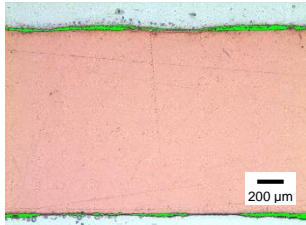
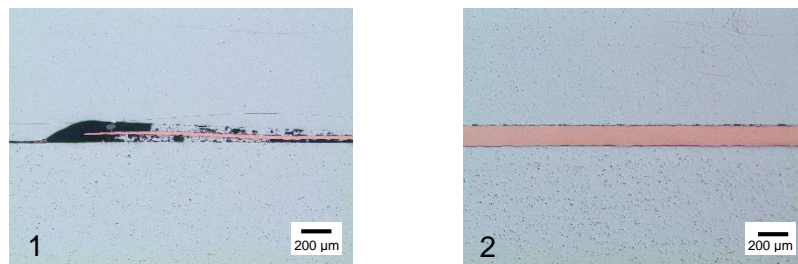
Plug	Microscopy	Recognized gap	$\bar{d}$
1 →			Outside: 1.4 μm Inside: 1.0 μm Sum: 2.4 μm
2 ←			
3 →			
4 ←			

Figure 94: Result of hydraulic forming using the optimized forming procedure.

The presented optimized forming procedure together with the given plug diameters works well when the layer has a thickness of approximately 150 μm. For smaller layer thicknesses, the diameter of the plug needs to be increased accordingly. This can be seen at the layer presented in Figure 95. This foil was PVD coated and optimized for a high material utilization as presented in chapter 4.3.4. Therefore, the layer is thinner at its ends compared to its center. With the given plug diameters, a good contact was achieved in the middle section (image 2). No difference to the forming procedure using pre-produced foils could be observed. However, at the end of the foil the deformation of the target cylinders was not sufficient (image 1). This can be compensated, by either adding a deformation step with an increased plug diameter or by an accordingly shaped indentation in the outer cylinder. As an alternative, the oscillation of the sputter source, can be increased. In this way, a homogenous layer thickness can be achieved along the whole indentation. This would, eliminate any gap at the beginning of the indentation as it is unavoidable when using pre-produced foils (see e.g. Figure 93). However in this case, the material utilization would be reduced due to a higher coating of the coating shields (see Figure 57).





**Figure 95: Assembled target with a layer thickness profile.** The images show the layer in the center of the target (1) and at the beginning of the indentation (2).

### 5.3 MAGNETIC FORMING

As an alternative to hydraulic forming, electromagnetic forming was investigated. Electromagnetic forming is a method for forming electrically conductive objects by the application of strong magnetic fields. A detailed explanation of the process can be found in [76]. The investigation at hand was performed by *GSI Gesellschaft für Schweißtechnik International mbH München* in the framework of the study *Magnetimpulsschweißen (MPW): Machbarkeitsuntersuchung zum Schweißen/Crimpen von Al-Rohren mit Cu-Folie* [77].

#### 5.3.1 BACKGROUND AND INSTRUMENTATION

In general, a magnetic forming device consists of a magnetic coil, its electric supply circuitry and a magnetic field concentrator. The work piece, which is supposed to be deformed, can either be located around the magnetic coil or inside the magnetic coil. Having the work piece around the coil leads to its expansion, whereas having it inside the coil causes its compression.

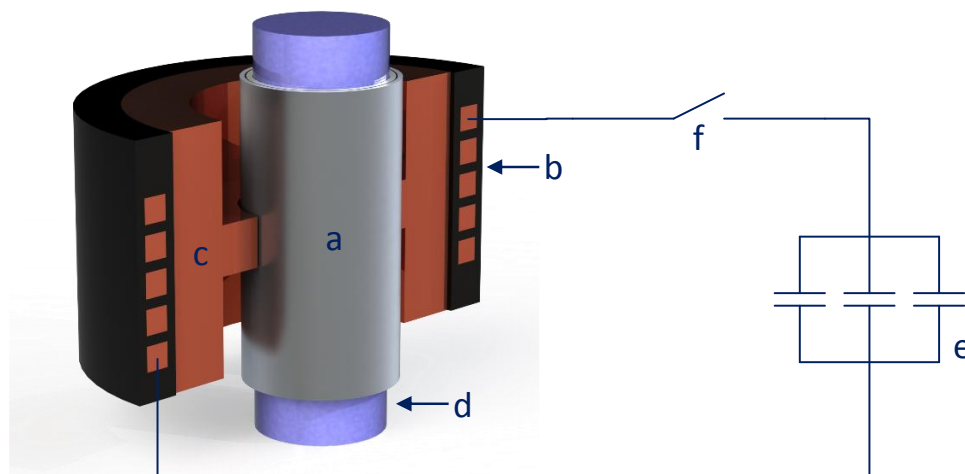


**Figure 96: Overview of the magnetic forming device and its circuitry.** The magnetic forming set-up consists of the work piece (a), the magnetic coil (b), the field concentrator (c), a mandrel (d), a capacitor bank (e) and an electric supply (f).

Due to the availability of the latter, the study at hand was performed with the specimen inside the coil. Thus, the outer target cylinder was crimped on the inner cylinder. In this way, the general qualification of this process for the target assembly could be investigated without

having to construct a new forming coil. A simplified illustration of the set-up used for the current study is shown in [Figure 96](#).

Caused by a rapidly changing magnetic field created by the coil, a magnetic pressure builds up, which applies a force to the work piece. To make the forming process more efficient and to localize the area of deformation, a magnetic field concentrator (c) is used. The field concentrator consists of a well conducting metal, with at least one slit in radial direction. When a quickly oscillating magnetic field is applied, an electric current is induced in the field concentrator. Due to the skin effect at high frequencies, this current appears on its surface. As shown in [Figure 97](#), this current is concentrated in close proximity of the work piece and, thus, leads to a high magnetic pressure in this area. The inner surface of the field concentrator used in the following experiments had an axial length of 15 mm.

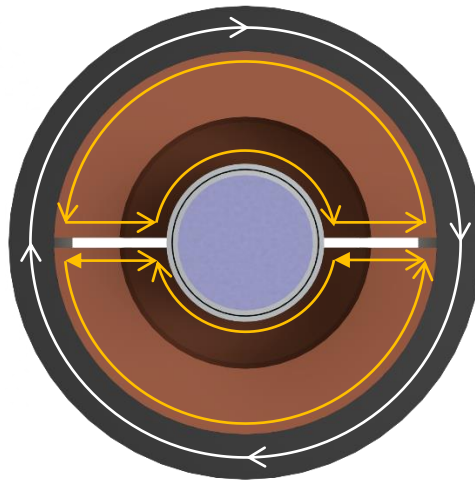


**Figure 97: Working principle of a magnetic field concentrator.** The image shows the electric current flowing through the magnetic coil (white) and the induced current in the field concentrator (yellow). Due to the skin effect, the induced current appears on the surface of the field concentrator, which leads to a concentration of the current and, thus, the magnetic field in close proximity to the work piece.

To deform a work piece ([Figure 96](#), a), it is fixed in the center of the magnetic coil (b) and the field concentrator (c). Then the capacitor bank (e) is charged and the charge is released by closing the electrical connection (f). In this way, the coil and the capacitor build a damped oscillating circuit, whose electric current can be described by

$$I(t) = I_0 \sin(\omega t) e^{-\delta t} \quad (39)$$

with  $I_0$  being the maximum amplitude of the current,  $\omega$  the oscillating frequency and  $\delta$  the damping constant.

Due to this current, the coil creates an oscillating magnetic field:

$$B(t) \sim I(t) \quad (40)$$

This field leads to an induction of an electric current in the work piece and, thus, to the build-up of a corresponding magnetic field. This induced field counteracts the external field. Therefore, the magnetic field on the inside of the work piece is significantly lower than around it. This radial field gradient effects a magnetic pressure on the work piece. The magnetic

pressure is directed towards the lower field strength and, therefore, to the center of the coil. According to [78], the magnetic pressure can be approximated by

$$p_{mag}(t) = \frac{B(t)^2}{2\mu_0} \quad (41)$$

This pressure mainly acts on the outer cylinder, as the inner cylinder is partially shielded by the field induced in the outer one. In **Figure 98**, a typical current behavior and the resulting magnetic pressure is shown. The plot presents typical values based on [79].

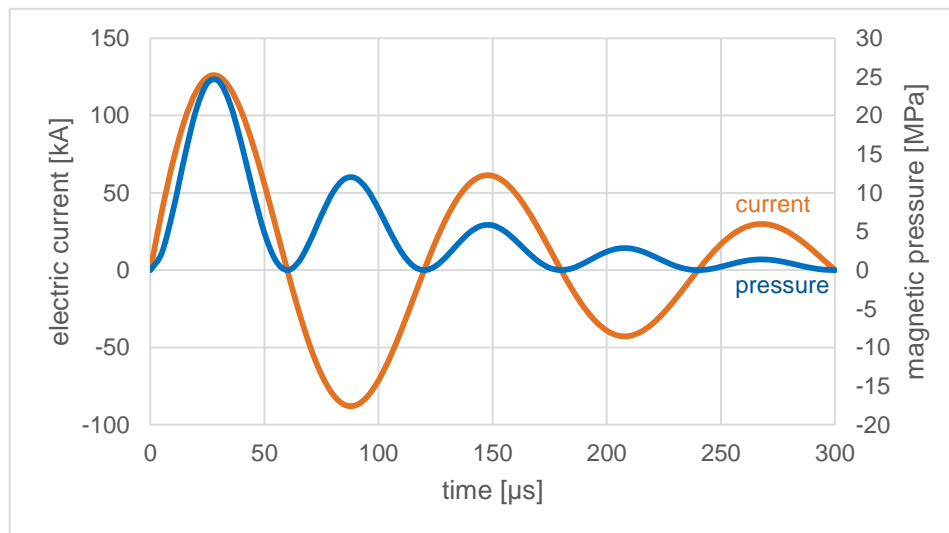


**Figure 98: Typical electric current and magnetic pressure behavior.** The electric system can be approximated by a dampened oscillating circuit. Its time behavior is given by formula (39). The magnetic pressure can be approximated by formula (41).

### 5.3.2 PROCESS PARAMETERS AND SAMPLE ANALYSIS

An important process parameter of the electromagnetic forming is the energy, which is released from the capacitor bank. This energy  $W$  is defined by its capacity  $C$  and the voltage  $U_C$ , which is used for charging the capacitor:

$$W = \frac{1}{2} C U_C^2 \quad (42)$$

In the following experiments the influence of three different forming energies was investigated:

- 3.5 kV / 6.0 kJ
- 4.5 kV / 13.7 kJ
- 5.5 kV / 20.3 kJ

To fit the available forming set-up, the geometry of the work piece had to be slightly altered. **Figure 99** shows the specimen used for the experiments. The specimen consists of two aluminum cylinders with a wrapped-up copper foil placed in an indentation in the outer cylinder. The indentation and the foil had a thickness of 150 μm. The dimensions of the foil were 30 mm × 70 mm. Therefore, the foil does not cover the whole circumference but there is a gap of approximately 2.5 mm, where the inner cylinder faces the outer cylinder directly. In contrast to the previously described hydraulic forming, the electromagnetic forming is a pulsed process. Therefore, the target needs to be deformed in a series of dedicated deformations, instead of one continuous process. In this feasibility study, the specimen was crimped at two positions,

at the beginning of the indentation and at the end of the specimen. Both positions are shown in **Figure 99**.

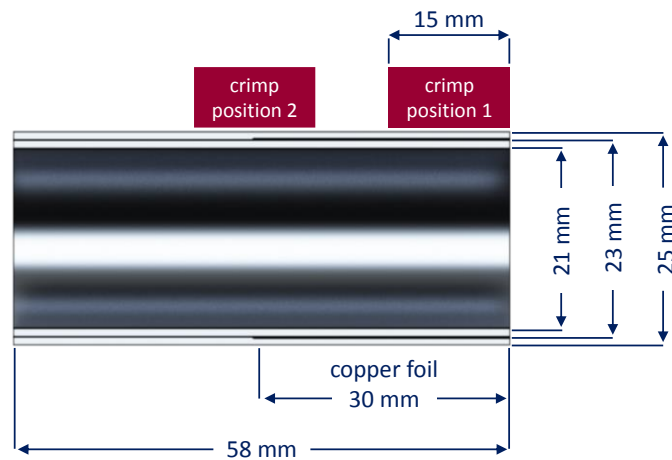


**Figure 99: Specimen used for the magnetic forming experiments.**  
The sample geometry was changed to fit the available electromagnetic forming. The figure shows the altered dimensions as well as the two crimp positions. The length of the crimp position is equal to the length of the field concentrator.

Due to the magnetic pressure, the outer aluminum cylinder is compressed on the inner cylinder. To prevent the inner cylinder of deformation and to align the specimen in the magnetic coil, a mandrel (**Figure 96, d**) is inserted. In this study, two type of mandrels were investigated.

In a first try a mandrel made of polyethylene was used. The mandrel consisted out of one cylindrical shaped piece and had an outer diameter of 20 mm. It showed that this mandrel could not be removed nondestructively from the specimen after magnetic forming even with low forming energies. Due to the deformation of the inner cylinder, the mandrel was clamped inside the specimen.

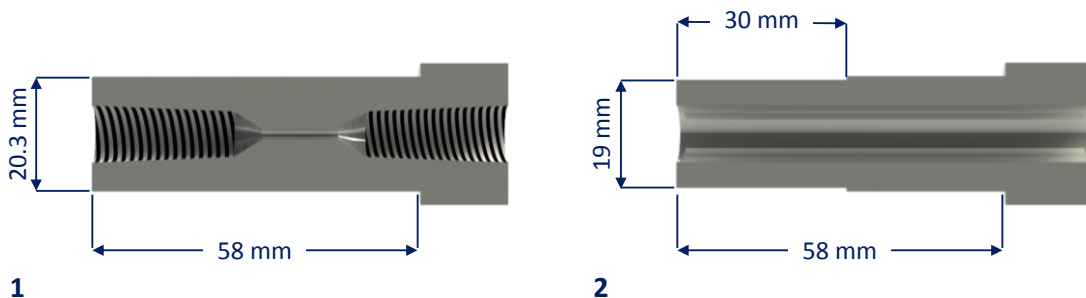


**Figure 100: Removable mandrel design.** Each of the two investigated mandrels consists of two half cylinders, which can easily be removed after forming. The figure shows a side view of one half cylinder of each design. Design 1 can be stretched after insertion by screwing in two locking screws in the conical threads. Design 2 features a smaller outer diameter, which allows a certain compression of the work piece.

Therefore, two new types of mandrels were constructed, which allowed a simple removal after forming. Variant 1 (**Figure 100**, image 1) consists of two half cylinders, which feature two opposing conical threads on their central axis. After insertion of both halves in the specimen,

the mandrel can be stretched by screwing in two locking screws. After the specimen is formed, the locking screws are removed and the mandrel can be extracted. This mandrel has an outer diameter of 20.3 mm. After stretching of the mandrel, this does not allow a compression of the inner cylinder during forming. In contrast, variant 2 (Figure 100, image 2) was designed to allow a certain compression. In the forming zone, this mandrel has an outer diameter of 19 mm, what allows a radial compression of up to 1 mm. Therefore, no locking screws were required to stretch or remove the mandrel.

To qualify the forming results, two cuts were made at the center of the crimp positions and radial samples were prepared according to chapter 4.3.1. Then the gaps between the aluminum cylinders and the copper layer were measured using an optical microscope and the image processing algorithm described in 5.2.2. Measurements were taken at a magnification of 100 at the angles 90°, 180° and 270°. The angle 0° is defined by the center between the two ends of the wrapped-up copper foil.

### 5.3.3 RESULTS

Figure 101 and Figure 102 show a typical microscopy of each forming energy and crimp position. Figure 101 presents the results obtained with mandrel 1 and Figure 102 the results of mandrel 2.  $d_{90^\circ}$ ,  $d_{180^\circ}$  and  $d_{270^\circ}$  give the sum of the inner and the outer gap thickness measured at the according angle.  $\bar{d}$  is the arithmetic mean of those three values.

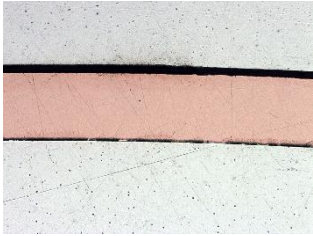
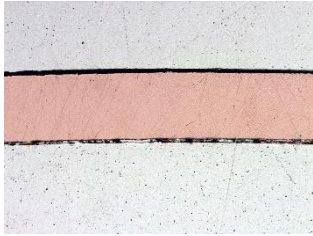
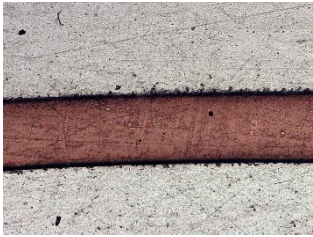
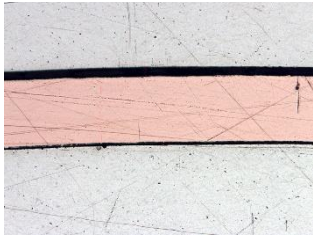
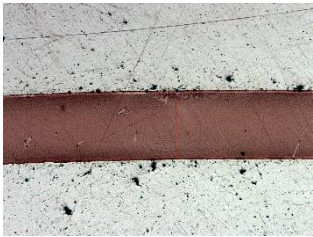
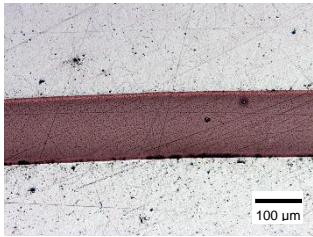


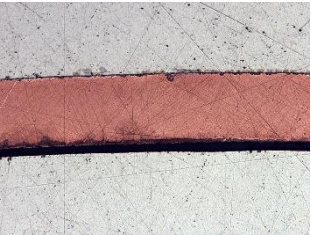
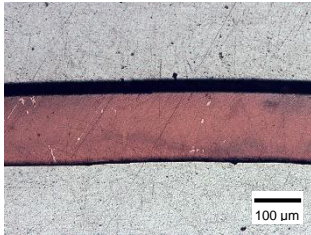
Energy	Crimp position 1		Crimp position 2	
	Typical microscopy	Results [ $\mu\text{m}$ ]	Typical microscopy	Results [ $\mu\text{m}$ ]
8.2 kJ		$d_{90^\circ} = 16.7$ $d_{180^\circ} = 15.4$ $d_{270^\circ} = 19.1$ $\bar{d} = 17.1$		$d_{90^\circ} = 17.6$ $d_{180^\circ} = 29.1$ $d_{270^\circ} = 24.6$ $\bar{d} = 23.8$
13.7 kJ		$d_{90^\circ} = 13.4$ $d_{180^\circ} = 11.1$ $d_{270^\circ} = 10.9$ $\bar{d} = 11.8$		$d_{90^\circ} = 25.4$ $d_{180^\circ} = 23.7$ $d_{270^\circ} = 29.5$ $\bar{d} = 26.2$
20.3 kJ		$d_{90^\circ} = 10.4$ $d_{180^\circ} = 0$ $d_{270^\circ} = 0$ $\bar{d} = 3.5$		$d_{90^\circ} = 0$ $d_{180^\circ} = 6.8$ $d_{270^\circ} = 0$ $\bar{d} = 2.3$

Figure 101: Results of magnetic forming using mandrel 1. The figure show a typical microscopic image and the measured gap thicknesses for each tested energy and crimp position.

When comparing the results of both mandrels, it can be seen that the measured thicknesses are in good accordance. Therefore, it was followed that the forming is fairly independent of the

mandrel type. However, a dependency on the crimp position was found. At crimp position 1, the average gap thickness shows a clear dependency on the forming energy. As to expect, the gap decreases with higher energy. This is in contrast to crimp position 2, where no such relation can be seen. In this case, the average gap thickness increases at an energy of 13.7 kJ compared to 8.2 kJ and 20.3 kJ. Though, a complete deformation could be achieved with a forming energy of 20.3 kJ for both crimp positions using mandrel 1. In this case the sample showed no gap at almost its entire circumference.

Energy	Crimp position 1		Crimp position 2	
	Typical microscopy	Results [ $\mu\text{m}$ ]	Typical microscopy	Results [ $\mu\text{m}$ ]
8.2 kJ		$d_{90^\circ} = 17.6$ $d_{180^\circ} = 14.5$ $d_{270^\circ} = 20.8$ $\bar{d} = 17.6$		$d_{90^\circ} = 13.1$ $d_{180^\circ} = 27.9$ $d_{270^\circ} = 18.7$ $\bar{d} = 19.9$
13.7 kJ		$d_{90^\circ} = 12.1$ $d_{180^\circ} = 15.0$ $d_{270^\circ} = 16.9$ $\bar{d} = 14.6$		$d_{90^\circ} = 36.4$ $d_{180^\circ} = 33.2$ $d_{270^\circ} = 32.2$ $\bar{d} = 33.9$

**Figure 102: Results of magnetic forming using mandrel 2.** The figure show a typical microscopic image and the measured gap thicknesses for each tested energy and crimp position.

However, the high forming energy leads to a very strong unintended deformation of the aluminum cylinders. With an energy of 20.3 kJ, the deformed specimen caused a damaging of the mandrel. This prevented a nondestructive separation of the specimen and the mandrel. In case of mandrel 2, already an energy of 13.7 kJ led to clear signs of unintended deformation. This can be seen by the step-shaped deformation of the inner cylinder shown in [Figure 103](#).

The conducted experiments showed that on the one hand, magnetic forming is able to establish a sufficient contact between the layers, however on the other hand, the deformation is difficult to control due to the high required forming energy. Therefore, and due to the fact that no significant advantage over the conventional method was found, it is concluded that magnetic forming is not advisable for the irradiation target manufacturing.

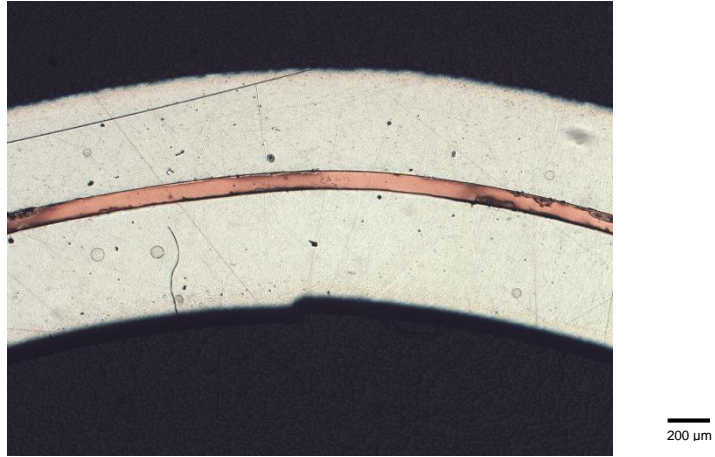


**Figure 103: Deformation of the inner cylinder when using mandrel 2.** The inner cylinder shows a step –shaped deformation. This unintended deformation is caused by a displacement of the two halves of the mandrel due to the high forming energy.





## 6 CONCLUSION AND OUTLOOK

Within this work, a complete PVD based manufacturing process of cylindrical LEU foil targets was demonstrated. **Figure 104** shows the developed process from a potentially oxidized uranium ingot to a completely assembled and welded irradiation target.

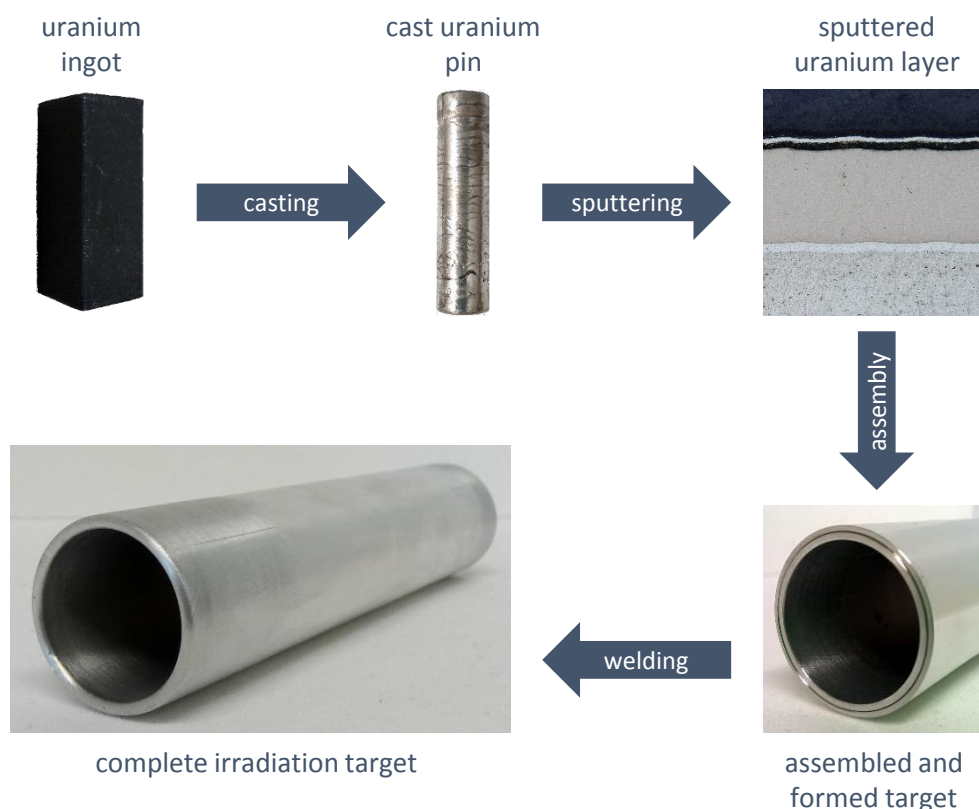


**Figure 104: The complete irradiation target manufacturing process.**

It was the aim of this study, to demonstrate the feasibility of PVD coating for the production of cylindrical LEU foil targets. Therefore, a demonstration PVD reactor was developed, which allowed to study the relevant sputter parameters. The apparatus was extensively characterized using copper as surrogate material. In this way, the process could be well understood and an algorithm was derived, which can be used to describe the layer growth in real time or to simulate different coating procedures. This algorithm uses a set of four material dependent constants to calculate the sputter rate and the emission profile of the sputter source. By combining these values with the position of the sputter source, the resulting layer thickness profile can be calculated. This algorithm was successfully validated by comparing calculated and measured thickness profiles. Using this knowledge, the sputter process was optimized to a homogenous layer thickness and a high material utilization of approximately 92% in case of uranium.

A major requirement for the feasibility of the presented manufacturing technique is the separability and the mechanical stability of the produced foils. As shown in chapter 4.5, the mechanical strength of the foils mainly depends on the coating temperature. By applying

sufficient values, mechanically stable copper and uranium foils were produced. These foils were self-supporting and showed no mechanical impairment due to oxidation.

It was also demonstrated that the adhesion of the uranium layer to the substrate can successfully be controlled by the usage of a suitable interlayer. Experiments were performed using aluminum and graphite. In both cases the produced foils were easily separable from the subjacent substrate. In this way, aluminum-uranium-aluminum multilayers were produced. These multilayers are in accordance to the ANL target design, which already proved to be successful in irradiation tests.

The developed coating process features three major advantages. The first advantage is its high degree of flexibility. Thickness, length and mass of the uranium foil and the interlayer material can easily be modified. This can be used to optimize the irradiation target and the overall cost efficiency. A second important advantage is the high material utilization. At the uranium pin casting an efficiency of 95% was achieved. Together with the maximum sputter efficiency of 92% for uranium, this results in an overall efficiency of 87%. These numbers do not consider any material recovery from the electron reflectors, which would lead to a further increase. A third advantage of the presented technique, is the high degree of automation. After loading the target and the substrate in the PVD reactor, the process is PLC controlled and fully autonomous.

In the second part of this thesis, the mechanical assembly of the coated targets was studied. Therefore, two different methods were investigated: hydraulic axial forming and electromagnetic forming. It showed that sufficient results could be achieved by both methods. However, hydraulic forming is by far more practical and less cost intensive. Therefore, hydraulic forming is the recommended forming technique for the target production.

In summary it can be concluded that the presented technique proved to be suitable for the irradiation target manufacturing. Therefore, further development will take place, which is oriented towards an industrial application. One aim of the future development is the increase of the material spectrum for the interlayer material. To deposit materials with a higher melting point, higher coating temperatures are necessary. Therefore, an additional substrate heating needs to be installed, which is independent of the coil's cooling system. To overcome the problem of sputtering ferromagnetic nickel, two possible solutions have to be investigated. One approach is the usage of a non-ferromagnetic nickel alloy, which allows a deposition in the current PVD apparatus. An alternative option is a target temperature control system, which keeps the target temperature above the material's Curie temperature.

Another important factor for an industry-scale production is the necessary time to produce one target. In the current set-up, the deposition of 20 g of uranium takes approximately 24 h. By installing an improved target cooling system and the usage of krypton instead of argon, this time can be reduced to approximately 8 h. Taking into consideration the high amount of automation and the possibility to easily parallelize the process, this value is suitable for an industrial application.

All of the discussed improvements can technically be realized. Therefore, the presented manufacturing process for monolithic LEU-targets is a promising alternative to conventional techniques.

# 7 APPENDIX

## A LIST OF FIGURES

<b>Figure 1: Detailed decay scheme of <math>^{99}\text{Mo}</math>.</b> [1].....	1
<b>Figure 2: Bone scintigraphy of the Articulatio talocruralis.</b> The images show a SPECT-CT recording of a left ankle. Hereby a conventional X-ray CT is superposed by a scintigraphy using $^{99\text{m}}\text{Tc}$ as a $\gamma$ -emitting radioisotope. The bright/red areas show an increased bone metabolism due to inflammation. [6].....	2
<b>Figure 3: Overview of <math>^{99}\text{Mo}</math> and <math>^{99\text{m}}\text{Tc}</math> production schemes.</b> [9].....	3
<b>Figure 4: Chain yield for the thermal neutron fission of <math>^{235}\text{U}</math>.</b> The red marking shows mass number 99 with a fission yield of 6.132%. [1] .....	4
<b>Figure 5: <math>\beta^-</math>-decays of mass number 99.</b> Due to their neutron excess the isotopes with a mass number of 99 and a proton number below 44 undergo a $\beta^-$ -decay with the indicated half-life times. [11].....	4
<b>Figure 6: <math>^{99\text{m}}\text{Tc}</math> supply chain.</b> [13].....	5
<b>Figure 7: Build-up of <math>^{99}\text{Mo}</math>.</b> During an irradiation time from 5 to 7 days $^{99}\text{Mo}$ is built-up to approximately 78% of the saturation value. Afterwards the target is mechanically and chemically processed to extract the $^{99}\text{Mo}$ from the irradiation targets. In this process around 10% of activity is lost. After a processing time of 24h, the $^{99}\text{Mo}$ is ready for shipping. The $^{99}\text{Mo}$ is sold on units of activity, usually calibrated to the activity 6 days after processing. This quantity is called 6-day curies. [12].....	5
<b>Figure 8: <math>^{99\text{m}}\text{Tc}</math> generator.</b> 1) Photo of a Ultra-TechneKow DTE generator from Mallinckrodt Pharmaceuticals [20]. 2) Working principle of a $^{99\text{m}}\text{Tc}$ generator: A saline solution is passed through an alumina column with adsorbed molybdenum. In this process the liquid gets enriched with pertechnetate. The enriched solution is then filtered to remove any particles from the liquid and guarantee a sterile product. [21].....	8
<b>Figure 9: Elution of a <math>^{99\text{m}}\text{Tc}</math>-generator.</b> The upper line shows the activity of $^{99}\text{Mo}$ , which is defined by its radioactive decay. The lower line represents the $^{99\text{m}}\text{Tc}$ activity in the generator. In this example the $^{99\text{m}}\text{Tc}$ -generator is eluted once every 24h. As one can see, the $^{99\text{m}}\text{Tc}$ activity restores after each elusion until it reaches the activity of its mother isotope $^{99}\text{Mo}$ . .....	8
<b>Figure 10: The cylindrical LEU foil target.</b> The target consists of two coaxial aluminum tubes. In an indentation on the inner tube is a sandwich of a uranium foil wrapped or coated in an interlayer material. To guarantee a good thermal contact between the aluminum and the uranium, the inner tube is widened after assembly. To ensure a safe encapsulation of the fission products, both tubes are welded together on both ends. All given dimensions in the drawings are in inches. The diameter marked by the asterisk * is the inner diameter before the widening of the inner tube. [29] .....	11
<b>Figure 11: Irradiation target manufacturing with a prepared uranium foil.</b> (1) The uranium foil is manufactured. (2) The interlayer is applied to the uranium foil. (3) The covered uranium foil is placed in an indentation on the inner aluminum tube. (4) The inner tube is inserted in the outer tube. (5) The inner aluminum tube is widened.....	12
<b>Figure 12: Irradiation target manufacturing by PVD coating.</b> (1) The first recoil barrier is applied to the outer tube. (2) The uranium foil is grown by PVD coating. (3) The second recoil barrier is applied. (4) The inner aluminum tube is inserted. (5) The inner aluminum tube is widened. ....	13

- Figure 13: Basic principle of dc sputtering.** a) Electrons in a low-pressure atmosphere are accelerated by an electric field. b) Having enough kinetic energy, these electrons can ionize the gas atoms (G). c) Positively ionized gas atoms ( $G^+$ ) are accelerated by the electric field towards the sputter target, where they can knock out surface atoms (T). d) These atoms condense on the substrate and form a layer. [39]..... 15
- Figure 14: Ionization cross section.** The ionization cross-section is a measure for the ionization probability and has a big influence on the degree of ionization of a plasma. For the noble gases this ionization cross-section has a maximum at around 100eV. At higher energies the ionization cross-section decreases and the electrons can pass through the gas easily. [45] ..... 17
- Figure 15: Dc glow discharge inside a vacuum tube and its electric potential.** The glow discharge can be separated into five optically visible main regions: a) the Aston dark space, b) the cathode glow, c) the cathode dark space, d) the negative glow, e) the Faraday dark space, f) the positive column, g) the anode dark space and h) the anode glow. Close to the cathode a deep potential drop occurs, which is caused by a high density of positive ions on the border between region c) and d). The electrons ejected from the cathode gain most of their energy in this region and cause an intensive ionization in region d). Its glowing is caused by recombinations of ions and electrons. The positive column f) is characterized by a high and constant density of electrons and ions. The potential in this region is nearly constant. Its glowing is caused by the excitation of the gas atoms. [47] ..... 18
- Figure 16: General energy dependency of the sputter yield.** [49] ..... 20
- Figure 17: Angle of impact dependency on the sputter yield for different target materials sputtered by 1.05keV Ar ions.** The sputter yield has a maximum at approximately  $70 - 80^\circ$ . This is caused by a growing energy deposition in the surface region at higher impact angles. However, above this maximum the reflection of the impinging particles is growing, which leads to a decrease of the sputter yield. [50] ..... 20
- Figure 18: Differential sputter yield.** The two figures show the influence of the incidence angle and the energy of the impinging particle on the differential sputter yield. The values show tungsten sputtered with 500eV (1) and 1500eV (2)  $Kr^+$  ions. The particles imping from the left side with the given angle in respect to surface normal. Especially at a low particle energy, the sputter distribution is strongly deformed in the forward direction. [53] ..... 22
- Figure 19: Pressure dependency on the sputtered atom flux.** The SEM images show sputter deposited copper on a surface with submicron contact holes. Case 1) is performed at a pressure of  $1 \cdot 10^{-5}$  Torr and case 2) is performed at  $1 \cdot 10^{-3}$  Torr. Due to lower scattering in case 1), the copper flux impinges mostly normal to the surface and, therefore, leads to a higher deposition in the contact hole. In contrast, the higher pressure in case 2 leads to a non-uniform flux and therefore to a higher shadowing effect. [54] ..... 23
- Figure 20: Mean free path  $\lambda$  of argon.**..... 23
- Figure 21: Structure zone diagram according to Thornton [56].** The structure zone diagram shows the different forms of layer growth depending on the inert gas pressure and the homologous temperature. The homologous temperature is the absolute substrate temperature relative to the melting temperature of the deposited material. In zone 1 the mobility of the adatoms is low. Therefore, their energy is too low to overcome the geometrical shadowing of surface structures. As a result, a layer with a strong columnar character, a low density and large voids between the columns is formed. Zone T is a transition zone between zone 1 and zone 2. It features a fibrous crystal structure and a higher density than zone 1. In zone 2 the adatoms diffusion on the surface is the dominating factor. In this zone the columnar boundaries are densified, however their basic morphology remains. Zone 3 is governed by bulk diffusion, which allows recrystallization, grain growth and densification. The recrystallization leads to random grain orientation and a reduction of the columnar orientation. [40] ..... 26
- Figure 22: Schematic of a dc sputter device.**..... 27
- Figure 23: Schematic of a dc magnetron sputter device.** ..... 28

**Figure 24: Electron drift and sputter erosion of a planar magnetron device.** 1) The magnetic field  $B$  and the electric field  $E$  force the electrons on spiral paths around the magnetic field lines (a). Additionally, the electrons experience a drift in the  $E \times B$  direction (b). This leads to the formation of a so-called racetrack, a closed path around the target surface with a very high electron density. Due to the high ionization rate of these electrons, a characteristic erosion profile along this racetrack is formed. A used copper target of a planar magnetron is shown in 2). [58] ..... 29

**Figure 25: Cylindrical magnetron configurations.** 1) A negatively charged target is placed coaxial to a grounded cylindrical substrate. A magnetic field is applied in the axial direction. The electric and the magnetic field lead to an electron movement around the target. In a simple magnetron configuration (1) an additionally movement of the electrons in axial direction leads to the loss of electrons on both ends. This can be hindered by electron reflecting surfaces (2). ..... 30

**Figure 26: Electron transport processes in a cylindrical magnetron device.** The section drawing of the  $B$ -plane in a cylindrical magnetron device shows the paths of different representing electrons in the sputter process. Secondary electrons ejected from the target surface describe a cycloidal-like path with a radius, which is dependent on the magnetic field. When these electrons lose momentum on their trajectory they get trapped on a circular orbit around the target. Low energy electrons, which are generated in ionization processes in the outer region, also follow a circular orbit around the target. .... 31

**Figure 27: Fixed target set-up.** The FTS consists of a not movable sputter target, which is located in the center of the substrate cylinder. The substrate cylinder is placed in a substrate carrier tube, which is surrounded by a magnetic coil. The coil is wound of an isolated copper pipe and is cooled by water flowing through the pipe. [39] ..... 33

**Figure 28: Schematic of the FTS.** The FTS is placed in a vacuum chamber. The chamber is equipped with a pumping system and an argon gas supply. The gas pressure is controlled by regulating the gas inflow by a mass flow controller while pumping at a constant rate. The gas pressure is measured by two sensors: a cold cathode/pirani sensor for a rough measurement in a wide pressure range and a capacitive sensor for a more precise measurement in the range of the sputter process. The magnetic field is generated by a coil powered by a high current power supply. The generated heat is removed by cooling water flowing through the copper coil pipe. The sputter target is connected to a high voltage supply in order to ignite the plasma discharge. To guarantee a safe operation the temperature of the sputter target and the magnetic coil is monitored by two Pt-100 sensors. [39]..... 34

**Figure 29: FTS sputter target fixations.** In order to arrange the sputter target in the center of the substrate tube and to define the area to be coated, different target fixations were investigated. The figure shows three examples made of boron nitride (1), PTFE (2) and an assembly of glass and iron (3). The holes in the target fixation allow the sputter gas to reach the plasma volume. [39]..... 35

**Figure 30: Overview of the MTS.** 1) Front view of the glove box housing the MTS apparatus. 2) The MTS consists of a magnetic coil, a linear shift mechanism, a support flange with the necessary vacuum feedthroughs and a pressure sensor. A mount on the left side of the glove box is housing all the power supplies and the mass flow controller. .... 36

**Figure 31: Cut view of the MTS.** In the center of the magnetic coil, the substrate capsule rests on a fixation. The sputter source is able to freely move in axial direction in a range of  $\pm 46$  mm from the center of the substrate. An adjustable joint allows to compensate manufacturing inaccuracies..... 37

**Figure 32: Substrate capsule of the MTS.** The substrate (a) is housed in a copper capsule (c). This allows an easy loading and unloading of the substrate and provides a good thermal contact to the magnetic coil surrounding the vacuum vessel. Two deposition shields (b) avoid the coating of the end parts of the substrate. .... 39

**Figure 33: Sputter source of the MTS.** The sputter source consists of a cylindrical sputter target (a), which is mounted in a ceramic socket in a copper heat sink. The heat sink is cooled by a cooling water flow provided through an inflow (e) and an outflow (f). The temperature of the heat sink is monitored by two type K thermocouples mounted inside the copper body (g). The target is connected to a high voltage power supply by a tungsten pin (d). During the evaporation the plasma is encapsulated by two ceramic electron reflecting surfaces (b) and (c). The sputter gas is provided to the process chamber via four holes in the support shaft (h). ..... 40

**Figure 34: Designs of the electron reflecting surfaces.** In a first attempt (1), copper disks were installed. The purpose of these disk was to prevent end losses of the plasma by electrostatically trapping the electrons in the plasma volume. However, it showed that even without the copper rings a similar effect was reached by the build-up of negative charges on the insulating ceramic surfaces. Since it was difficult to ensure a proper electrical contact between the target and the ring, this element was dropped in the second iteration (2). Also a small increment at the end of the ceramic parts was introduced. In this way, arcing could be avoided, which occurred after some hours of sputtering when using design 1. In a third iteration step (3), this increment was made higher and a second one was introduced to enforce the geometric shielding effect. In addition, the lower electron reflecting surface now also covers the ceramic socket. In this way, the socket does not need to be cleaned after every coating run. The upper cap, now features a small pinhole to avoid virtual leaks. .... 41

**Figure 35: Vacuum and gas supply system of the MTS.** The operating pressure in the MTS reactor is established in form of a dynamic equilibrium. The system features a mass flow controller (a), magnetic operated valves (b), a gate valve (c), an overpressure valve (d), a manually operated valve (e), ventilation valves (f) and three pressure sensors (g). ..... 42

**Figure 36: Inflow-pressure-diagram of the MTS.** The diagrams show the measured dependency of the system pressures on the gas inflow. This measurement was performed using argon having the linear shift mechanism in the lowest position. .... 44

**Figure 37: Magnetic field of the MTS.** The diagram shows a comparison of the measured (dots) and calculated (line) magnetic field in axial direction along the central axis of the coil. The pink area from -46 mm to 46 mm indicates the actual coating zone. .... 46

**Figure 38: Cooling system of the MTS.** The cooling water flow line of the MTS is split in three separated cooling lines: one to supply the sputter source and two to supply the magnetic coil. The outer layers of the coil (f) are cooled directly with a flow direction from the outer layer to the inner layer. In this way, a temperature gradient from the outer layer to the inner layer builds up, which allows a better heating of the substrate in the center of the magnetic coil. The substrate temperature is regulated by the cooling water flow through the two inner windings (d) and (e), which is controlled by a proportional valve (a). The cooling water system is monitored by thermocouples directly measuring the water temperature (b), a flow meter (c) and temperature sensors (g) between the layers of the magnetic coil. .... 47

**Figure 39: Inner layer of the magnetic coil.** The inner layer of the magnetic coil consists of two copper pipes wound in form of a double helix. The cooling water flow through these pipes is in opposite direction in order to receive an even substrate temperature across the substrate length. .... 48

**Figure 40: Control interface of the MTS.** The control interface consists of different controlling and monitoring panels for logging (a), substrate temperature (b), sputter power supply (c), linear shift mechanism (d), gas supply (e), cooling water temperature (f), end conditions for the sputter process (g), magnetic field (h), calculated real-time layer thickness profile (i), plasma monitor (j), calculated real-time emission profile (k), plot (l) and material selection (m). ..... 49

**Figure 41: Glove box system.** The glove box system, which houses the MTS reactor (a), consists of a sputter glove box (b) and a chemistry glove box (c). Both glove boxes are connected by a T-shaped antechamber (d) and have separated gas purification systems (e) and (f). From the chemistry cabinet (g) chemicals can be taped inside the chemistry glove box.

The turbomolecular pump (h) is mounted on the back of the sputter glove box and directly connected to the vacuum chamber of the experimental planar reactor. For easy maintenance, the backing pump (i) is installed on a rolling base next to the sputter glove box..... 50

**Figure 42: Workspace in the MTS glove box.** The MTS (a) can be accessed from inside the glove box by the 6-way manifold (b). The manifold is equipped with a ventilation valve (e) and a hand valve (d). The hand valve is used to separate the MTS from the vacuum system (pumps etc.), which is also used by another experimental PVD reactor (f). To load and unload the sputter target and the substrate, the manifold has a removable vacuum window on its top. During the coating process this window is used to observe the plasma with a camera (c). The target assembly and the substrate assembly can be put together on the free workspace (g). The components can be cleaned in an inert gas atmosphere in the chemistry glove box, which is connected through a T-shaped antechamber (h). ..... 51

**Figure 43: Pin casting.** Bars of depleted uranium are cut into three pieces. These pieces are cleaned by nitric acid and then cast to uranium pins. These pins are then correctly shaped by removing the upper and lower end..... 57

**Figure 44: SRIM simulations.** The plots show the distribution and the energy loss of niobium and iodine ions entering various interlayer materials with an energy of 80 MeV. All simulations were performed with the software SRIM using a total number of 5000 ions for each simulation. .... 59

**Figure 45: Magnetic field dependency of the coil's electrical current and power.** The values were measured in the center position of the coil. The red area indicates power values of more than 1200 W. Due to safety considerations, the power supply output was limited to this value and in most experiments the normal operation was set to 85 mT, resulting in a power of approximately 750 W (red marker)..... 61

**Figure 46: Magnetic field dependency of the plasma parameters.** The values were measured with a copper target at a pressure of 0.035 mbar in the center position of the coil. The sputter power supply was limited to a maximum power output of 100 W and a maximum voltage of 800 V. The grey area indicates the field values, where no plasma could be ignited. In this region the power supply showed a certain offset in the electrical current. The dark purple area shows the magnetic field values where a plasma was ignited, but rather unstable. This instability could be seen by a fluctuating sputter current and voltage. The fluctuation in the current is indicated by error bars. The light purple area shows the region, where a stable plasma was ignited. The red marker indicates the operation point for most experiments at 85 mT. .. 62

**Figure 47: Magnetic field compensation.** At each position of the sputter source, the electric current of the coil is adjusted to reach a constant magnetic field of 100 mT. The plot shows the measured electric current (blue dots), the fitted function (line) and the resulting field (orange dots) when using the fitted function..... 63

**Figure 48: Pressure dependency of the plasma parameters.** The values were measured with a copper target at a magnetic field of 85 mT in the center position of the coil. The power supply was limited to a maximum power output of 100 W and a maximum voltage of 800 V. The dark purple area shows the magnetic field values where a plasma was ignited but rather unstable. This instability could be seen by a fluctuating sputter current and voltage. The fluctuation in the current is indicated by error bars. The light purple and green area show the region, where a stable plasma was ignited. A higher pressure causes a higher ionization of copper in the plasma, what can be seen by a green color in the plasma. The red marker at 85 mT indicates the operation point for most experiments. .... 64

**Figure 49: Gas pressure in the coating zone.** The argon pressure in the coating zone was measured at different positions of the sputter source. The gas inlet was 15.4 sccm. The plot shows the readings of a pressure sensor mounted directly on the heat sink in the coating zone and the CTR 100 bottom sensor close to the gas inlet. .... 65

**Figure 50: Pressure compensation.** At each position of the sputtering source, the gas inflow is adjusted to reach a pressure of 0.03 mbar in the sputter zone. The plot shows the measured

gas inflow (blue dots), the fitted function (line) and the resulting pressure (orange dots) when using the fitted function. ....	66
<b>Figure 51: Dependency of the target mass loss on the sputter parameters.</b> 15 different sputter runs using argon and copper are plotted with applied electric energy versus mass loss of the sputter target. The plot shows the measured (dots) and calculated values according to equation (20) (line) and (21) (crosses). ....	68
<b>Figure 52: Sample preparation.</b> .....	69
<b>Figure 53: Coordinate system.</b> The coordinate system used for the simulation algorithm uses cylindrical coordinates. The z-axis is equal to the central axis of the substrate cylinder and centered at the substrate's center position. The coating zone goes from -46 mm to +46 mm. $z_S$ marks the central position of the sputter source. The sputter source can freely move from -48 mm to +48 mm. ....	70
<b>Figure 54: Emission characteristic of copper under standard operation conditions.</b> The emission characteristic of the sputter source was determined by measuring the thickness profile of a deposited layer using microscopy. The plot shows the measured values (dots) and the fitted function (line). ....	72
<b>Figure 55: Mass on substrate.</b> The plot shows a comparison of the measured mass on substrate (dots) against the values calculated by the simulation algorithm (line). ....	73
<b>Figure 56: Thickness profiles of sputtered copper layers.</b> Experiments 1 and 2 were performed with a sputter power of 100 W, a magnetic field of 100 mT and a pressure of 0.035 mbar. In experiment 3 the sputter power was changed to 150 W and the magnetic field to 85 mT. ....	74
<b>Figure 57: Efficiency of the sputter process.</b> With increasing maximum oscillation of the sputter source, the mass efficiency of the coating process decreases due to the increased coating of the coating shields. The maximum efficiency of 94.7% is defined by the coating of the electron reflecting surfaces. The displayed maximum layer thickness is calculated for a total of 20 g uranium in the coating zone. With increasing range of movement the sputtered material is spread over a larger area and, therefore, the maximum layer thickness decreases. ....	75
<b>Figure 58: Typical sputter behavior of copper.</b> The copper target was sputtered for 10.5 h at a magnetic field of 85 mT. The eroded mass was 7682 g. ....	76
<b>Figure 59: Copper target burn-up.</b> Three different copper targets with different burn-ups are shown: 1) $0.6 \text{ cm}^3 \approx 5.4 \text{ g}$ , 2) $1.2 \text{ cm}^3 \approx 10.7 \text{ g}$ and 3) $1.5 \text{ cm}^3 \approx 13.4 \text{ g}$ . ....	77
<b>Figure 60: Radial layer profile of deposited copper.</b> .....	77
<b>Figure 61: Longitudinal layer profile of deposited copper.</b> .....	78
<b>Figure 62: Longitudinal close-up of a deposited copper layer.</b> .....	78
<b>Figure 63: Aluminum target burn-up.</b> .....	79
<b>Figure 64: Emission characteristic of aluminum under standard operation conditions.</b> The emission characteristic of the sputter source was determined by measuring the thickness profile of a deposited layer using microscopy. The plot shows the measured values (dots) and the fitted function (line). ....	79
<b>Figure 65: Deposited aluminum layers.</b> The presented layers were produced using a fixed (image 1) and a moving (image 2) sputter source. A clear layer structure, which is caused by temperature differences, can be seen in the second case. ....	81
<b>Figure 66: Ruptured aluminum layer.</b> A rupture of the aluminum coating occurred due to the contraction of the mounting resin. ....	81
<b>Figure 67: Axial component of the magnetic field <math>B</math>.</b> Image 1 shows the axial component of the magnetic field when using a non-ferromagnetic target. In case 2, a ferromagnetic nickel	



target was assumed. The values are given in mT. The simulations were performed using the finite element analysis software COMSOL Multiphysics [73].	82
<b>Figure 68: Nickel target burn-up.</b> The burn-up profile of a cast nickel target shows a strong erosion on the upper half and almost no erosion in the lower part. The indentation in the lower part is a defect, which occurred due to a too rapid cooling during the casting process.	82
<b>Figure 69: Copper on a zirconium layer.</b> View inside a substrate cylinder after applying a copper layer on a previously sputtered zirconium layer.	84
<b>Figure 70: Flaking of zirconium layers on air.</b> View inside a substrate cylinder coated with zirconium approximately 20 minutes after exposure to air (image 1). The coating comes off in form of small flakes (image 2) due to the oxidation of the layer.	84
<b>Figure 71: Uranium target burn-up.</b>	85
<b>Figure 72: Emission characteristic of uranium under standard operation conditions.</b> The emission characteristic of the sputter source was determined by measuring the thickness profile of a deposited layer using microscopy. The plot shows the measured values (dots) and the fitted function (line).	86
<b>Figure 73: Thickness profile of a sputtered uranium layer.</b> The experiment was performed with a sputter power of 90 W, a magnetic field of 85 mT and a pressure of 0.035 mbar. The movement speed of the sputtering source was 0.05 mm/s.	87
<b>Figure 74: Deposited uranium layer.</b> The presented layer was produced using a substrate temperature of 75°C and a sputter power of 80 W.	87
<b>Figure 75: Deposited uranium layer.</b> The presented layer was produced using a substrate temperature of 90°C and a sputter power of 90 W.	88
<b>Figure 76: Al-U-Al multilayer system.</b> The presented uranium layer was produced using a substrate temperature of 90°C and a sputter power of 90 W.	88
<b>Figure 77: Copper deposited in the low energy mode.</b> The deposited layer was very brittle and had a bad adhesion to the aluminum substrate.	91
<b>Figure 78: Copper deposited in the high energy mode.</b> When using the high energy mode, the deposited layers showed no signs of debonding or brittleness. Their adhesion to the subjacent was strong.	91
<b>Figure 79: Copper deposited in two stages.</b> Using a combination of low and high energy mode resulted in a removable copper foil. However, the foil was brittle and some copper remained on the substrate.	92
<b>Figure 80: Copper deposited with a graphite interlayer.</b> The graphite interlayer successfully prevented the applied copper coating from bonding to the subjacent aluminum substrate.	92
<b>Figure 81: Al-Cu-Al multilayer system.</b> When using Aluminum as interlayer material, the Al-Cu-Al sandwich can easily be removed from the Al substrate. The outer Al interlayer showed no adhesion to the copper foil; whereas the inner aluminum was loosely bond to the copper layer.	93
<b>Figure 82: Al-U multilayer system.</b> When using an aluminum interlayer between the substrate and the uranium layer, a bonding of the foil to the substrate can be prevented.	94
<b>Figure 83: Uranium deposited with a graphite interlayer.</b> The graphite interlayer successfully prevented the applied uranium coating from bonding to the subjacent aluminum substrate.	94
<b>Figure 84: Al-U-Al multilayer system.</b> Using aluminum as interlayer material and a high deposition temperature, easily separable and self-supporting foils can be produced. The foils are mechanically stable and do not show crumbling due to oxidation.	95
<b>Figure 85: Engineering stress-strain-curve for AL6061-T6 sheets.</b> The sheets were tested at room temperature and in longitudinal direction. [74]	97

- Figure 86: Geometry used for the deformation model.** The figure shows a section of aluminum cylinder, which is supposed to be widened. The section is geometrically defined by the outer Diameter  $D_a$ , the inner diameter  $D_i$  and a characteristic diameter  $D_m$ . The length of the section is given by  $dz$ . Both stress  $S$  and strain  $e$  act along the circumference of the cylinder. .... 98
- Figure 87: Overview of the axial hydraulic forming device and its hydraulic system.** The forming device consists of the hydraulic cylinder (a), a steel capsule to fix the target (b), an end stop (c), a hydraulic pump (d), a pressure tank (e), a throttle valve (f), a directional valve (g) and a reservoir (h). .... 100
- Figure 88: Detailed view of the axial hydraulic forming device.** The figure shows the piston rod (a), the forming plug (b), the target cylinder (c), the surrounding steel capsule with an PTFE inlay (d) and the end stop with variable radius (e). .... 101
- Figure 89: Plug geometries.** Image 1 shows the conical forming plug. Its forming surface has an inclination of  $5^\circ$ . The edges are rounded with a radius of 2 mm to allow a smooth forming procedure. In image 2 the spherical forming plug is displayed. The used spherical plugs had a G28 quality grading. .... 102
- Figure 90: Image processing.** The image processing algorithm detects gaps between the layers by analyzing the RGB color code of each pixel. Image 1 one shows a typical microscopic picture of a deformed target cylinder. In image 2, the gap found by the algorithm is marked in green. .... 103
- Figure 91: Results of hydraulic forming using plugs 1-5.** .... 104
- Figure 92: Results of hydraulic forming using plugs 1-5.** .... 105
- Figure 93: Result of hydraulic forming using the optimized forming procedure.** ..... 106
- Figure 94: Result of hydraulic forming using the optimized forming procedure.** ..... 106
- Figure 95: Assembled target with a layer thickness profile.** The images show the layer in the center of the target (1) and at the beginning of the indentation (2). .... 107
- Figure 96: Overview of the magnetic forming device and its circuitry.** The magnetic forming set-up consists of the work piece (a), the magnetic coil (b), the field concentrator (c), a mandrel (d), a capacitor bank (e) and an electric s (f). .... 107
- Figure 97: Working principle of a magnetic field concentrator.** The image shows the electric current flowing through the magnetic coil (white) and the induced current in the field concentrator (yellow). Due to the skin effect, the induced current appears on the surface of the field concentrator, which leads to a concentration of the current and, thus, the magnetic field in close proximity to the work piece. .... 108
- Figure 98: Typical electric current and magnetic pressure behavior.** The electric system can be approximated by a dampened oscillating circuit. Its time behavior is given by formula (39). The magnetic pressure can be approximated by formula (41). .... 109
- Figure 99: Specimen used for the magnetic forming experiments.** The sample geometry was changed to fit the available electromagnetic forming. The figure shows the altered dimensions as well as the two crimp positions. The length of the crimp position is equal to the length of the field concentrator. .... 110
- Figure 100: Removable mandrel design.** Each of the two investigated mandrels consists of two half cylinders, which can easily be removed after forming. The figure shows a side view of one half cylinder of each design. Design 1 can be stretched after insertion by screwing in two locking screws in the conical threads. Design 2 features a smaller outer diameter, which allows a certain compression of the work piece. .... 110
- Figure 101: Results of magnetic forming using mandrel 1.** The figure show a typical microscopic image and the measured gap thicknesses for each tested energy and crimp position. .... 111

**Figure 102: Results of magnetic forming using mandrel 2.** The figure show a typical microscopic image and the measured gap thicknesses for each tested energy and crimp position. .... 112

**Figure 103: Deformation of the inner cylinder when using mandrel 2.** The inner cylinder shows a step –shaped deformation. This unintended deformation is caused by a displacement of the two halves of the mandrel due to the high forming energy. .... 113

**Figure 104: The complete irradiation target manufacturing process.**..... 115



## B LIST OF TABLES

<b>Table 1: Major <sup>99</sup>Mo producers.</b> [13, 16] .....	6
<b>Table 2: Current suppliers of <sup>99</sup>Mo.</b> The potential annual production is the maximum weekly production times the operation weeks. This value does not represent the actual production of the reactor. [23, 24].....	9
<b>Table 3: Ionization energies of the non-radioactive noble gases.</b> The ionization energies of the different ionization states are given in eV. [43] .....	16
<b>Table 4: Energy threshold <math>E_s</math>.</b> The necessary kinetic energy of argon and krypton as sputter gases for sputtering several materials is given in eV. [48] .....	19
<b>Table 5: Examples of sputter yields.</b> The given numbers show calculated sputter yield at $\vartheta=0^\circ$ and $E_i=500$ eV. These sputter yields only give a rough idea about the achievable deposition rate, since the deposition rate strongly depends on the sputter device. [51].....	21
<b>Table 6: Adapted substrate dimensions.</b> .....	38
<b>Table 7: Properties of AlN and BN.</b> If applicable, all values are at 20°C. [60, 61] .....	41
<b>Table 8: Important material properties of copper, gold and uranium.</b> If applicable, data are valid for a temperature of 20°C [64]. .....	56
<b>Table 9: Cast uranium pins.</b> The densities were determined using the Archimedes' principle. ....	58
<b>Table 10: Fitting parameters for the magnetic field compensation.</b> .....	63
<b>Table 11: Influence of the gas pressure on the deposition rate.</b> The experiments were performed with a magnetic field of 85 mT. ....	65
<b>Table 12: Fitting parameters for the pressure compensation.</b> The position $z$ is given in mm, the inflow in sccm and $p$ in mbar. The parameters $a_{ij}$ have correspondent units. ....	66
<b>Table 13: Fitting parameters for the sputter rate of copper with argon ions.</b> .....	68
<b>Table 14: Fitting parameters for the emission characteristic of copper.</b> .....	72
<b>Table 15: Fitting parameters for the emission characteristic of aluminum.</b> .....	80
<b>Table 16: Fitting parameters for the sputter rate of aluminum with argon ions.</b> .....	80
<b>Table 17: Fitting parameters for the sputter rate of zirconium with argon ions.</b> .....	83
<b>Table 18: Fitting parameters for the sputter rate of uranium with argon ions.</b> .....	85
<b>Table 19: Fitting parameters for the emission characteristic of uranium.</b> .....	86
<b>Table 20: Adhesion experiments with Cu.</b> .....	90
<b>Table 21: Adhesion experiments with U.</b> .....	93
<b>Table 22: Dimensions of the inner and outer cylinder at various deformations.</b> To calculate the maximum elastic deformation, the minimum plastic deformation and the minimum total deformation equations (34)-(36) are applied. It was assumed that the cylinders do not undergo any change in length during the deformation process. ....	99
<b>Table 23: Deformation results using plugs 1-5.</b> .....	103



## C BIBLIOGRAPHY

- [1] Nucleonica GmbH: Mo 99 Decay Scheme, 2012.  
<http://www.nucleonica.net/wiki/index.php?title=File%3AMo99DS.png>
- [2] Zolle, I.: Technetium-99m Radiopharmaceuticals. Preparation and Quality Control in Nuclear Medicine. Berlin: Springer 2006
- [3] Fanti, S., Farsad, M., Mansi, L.: Atlas of SPECT-CT. Berlin, Heidelberg: Springer 2011
- [4] Martin Wiewiorski: Osteochondrale Läsionen am Talus im Sport. Sportmedizin und Sporttraumatologie. Basel 2011
- [5] Ziessman, H. A., O'Malley, J. P., Thrall, J. H., Fahey, F. H.: Nuclear medicine. The requisites. Philadelphia: Elsevier Saunders 2013
- [6] Klinikum rechts der Isar, MRI, TUM: SPECT-CT scintigraphy. 2014
- [7] John J. Szymanski, Parrish Staples: Ensuring a Reliable Supply of Medical Radioisotopes. 2012. <http://www.whitehouse.gov/blog/2012/03/27/ensuring-reliable-supply-medical-radioisotopes>
- [8] International Atomic Energy Agency: Feasibility of producing molybdenum-99 on a small scale using fission of low enriched uranium or neutron activation of natural molybdenum. Technical reports series, no. 478. Vienna: International Atomic Energy Agency 2015
- [9] Bradley, E.: Non-HEU production technologies for molybdenum-99 and technetium-99m. IAEA nuclear energy series, no. NF-T-5.4. Vienna: International Atomic Energy Agency
- [10] International Atomic Energy Agency: Nuclear Data Services, Vienna 2015. <https://www-nds.iaea.org/>
- [11] Magill, J.: Karlsruher Nuklidkarte. Eggenstein-Leopoldshafen: Haberbeck; Nucleonica GmbH 2012
- [12] Committee on Medical Isotope Production Without Highly Enriched Uranium, National Research Council: Medical isotope production without highly enriched uranium. Washington, D.C.: National Academies Press 2009
- [13] Organisation for Economic Co-operation and Development: The Supply of Medical Radioisotopes. The Path to Reliability. Nuclear Development. Paris: OECD Publishing 2011
- [14] A. Röhrmoser: Feasibility study for a <sup>99</sup>Mo production facility at the FRM II research reactor. München: Technische Universität München 2009
- [15] Glaser, A.: On the Proliferation Potential of Uranium Fuel for Research Reactors at Various Enrichment Levels. Science & Global Security 14 (2006) 1, S. 1–24
- [16] International Atomic Energy Agency: Production and Supply of Molybdenum-99. Vienna: International Atomic Energy Agency 2012
- [17] C. J. Fallais: Production of Radioisotopes with BR2 Facilities. Vienna: International Atomic Energy Agency 1978
- [18] Salacz, J.: Reprocessing of irradiated <sup>235</sup>U for the production of <sup>99</sup>Mo, <sup>131</sup>I and <sup>133</sup>Xe radioisotopes. Brussels: Institut National des Radioelements 1989
- [19] McDonald, M. J., Carson, S. D., Naranjo, G. E., Wemple, J. A.: Challenges of Extracting and Purifying Fission-Produced Molybdenum-99. Ind. Eng. Chem. Res. 39 (2000) 9, S. 3146–3150
- [20] Mallinckrodt Pharmaceuticals: ULTRA-TECHNEKOW™ DTE GENERATOR, 2014.  
[http://www.mallinckrodt.com/Nuclear\\_Imaging/Ultra-Technekow\\_DTE\\_Generator.aspx](http://www.mallinckrodt.com/Nuclear_Imaging/Ultra-Technekow_DTE_Generator.aspx)
- [21] International Atomic Energy Agency: Design principles of the <sup>99</sup>Mo → <sup>99m</sup>Tc radionuclide generator, 2013.

[http://nucleus.iaea.org/HHW/Radiopharmacy/VirRad/Eluting\\_the\\_Generator/Generator\\_Module/Design\\_principles/index.html](http://nucleus.iaea.org/HHW/Radiopharmacy/VirRad/Eluting_the_Generator/Generator_Module/Design_principles/index.html)

- [22] Organisation for Economic Co-operation and Development: The Supply of Medical Radioisotopes. Medical Isotope Supply in the Future: Production Capacity and Demand Forecast for the  $^{99}\text{Mo}/^{99\text{m}}\text{Tc}$  Market, 2015-2020. Nuclear Development. Paris: OECD Publishing 2014
- [23] Organisation for Economic Co-operation and Development: The Supply of Medical Radioisotopes. Market impacts of converting to low-enriched uranium targets for medical isotope production. Nuclear Development. Paris: OECD Publishing 2012
- [24] International Atomic Energy Agency: Research reactor database, 2015.  
<http://nucleus.iaea.org/RRDB/RR/ReactorSearch.aspx>
- [25] Organisation for Economic Co-operation and Development: The Supply of Medical Radioisotopes. Progress and Future Challenges in Implementing the HLG-MR Policy Principles: Final Report of the Second Mandate of the HLG-MR (2011-2013). Nuclear Development. Paris: OECD Publishing 2013
- [26] C. Conner, E. F. Lewandowski: Development of annular targets for  $^{99}\text{Mo}$  production. RERTR 1999. 1999
- [27] John Creasy: Progress of the High Density LEU Mo-99 Target Project. 2014 Mo-99 Topical Meeting. Washington, D.C. 2014
- [28] George Vandegrift: HEU vs. LEU Targets for  $^{99}\text{Mo}$  Production - Facts and Myths. RERTR 2005. 2005
- [29] Annemarie Hoyer: Target design MURR. 28.11.12
- [30] M. Alex Brown: Development of frontend processing to allow use of high-density LEU foil targets in current Mo-99 production facilities. Mo-99 Topical Meeting. Washington, D.C. 2014
- [31] Lloyd Jollay: Equivalent Fission Mo-99 Target without Highly Enriched Uranium. Mo-99 Topical Meeting, 4-7 December, 2011. Santa Fe, NM 2011
- [32] Chang-Kyu Kim: KAERI Recent Activities on Research Reactor Fuel. 2010
- [33] Behrisch, R., Eckstein, W.: Sputtering by particle bombardment. Experiments and computer calculations from threshold to MeV energies. Topics in applied physics, v. 110. Berlin, New York: Springer 2007
- [34] Mattox, D. M.: Deposition Processes. In: The Foundations of Vacuum Coating Technology. Springer Berlin Heidelberg 2003, S. 11-33
- [35] J. Plücker: Observations on the electrical discharge through rarefied gases. 1858
- [36] A. W. Wright: On the production of transparent films by the electrical discharge in exhausted tubes. 1877
- [37] Kelly, P. J., Arnell, R. D.: Magnetron sputtering: a review of recent developments and applications. Vacuum 56 (2000) 3, S. 159–172
- [38] Donald M. Mattox (Hrsg.): Handbook of Physical Vapor Deposition (PVD) Processing. Elsevier 2010
- [39] Bruno Baumeister: Construction and commissioning of a sputtering device for the production of cylindrical targets for  $^{99}\text{Mo}$  production. Master Thesis. Technische Universität München 2013
- [40] Thornton, J. A.: High Rate Thick Film Growth. Annual Review of Materials Science 7 (1977) 1, S. 239–260
- [41] Goldston, R. J., Rutherford, P. H.: Introduction to plasma physics. Bristol [u.a.]: Inst. of Physics Publ 1995



- [42] Thompson, W. B.: An introduction to plasma physics
- [43] National Institute of Standards and Technology: NIST Atomic Spectra Database, 2014. <http://www.nist.gov/pml/data/asd.cfm>
- [44] Kanegsberg, B., Kanegsberg, E.: Handbook for critical cleaning. Boca Raton: CRC Press 2011
- [45] Schram, B. L., Moustafa, H. R., Schutten, J., Heer, F. J. de: Ionization cross sections for electrons (100–600 eV) in noble and diatomic gases. *Physica* 32 (1966) 4, S. 734–740
- [46] Fridman, A. A., Kennedy, L. A.: Plasma physics and engineering. New York: Taylor & Francis 2004
- [47] Willett, C. S., Haar, D. t.: Introduction to gas lasers: population inversion mechanisms. With emphasis on selective excitation processes. International series of monographs in natural philosophy, v. 67. Oxford, New York: Pergamon Press 1974
- [48] Döbele, H. F.: Vakuumbeschichtung. Düsseldorf: VDI-Verl. 1995
- [49] Eckstein, W., Garcíá-Rosales, C., Roth, J., László, J.: Threshold energy for sputtering and its dependence on angle of incidence. *Nuclear Instruments and Methods in Physics Research Section B: Beam Interactions with Materials and Atoms* 83 (1993) 1-2, S. 95–109
- [50] Kienel, G., Frey, H. (Hrsg.): Vakuumbeschichtung. Düsseldorf: VDI 1995
- [51] Michael Schmid: A Simple Sputter Yield Calculator. Institut für Angewandte Physik, Technische Universität Wien 2009
- [52] Behringer, U.: Vakuumbeschichtung. Düsseldorf: VDI-Verl. 1995
- [53] Kirk Zoerb: Differential Sputtering Yields of Refractory Metals by Ion Bombardment At Normal and Oblique Incidences. 2007
- [54] Radzimski, Z. J.: Directional copper deposition using dc magnetron self-sputtering. *Journal of Vacuum Science & Technology B: Microelectronics and Nanometer Structures* 16 (1998) 3, S. 1102
- [55] Stuart, R. V.: Vacuum technology, thin films, and sputtering. An introduction. New York: Academic Press 1983
- [56] Anne-Marie Valente-Feliciano: Review on Energetic Deposition, 2012
- [57] Anders, A.: A structure zone diagram including plasma-based deposition and ion etching. *Thin Solid Films* 518 (2010) 15, S. 4087–4090
- [58] Wolfgang Schmid: Construction of a sputtering reactor for the coating and processing of monolithic U-Mo nuclear fuel. PhD Thesis. München: Technische Universität München 2011
- [59] Thornton, J. A.: Magnetron sputtering: basic physics and application to cylindrical magnetrons. *Journal of Vacuum Science and Technology* 15 (1978) 2, S. 171
- [60] Henze BNP AG: HeBoSint Bornitridqualitäten, 2015. [http://www.henze-bnp.de/PDF/HeBoSint\\_Uebersicht.pdf](http://www.henze-bnp.de/PDF/HeBoSint_Uebersicht.pdf)
- [61] J. Kriegesmann: Technische keramische Werkstoffe. Köln: Dt. Wirtschaftsdienst 1989
- [62] Haynes, W. M., Lide, D. R., Bruno, T. J.: CRC handbook of chemistry and physics. A ready-reference book of chemical and physical data : 2013-2014. Boca Raton (Fla.), London, New York: CRC Press op. 2013
- [63] Deutsches Kupferinstitut: Werkstoff-Datenblatt Cu-ETP - CW004A (2.0065, 2.0060), 2015. [https://www.kupferinstitut.de/fileadmin/user\\_upload/kupferinstitut.de/de/Documents/Shop/Verlag/Downloads/Werkstoffe/Datenblaetter/Kupfer/Cu-ETP.pdf](https://www.kupferinstitut.de/fileadmin/user_upload/kupferinstitut.de/de/Documents/Shop/Verlag/Downloads/Werkstoffe/Datenblaetter/Kupfer/Cu-ETP.pdf)
- [64] MatWeb, LLC: Material property data, 2015. [www.matweb.com/](http://www.matweb.com/)

- [65] Parashar, B. S. Nagendra, Mittal, R. K.: Elements of manufacturing processes. New Delhi: Prentice-Hall of India 2003
- [66] Rainer Jungwirth: Irradiation behavior of modified high-performance nuclear fuels. PhD Thesis. München: Technische Universität München 2011
- [67] Ziegler, J. F., Biersack, J. P., Ziegler, M. D.: SRIM, the stopping and range of ions in matter. Chester, Maryland: SRIM Co 2008
- [68] Hsin-Yin Chiang: Material Selection of UMo Fuel for Research Reactors: Swift Heavy Ion Irradiation Studies. PhD Thesis. München: Technische Universität München 2014
- [69] Vandegriff, G. F., Conner, C., Hofman, G. L., Leonard, R. A., Mutalib, A., Sedlet, J., Walker, D. E., Wiencek, T. C., Snelgrove, J. L.: Modification of targets and processes for conversion of <sup>99</sup>Mo production from high- to low-enriched uranium. Industrial and Engineering Chemistry Research 39 (2000) 9, S. 3140–3145
- [70] Stokes, R. J., Evans, D. F.: Fundamentals of interfacial engineering. Advances in interfacial engineering series. New York: Wiley-VCH 1997
- [71] W. Verscharen: Geometrie des Sputterprozesses. Sputtergeschwindigkeit. 11. Deutsches Anwendertreffen "Analytische Glimmentladungs-Spektrometrie". Dresden 2004
- [72] Vossen, J. L., Kern, W.: Thin film processes. New York: Academic Press 1978
- [73] COMSOL: COMSOL Multiphysics. 2015
- [74] Atlas of stress-strain curves. Materials Park, OH: ASM International 2002
- [75] Luis Olivares, Jame Lisboa: Coating of LEU foil with electrodeposited nickel for <sup>99</sup>Mo production. RRFFM. Bucharest 2015
- [76] Psyk, V., Risch, D., Kinsey, B. L., Tekkaya, A. E., Kleiner, M.: Electromagnetic forming—A review. Special Issue: Impulse Forming 211 (2011) 5, S. 787–829
- [77] Michael Huber: Magnetimpulsschweißen (MPW): Machbarkeitsuntersuchung zum Schweißen/Crimpen von Al-Rohren mit Cu-Folie. München 2014
- [78] Hahn, R.: Werkzeuge zum impuls-magnetischen Warmfügen von Profilen aus Aluminium- und Magnesiumlegierungen. Berichte aus dem Produktionstechnischen Zentrum Berlin. Stuttgart: Fraunhofer-IRB-Verl. 2004
- [79] Thibaudeau, E., Kinsey, B. L.: Analytical design and experimental validation of uniform pressure actuator for electromagnetic forming and welding. Journal of Materials Processing Technology 215 (2015) 0, S. 251–263

# Danksagung

---

Zum Schluss meiner Doktorarbeit möchte ich mich noch bei all denen bedanken, die mich während meiner Promotion, aber auch in der Studienzeit unterstützt haben.

Ein herzlicher Dank gilt dabei meinem Doktorvater Prof. Dr. Winfried Petry, der mir die Promotion über dieses höchst interessante Thema ermöglicht hat. Ich bedanke mich für das in mich gesetzte Vertrauen und die gute Betreuung.

Darüber hinaus möchte ich mich bei Dr. Rainer Großmann für die gute Zusammenarbeit und seine Unterstützung in allen genehmigungstechnischen Fragen bedanken. Dank seiner Hilfe konnten viele Hürden überwunden werden.

Für die hervorragende fachliche und kollegiale Zusammenarbeit danke ich meinem Kollegen Christian Steyer. Durch unserer meist konträren Standpunkte sind viele fruchtbare Diskussionen entstanden, die wir immer mit guten innovativen Lösungen beenden konnten.

Ein herzliches Vergelt's Gott geht an Arnulf Grimm und Max Kraut für ihren unermüdlichen Einsatz bei der Probenpräparation und anderen spannenden Aufgaben.

Darüber hinaus gilt mein Dank natürlich auch der restlichen Arbeitsgruppe: Dr. Anton Röhrmoser, Bruno Baumeister, Christian Steyer, Christian Reiter, Dr. Harald Breitreutz, Dr. Hsin-Yin Chiang, Dr. Rainer Jungwirth, Robert Schenk, Rupert Schauer, Steffen Säubert, Tanja Huber, Tobias Chemnitz, Dr. Tobias Zweifel und Dr. Wolfgang Schmid. Vielen Dank für das gute Arbeitsklima und die vielfältige Unterstützung bei meiner Doktorarbeit!

Dem Werkstatt-Team des FRMs und des Physikdepartments danke ich für die fertigungstechnische Umsetzung all meiner Ideen. Besonders bedanken möchte ich mich hier bei Uwe Stiegel, der mir stets mit Rat und Tat zur Seite stand. Ebenso danke ich Katherina Bulla und Philip Schultheiß für ihre tatkräftige Unterstützung.

Des Weiteren danke ich Dr. Thorsten Lauer für die wertvolle Hilfe in der Anfangszeit meiner Doktorarbeit. Das von ihm zur Verfügung gestellte Equipment hat meinen Einstieg in die Kathodenzerstäubung (trotz des einen oder anderen Missgeschicks) sehr erleichtert. Vielen Dank auch an Walter Carli, Fritz Haftlmeier und Georg Obermaier des Maier-Leibnitz-Laboratoriums für die große Hilfe bei all den „kleinen“ technischen Problemen.

Ein herzlicher Dank gilt meinen Eltern Karin und Franz, die mich stets finanziell und moralisch während des gesamten Studiums und der Promotion unterstützt haben.

Nicht zuletzt bedanke ich mich aus tiefstem Herzen bei meiner Freundin Julia. Sie hat mich mit viel Geduld durch die letzten Monate der Promotion begleitet und mich stets moralisch sowie praktisch unterstützt.